

NORTHWESTERN UNIVERSITY

Synthesis and Characterization of Hybrid Organic-Inorganic Structures for
Photovoltaic Devices

A DISSERTATION

SUBMITTED TO THE GRADUATE SCHOOL
IN PARTIAL FULFILLMENT OF THE REQUIREMENTS

for the degree

DOCTOR OF PHILOSOPHY

Field of Materials Science and Engineering

By

Daniel Joseph Fairfield

EVANSTON, ILLINOIS

June 2018

© Copyright by Daniel Joseph Fairfield 2018
All Rights Reserved

ABSTRACT

Synthesis and Characterization of Hybrid Organic-Inorganic Structures for Photovoltaic Devices

Daniel Joseph Fairfield

Developing low-cost, scalable, high-efficiency photovoltaic materials is an important technological challenge because of the projected increase in global energy consumption in coming years, the environmental cost of carbon emissions, and the widespread availability of solar energy. This dissertation contains three studies on the development of novel hybrid materials as photovoltaic active layers and uses structure-processing-property relationships to improve efficiency and stability in these photovoltaic devices. In the first study, an electrodeposited hybrid zinc oxide-organic lamellar structure was investigated as a potential photovoltaic active layer. The zinc oxide-organic lamellar structure formed nanoscale p-n junctions, and novel synthetic organic dyes balanced visible light absorption with solubility in the electrodeposition solvent mixture. Morphological characterization revealed that the electrodeposited structures formed thick, porous films. Grazing-incidence X-ray scattering studies showed that the hybrid lamellar structure will electrodeposit with a variety of organic dyes with non-crystalline packing, but the inorganic domains were invariably sub-nanometer thick sheets based on the layered double hydroxide structure. Initial thin film device experiments yielded very low power conversion efficiency, and thus dye-sensitized solar cells were fabricated with this nanoscale architecture as the active layer to improve efficiency in these devices. Single-step electrodeposition of these active layers represents a significant improvement to the throughput of the dye-sensitized solar cell manufacturing process. Functioning dye-sensitized devices were prepared from these lamellar scaffolds, although at lower efficiency than control bulk heterojunction or dye-sensitized devices. Various control devices and impedance spectroscopy explained why conventional device architectures such as dye-sensitized mesoporous scaffolds and bulk heterojunctions outperform this new nanostructured photovoltaic active layer. Specifically, within a dye-sensitized

device, the electrolyte did not access the interior lamellar surfaces, and the dye molecules aggregated on the inorganic surface which caused recombination at the dye-electrolyte interface. In the second study, the stability of methylammonium lead iodide-based perovskite solar cells is improved by adding poly(acrylic acid) to the active layer. Adding polymers to methylammonium lead iodide perovskite solar cell active layers has previously been shown to increase the stability of the perovskite devices in dark, ambient conditions, but the nanostructures and stabilization mechanisms of these hybrid materials were poorly understood in these other studies. In this work, a structural and spectroscopic investigation on a number of perovskite-polymer hybrid materials was carried out, and their temporal stability as well as solar cell performance under operating conditions were compared. Using nanomechanical atomic force microscopy and transmission electron microscopy, perovskite crystallite sizes were observed to decrease with the addition of polymers, and the perovskite-polymer hybrid formed sub-micrometer-scale domains upon film casting. It is suggested that acid-base interactions, as well as facet-dependent interfacial interactions between perovskite and polymer, contributed to differences in stabilities of these hybrid materials. The polymers studied tended to suppress the formation of the hydrate crystal phase that accelerates the degradation reaction. Among these polymers, adding poly(acrylic acid) was found to significantly increase the stability of perovskite films under humid air and ambient illumination. Under these conditions, poly(acrylic acid)-perovskite hybrid solar cells maintained stable performance over a much longer time period than control devices. These results highlight the importance of choosing suitable functional groups in the polymer phase of perovskite solar cells to prolong their device lifetime. In the last study, novel layered perovskite structures were prepared using a systematic organic synthetic approach inspired by the approach followed in the zinc oxide studies. Layered perovskites have excellent environmental stability but poor photovoltaic function due to the preferential orientation of the semiconducting layers parallel to the substrate and the typically insulating nature of the cation. A series of these $n = 1$ layered perovskites with the form (aromatic-O-linker-NH₃)₂PbI₄ were synthesized and characterized. These materials achieved enhanced conductivity perpendicu-

lar to the inorganic layers over three orders of magnitude higher than control layered perovskites with aliphatic organic cations due to better energy level matching between the inorganic layers and organic galleries. This study revealed two key structure-property relationships between cation conformation and optoelectronic properties. First, hydrogen bonding within the organic galleries can be used to avoid distortions of the inorganic lattice, resulting in narrower bandgaps. Secondly, out-of-plane conductivity in layered perovskites is enhanced by favorable π -stacking interactions within the organic galleries. The enhanced conductivity and absorption of these materials led to a champion power conversion efficiency of 1.24%, which is the highest value reported for a chemically stable $n = 1$ layered perovskite. As a whole, these studies demonstrate three different approaches to creating hybrid organic-inorganic photovoltaic active layers and demonstrate the importance of leveraging the optoelectronic properties of organic constituents in order to enhance the chemical stability and photovoltaic efficiency of devices.

ACKNOWLEDGEMENTS

First and foremost, I would like to thank Professor Stupp for his support of my research over the past 6 years. He has given me the freedom to pursue a variety of projects throughout my time as a PhD student, and under his leadership I have become a better scientist. Graduate students in this lab are the managers of their own projects, and this directive has led me in some interesting directions and provided me with a sense of self-sufficiency that should serve me well in the future.

I would like to thank my committee members: Professor Lincoln Lauhon, Professor Jiaxing Huang, and Professor Danna Freedman for their valuable time and feedback on my thesis. I hope that this thesis proves to be fertile ground for scientific discussion and insight. I would also like to thank Dr. Liam Palmer for his help throughout graduate school. He has given me a lot of feedback on paper drafts, the direction of my research, advice in subgroup, and navigating the interpersonal aspects of graduate school. Two Professors from my undergraduate career at University of Illinois at Urbana-Champaign, Professor Nancy Sottos and Professor David Ruzic, gave me my start in academic research. I would like to thank them both for giving me the opportunity to learn more about academic research at a time in my career where I didn't know how to do very much in a laboratory yet.

I would like to thank my colleagues in the Stupp group. The projects that we work on in our group are ambitious, and we would not reach our targets without open collaboration between the many hard-working scientists in our laboratory. I would like to thank Dr. Dave Herman for mentoring me as a first-year student. He spent a lot of time teaching me new techniques, giving me advice on graduate school, and helping me in my first graduate research project. I would also like to thank Dr. Taner Aytun. He taught me a lot about solar cell fabrication, and I was always able to ask him for help or advice throughout my time here. My biggest thanks goes to Dr. Hiroaki Sai and James Passarelli. The two of you have given so much of your time and effort towards the projects we collaborate on, and the questions and insights you have given to me have dramatically improved

the perovskite projects we worked on together. Without the two of you, these projects would not have gotten off the ground. Other collaborators on my studies include Leonel Barreda, Ashwin Narayanan, Michelle Chen, Nicholas Sather, Dr. Mark Hendricks, and Charlotte Stern. They have all contributed their time and talents to my projects and I am grateful for their help. I would also be remiss if I did not thank the undergraduates who have helped me during my PhD studies. Raymond Blackwell, Joe Palasz, and Karen Qu all worked very hard on portions of my research projects. I hope that my guidance has proved as useful in your studies as the mentoring that I received as an undergraduate researcher. I would also like to thank the researchers who have graciously asked for my help in their studies. Dr. Roman Kazantsev, Dr. Adam Weingarten, and Adam Dannenhoffer have all asked for my help in their studies of self-assembling photocatalytic hydrogen production scaffolds. My contributions to their projects helped me learn more about photocatalysis, and I am happy that my skills with X-ray photoelectron spectroscopy and grazing-incidence wide-angle X-ray scattering proved to be useful contributions to your projects.

My research wouldn't have been possible without the help of the administrative staff of the Stupp group, the central facilities at Northwestern, the Advanced Photon Source at Argonne National Lab, and funding. I would like to specifically thank Laura Fields, Maura Walsh, and Todd Linton for administrative help during my time in the Stupp group. Our organization would not run without the hard work of these individuals. I was able to use a number of central facilities at Northwestern during the course of my research including NUANCE, Keck, Keck-II, IMSERC, the Energy Materials Laboratory, NUFAB, the J.B. Cohen X-ray Laboratory, and MATCI. A lot of work goes into the maintenance and operation of those facilities, and without them I wouldn't have been able to acquire most of the data contained in this thesis. I would like to thank Joe Strzalka at Sector 8 of the Advanced Photon Source at Argonne National Lab for his help with X-ray experiments at ANL. He has always been extremely helpful to our lab's research. My research was funded by the United States Department of Energy.

Finally, I would like to personally thank my family, my friends, and my lovely wife, Katie. Their love and support have kept me going over the years. They have been there for me through the good times and bad times in graduate school. About two years ago, I broke my ankle playing intramural sports at NU, and they were the ones who helped me when I couldn't walk. I can't thank you all enough for being there for me when I needed it most.

LIST OF ABBREVIATIONS

AFM Atomic Force Microscopy

BHJ Bulk Heterojunction

CA Chromophore Amphiphile

DCM Dichloromethane

DMF Dimethylformamide

DMSO Dimethyl sulfoxide

d_{N-I} Peripheral nitrogen-to-iodine distance

DSSC Dye-sensitized solar cell

E_b Energy barrier

E_{S1} Energy of S1 exciton peak

EQE External quantum efficiency

GIWAXS Grazing-incidence Wide-Angle X-ray Scattering

η Power conversion efficiency

HPLC High-Performance Liquid Chromatography

J_{SC} Short-circuit current

LCOE Levelized cost of energy

MAI Methylammonium Iodide

NMP N-Methyl-2-pyrrolidone

NREL National Renewable Energy Laboratory

OPV Organic Photovoltaic

PAA Poly(acrylic acid)

PCBM Phenyl-C61-butyric acid methyl ester

PCE Power conversion efficiency

PEDOT:PSS Poly(3,4-ethylenedioxythiophene) polystyrene sulfonate

PEG Polyethylene glycol

PSC Perovskite Solar Cell

PV Photovoltaic

P3HT Poly(3-hexylthiophene-2,5-diyl)

PVP Polyvinylpyrrolidone

RT Room Temperature

SAXS Small-angle X-ray Scattering

SCE Saturated calomel electrode

SEM Scanning Electron Microscopy

Spiro-OMeTAD N²,N²,N^{2'},N^{2'},N⁷,N⁷,N^{7'},N^{7'}-octakis(4-methoxyphenyl)-9,9'-spirobi[9H-fluorene]-2,2',7,7'-tetramine

TEM Transmission Electron Microscopy

V_{OC} Open-circuit voltage

3T Terthiophene

5T Quinquethiophene

5TmDCA Dicarboxylic acid 3-methyl-quinquethiophene

This dissertation is dedicated to my wife Katie and to my parents.

CONTENTS

ACKNOWLEDGEMENTS	6
LIST OF ABBREVIATIONS	9
1 INTRODUCTION	18
1.1 Significance of solar cell research	18
1.2 Theoretical background of photovoltaics	25
1.3 Organic chemistry, design, and self-assembly within hybrid organic-inorganic materials	34
1.4 Thesis overview	36
2 LAMELLAR HYBRID SOLAR CELLS	37
2.1 Objectives and significance	37
2.2 Background	38
2.3 Results and discussion	46
2.3.1 Morphology and structure of ZnO-organic dye hybrids	46
2.3.2 Lamellar Hybrid Photovoltaic Devices	56
2.3.3 PEG-DPPCN control device study	60
2.3.4 N719 control device study and electrochemical impedance spectroscopy	66
2.4 Conclusions, limitations, and future outlook	70
2.5 Materials and methods	74
3 STRUCTURE-PROPERTY RELATIONSHIPS IN PEROVSKITE-POLYMER HYBRID SOLAR CELLS	83
3.1 Objectives and Significance	83
3.2 Background	83
3.3 Results and discussion	86
3.3.1 Active layer morphology	86
3.3.2 Film stability and intermolecular interactions	94
3.3.3 Photovoltaic performance and stability	109
3.4 Conclusions	117
3.5 Materials and methods	118
3.5.1 Chemical synthesis	118
3.5.2 Characterization	118
3.5.3 Substrate preparation	119
3.5.4 Single crystal growth	120
3.5.5 Device fabrication	120
3.5.6 Long term stability testing	120

4	ENHANCED OUT-OF-PLANE CONDUCTIVITY AND PHOTOVOLTAIC PERFORMANCE IN N = 1 LAYERED PEROVSKITES THROUGH ORGANIC CATION DESIGN	122
4.1	Objectives and significance	122
4.2	Background	122
4.3	Results and discussion	125
4.3.1	Synthesis and characterization of organic ammonium iodide salts	125
4.3.2	Crystal growth and optical properties	127
4.3.3	Out-of-plane conductivity	138
4.3.4	Device fabrication and photovoltaic performance	145
4.4	Conclusions and future outlook	153
4.5	Materials and methods	156
4.5.1	Synthesis	156
4.5.2	Single crystal preparation for structure evaluation and conductivity measurements	170
4.5.3	Crystal structure determination	173
4.5.4	Substrate preparation	173
4.5.5	Thin film preparation	175
4.5.6	Device fabrication	176
4.5.7	NMR characterization	176
4.5.8	Mass determination	176
4.5.9	UPS Measurements	176
5	SUMMARY	178
	REFERENCES	180
	VITA	188

LIST OF TABLES

- 4.1 Crystal data for layered perovskites 129
- 4.2 Photovoltaic parameters for control devices 150
- 4.3 Crystallization conditions for layered perovskites 171

LIST OF FIGURES

- 1.1 World solar PV production 19
- 1.2 Historical greenhouse gas levels 21
- 1.3 Recent atmospheric CO₂ levels 22
- 1.4 Cost trends in solar panels 2011-2017 23
- 1.5 Levelized cost of PV energy 2010-2017 24
- 1.6 Spectral intensity of solar irradiance 28
- 1.7 PV device cross section and energy band diagram 29
- 1.8 Labeled I-V curve of a typical PV device 30
- 1.9 PV equivalent circuit 31
- 1.10 Efficiency vs. relative bandgap of various PV materials 32
- 1.11 Best research cell efficiencies 33

- 2.1 Layered double hydroxide structure 38
- 2.2 Lamellar electrodeposited structure 41
- 2.3 Orientational control of hybrid nanostructures 43
- 2.4 Preliminary morphological characterization 44
- 2.5 5TmDCA thin film solar cells 45
- 2.6 EQE and Cross-sectional SEM of 5TmDCA solar cells 46
- 2.7 2TDPP-C3CA structure and characterization 48
- 2.8 PEG-DPPCN structure and characterization 50
- 2.9 3T-E2 structure and characterization 52
- 2.10 3T-E3 structure and characterization 53
- 2.11 Small-angle X-ray scattering of 3T molecules 55
- 2.12 Energy levels of 2TDPP-C3CA in a solar cell 57
- 2.13 2TDPP-C3CA thin film I-V curve and EQE 58
- 2.14 DSSC device schematic and PEG-DPPCN energy band diagram 59
- 2.15 Lamellar DSSC device comparison 61
- 2.16 Desorption of PEG-DPPCN from lamellar structure 63
- 2.17 EQE of PEG-DPPCN DSSCs 64

2.18	AFM of PEG-DPPCN-PCBM bulk heterojunction	65
2.19	PEG-DPPCN control device study	67
2.20	TiO ₂ DSSC control device study	68
2.21	Electrochemical impedance spectroscopy study	69
2.22	Synthetic scheme for 2TDPP-C3CA	75
2.23	Synthetic scheme for PEG-DPPCN	75
2.24	Synthetic scheme for 3T-E2	76
2.25	Synthetic scheme for 3T-E3	77
2.26	AFM of ZnO sol-gel	78
2.27	Critical aggregation concentration study	80
2.28	DSSC device fabrication procedure	82
3.1	Preliminary morphological characterization	88
3.2	TEM of perovskite-polymer hybrids	89
3.3	TEM phase contrast in perovskite-polymer hybrids	91
3.4	Nanomechanical AFM of MAPbI ₃ and MAPbI ₃ -PAA	92
3.5	Linecuts of MAPbI ₃ AFM data	93
3.6	Nanomechanical AFM of poly(acrylic acid)	94
3.7	Nanomechanical AFM of MAPbI ₃ -PEG and MAPbI ₃ -PVP	95
3.8	Film degradation under 85% humidity and illumination	97
3.9	Film degradation under 43% humidity and illumination	98
3.10	Water absorption of polymers	99
3.11	FT-IR of perovskite-polymer hybrids	100
3.12	NMR of perovskite-polymer solutions	102
3.13	NMR of polymers vs. perovskite-polymer solutions	103
3.14	Polymer-dependent single crystal faceting of MAPbI ₃	106
3.15	MAPbI ₃ cut along single crystal termination planes	107
3.16	Iodine vapor degradation of perovskite-polymer hybrids	108
3.17	Iodine absorption by polymers	109
3.18	Device cross-section	110
3.19	Effect of processing on hybrid crystallinity	112
3.20	Steady-state photoluminescence of perovskite-polymer hybrids	113
3.21	Time-resolved photoluminescence of perovskite-polymer hybrids	114
3.22	Perovskite-PAA solar cell performance in illuminated, humid conditions	115
3.23	Perovskite-PAA solar cell performance in dark, humid conditions	116
4.1	Modular molecular design of layered perovskites and energy band diagram	126
4.2	GIWAXS fitting vs powder XRD of layered perovskite thin films	130
4.3	GIWAXS fitting of layered perovskite thin films	131
4.4	UV-Vis spectroscopy of layered perovskite thin films	132

- 4.5 E_{S1} and bandgap energies in UV-Vis spectra 133
- 4.6 Octahedral distortion vs. E_{S1} in layered perovskites 133
- 4.7 E_{S1} vs. ammonium penetration past peripheral iodides 134
- 4.8 E_{S1} vs. d_{N-I} 136
- 4.9 XRD and UV-Vis of two (pyrene-O-propyl-NH₃)₂PbI₄ phases 137
- 4.10 Out-of-plane conductivity of layered perovskite single crystals 139
- 4.11 Out-of-plane conductivity values in the dark 140
- 4.12 Median conductivity vs. layered spacing 142
- 4.13 Packing within organic galleries compared to conductivity 143
- 4.14 edge-to-edge packing of (perylene-O-ethyl-NH₃)₂PbI₄ 144
- 4.15 Photovoltaic devices, efficiency, morphology and stability of (pyrene-O-propyl-NH₃)₂PbI₄ 147
- 4.16 Ultraviolet photoelectron spectroscopy of (pyrene-O-propyl-NH₃)₂PbI₄ 148
- 4.17 Herman's factor orientational analysis of (pyrene-O-propyl-NH₃)₂PbI₄ 152
- 4.18 Degradation study of (pyrene-O-propyl-NH₃)₂PbI₄ in water 154
- 4.19 Comparison of perovskite thin film degradation in water 154
- 4.20 Unit cell parameters and orientation of layered perovskite crystals 174

1 INTRODUCTION

1.1 SIGNIFICANCE OF SOLAR CELL RESEARCH

Developing low-cost, scalable, high-efficiency solar cells is an important technological challenge because of the projected increase in global energy consumption in coming years, the environmental cost of carbon emissions, and the widespread availability of solar energy. World energy consumption is expected to roughly double by 2050 to 27 TW/year.¹ According to Lewis and Nocera, “By almost any reasonable estimate, stabilization of atmospheric CO₂ levels at 550 ppm or lower will require as much carbon-neutral power by approximately the year 2050 as the amount of power produced at present from all energy sources combined.”¹ Solar energy is the most abundant and accessible form of energy that we have, with more energy from the sun striking the earth in 90 minutes¹ (6.45×10^{20} J) than all of the energy currently consumed on the planet in 1 year (5.381×10^{20} J in 2012).² Harvesting even a small fraction of the incident light on our planet could theoretically allow us to generate enough electricity for all our energy needs. However, improvements need to be made both in photovoltaic technology and energy storage to meet the growing global demand for energy. Organic and hybrid solar cells are candidates for addressing part of this demand because they can be made from earth-abundant materials with solution-based processes. In the most general sense, this thesis works towards improving photovoltaic technology through research in developing new materials for hybrid solar cells.

Within the current energy landscape, solar energy, as of 2016, produces 1.3% of the total electricity generated globally.³ This seemingly small percentage belies the exponential increase in the installed capacity of photovoltaics in the decade between 2005 and 2015. Over this 10-year span, global energy production has grown from 4 TWh to 247 TWh (figure 1.1).⁴ The amount of capacity installed per year is increasing every year which represents an exponential growth rate. In 2016, the growth of solar energy represented 20% of the total increase in global power generation.³ When

World solar PV electricity production from 2005 to 2015 by region (TWh)

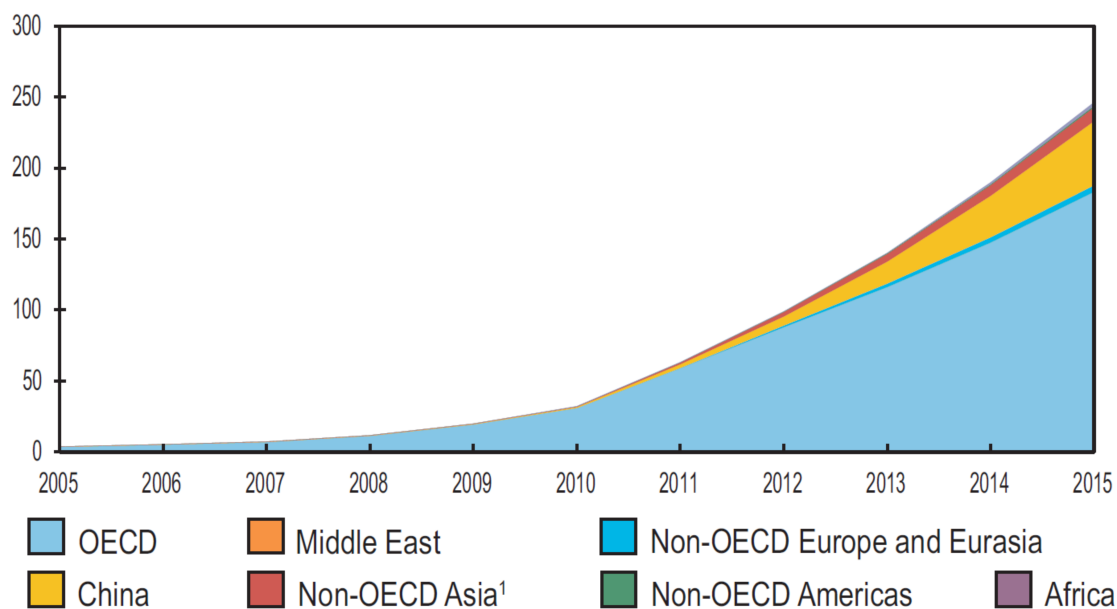


Figure 1.1: Graph showing increase in global solar PV production from 2005 to 2015. Global production increased over this time from 4 TWh to 247 TWh. Figure adapted from International Energy Agency report.⁴

compared to other energy sources (coal, nuclear, natural gas, wind), wind is the only other energy source experiencing this same degree of growth. Over the same period, 2005 to 2015, annual wind power generation grew from 104 TWh to 838 TWh.⁴

Two significant factors can explain the growth in renewable energy generation in the past decade. First, and foremost, is concern over global warming. Anthropogenic carbon dioxide generation continues to increase at an alarming rate (figure 1.2)⁵, and global CO₂ levels have risen above 400 ppm for the first time in modern history (figure 1.3).⁶ The increase in greenhouse gases shown in figure 1.2 causes a phenomenon known as radiative forcing. As the concentration of CO₂, methane, and nitrous oxide in the atmosphere increase, the balance of the energy that the earth absorbs and emits shifts towards absorption, leading to an overall warming of the planet⁵.

This warming can have dire consequences for the environment as the Intergovernmental Panel on Climate Change clearly states:

Palaeoclimatic information supports the interpretation that the warmth of the last half century is unusual in at least the previous 1,300 years. The last time the polar regions were significantly warmer than present for an extended period (about 125,000 years ago), reductions in polar ice volume led to 4 to 6 m of sea level rise.⁵

The grim warnings given by the climate science community point towards a clear conclusion: the electricity that we produce going forward needs to be carbon-neutral, and the only large-scale energy sources that fit that criterion are photovoltaic solar, wind, and nuclear.

The second factor relevant to the expansion of renewable energy is that reductions in cost have made them economically viable compared to other forms of electricity generation. The SunShot initiative, one of the goals of the U.S Department of Energy, was launched in 2011 to reduce the cost of solar energy so that it is competitive with other forms of electricity generation. From 2010 to 2017, the cost of utility-scale PV installations has gone down from \$5.44/Watt to \$1.11/Watt (figure 1.4).⁷ The 2020 goal of the SunShot initiative was for the levelized cost of electricity (LCOE) for unsubsidized solar power to cost 6 cents/kWh. We have reached that goal 3 years ahead of schedule as of September 2017, as shown in figure 1.5.⁷ If we consider just the cost of the module, the cost has significantly declined from ~\$1.50/Watt to \$0.35/Watt due to technology improvements and economies of scale associated with the production of crystalline silicon solar cells.⁷ Thus, crystalline silicon solar cells are being manufactured and installed at the utility scale as cheaply as conventional power sources.

With such a significant expansion in installed photovoltaic capacity in recent years, then, there needs to be another justification for development of so-called “third generation photovoltaics” rather than simply module cost. These newest technologies, namely dye-sensitized solar cells (DSSCs), organic solar cells (OPVs), and perovskite solar cells (PSCs), may never supplant crystalline silicon solar cells as the active layer material in utility-scale solar installations. Many reviews on DSSCs

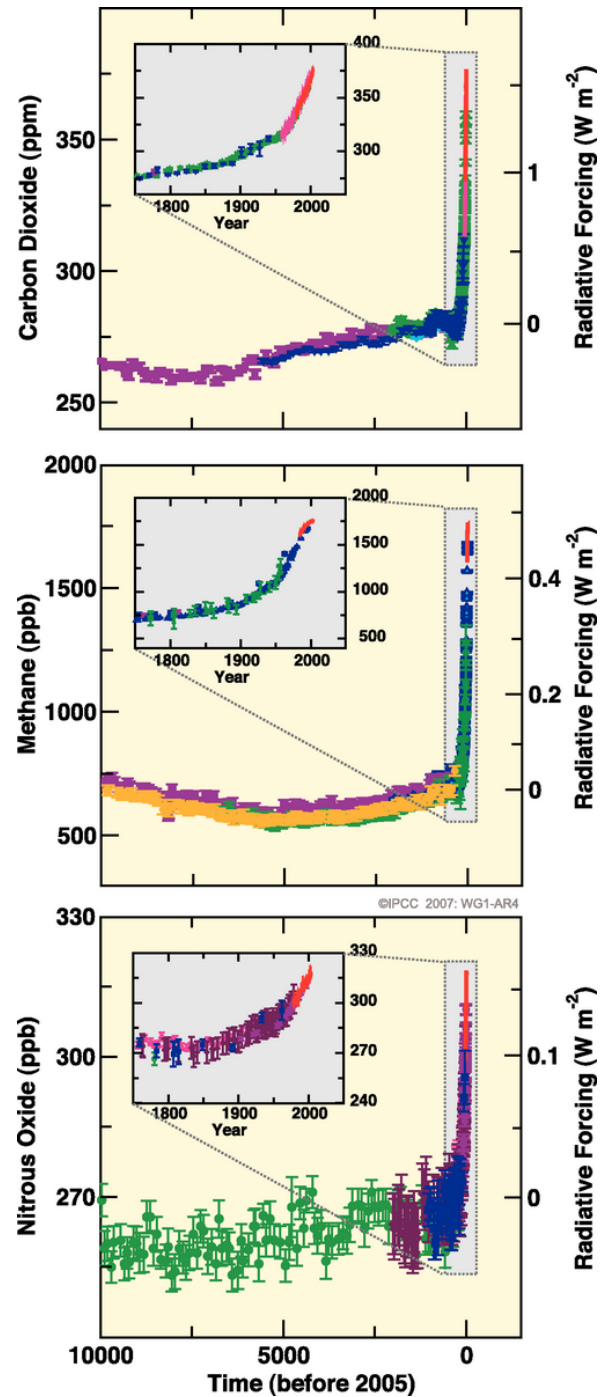


Figure 1.2: Graphs showing the contribution of CO₂, methane, and nitrous oxide to global warming over the past 10,000 years. Figure adapted from the Intergovernmental Panel on Climate Change 2007 report.⁵

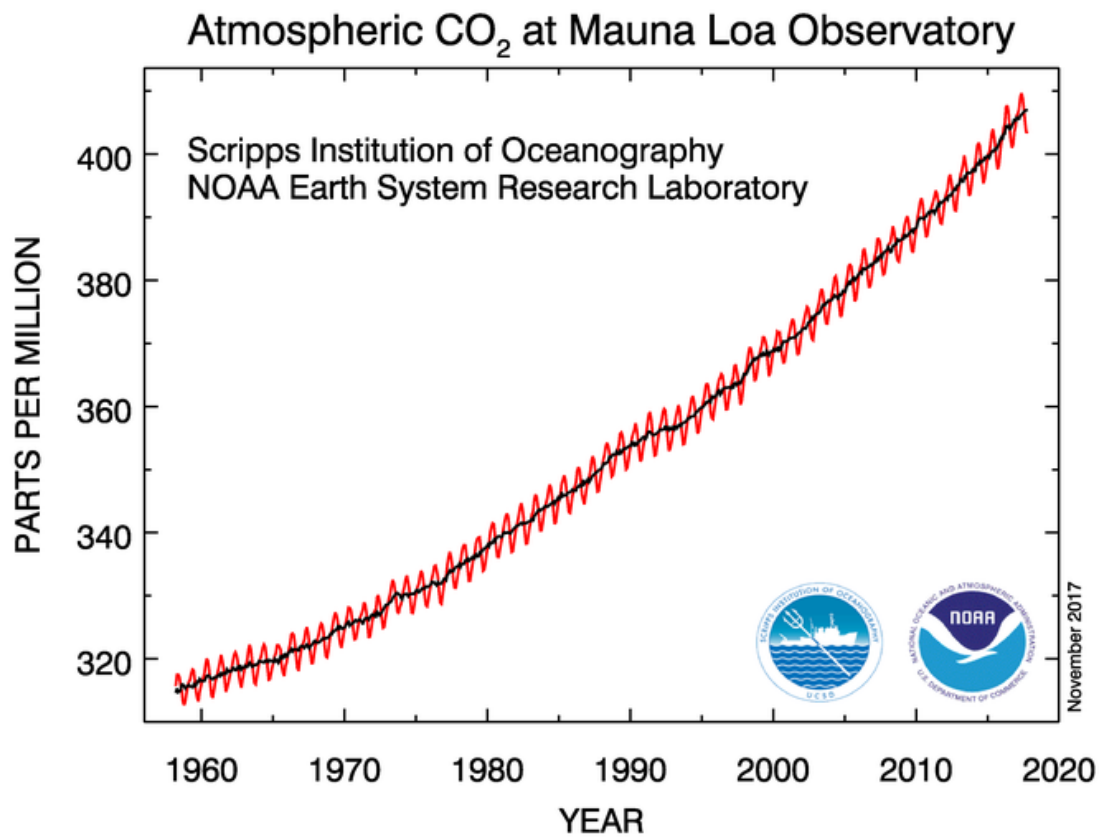


Figure 1.3: Atmospheric CO₂ recordings from 1960 to 2017 taken at Mauna Loa Observatory. Figure adapted from NOAA.⁶

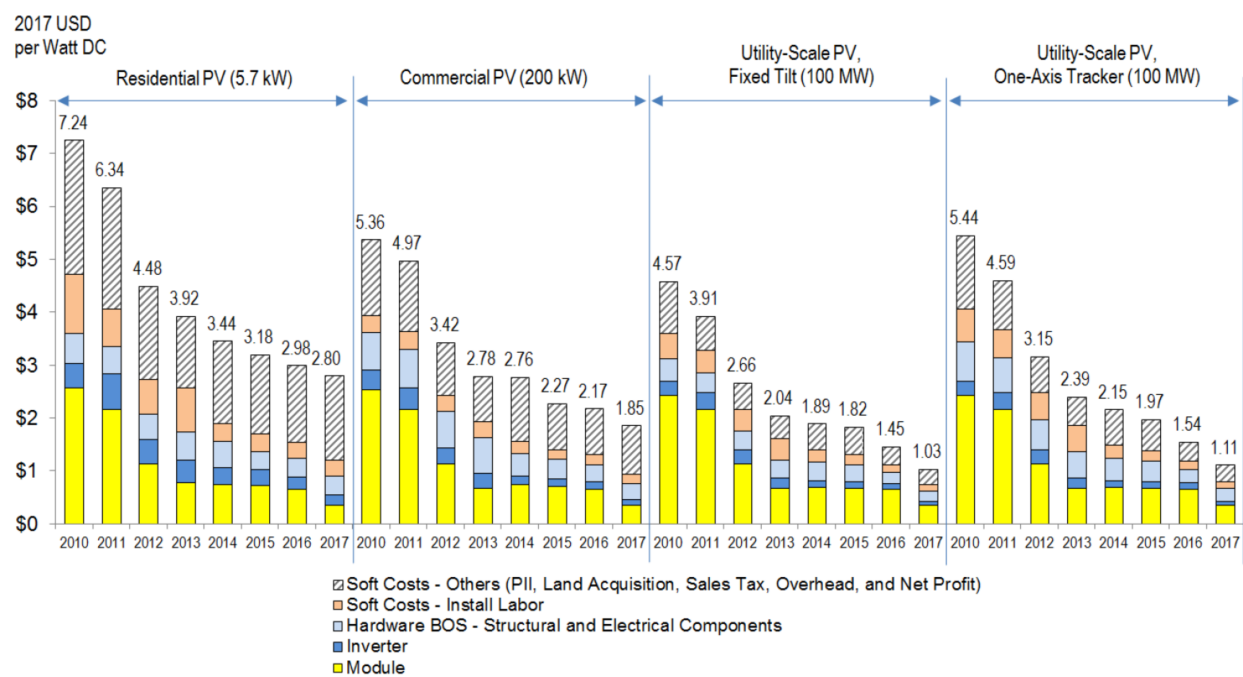


Figure 1.4: Price of solar installations in the U.S. broken down by cost per watt from 2010 to 2017. The module price in 2017 was \$0.35, and overall costs have declined by 57% since 2009. Figure adapted from NREL report on PV prices.⁷

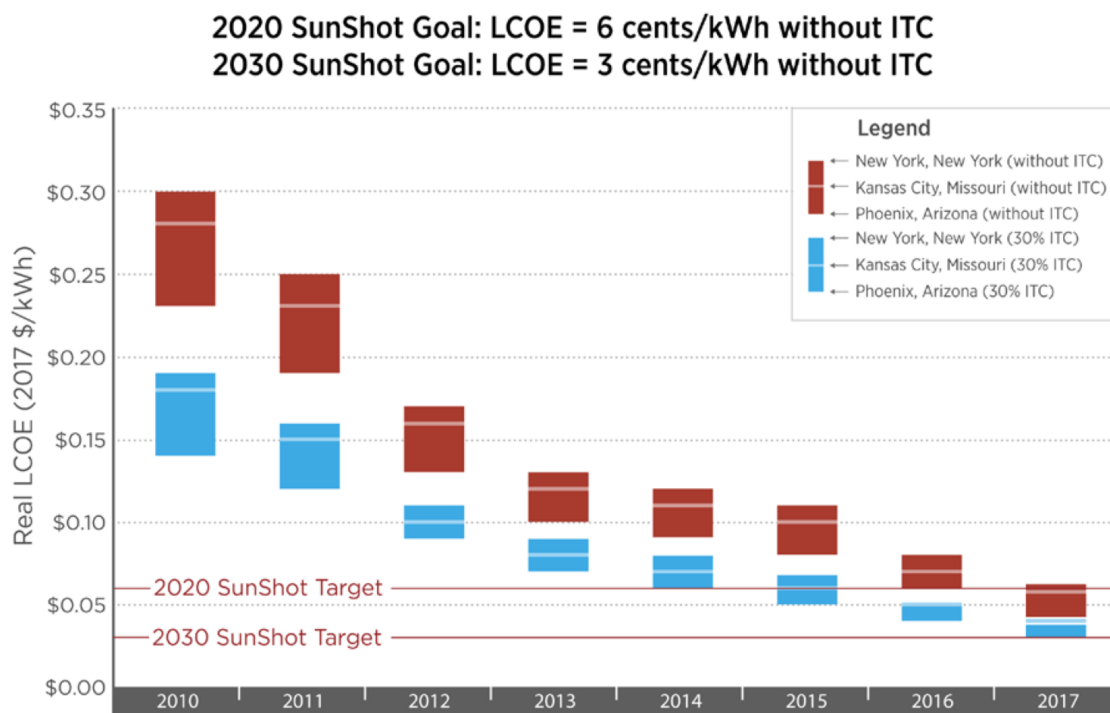


Figure 1.5: Graph showing LCOE of solar power from 2010 to 2017. Unsubsidized utility-scale solar power has achieved an LCOE of 6 cents per kWh which is the SunShot target for 2020. Figure adapted from NREL report on PV prices.⁷

and OPVs have touted the advantages of roll-to-roll processing^{8,9,10} allowing these materials to be printed cheaply on flexible substrates, but the price drop of silicon cells has caused most of these cost-oriented arguments to fall short. For example, one analysis from 2009 estimated that at 10% efficiency, the module cost of printed OPVs would be between \$0.50/Watt and \$1.41/Watt with a 5 year lifetime.⁸ They claim that for the LCOE to drop to about \$0.07/kWh OPVs would need to achieve efficiencies of 15% and lifetimes of 15-20 years⁸. The current \$0.06/kWh of silicon solar cells is already better than that benchmark, and even 8 years later efficiencies and lifetimes of laboratory-based OPVs have not reached those levels. Another analysis examining costs of DSSCs from 2011 optimistically projected that using roll-to-roll processes and flexible substrates for DSSCs could reduce the module cost to \$1/Watt,⁹ which again falls significantly short of current module costs for silicon-based PVs.

Therefore, we may hope to develop other applications for OPVs, DSSCs, and PSCs that aren't specifically tied to utility-scale generation. Some proposed applications of thin-film photovoltaics that are still possibilities for applications include¹⁰: semitransparent solar windows, solar textiles for wearable PV, high bandgap materials for tandem devices, and on-chip power for devices. One of the unique advantages of solar power is that it can be deployed almost anywhere at any size. New materials for photovoltaics, therefore, should leverage this advantage towards unique applications that can't be addressed by crystalline silicon solar cells.

1.2 THEORETICAL BACKGROUND OF PHOTOVOLTAICS

To discuss PV materials, we must first establish a baseline understanding of semiconductor devices. Although there are textbooks devoted to this subject, it is worthwhile here to at least introduce a few important concepts that are fundamental to the work described in later chapters of this dissertation. The following section uses material from Pierret's "Semiconductor Device Fundamentals,"¹¹ but the concepts herein should be explained thoroughly in any other similar text.

The energy band model of semiconductors describes the valence electrons in a crystalline solid as occupying a continuum of electronic states in accordance with the Pauli Exclusion principle disallowing multiple electrons from occupying the same electronic state. From this model, it follows that metallic materials do not have a band gap between valence electrons and conduction states, semiconductors have a moderate bandgap, typically 1-2 electron volts (eV), and insulators have wider bandgaps than that ($>5\text{eV}$). As the band gap of a material increases, the intrinsic carrier concentration also decreases, reducing overall conductivity of the material.¹¹

A unique property of semiconductors is that they can be doped (alloyed in very low concentrations) with other materials to create excess positive or negative charge carriers in the lattice which can modulate the conductivity of the semiconductor by several orders of magnitude. Generally, an atom that is doped into a semiconductor lattice with extra valence electrons compared to the host lattice will donate extra electrons as mobile charge carriers in the lattice. This is known as n-type doping since extra negative charge is mobile in the lattice. Similarly, an atom that is doped in with fewer valence electrons than the host lattice can lead to extra positive charge in the lattice in the form of an unsatisfied chemical bond. This positive charge is known as a hole, and it is also a mobile charge carrier in the lattice and doping to create excess holes in the material is known as p-type doping. When a p-type material and an n-type material are put into contact with each other, a pn junction is formed. The pn junction is the electronic device that is fundamental to every photovoltaic material. When a p-type material and an n-type material are put into contact with each other, excess electrons and holes diffuse into the oppositely-doped material. However, their parent donor and acceptor atoms remain fixed in the lattice, which creates a region with charged ions at the interface known as the space charge region. This built-in junction of positively and negatively charged donors gives rise to an electric field across the junction. When excess carriers are injected into this junction, either through carrier excitation (light absorption) or carrier injection (applied electrical bias), they are swept across the junction due to the electric field that is built-in to the pn junction. Therefore, the pn junction, in the simplest sense, can be conceptualized as a diode. Before

delving into the current-voltage characteristics of pn junctions and solar cells, it will be useful to first explain a bit more about the optoelectronic processes in a PV material.¹¹

The active layer of a photovoltaic material is a semiconductor pn junction with a band gap conducive to the absorption of photons from the sun. Optimal semiconductors for PV applications will have absorption spectra that closely match the peak of the solar irradiance spectrum (figure 1.6). When light with an energy higher than the bandgap is incident on a semiconductor, an electron-hole pair is formed. In inorganic semiconductors, the electron and hole immediately form free charge carriers in the device. In organic semiconductors, the electron-hole pair forms a more tightly-bound exciton. The exciton is confined to a single molecule, and needs to diffuse to an interface between a donor and acceptor to split into a free electron and hole. Once split into free charges, the electrons and holes need to diffuse to the contacts which is a process aided by both the built-in electric field of the device and the externally applied bias.

A band diagram is a useful tool to visualize the energy levels in materials that are placed in contact with each other. By placing the energy levels of materials in a solar cell onto a single plot, it is possible to visualize the energy cascade that charge carriers will experience as they are transported across the layers of the photovoltaic device. In an energy band diagram, we define 0 V to be the vacuum level energy, and the downward direction on the graph is lower in energy for negative charges. Therefore, electrons will have a driving force to go downhill in these diagrams, while holes, which represent positive charge, will go “uphill” in these diagrams. So far, we have discussed the active layer pn junction and how electrons and holes move within that layer. The other layers of the solar cell device act to reinforce the movement direction of electrons and holes in the device while providing electrical conductivity to transport charge and transparency to allow exciton generation to occur. A schematic band diagram and device cross section are shown in figure 1.7. Indium tin oxide, a transparent conductor, is a typical bottom contact in these devices. The active layer is sandwiched between hole and electron transport layers which have work functions or frontier orbital energy levels appropriate to conduct electrons or holes while excluding the other type of charge.

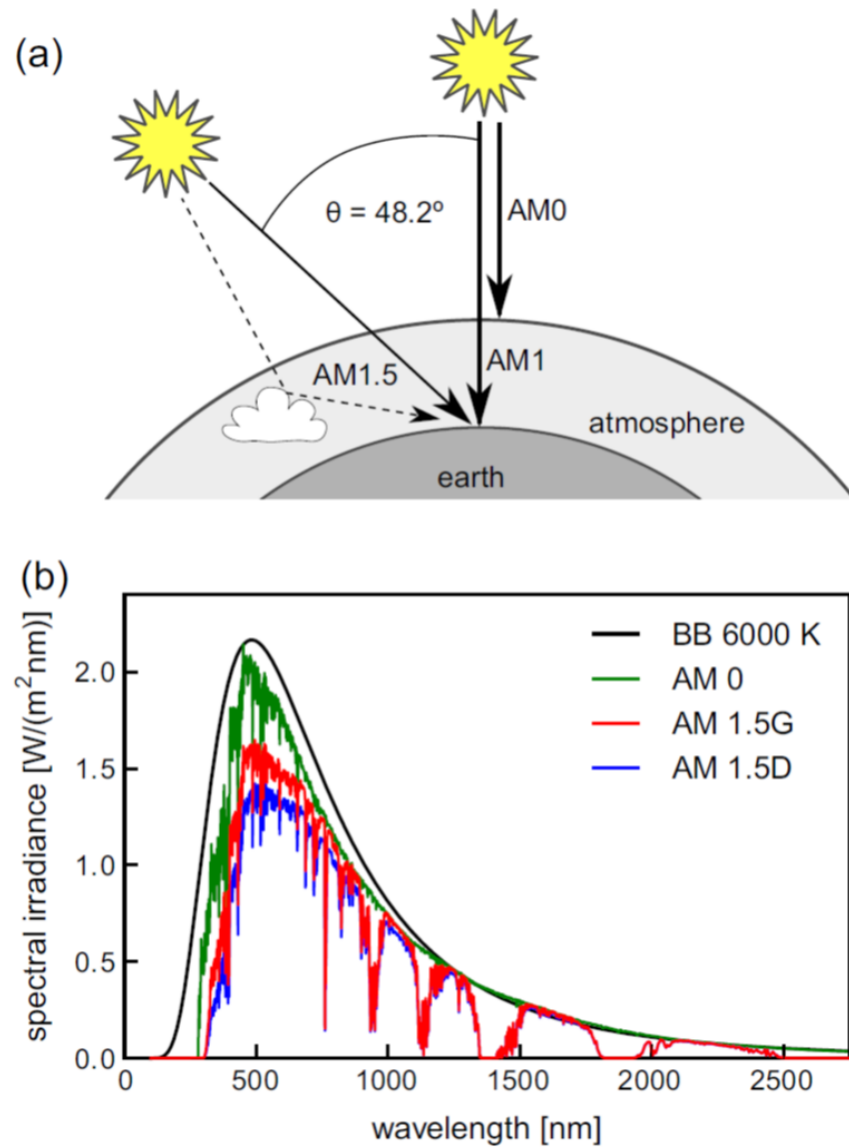


Figure 1.6: (a) a schematic showing the differences between how the solar spectrum is defined at different locations, and (b) a graph showing the solar spectrum as defined by the various AM standards. The black curve represents the blackbody radiation spectrum of an object at 6000 K. Figure adapted from Rühle.¹²

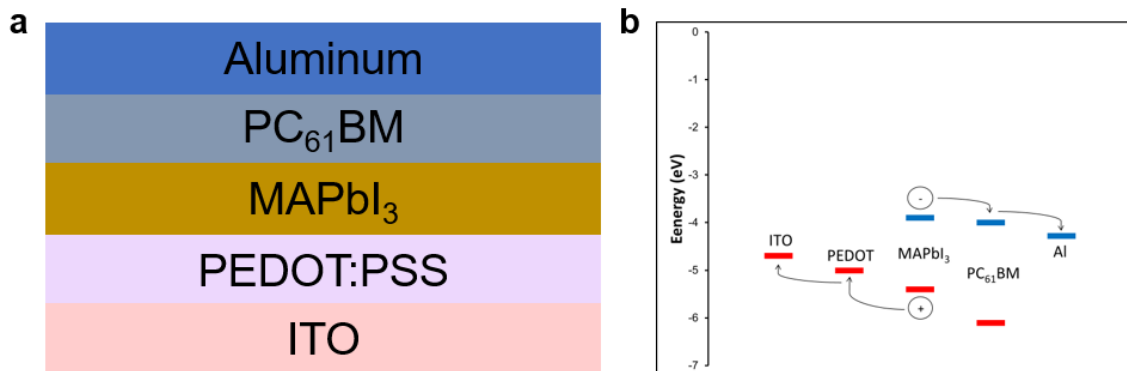


Figure 1.7: (a) a schematic cross-section and (b) an energy band diagram of a perovskite solar cell. Arrows on the diagram indicate the direction of charge transport for electrons and holes.

Finally, a metal top contact is applied to the top material, typically through thermal evaporation. The work function of this top contact is, again, appropriate to conduct the charge carrier that it is collecting during operation of the device.

The fundamental device in a photovoltaic, as described above, is the pn junction diode. This diode can be described mathematically by the ideal diode equation: $I = I_0(e^{\frac{V_a q}{kT}} - 1)$, where I =current, V_a = applied voltage, q =charge, k =boltzmann constant, and T =temperature. The form of this equation suggests that an I-V curve for a diode will have the shape of an exponential curve, and at $V_a = 0$, there will be a very small negative bias, I_0 . When light with an energy higher than the bandgap of the semiconductor is absorbed by the semiconductor, an electron-hole pair is formed. Under constant illumination, this can be mathematically described as a constant generation rate for electron-hole pairs, G_L . This generation rate, G_L describes the charge generated per second (which is another way of describing electrical current), and within the pn junction diode of the photovoltaic, this will add a constant current, I_L . The ideal diode equation is then modified by the current added by the absorption of light as a second term: $I = I_0(e^{\frac{V_a q}{kT}} - 1) + I_L$. Thus, when light is shined on a pn junction, the I-V curve shifts downwards on the y-axis. If we then consider that electrical power = current \times voltage ($P = IV$), we note that within the 4th quadrant of the I-V curve power is generated since we produce electrical current simply by applying a voltage. A typical I-V curve

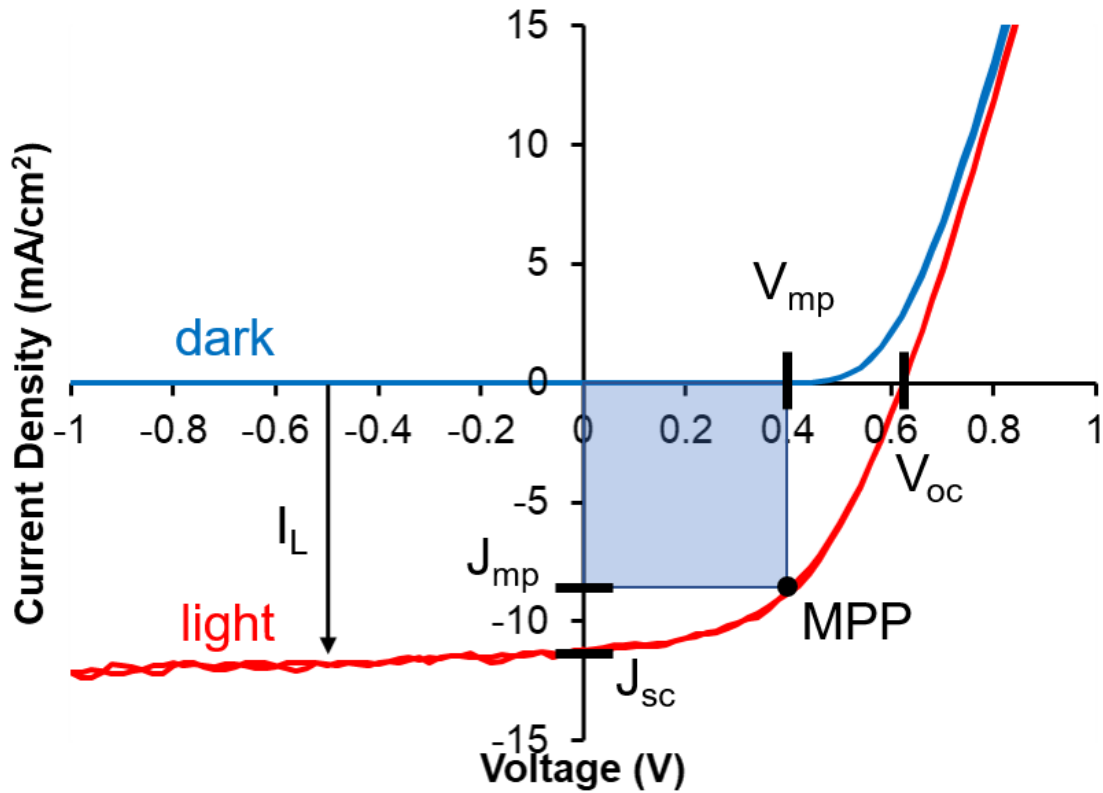


Figure 1.8: Labeled I-V curve for a P3HT-PCBM OPV device in the dark (blue) and under illumination (red). The curve shifts downwards by I_L under illumination.

for one of our solar cells is shown in figure 1.8. We include a curve in the dark and in the light to show how the curve shifts downwards under illumination from an AM 1.5 solar simulator which has an intensity of roughly 100 mW/cm^2 . We define several important points on this curve in the following way: J_{sc} is the short-circuit current, or the current at $V_a = 0$; V_{oc} is the open circuit voltage, or the V_a at which current drops to 0; MPP is the maximum power point, or the point along the curve which maximizes the equation $P = IV$. From MPP, we define J_{mp} and V_{mp} to be the current density and applied voltage at the MPP. From these points, we can define the fill factor, FF: $FF = \frac{J_{mp}V_{mp}}{J_{sc}V_{oc}}$. The fill factor is an important metric for quickly understanding how far from ideal a solar cell's I-V characteristics are.

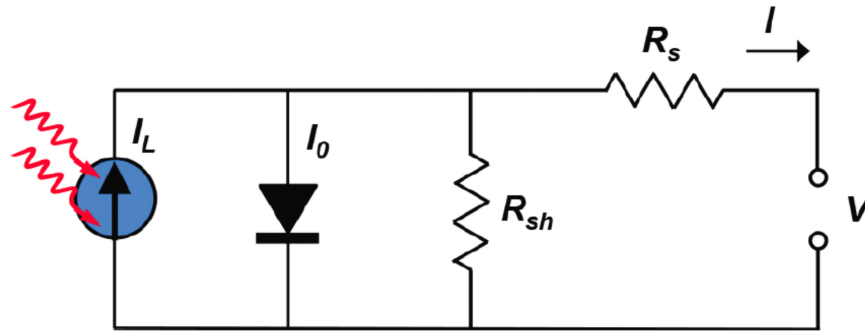


Figure 1.9: An equivalent circuit diagram for a PV device. R_s is series resistance which should be minimized, and R_{sh} is shunt resistance which should be maximized. Figure adapted from Tao et al.¹³

The equivalent circuit model for a PV device is included as figure 1.9. The series resistance, R_s , is any resistance in the device between the diode and the output current. This could include factors such as contact resistance, carrier recombination, non-radiative relaxation, and material resistivity, and R_s should generally be minimized in any device for best performance.¹³ The shunt resistance, R_{sh} , is the parallel resistance in the device, which could be caused by pinhole defects in the device allowing generated current to travel through an alternate path across the junction. R_{sh} should generally be maximized to ensure good I-V characteristics. Finally, the efficiency of the solar cell is defined as $\eta = \frac{P_{max}}{P_{in}} = \frac{FF \cdot I_{sc} V_{oc}}{P_{in}}$, and we have already defined P_{in} as roughly 100 mW/cm^2 .

The Shockley-Queisser limit describes the maximum theoretical efficiency for a solar cell based on a single pn junction.^{12,14} The efficiency of any PV material is limited by its bandgap because any incident photons with energy lower than the bandgap won't excite an electron into the conduction band, and any incident photons with energy higher than the bandgap will relax down to the bandgap energy non-radiatively. Blackbody radiation, recombination, and impedance matching also limit efficiency in solar cells to a lesser extent, and in total, the maximum efficiency for a single junction device is 33.7% for a device with a 1.34eV bandgap.¹² Different semiconductors have different bandgap values, and thus different maximum theoretical efficiencies. These have been included as figure 1.10 as a way to compare various PV technologies vs. their theoretical maximum

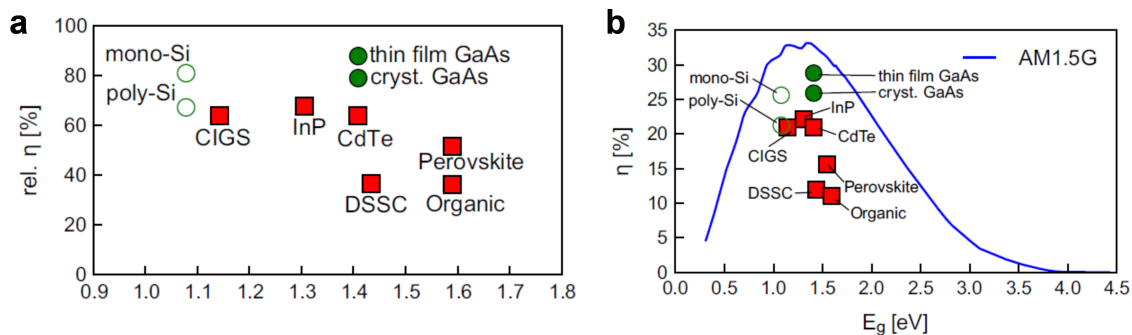


Figure 1.10: (a) Efficiency of various PV technologies relative to their maximum theoretical efficiency vs. bandgap and (b) maximum achieved efficiency of various PV technologies vs. bandgap showing the Shockley-Quessier limit under solar radiation as a maximum possible in blue. The maximum efficiency values are from 2015. Figure adapted from Rühle¹².

under the Shockley-Quessier limit.¹² To see a more complete picture of the efficiency improvements these technologies have undergone over the years, a chart of record efficiencies over time has also been included (figure 1.11). A few things to note from these graphs are, first, that most of the inorganic semiconductor devices have achieved efficiencies close to their theoretical maximum, but DSSCs, OPVs, and PSCs still have a significant amount of research needed to improve their efficiencies. Second, DSSCs have not seen any meaningful increase in laboratory efficiency in the past 20 years of development, and OPVs have likewise stalled in their peak efficiency over the past 4 years. PSCs have benefitted tremendously from the knowledge gained in development of DSSCs and OPVs which is why they have rapidly improved from 3.8% in 2009¹⁵ up to 22.1%¹⁶ in 2017.

The devices in chapter 2 of this thesis are a mixture of BHJs and DSSCs, while chapters 3 and 4 focus on PSCs. To briefly explain the differences between OPVs, DSSCs, and PSCs, we can use the earlier explanation of pn junctions as a starting point. In a silicon solar cell, part of the single-crystal semiconductor absorber is doped p-type, and part of the semiconductor is doped n-type to form the active layer of the solar cell. Growing silicon wafers and electronically doping them is inherently a high-temperature process. OPVs use organic molecules (small molecule or polymer) as the separate p-type and n-type components of the active layer. Because the electronic mobility of

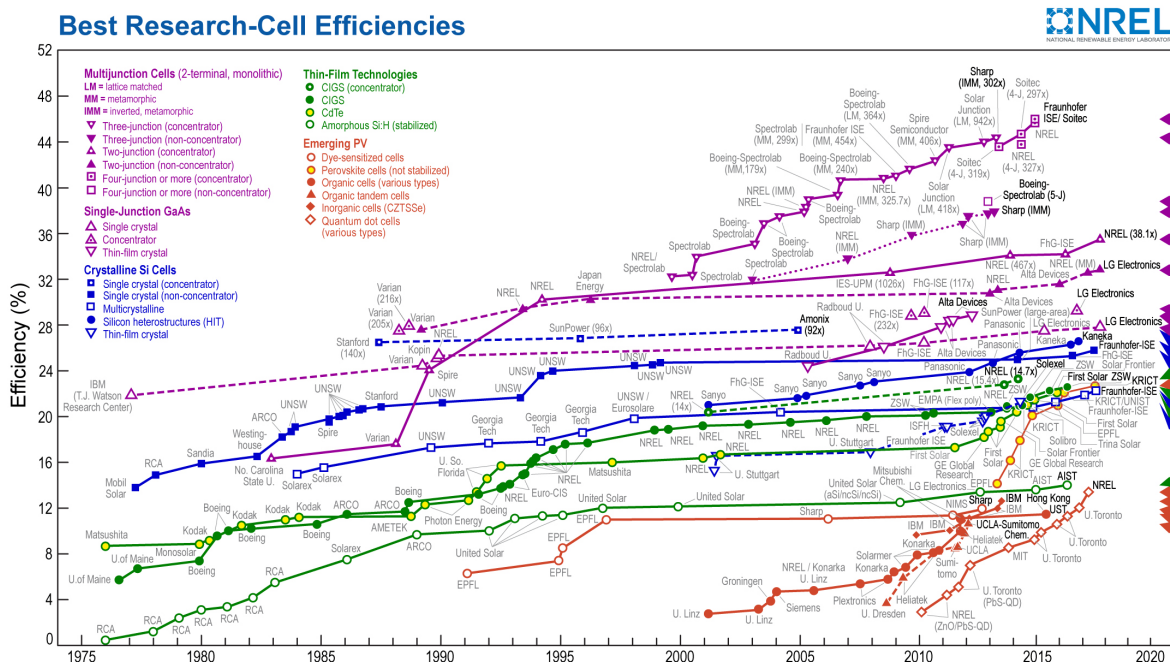


Figure 1.1.1: Best research cell efficiencies over time as published by the National Renewable Energy Laboratory.⁴

organic molecules is significantly lower than inorganic semiconductors such as silicon, nanostructured electrodes must be made to intimately mix the p-type and n-type domains. Practically, this is done by spin-casting the donor and acceptor components from solution, and as they dry they phase separate in a spinodal decomposition process to form a random, tortuous pathway for charge conduction to the electrodes known as a bulk heterojunction (BHJ). The size of these domains can be controlled through solution processing, solvent additives,¹⁷ annealing, and molecular design.^{18,19} Solution processability of OPVs theoretically allows them to be printed on flexible substrates at low temperatures to reduce material and capital cost of fabrication. Dye-sensitized solar cells (DSSCs) can be thought of as an alternative way to solve the problem of organic molecules having low electronic mobility. In these devices, the role of electron transport is given to an inorganic scaffold (typically n-type TiO_2), and a monolayer of dye chemisorbed to the surface acts as the absorption layer for the device. When light is absorbed by the dye molecule, the electron from the electron-hole pair is passed to the inorganic scaffold. The entire scaffold is immersed in a liquid electrolyte

in a DSSC whose purpose is to pass electrons to the dye molecules to restore charge neutrality and then transport that charge to the opposite electrode using a redox couple in solution.²⁰ Therefore, a DSSC removes the need for organic molecules to transport charge through the device by passing electrons to an inorganic scaffold and passing holes to a redox couple in a liquid electrolyte.

PSCs have an active layer that is based on the methylammonium lead iodide (MAPbI₃) perovskite crystal structure. This crystal structure is composed of a tetragonal unit cell with methylammonium at the corner sites, Pb²⁺ at the body center, and iodide at the face centers. This hybrid organic inorganic material is a semiconductor with high ambipolar conductivity,²¹ high absorptivity,²² and a band gap that is close to ideal for a solar cell. What makes PSCs unique is that they have electronic properties similar to inorganic semiconductors, but they crystallize at low temperature from solution.²³ This means that many of the processes and transport layers that were optimized for OPVs and DSSCs have been directly applicable to PSCs, which, in addition to favorable optoelectronic properties, explains why PSCs have reached such high efficiency values in the few years since they have been discovered.²⁴ The biggest roadblock for PSCs, however, is their low stability caused by the instability of the methylammonium cation in the crystal structure. This cation can decompose into methylamine gas by various decomposition pathways under light, heat, applied voltage, and humidity.²⁵ A more detailed explanation of the degradation pathways in PSCs is included in chapter 3.

1.3 ORGANIC CHEMISTRY, DESIGN, AND SELF-ASSEMBLY WITHIN HYBRID

ORGANIC-INORGANIC MATERIALS

Hybrid organic-inorganic materials have been the subject of renewed research interest because our current understanding of self-assembly has allowed us to use hybrid materials to design complex architectures over multiple length scales.²⁶ Self-assembly is the process by which disordered components spontaneously form a more ordered structure as a result of thermodynamic, electrostatic, and kinetic factors. Isrealachvili explained self-assembly of amphiphiles in terms of a geometric model.²⁷

By comparing the size of the head group to the length of the molecule, individual molecules can be modeled as cones, truncated cones, or cylinders and each of these building blocks packs into a different assembled structure. Micelles, cylindrical micelles, bilayers, vesicles, and inverse micelles are all possible assemblies from this very simple model. Organic materials with amphiphilic character can template inorganic phases through self-assembly in solution. An application of this understanding from our group is as follows: CdS, CdSe, and ZnS can be mineralized into semiconducting superlattices through the templation of an organic liquid crystal phase. The mesopores in the organic hexagonal liquid crystal directly template the growth of the inorganic phase.²⁸ From a materials science perspective, this study demonstrates that nucleation and growth of an inorganic phase can be precisely controlled on the microscale in order to create a functional material. Therefore, an understanding of self-assembly allows hybrid materials to be tailored to fit applications related to energy production and storage.

The effects of interfaces, changing concentration, and mineralizing inorganics in these types of systems can create even more complex structures. For example, our group also demonstrated that evaporation induced self-assembly can be used to create hexagonally packed cylindrical micelles of a bolaamphiphile with silica on a substrate surface.²⁹ It was shown that in this case, the presence of the inorganic phase was necessary to screen charge in the assembled organic phase. Thus, these hybrid assemblies often involve a cooperative effect between the two phases to create an assembled mesophase.

Creating a hybrid material allows us to combine the properties of two materials in an advantageous way. In the case of hybrid solar cells, inorganic semiconductors have much higher electron mobilities, better thermal stability, and higher dielectric constants³⁰ than organic electron acceptors (typically PCBM). The advantages of organic semiconductors as a donor material are that they have a high absorption coefficient³¹ (ca. 10^5 cm^{-1}) and tunable properties. More specifically, an organic polymer or small molecule will have tunable solubility, electron mobility, crystallinity, molecular

shape, energy levels, and band gap whereas these properties are relatively fixed in an inorganic semiconductor.

1.4 THESIS OVERVIEW

As outlined above, the work presented in this dissertation focuses on an approach towards designing hybrid organic-inorganic materials for photovoltaics focused on the design and structure of the organic components. Chapter 2 summarizes our work on electrodeposited hybrid zinc oxide solar cell active layers. Hybrid lamellar zinc oxide structures have been previously shown in the group to form photoconductors,^{32,33} and this chapter shows how these materials can be applied to dye-sensitized solar cells. Important aspects of this chapter are the design and synthesis of high visible-light absorption chromophores compatible with the electrodeposition process to form oriented lamellar structures as well as the comparison between electrodeposited active layers with bulk heterojunction and dye-sensitized devices fabricated with traditional techniques. Chapter 3 describes our investigation into perovskite-polymer hybrid thin films. Using new techniques to analyze these hybrid thin films, we can characterize the morphology and chemical differences between various polymer functional groups in these active layers. We find that poly(acrylic acid) helps to improve the stability of perovskite solar cells under illumination significantly better than other polymers. Finally, Chapter 4 summarizes our work with 2D layered perovskite materials. This work outlines a systematic approach towards making new 2D layered perovskites with conjugated organic cations. Through our investigation we find that organic packing and intramolecular hydrogen bonding influence the inorganic lattice structure and optoelectronic properties of the resultant 2D perovskite material. Improved conduction and optical absorption in these materials leads to improved photovoltaic device efficiency.

2 LAMELLAR HYBRID SOLAR CELLS

2.1 OBJECTIVES AND SIGNIFICANCE

Fabrication of dye-sensitized solar cell active layers typically utilizes a low-throughput two-step process. First, an inorganic nanoparticle scaffold is cast and annealed through a sol-gel process, and then that scaffold is sensitized by soaking it in a solution of carboxylic acid-functionalized dye molecules over the course of several hours. In this chapter, we outline the development of a hybrid material with nanoscale pn junctions designed to absorb visible light for photovoltaic applications. Zinc oxide, an n-type semiconductor, has been shown to form lamellar, orientable nanostructures when electrodeposited from solution with organic dyes.³⁴ We first synthesize and study the structure of several dyes in the lamellar ZnO hybrid film. The orientation of these nanoscale domains perpendicular to the substrate surface is critical to charge transport across the active layer in a thin film photovoltaic device.³⁵ Through our initial device experiments, we find that the thick, porous microscale morphology of the photovoltaic active layer is better suited for dye-sensitized devices than for thin film devices. Our goal for this project is to create a technique for fabrication of dye-sensitized solar cell active layers using electrodeposition to deposit both the inorganic scaffold and dye molecules in a single step. In this chapter, our morphological study shows that the hybrid lamellar structure will electrodeposit with a variety of organic dyes with non-crystalline packing, but the inorganic domains are invariably sub-nanometer thick sheets based on the layered double hydroxide structure. We also showed how deposition conditions could be rationally tuned in these systems using control of temperature, concentration, and solvent composition to keep the dye molecule below its critical aggregation concentration in solution for deposition. Functioning dye-sensitized devices can be made from these lamellar scaffolds, although at lower efficiency than control bulk heterojunction or dye-sensitized devices. In this study, various control devices and impedance spec-

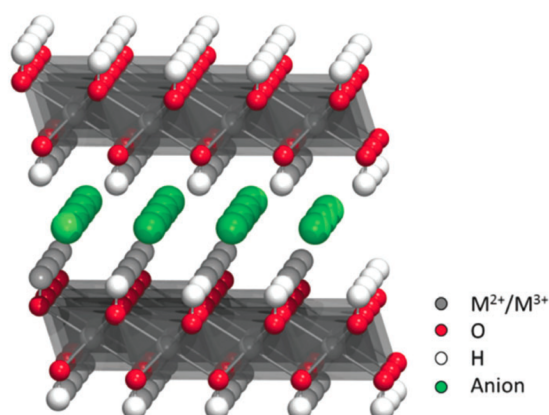


Figure 2.1: Schematic model of the layered double hydroxide structure adapted from Yu et al.³⁷

troscopy explain why conventional device architectures such as DSSCs and BHJs outperform this new nanostructured photovoltaic active layer.

2.2 BACKGROUND

Zinc oxide is an n-type inorganic material with relatively high abundance, high electron mobility, and it can be synthesized either with a wurtzite crystal structure or as a layered double hydroxide (LDH). The layered double hydroxide structure generally consists of metal cations with +2 charge coordinated to hydroxide ions in a layered structure (figure 2.1). Oxygen vacancies and Zn interstitials³⁶ in the $\text{Zn}(\text{OH})_2$ LDH structure allow various anionic organic species to intercalate into the structure, and these hybrid materials have been used in applications such as drug delivery, supercapacitors, and catalysis.³⁷ These LDH materials are scientifically interesting because in addition to their various potential applications, they have been shown to have a significant amount of structural diversity on the nanoscale including structures such as nanosheets, nanowires, flat spicules, nanotubes, and spiral sheets depending on the packing of the organic intercalant into the hybrid structure.^{32,38,39}

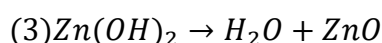
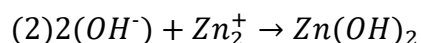
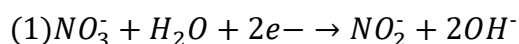
Recent examples in the literature have shown that controlling the nanostructure of the active layer of ZnO in hybrid organic-inorganic devices is crucial for improvements in photovoltaic effi-

ciency. The Janssen group was able to create a relatively high efficiency device ($\eta = 2\%$) by creating the inorganic ZnO phase in situ by spincoating a mixture of Poly(3-hexylthiophene-2,5-diyl) (P3HT) and diethylzinc — an organometallic ZnO precursor.³⁰ Upon exposure to moisture, the diethylzinc in the active layer converts to ZnO, creating a bulk heterojunction (BHJ) hybrid device. They mapped the morphology of this active layer using 3D electron tomography and found that two limiting factors for their device efficiency were unfavorable phase separation leading to poor exciton separation, possibly due to vastly different properties of ZnO and P3HT, and tortuous and isolated charge transport pathways in the device. It would be a logical step forward to postulate that a more ordered and organized nanostructure could achieve higher solar power conversion efficiencies.

The Peidong Yang group has attempted to fabricate a more ordered system by pre-fabricating oriented ZnO nanorods on a substrate and attaching either a phosphonic acid-functionalized quaterthiophene small molecule or a phosphonic acid-functionalized P3HT polymer to the nanorods from solution.⁴⁰ In this study, they found that the acid groups bound the small molecule or polymer dyes into ordered domains on the ZnO surface, but the π - π stacking direction was orthogonal to the ideal orientation for charge transport. Because of this, when they measured the efficiency of the single-nanowire devices, they found that $\eta \approx 0.03\%$ for both the polymer and small molecule. The efficiency in this device was significantly lower than in the example from the Janssen group for two reasons: charge diffusion length and orientation of organic domains. The single nanowire devices were fabricated with up to $5 \mu\text{m}$ between contacts which is significantly longer than the carrier diffusion length of an organic semiconductor, and random orientation of the conductive P3HT domains is more favorable than an aligned orientation along an axis orthogonal to charge transport. Thus, directing order in these hybrid systems is not only a matter of organizing phases into appropriate length scales and dimensions, but also of orienting the domains within the organic phase.

Another method of creating ZnO hybrid materials is via electrodeposition. Izaki et al. pioneered the electrodeposition of wurtzite ZnO structures using an aqueous zinc nitrate solution.^{41,42}

Yoshida et al. later explained the mechanism by which ZnO is formed on the substrate surface in this process:⁴³



In the electrodeposition bath, zinc nitrate is reduced to nitrite under applied bias (1), which produces hydroxide ions in the local environment of the cathode. The hydroxide then reacts with zinc ions to deposit zinc hydroxide on the surface of the electrode (2). This zinc hydroxide is converted to zinc oxide upon the removal of water (3), a process that is fully completed upon annealing. Using this technique, ordered ZnO pillars can be deposited on a surface at a potential of -1 V vs. Ag/AgCl reference electrode at relatively low temperatures (60°C).

This technique became interesting from a self-assembly perspective following the work of K.S. Choi's lab because they showed that with the addition of a charged surfactant to the deposition bath, the ZnO structures could form a lamellar LDH structure on a conductive substrate.⁴⁴ In their work, they showed that lamellar structures parallel to the substrate surface could be formed between ZnO and alkyl surfactants such as sodium dodecyl sulfate and decanoic acid.

Drawing inspiration from Choi's alkyl surfactant work, our group's previous work has shown that ordered lamellar ZnO-organic hybrids can be electrodeposited from dimethyl sulfoxide (DMSO)/H₂O mixtures on a transparent conductive substrate to form photoconductors (figure 2.2).³² By substituting conjugated organic surfactants for the alkyl surfactants demonstrated by Choi et al., we create nanoscale p-n junctions. The n-type ZnO domains are less than 1 nm thick and are bound by 2-3 nm p-type domains of conjugated surfactant. One important feature of the conjugated surfactants is that they can stabilize the ZnO lamellar upon annealing at 150°C whereas

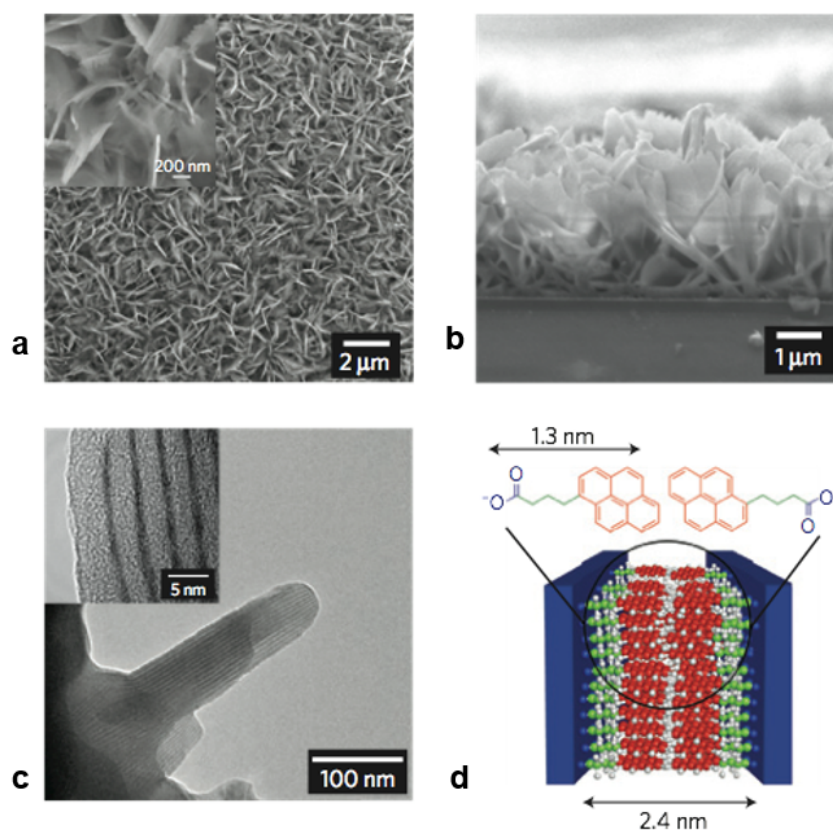


Figure 2.2: SEM (a) reveals a flake-like morphology on the sample surface from an electrodeposition with pyrenebutyric acid (PyBA) and Zinc nitrate. The cross-sectional SEM (b) shows that the majority of these flakes are oriented upwards from the sample surface, and TEM (c) shows that within a single flake there is a nanoscale lamellar structure present with ZnO domains <1 nm thick. The schematic (d) shows how these structures pack qualitatively. Each PyBA molecule attaches to a sheet of ZnO and stacks end-to-end with another PyBA within the lamellar gallery. Figure adapted from Sofos et al.³²

the ZnO-alkyl surfactant lamellar structures collapse. The annealing process fully converts the $\text{Zn}(\text{OH})_2$ to ZnO as shown by X-ray absorption near edge structure spectroscopy in the study. It was shown that these nanostructures could make excellent photoconductors with detectivities greater than $2 * 10^{10}$ Jones and photocurrent gains of 120 at $1.2 \text{ V}/\mu\text{m}$. Furthermore, the lamellar repeat distance of these hybrids (3-5 nm) is on an ideal length scale for exciton diffusion in an organic semiconductor.³¹

For this architecture to be effective in a thin-film photovoltaic device, the lamellar domains need to be oriented perpendicular to the substrate surface. These oriented domains represent ideal charge transport pathways in a solar cell because minimizing the charge percolation distance in the active layer reduces the chance of exciton recombination³¹ (i.e. a straight path is shorter than a tortuous one). We have shown that orientation of these structures can be controlled through surfactant design and surface chemistry.³³ Specifically, in the case of a ZnO-pyrenebutyric acid lamellar structure, the orientation of the layered axis of the lamellar structure on an ITO surface is primarily in the horizontal plane, whereas under specific solution conditions on a PEDOT:PSS surface the lamellar structure is oriented primarily in the vertical plane. These findings are summarized in figure 2.3.

In the interest of finding a more general trend for this phenomenon, our group designed a series of terthiophene (3T) surfactants to be electrodeposited on ITO and PEDOT:PSS surfaces.³⁴ By varying the aspect ratio, linker length, and amphiphilic character of the 3T molecules, we were able to ascertain that high aspect ratio, long linker length, amphiphilic surfactants can be deposited in a lamellar structure that is oriented vertically with respect to the substrate surface (figure 2.4).

In parallel with the study of the 3T structures, we fabricated lamellar thin film photovoltaic devices with a dicarboxylic acid 3-methyl-quinquethiophene (5T) bolaamphiphile surfactant ($\eta = 0.035\%$). This surfactant similarly shows a lamellar structure oriented vertically with respect to the substrate as shown in 2D-GISAXS and has better visible-spectrum absorptivity than 3T molecules. Unfortunately, device efficiencies with this surfactant are limited by active layer thickness, active layer porosity, and low absorption in the visible spectrum compared to typical OPV dyes. The active layer of our lamellar devices needs to be >500 nm thick to prevent electrical short-circuiting in the devices because the wire-like morphology of the active layer creates a porous microstructure (figure 2.5). This microstructure leads to pinhole shorts through the active layer unless the active layer is sufficiently thick to prevent this from occurring. The overall thickness of the cell involves a balance between the processes of the electron donor transporting holes to the electrode before recombination occurs (which favors a thin active layer) with the overall light absorption of the de-

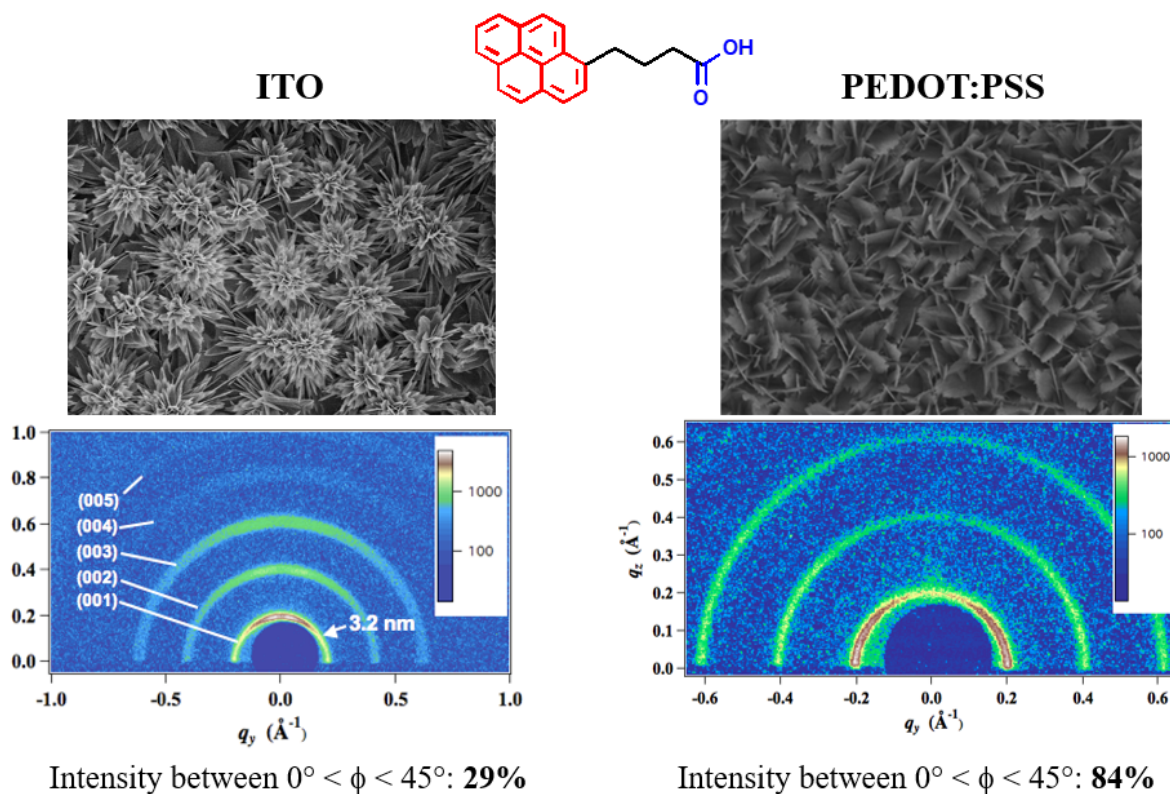
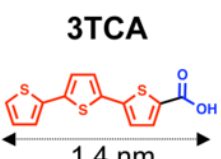
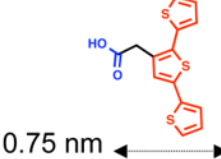
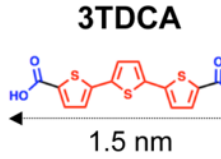
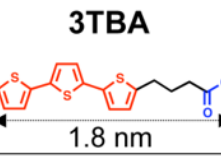
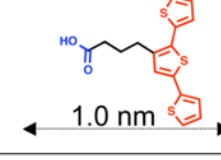
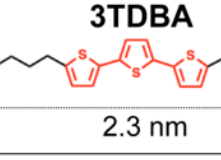


Figure 2.3: The SEM and 2D-GISAXS data presented on the left show that when PyBA is electrodeposited with zinc nitrate on ITO, there is a bloom-like morphology present with a majority of the lamellar domains directed parallel to the substrate surface. However, on the right we see that on PEDOT:PSS there is a flake-like morphology and the majority of the domains are oriented perpendicular to the substrate surface. Figure adapted from Herman et al.³³

		Amphiphile		Bolaamphiphile		
		High Aspect Ratio	Low Aspect Ratio	High Aspect Ratio		
Short Linker	3TCA		TAA(T)₂		3TDCA	
	Long Linker	3TBA	TBA(T)₂	3TDBA		
						

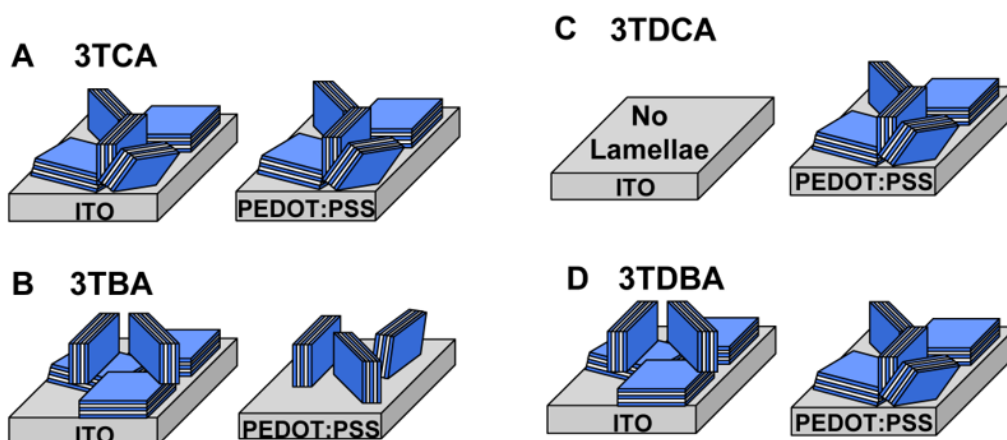


Figure 2.4: Our group synthesized a series of 3T molecules investigating the variables of linker length (carboxylic vs. butyric acid), aspect ratio (high vs. low), and amphiphilic character (amphiphilic vs. bolaamphiphilic). Below the molecular structures table, we show schematically what 2D-GISAXS revealed about the orientation of the lamellar structure on ITO and PEDOT:PSS surfaces. The structures were only oriented vertically with respect to the substrate surface in the case of (B) 3TBA. Figure adapted from Bruns et al.³⁴

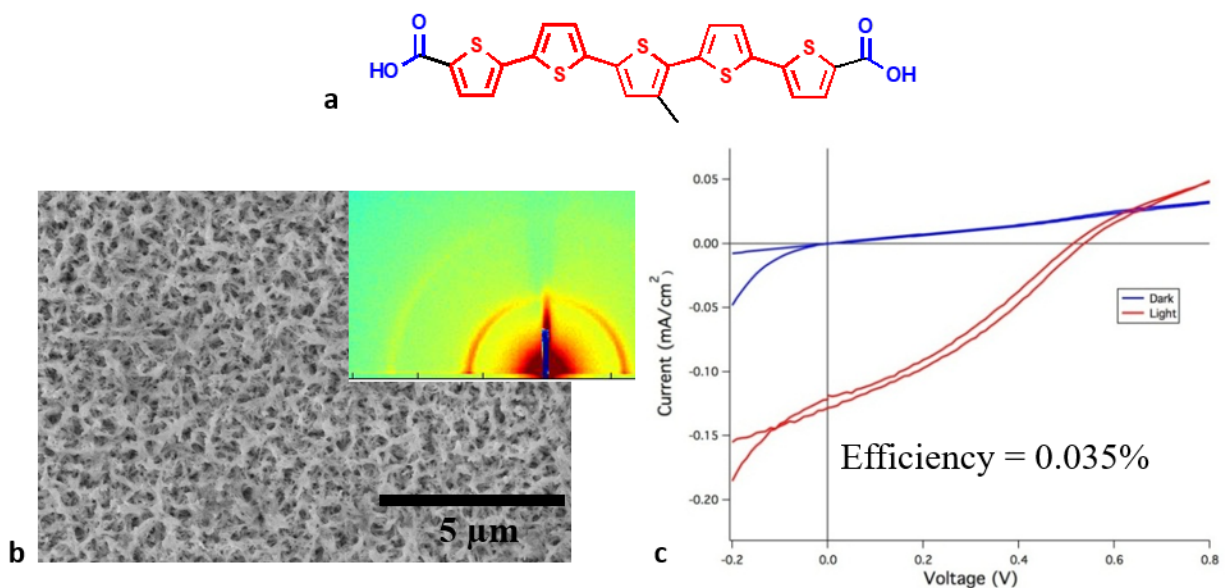


Figure 2.5: Electrodeposition of the 5TmDCA molecule (a) with zinc nitrate results in a wire-like morphology with a lamellar orientation that is somewhat aligned vertically with respect to the substrate surface as shown by SEM (b) and 2D-GISAXS (b, inset). Optimized thin film solar cells give an efficiency of 0.035% (c) (figure from Dave Herman, unpublished manuscript).

vice (which favors a thick active layer).³¹ Furthermore, in an OPV, the electron mobility needs to be somewhat balanced with the hole mobility in order to avoid the buildup of a space-charge in the device.³¹ Since the electrons move through the device much more quickly than the holes, there is a buildup of holes in the active layer that creates an unfavorable electric field within the device. In the case of our ZnO hybrid lamellar devices we have increased the electron mobility by orders of magnitude over PCBM, but the hole mobility is still near values of a typical organic semiconductor. In addition to our concerns about porosity and active layer thickness, the absorption of the 5T molecule does not overlap well with the visible spectrum (figure 2.6).

The goals of this study, then, are twofold. First, we must create a hybrid, oriented ZnO-dye scaffold with high absorption over the visible spectrum while maintaining water-solubility so that it is compatible with the electrodeposition process. Second, we then aim to fabricate a higher-efficiency photovoltaic device using the hybrid film as the active layer. As we describe in the following sections

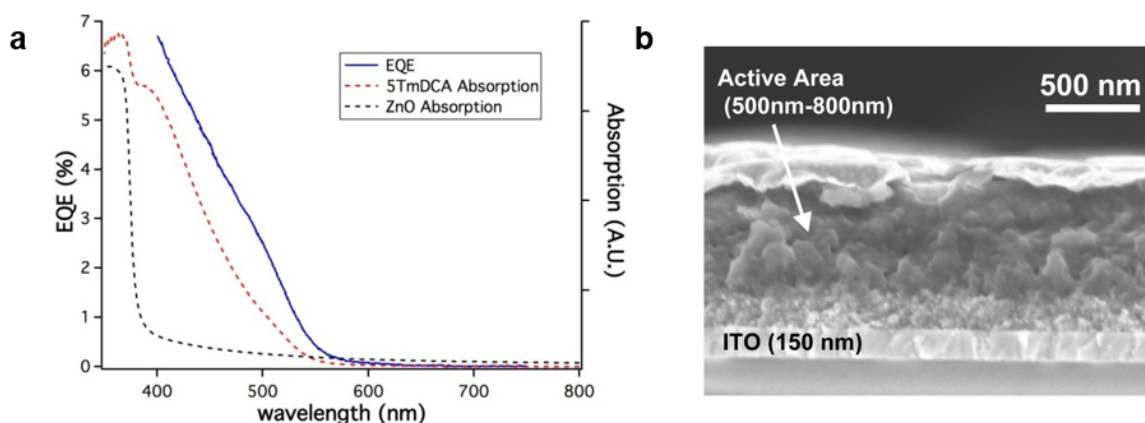


Figure 2.6: The external quantum efficiency of a thin film 5TmDCA device is plotted vs. the absorption of the 5TmDCA and the absorption of the ZnO (a). It is clear from this figure that the EQE tracks with the absorption of the 5T indicating that the photocurrent is a result of excitons generated in the 5T, and that this absorption cuts off at around 550 nm. The cross-sectional SEM of the device (b) shows that the active layer is porous and has a thickness of 500-800 nm (figure from Dave Herman, unpublished manuscript).

of this chapter, the porosity and high surface area of the electrodeposited active layers led us from low-efficiency thin-film PV devices to significantly improved DSSCs. The last section then describes the challenges with our approach as well as a more general outlook on hybrid PV materials.

2.3 RESULTS AND DISCUSSION

2.3.1 Morphology and structure of ZnO-organic dye hybrids

As described in the previous section, oligothiophene-based surfactants do not absorb strongly over the visible spectrum which is an important consideration for any PV material. To address the limitation of low visible spectrum absorption, we designed a new chromophore amphiphile (CA) that incorporates a diketopyrrolopyrrole (DPP) moiety instead of oligothiophene. DPP absorbs much more broadly over the visible spectrum and has higher hole mobility than oligothiophene.⁴⁵ The first molecule that we synthesized that included the DPP moiety was (2TDPP-C3CA) (figure 2.7a). Synthetic details for all the molecules in this study have been included in the materials and

methods section. This molecule was synthesized as a first attempt because it included a flexible linker, which we knew at the time should help the chromophore to fit into the structure, and because it was simple to synthesize due to its symmetric design. We electrodeposited this chromophore in a lamellar structure on top of a ZnO-coated ITO substrate. Plane-view SEM (figure 2.7b) shows a wire-like morphology, and cross-sectional SEM (figure 2.7c) shows that the structure is highly porous through the lamellar layer. This molecule absorbs much more strongly across the visible spectrum (figure 2.7d). 2TDPP-C3CA has an absorption maximum of 552 nm which is very close to the peak intensity of the solar spectrum, and an onset corresponding to a bandgap of 2.08 eV. Finally, we used 2D-GIWAXS to determine the periodicity and orientation of the structure with respect to the substrate surface (figure 2.7e). This technique showed that even though our mesoscale morphology is wire-like — as opposed to flakelike as in previous examples — these wires still retain the lamellar structure. However, the symmetrical molecular design motif would suggest that this molecule should form isotropic rather than oriented structures on the surface according to our previous 3T study,³⁴ and indeed we observe that these lamellar wires are isotropically oriented. The result confirms that the earlier results from the 3T study are more widely applicable to other chromophores than just the narrow case of oligothiophene molecules. Thus, we have shown that 2TDPP-C3CA increases the visible light absorption at the cost of both nanostructure orientation and increased porosity. These disadvantages led us to revise our molecular design to fulfill more of the design criteria for a PV device.

The second molecule we synthesized for this project was (PEG-DPPCN) while following the guidelines of our previous 3T study.³⁴ Specifically, we designed this CA with a carboxylic acid linker on one side, made the conjugated segment longer for a high aspect ratio and lower band gap, and included PEG tails for improved solubility (figure 2.8a). The first version of this molecule was synthesized with ethylhexyl tails instead of PEG tails, and it was insoluble in the DMSO/H₂O mixture necessary for electrodeposition. The absorption of this molecule (figure 2.8b) was red-shifted because of the addition of two extra thiophene groups reduced the band gap of the material. Our initial elec-

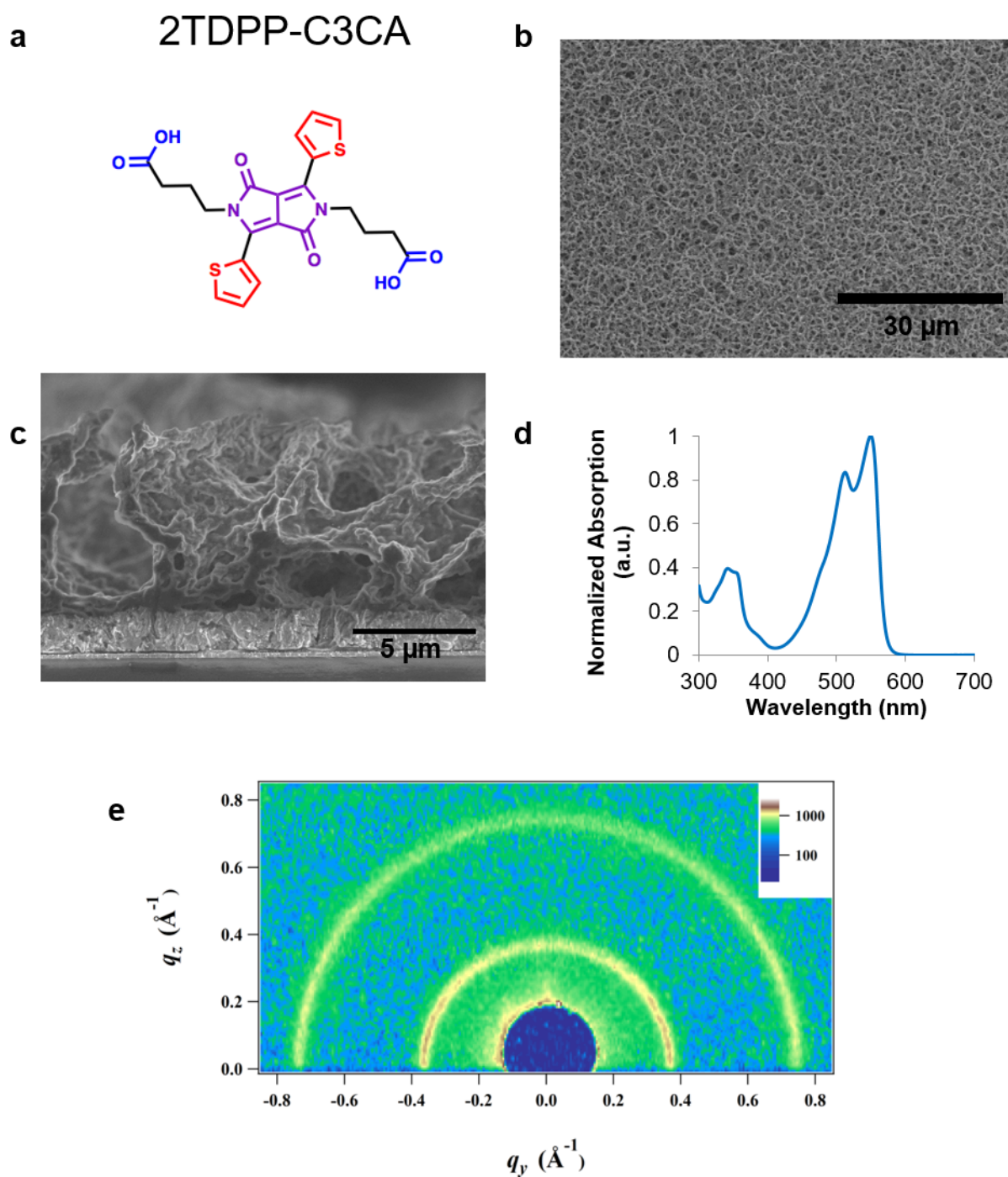


Figure 2.7: (a) Chemical structure, (b) plane-view and (c) cross-sectional SEM, (d) UV-Vis spectroscopy, and (e) 2D-GIWAXS of 2TDPP-C3CA electrodeposited with ZnO.

trodeposition experiments showed a wire-like morphology in SEM (figure 2.8c) Under these conditions, 2D-GIWAXS revealed that the PEG-DPPCN molecule also deposited into a lamellar structure with isotropic orientation on the ZnO substrate surface (figure 2.8d), similar to 2TDPP-C3CA. As discussed in the materials and methods section (as well as figure 2.27), it is possible to deposit the chromophore at higher concentration in solution by increasing the DMSO: H₂O ratio. By adjusting the solution conditions towards a higher DMSO content and higher chromophore concentration, we see that the lamellar structure becomes somewhat oriented in a vertical direction with respect to the substrate surface using 2D-GIWAXS (figure 2.8e). This feature is most evident for the (003) reflection near $q=0.33 \text{ \AA}^{-1}$. To be clear, it was only possible to increase the chromophore loading and change the orientation of this LDH structure by rationally tuning the deposition conditions as described in figure 2.27. Another interesting feature of this GIWAXS pattern is the reflections at $q = 0.65 \text{ \AA}^{-1}$ and $q = 1.3 \text{ \AA}^{-1}$. These are oriented horizontally with respect to the substrate surface, and since they correspond to a spacing of 9.7 \AA , this spacing most likely corresponds to the side-to-side packing of the chromophore within the galleries. This means that the chromophores themselves are not aligned for charge transport with respect to the lamellar packing since the highest-conductivity direction should be the pi-stacking direction. A schematic of the chromophore packing within the ZnO galleries has been included as figure 2.8f.

When we compare the deposition of 2TDPP-C3CA to PEG-DPPCN, there are several differences despite similar wire-like morphologies as seen in SEM. The first difference is in the orientation of the structures. The 2TDPP-C3CA is completely isotropic, while the PEG-DPPCN has some preferential orientation of the lamellar structure perpendicular to the substrate surface. This is a result that we expect given the shape of the two CA molecules and our previous study on 3T. Second, the d-spacing of the two structures is quite different. 2TDPP-C3CA has a lamellar d-spacing of 1.65 nm , while PEG-DPPCN has a lamellar spacing of 5.6 nm . The difference between the two structures is that the mono-functional PEG-DPPCN only binds to the ZnO on one side, and so it forms a bilayer within the organic gallery to bind to both sides of the lattice. This contrasts with

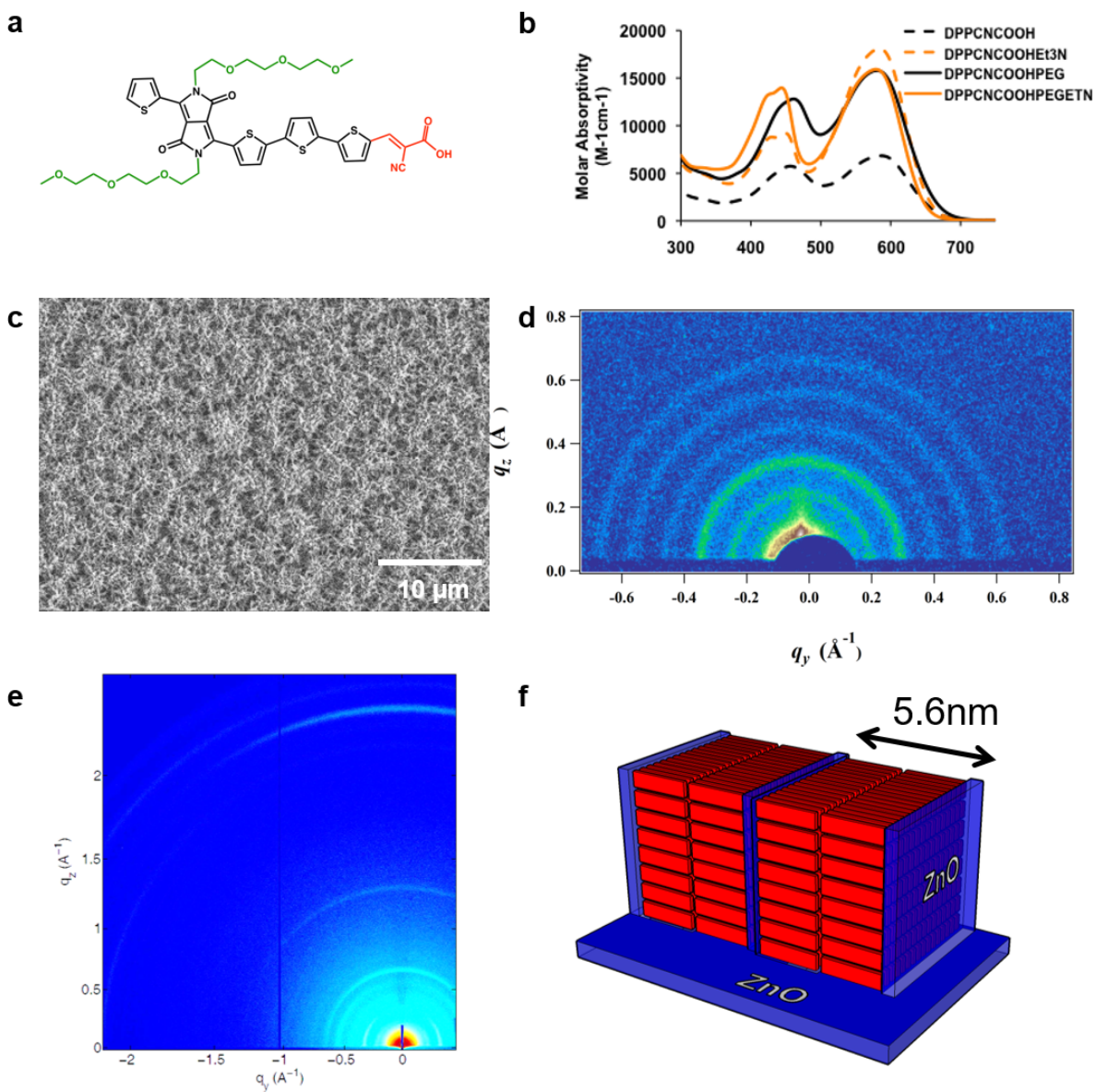


Figure 2.8: (a) Chemical structure, (b) UV-vis spectroscopy, (c) plane-view SEM, (d) 2D-GIWAXS of a film deposited in 50% DMSO (e) 2D-GIWAXS of a film deposited in 67% DMSO, and (f) a schematic of the lamellar structure of PEG-DPPCN electrodeposited with ZnO.

the bifunctional 2TDPP-C3CA which binds to the ZnO lattice by bridging across the gallery as a monolayer.

The binding behavior we observe here in ZnO lamellar structures is analogous to the binding behavior in layered perovskite structures.⁴⁶ In that case, the organic molecule has an ammonium cation that bonds to lead halide sheets to form a layered crystal structure. If we consider layered perovskites more generally as a class of materials, there are a variety of structures that can form depending on how a specific organic cation binds to the inorganic lattice. These structures can have 0D, 1D, 2D, or 3D connectivity between the components of the inorganic lattice.^{46,47} There are also a few examples of zinc oxide forming more diverse assemblies than just 2D lamellar structures. One example from our group showed that flat spicules, nanotubes, and spiral sheets could be formed with ZnO and peptide-functionalized 3T assemblies in water.³⁹ These examples are still based on the coordination of 2D ZnO layers to the organic moiety, but the packing and binding of the organic to the inorganic lattice influences the morphology of the assembly. Another example of a possible morphology in these assemblies comes from Yoshida et al.⁴⁸ In this case the assemblies they deposit are 3D bicontinuous phases without nanoscale ordering. The dye molecule that they use is eosin-Y, which has a more rounded molecular shape than the molecules that we have found to work in lamellar ZnO assemblies. With a 3D bicontinuous phase, it is possible to dissolve the chromophore from the assembly without destroying the inorganic ZnO scaffold, which would allow for a higher surface area structure relevant to DSSCs at the cost of adding processing steps to the active layer fabrication.

One hypothesis that we formed about the LDH hybrid is that the dye molecule may be able to bind to multiple sites on the ZnO if multiple functional groups (carboxylic acids) are on the dye molecule. By changing the binding of the organic to the inorganic, it may be possible to modulate the width of the inorganic domains and the shape of the nanoscale assemblies. To test this hypothesis, we synthesized two 3T molecules with different glutamic acid (E) linkers. The glutamic acid linkers contain carboxylic acids for binding to the ZnO lattice, and peptide synthesis is a straightforward

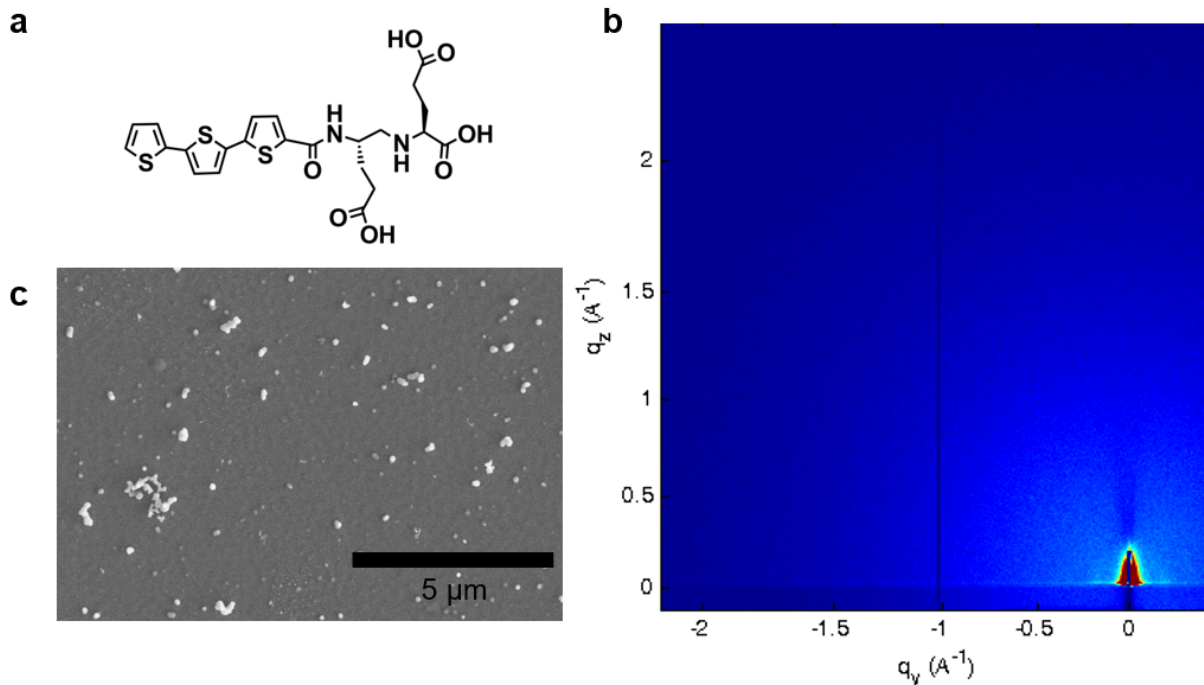


Figure 2.9: (a) molecular structure of 3T-E2, (b) GIWAXS of an electrodeposited thin film of 3T-E2 with zinc oxide, and (c) SEM morphology of the deposited film. The small amount of material that is deposited is amorphous.

process which allows for multiple peptides to be attached sequentially. We synthesized 3T-E2 (figure 2.9a) and 3T-E3 (figure 2.10a), using oligothiophene again since it is an easily-synthesized core in these systems. Synthetic details for these 3T molecules are included in the materials and methods section.

We attempted to electrodeposit and characterize both 3T-E2 and 3T-E3 with ZnO. The 3T-E2 molecule, unfortunately, does not electrodeposit with ZnO at all. When it is added to the electrodeposition bath, very little material deposits onto the surface. This is shown in SEM (figure 2.9c), where there are only small, sparse growths on the surface, as well as in 2D-GIWAXS (figure 2.9b) which shows no crystalline structure, even for ZnO. The 3T-E3 molecule, however, electrodeposits with a mixture of two morphologies. The first morphology consists of small, amorphous, curved flakes, and the second morphology consists of larger crystalline growths (figure 2.10c). The larger growths lack the higher d-spacing that is common to the lamellar structures we typically grow, but

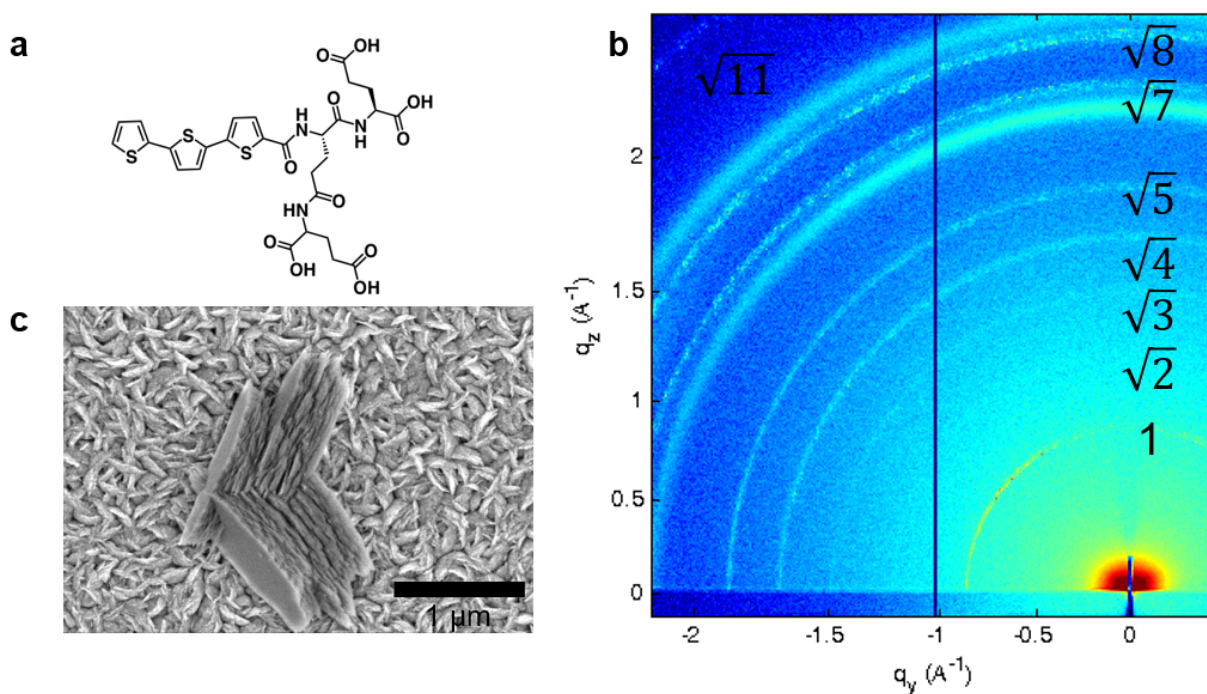


Figure 2.10: (a) molecular structure of 3T-E₃, (b) GIWAXS of an electrodeposited thin film of 3T-E₃ with zinc oxide with the periodicity of the structures labeled, and (c) SEM morphology of the deposited film. The periodicity in GIWAXS results from the larger structure shown in the SEM, and not the small flakes in the background.

they also have a larger-sized, and different periodicity than wurtzite ZnO (figure 2.10b). Films that did not have these large crystalline growths on them did not show crystalline peaks, indicating that the curved flakes are not crystalline nanostructures. The 3T-E3 molecules are affecting the packing of the ZnO, but it is not clear whether they are incorporating into the structures.

As discussed in the materials and methods section (and figure 2.27), the conditions for electrodeposition lie below the critical aggregation concentration for the dye molecules in solution. Using small-angle X-ray scattering (SAXS), we can characterize whether assemblies have formed in solution or not. The slope in the porod region of a log-log plot of SAXS data indicates the dimensionality of these assemblies.⁴⁹ We observe that after annealing in water and 50mM zinc nitrate, both 3T-E2 and 3T-E3 form assemblies (figure 2.11a and b). The 3T-E2 log-log plot has a slope of -2, indicative of sheet-like assemblies. The peaks in the curve can be fit to a lamellar spacing of 39 nm. In contrast, the 3T-E3 curve has a slope of -3.5 indicating that the assemblies have a higher dimensionality than a 2D structure. However, in DMSO/H₂O mixtures with zinc nitrate at their concentrations for electrodeposition, both 3T-E2 and 3T-E3 are no longer assembled in solution (figure 2.11c and d). Thus, despite forming assemblies in water, at electrodeposition conditions where most of the solvent is DMSO, these molecules do not assemble, as expected.

We must therefore conclude that the 3T-E2 molecule doesn't electrodeposit due to another reason aside from the assemblies that it forms in solution. The local pH at the working electrode surface is basic during the electrodeposition process, and even though we don't adjust the pH of the solution before deposition, we know that the pH is at least locally basic because reduction of the nitrate ion in solution is the source of hydroxide ions which are necessary to produce zinc hydroxide. We therefore hypothesize that the sterics of both the deprotonated 3T-E2 and 3T-E3 interfere with the lamellar packing of the ZnO hybrid, as observed, but the 3T-E2 interacts with zinc hydroxide in a way that prevents the 3T-E2 from forming ordered structures onto the electrode surface.

Overall, the results of our morphological study show that for the most part, these electrodeposited structures form porous, rough films. We demonstrate that it is possible to modulate the

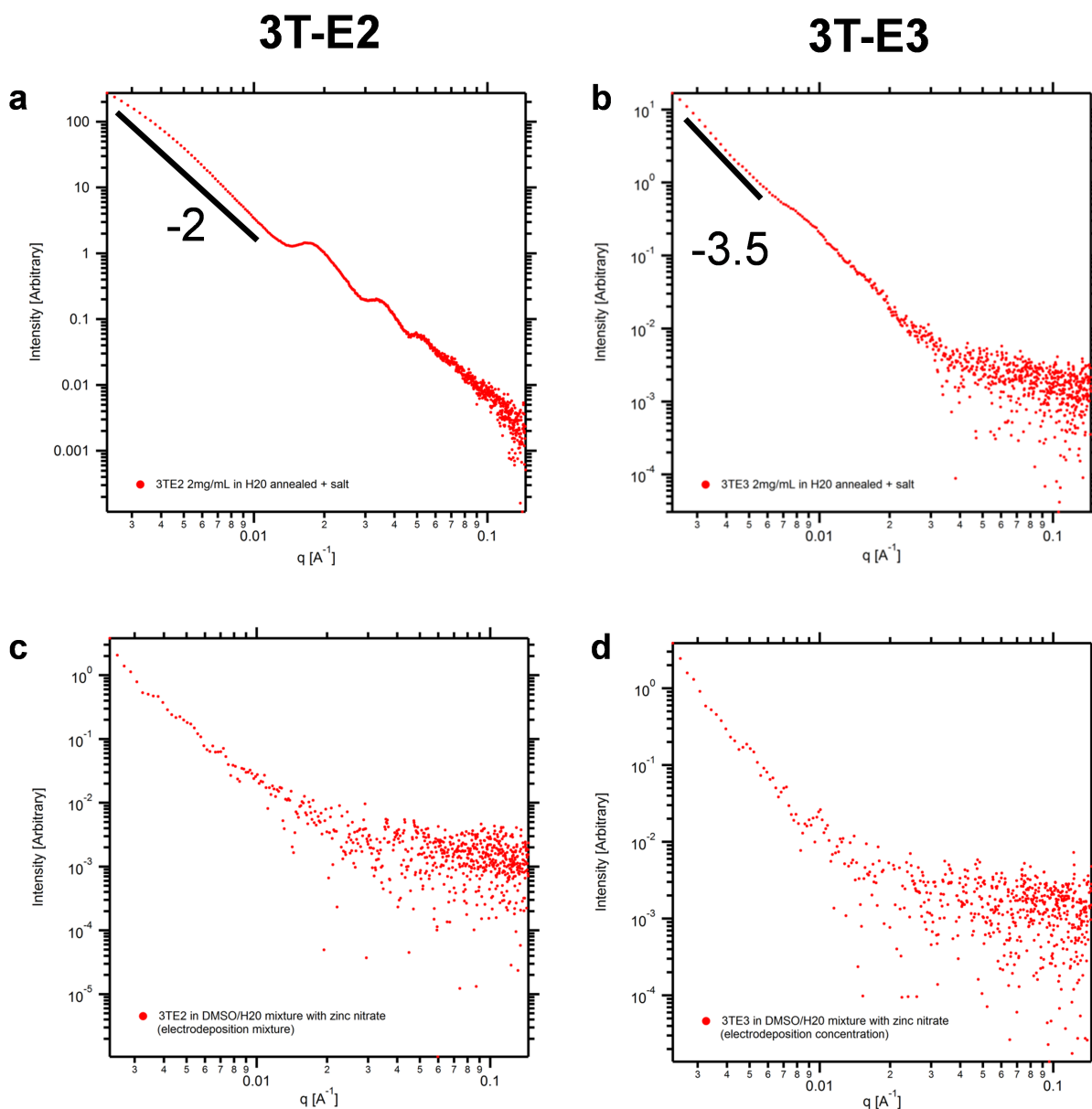


Figure 2.11: Small-angle X-ray scattering (SAXS) of (a) 3T-E2 in water annealed in $\text{Zn}(\text{NO}_3)_2$ salt, (b) 3T-E3 in water annealed in $\text{Zn}(\text{NO}_3)_2$ salt, (c) 3T-E2 in 2:1 DMSO:H₂O with $\text{Zn}(\text{NO}_3)_2$ salt, and (d) 3T-E3 in 2:1 DMSO:H₂O with $\text{Zn}(\text{NO}_3)_2$. Linear fits to the slope in the prod region indicate the dimensionality of the assemblies in solution in (a) and (b).

thickness and packing of the organic molecule within the gallery of the lamellar structure, but for the most part we observe that when the dyes are incorporated into the structure, the ZnO tends to form sheet-like growths. While there may be some conformational flexibility in these sheets to form curved flakes, wires, sheets, and concentric tubes, the thickness of the inorganic domains has been limited to a single layer in all the cases that we have observed thus far. It is unclear, thus far, whether these structures have favorable optoelectronic and structural properties for photovoltaic devices. PV devices, which are the subject of the next section, are a good way to compare the optoelectronic properties of the ZnO lamellar structure compared to traditional thin film and DSSC device architectures.

2.3.2 Lamellar Hybrid Photovoltaic Devices

The starting point for fabricating PV devices with our lamellar scaffolds is determining energy levels of the hybrid and to select appropriate charge transport and collection layers. To determine the HOMO level of the dye molecule, the p-type electron donor in the lamellar structure, we performed cyclic voltammetry on the molecule dissolved in acetonitrile using ferrocene as an internal standard (figure 2.12a). The HOMO level is defined as the onset of the first oxidation peak compared to ferrocene which has a known oxidation energy of -4.44 eV vs SCE. The onset of the absorption of the molecule shown in UV-Vis spectroscopy (figure 2.7d) indicates the band gap of the molecule, which is 2.08 eV for 2TDPP-C3CA. By adding the band gap to the HOMO level, we can determine the LUMO level. These energy levels are plotted against the energy levels used in our device in an energy band diagram shown in figure 2.12b. ZnO is a logical choice for the electron transport layer since it is already the n-type electron acceptor in the active layer. PEDOT:PSS was used as the hole transport material because it is one of the most commonly used HTL materials in organic photovoltaics, and it has an energy offset with the HOMO level of our dye molecule that is nearly ideal at $E_{offset} = 0.29$ eV. In order for PEDOT:PSS to adhere in a conformal coating on top of the rough active layer, 1 vol% of triton-x, a hydrophilic surfactant, was added to the PEDOT:PSS

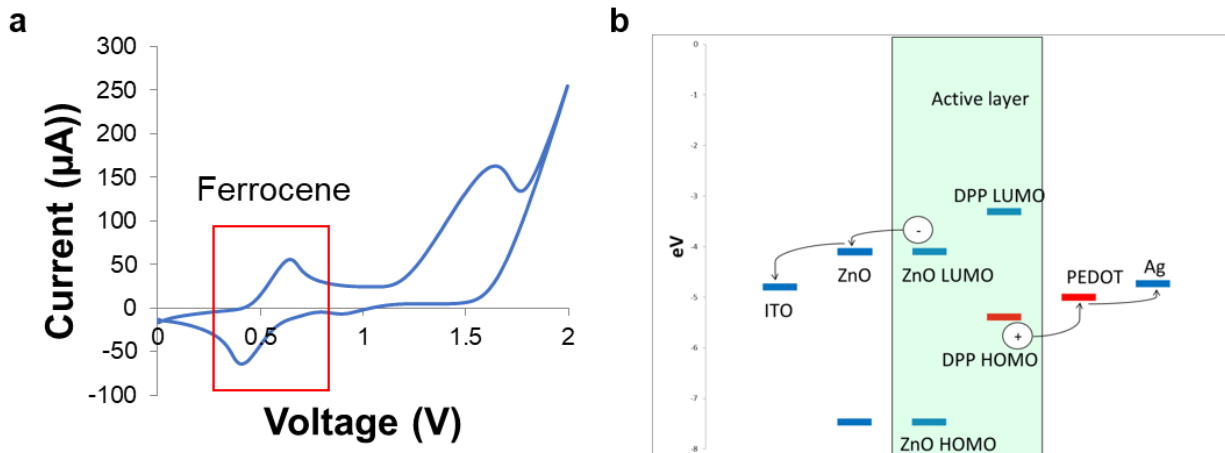


Figure 2.12: (a) Cyclic voltammetry of 2TDPP-C3CA in acetonitrile using ferrocene as an internal standard, and (b) an energy band diagram of the electrodeposited ZnO lamellar thin film solar cells using the HOMO level of -5.39 eV from the CV data and a band gap of 2.08 eV from the UV-Vis data.

formulation. Finally, 100 nm of aluminum, which has a work function of -4.08 eV, was thermally evaporated as the hole-collecting contact of the device.

Previous attempts to fabricate thin-film solar cells with oriented 5TmDCA lamellar structures achieved efficiencies of 0.035% (Figure 2.5c Herman et al, unpublished manuscript). Our hypotheses for the low efficiency of these devices were the roughness and porosity of the active layer, the thickness of the active layer (500-800 nm), and the low optical absorption of the 5TmDCA molecule. Initial attempts at thin film solar cells with 2TDPP-C3CA showed much lower device efficiencies ($\eta \sim 0.008\%$) despite better visible-spectrum absorption (figure 2.13). In this device, the light absorption of the film was improved compared to 5TmDCA, but the lamellar structure was not oriented with respect to the substrate surface. The design of PEG-DPPCN was an attempt to improve the orientation of these structures, and it does have a somewhat aligned lamellar structure when electrodeposited (figure 2.8e), but the device efficiency for this molecule was found to be even lower ($\eta \sim 10^{-4}\%$). It was at this point that it became clear that the porosity of the film and active layer

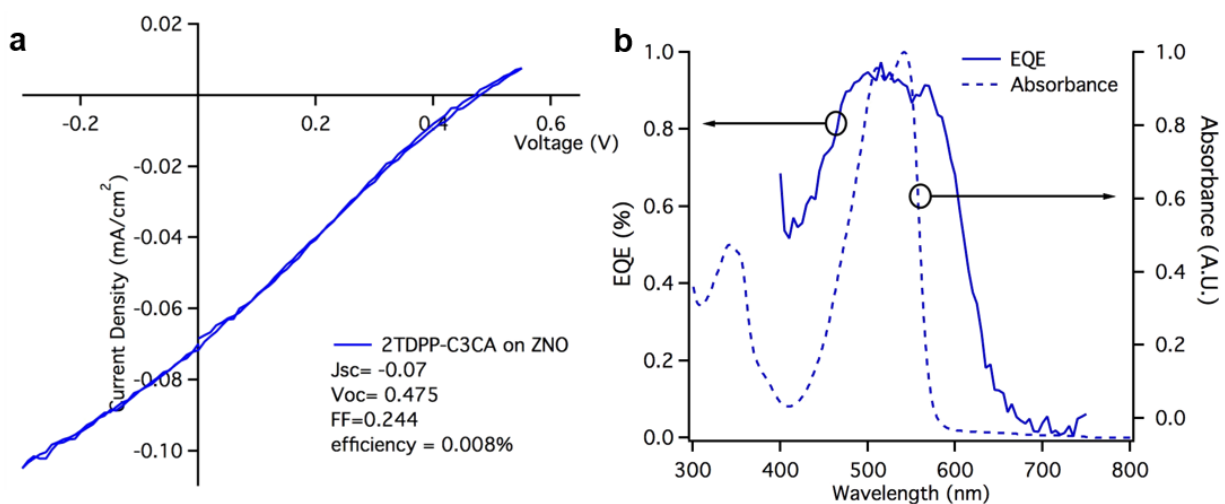


Figure 2.13: (a) an I-V curve of a 2TDPP-C3CA solar cell and (b) an external quantum efficiency measurement plotted against the visible light absorption of the 2TDPP-C3CA molecule in solution.

thickness were fundamental limitations to device efficiency that needed to be addressed. To that end, we transitioned to fabricating dye sensitized solar cells (DSSCs) rather than thin film devices.

The thickness and porosity of our active layer — which were detrimental to the efficiency of a thin film cell — are close to ideal for a dye sensitized solar cell (DSSC). A DSSC is different from a thin film solar cell in that a DSSC uses an electrolyte to transport the positive charge carrier to the electrode whereas a thin film cell transports holes through the bulk of the organic donor phase. Because positive charge transport happens in an electrolyte phase in a DSSC, a mesoporous architecture that maximizes contact between the electrolyte phase and dye molecules will be the most efficient. The process of power generation in a DSSC is outlined in figure 2.14. The open circuit voltage (V_{oc}) of an OPV is roughly based on the difference in energy level between the HOMO of the donor and the LUMO of the acceptor, while the V_{oc} of a DSSC is based on the energy level difference between the redox potential of the electrolyte and the Fermi level of the electron acceptor.⁵⁰ The mesoporous architecture of the DSSC is designed to maximize dye loading onto the surface of the semiconductor while allowing each dye molecule to contact the electrolyte for the regeneration process. The morphology in our films is slightly different than the typical DSSC, so it was initially

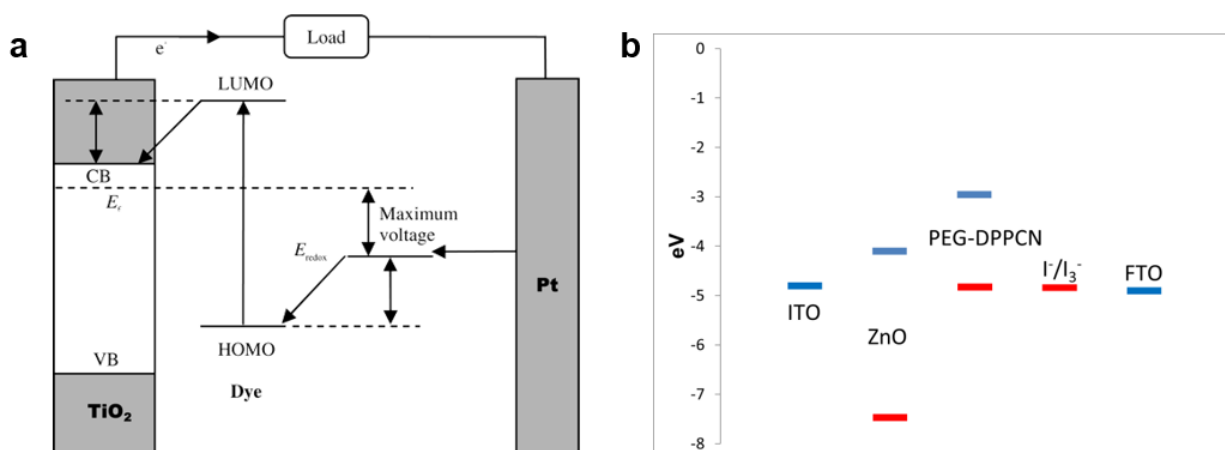


Figure 2.14: (a) The process of power generation in a DSSC is outlined in this figure. First, incident light excites an electron into the LUMO of the dye. Next, the electron is passed from the dye to the conduction band of the inorganic semiconductor. Then, the hole in the dye is reduced by iodide. Finally, the triiodide that is formed as a result of the redox reaction diffuses to the platinized electrode to be reduced back to iodide¹⁷. Panel adapted from Wang et al.⁵⁰ (b) The energy level diagram for this solar cell shows that the HOMO level of the dye molecule is almost identical to the redox potential of the I^-/I_3^- couple. This means that the electron from the iodide lacks an energetic driving force to transfer to the dye which limits the device efficiency.

unclear whether the electrolyte could penetrate into the galleries of the lamellar or the electrolyte only makes contact with dye molecules around the edges of sheets. We have greatly increased the interface area between the dye molecules and ZnO by arranging them into a lamellar architecture, but it remains to be seen whether this added area is accessible to the electrolyte.

Using the same deposition conditions as the thin film PEG-DPPCN solar cells ($\eta \sim 10\text{-}4\%$), we fabricated DSSC devices with PEG-DPPCN in a 1:1 DMSO: H_2O solution with an efficiency of $\eta = 0.006\%$. The steps for fabrication of DSSCs are detailed in the materials and methods section. Processing conditions for the active layer were then optimized by changing solution conditions ($\eta = 0.012\%$) and annealing ($\eta = 0.025\%$). Next, a set of 5TmDCA DSSCs were fabricated with the same electrodeposition conditions as the optimized $\eta = 0.035\%$ efficient thin film 5TmDCA devices. There was a modest improvement in the efficiency of these cells ($\eta = 0.05\%$) by switching to a DSSC device compared to thin film devices. Even though the 5TmDCA cells have lower vis-

ible absorption, they still performed better than the best PEG-DPPCN cells that we had made up to that point. These devices showed better efficiency than previous PEG-DPPCN devices partly because the electrolyte used in the 5TmCDA cells (A6141) leads to higher V_{oc} values compared to the commercially-available Solaronix electrolyte used in the PEG-DPPCN devices. In all following DSSC experiments, A6141 electrolyte was used. Other reasons for improved efficiency of the 5TmDCA devices could be due to better alignment of the lamellar structures, better packing of the chromophore in the lamellar gallery, or better alignment of the energy levels for a DSSC than the PEG-DPPCN molecule. Of these three possibilities, influencing the packing of the chromophore is the most straightforward variable to adjust. As outlined in the previous section on film morphology, in the hybrid dye-ZnO electrodeposition process the chromophore is only incorporated in the growing structures near their solubility limit in the DMSO/H₂O mixture. The dye molecules are generally more soluble in solutions with higher DMSO content, and therefore their optimal concentration for deposition increases in solutions with more DMSO. These findings are represented schematically in figure 2.27. Following the trend explained by this figure, and mirroring the solution conditions of the 5T deposition, the DMSO: H₂O ratio was increased from 1:1 to 2:1 and the concentration of chromophore added to the electrodeposition bath was also increased. This change in deposition conditions led to higher chromophore loading in the thin film as well as some preferential alignment of the structures on the surface (as shown in figure 2.8e). These new PEG-DPPCN-ZnO lamellar DSSCs have a significantly higher efficiency ($\eta = 0.125\%$) that is several orders of magnitude better than the PEG-DPPCN-ZnO thin film devices and almost a full order of magnitude better than the previous best 5T thin film devices (figure 2.15).

2.3.3 PEG-DPPCN control device study

To contextualize our results, the best PEG-DPPCN-ZnO DSSC should be compared to other control device architectures to probe the fundamental charge transport processes in DSSCs. The literature includes examples of both nanoparticle and electrodeposition techniques to deposit ZnO on

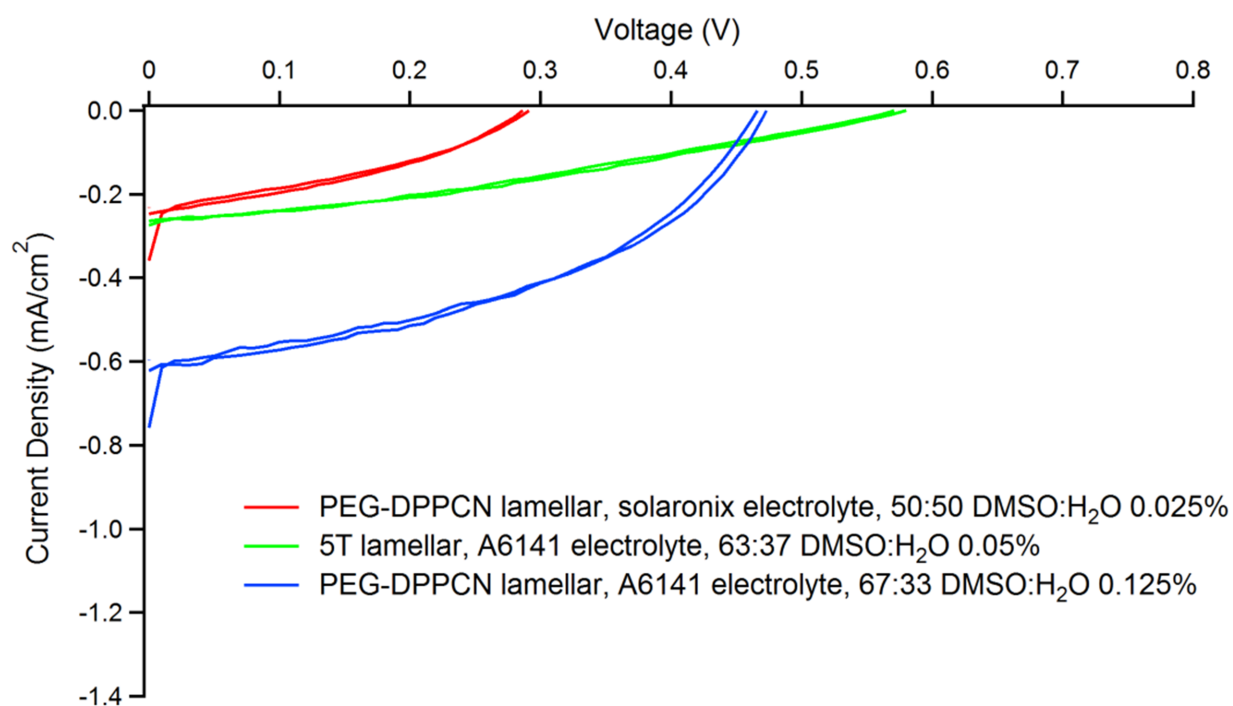


Figure 2.15: This graph compares the current-voltage behavior and efficiency of the 5T and the PEG-DPPCN lamellar before and after changing the electrolyte and DMSO:H₂O ratio. The 5T has slightly higher V_{oc} due to better energy level alignment, but we see that we get almost a factor of 3 improvement in short circuit current out of the PEG-DPPCN cell due to better absorption in the visible spectrum.

an electrode surface for DSSC active layers. As previously discussed, Yoshida et al. electrodeposited ZnO with eosin-Y dye as a surfactant to create a 3-D bicontinuous network.⁴⁸ They dissolved the dye from the structure using a mildly basic solution and then re-sensitized the remaining ZnO with the same dye. This process removed any dye aggregates that formed because of the electrodeposition process and added a monolayer of dye to the exposed ZnO surface. This led to a significant improvement in efficiency in their devices ($\eta = 2.7\%$). When we tried to replicate this approach with the hybrid lamellar ZnO structure, we find that the final device efficiency improves ($\eta = 0.19\%$), but the lamellar structure is destroyed when the dye is dissolved (figure 2.16). The as-deposited hybrid is an opaque purple film, and after desorption a white transparent film is left. After re-sensitization in an ethanolic solution of the chromophore overnight, the film is once again purple, but transparent rather than opaque, indicating that there is significantly less scattering from the re-sensitized film. From the SEM, the lamellar, wire-like morphology is gone after the dye desorption process, and therefore a significant amount of the total scattering and surface area comes from the lamellar structure despite not efficiency to the DSSC device. Our result from this experiment suggests that the inner surfaces of the lamellar structure aren't being accessed by the electrolyte in our hybrid system since the collapsed structure with just a monolayer of dye on the surface has higher efficiency than the as-deposited structure.

Another ZnO-based DSSC architecture from the literature can be made by synthesizing nanoscale ZnO flakes by mixing zinc nitrate with NaOH in solution and doctor-blading the flakes that formed onto the substrate surface.⁵¹ This technique leads to a porous network of flakes on the substrate surface that can then be sensitized with a ruthenium complex dye to form a 6.46% efficient device.⁵¹ When we fabricate ZnO nanoflakes with this method and sensitize them with PEG-DPPCN, the resulting device efficiency is significantly higher ($\eta = 0.39\%$) than what we observed in the electrodeposited device. In these devices, we observe that there is a substantial increase in the J_{sc} with pre-fabricated ZnO flakes compared to <1 nm thick lamellar sheets. Therefore, it appears that the active surface area of the ZnO nanoflake device is likewise higher than

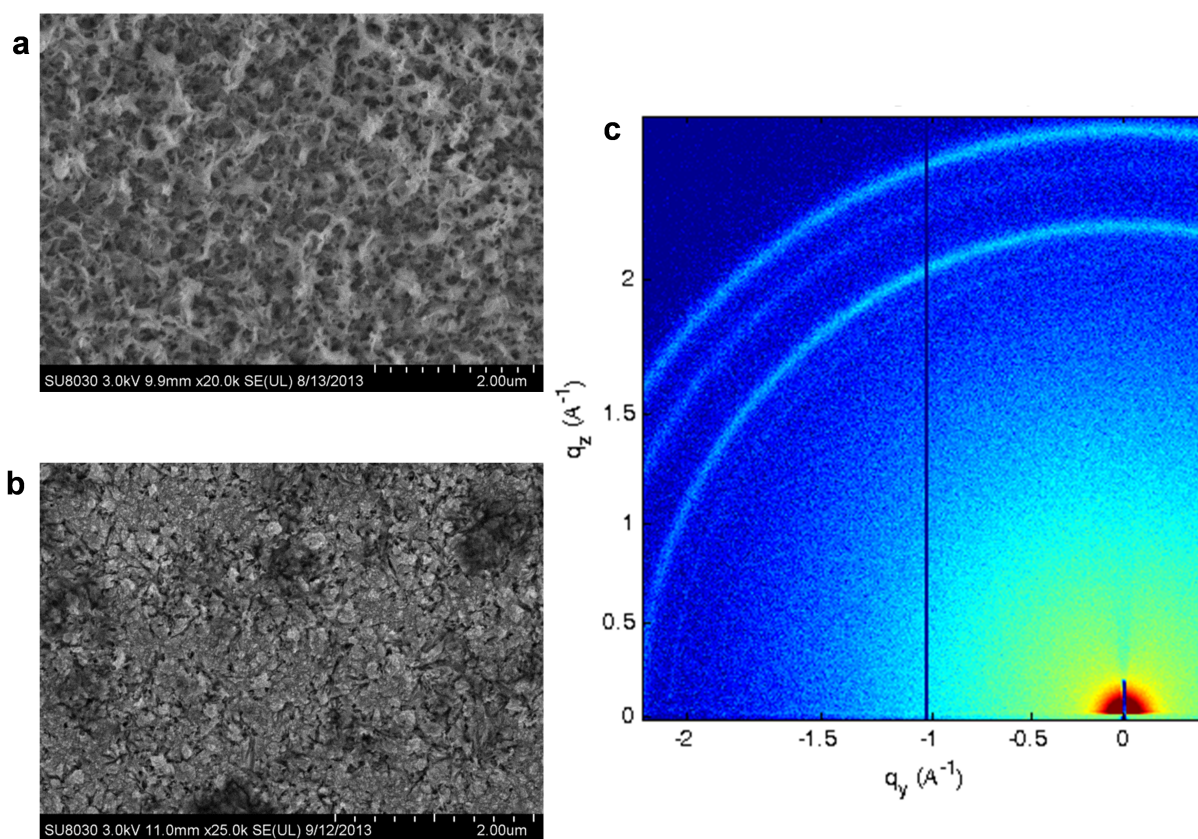


Figure 2.16: A PEG-DPPCN film a) freshly made and b) after dye desorption. Dye was desorbed by soaking in a 70°C pH10.4 H₂O/DMSO solution for 5 hours. c) 2D-GIWAXS on the film after desorption shows that the lamellar structure is not retained.

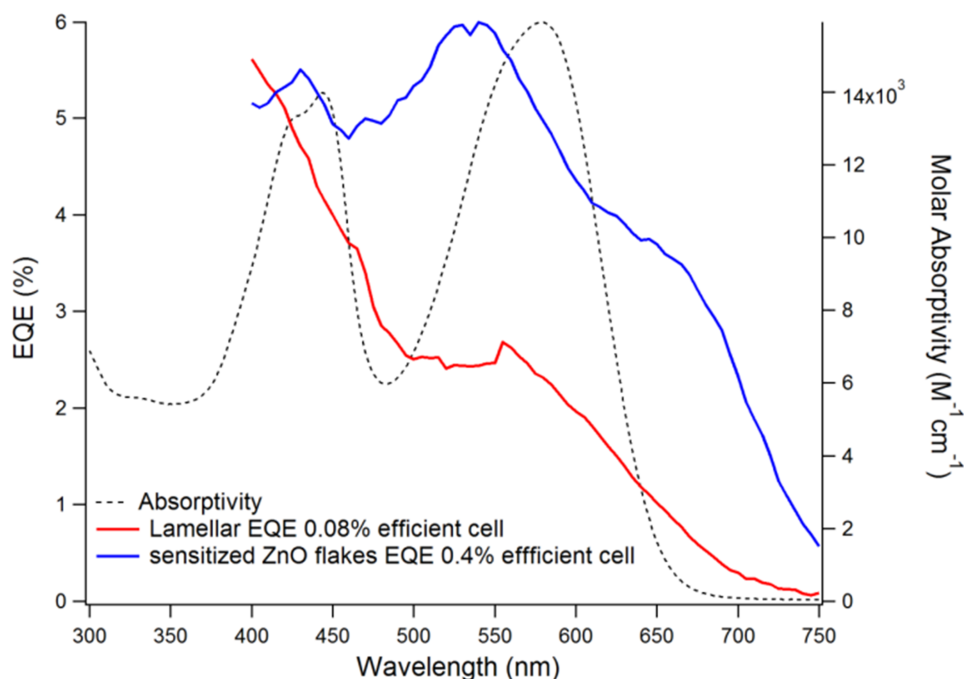


Figure 2.17: The EQE of a PEG-DPPCN cell is plotted against the EQE of the PEG-DPPCN sensitized pre-fabricated ZnO flakes. The absorptivity of PEG-DPPCN is given as well, showing that the EQE only tracks well with the lamellar in the case of lower wavelength (higher energy) incident light.

both the PEG-DPPCN lamellar structure and the collapsed, sensitized ZnO structure described in the previous paragraph. The EQE of nanoflake ZnO DSSC shows broader absorption profile than the dye alone in solution indicating that the dye molecules aggregate on the surface when they sensitize the scaffold (figure 2.17). DSSCs ideally have a non-aggregated monolayer of dye on the surface which allows for conformal coverage and minimal recombination,⁵² so this may explain why the efficiency of this device is still low compared to other DSSC devices in the literature.

PEG-DPPCN can also be used in BHJ organic solar cells with PCBM as the electron acceptor. Optimized PV devices with DPP as the core of the electron donor have reported efficiencies higher than $\eta = 4\%$.⁵³ Our BHJ device with PEG-DPPCN was fabricated on an ITO substrate with a MoOx hole transport layer. The solution was spin cast from 10mg/ml PEG-DPPCN and PC₆₁BM in a 1:1 ratio by weight in chloroform with a LiF/Al top contact. AFM of the active layer of this film shows

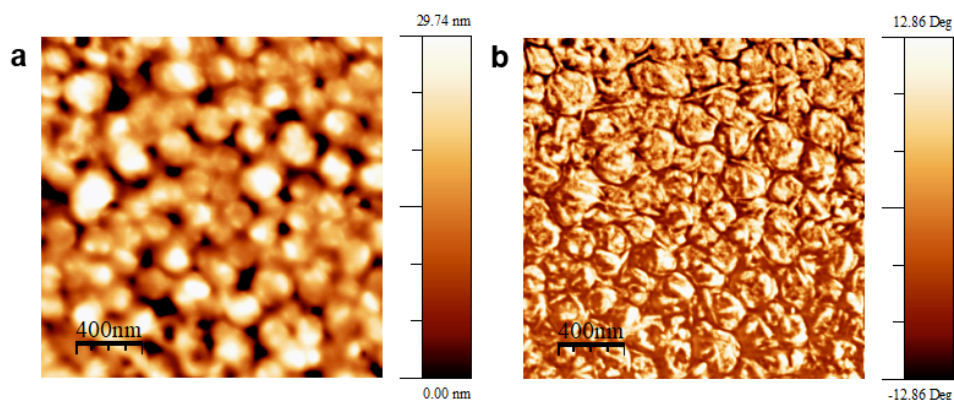


Figure 2.18: (a) Height and (b) phase AFM images of the BHJ active layer. The height image shows the phase separation between PCBM and PEG-DPPCN and the phase image shows fiber formation indicative of 1D assemblies of the PEG-DPPCN.

that its behavior is dominated by fiber formation of the PEG-DPPCN and phase separation from the PCBM (figure 2.18). The observed morphology is similar to what should be expected based on other similar DPP molecules that the group has previously synthesized for OPV projects.¹⁹ It is clear from the AFM data that the size of the PCBM and PEG-DPPCN phases in the BHJ device are significantly larger than the monolayers and bilayers of donor and acceptor present in the lamellar architecture. Although more optimization on this BHJ device could have been made, our first attempt yielded an efficiency of $\eta = 0.25\%$ which is better than our PEG-DPPCN thin film and DSSC devices. There are two possibilities for why the BHJ device performs better than these two devices. First, by moving away from the lamellar architecture as the nanostructure for the thin film device, there are much larger domains of donor and acceptor, which should lead to lower recombination, and thus, better device performance. Second, by switching the electron acceptor to PCBM instead of ZnO, there should be significantly lower electron mobility, which would lead to more balanced charge transport, and therefore prevent the formation of a space-charge region in the device.³¹ This second reason most likely plays a more minor role in device function than the organization of the two phases within the film.

The control devices from the previous two paragraphs are plotted against the best lamellar devices in figure 2.19. This figure shows that the un-optimized BHJ thin film cell ($\eta = 0.25\%$) and

pre-fabricated ZnO nanoflake DSSC ($\eta = 0.39\%$) both performed better than the best lamellar devices we have made. Two other control devices were also plotted in figure 2.19, the ZnO sol-gel ETL underlayer without dye, and the ZnO sol-gel ETL sensitized with PEG-DPPCN. This ETL is composed of ZnO nanoparticles, but it is essentially a flat surface. We observe that the device efficiency of these two control devices is significantly lower than the lamellar structure, indicating that the surface area and porosity of the electrodeposited scaffold is higher than an essentially flat surface, as expected. Preparation details and AFM are included in the materials and methods section as well as figure 2.26. From this full set of devices, we observe that when the PEG-DPPCN dye is placed in a conventional device geometry (BHJ or mesoporous DSSC), it outperforms the lamellar hybrid films. This result suggests that the lamellar structure itself is less than ideal for DSSCs, and that the porosity and thickness of the lamellar devices is worse for PV performance than a sensitized mesoporous inorganic scaffold. The next section of this chapter compares the efficiency of DSSCs with a commercially available dye compared to PEG-DPPCN to more conclusively show that the PEG-DPPCN dye itself performs poorly in DSSC devices and to explain why it performs poorly using electrochemical impedance spectroscopy (EIS).

2.3.4 *N719 control device study and electrochemical impedance spectroscopy*

One limitation of our devices tested thus far has been their low efficiency, and it is unclear whether that low efficiency is a result of poor-performing dye molecules or a bad device optimization process. To compare the efficiency and electrochemical processes between our highest-performing dye molecule, PEG-DPPCN, and the literature standard ruthenium complex dye, N719,⁵⁴ we fabricated a series of control devices and compared electrochemical impedance spectroscopy (EIS) between them. The results of this study are shown in figure 2.20. Our first attempt at fabricating an N719-TiO₂ DSSC resulted in a device with $\eta = 1\%$, and details of this fabrication process are included in the materials and methods section. The N719 device was then optimized further using process optimization techniques such as increasing surface passivation of

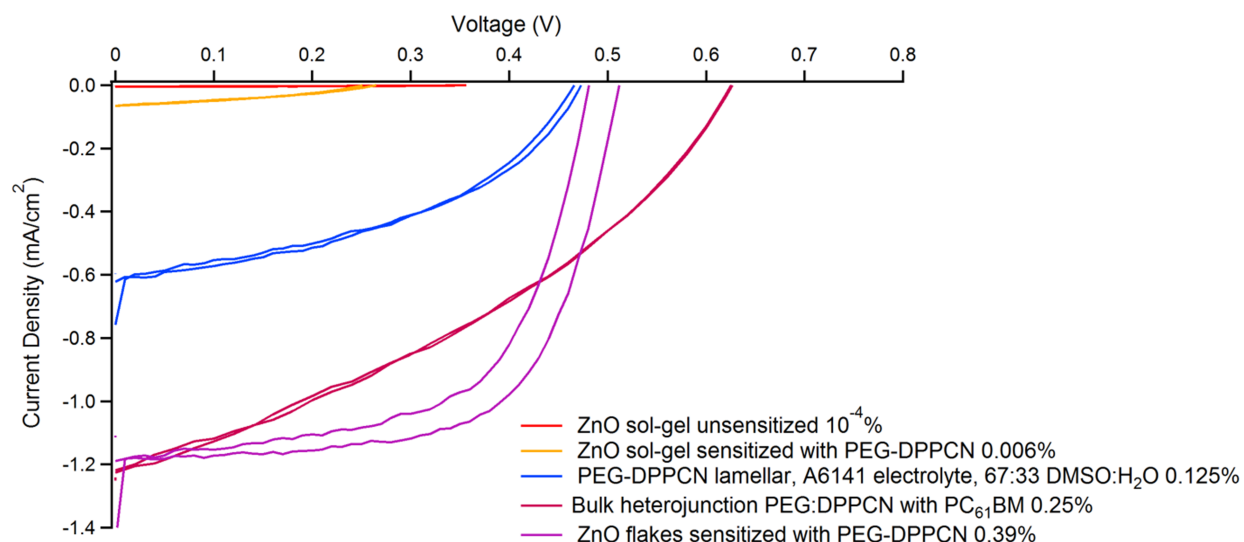


Figure 2.19: This graph compares the control PEG-DPPCN devices with the best lamellar PEG-DPPCN devices. On a flat layer of ZnO, we get very poor efficiencies without ($\eta \sim 10^{-4}\%$) and with ($\eta = 0.006\%$) PEG-DPPCN as a sensitizer. The optimized lamellar structure gives $\eta = 0.125\%$. The BHJ ($\eta = 0.25\%$) and the pre-fabricated ZnO flakes sensitized with PEG-DPPCN ($\eta = 0.39\%$) both perform better than the lamellar device.

TiO₂ ($\eta = 1.7\%$), adjusting the thickness of the TiO₂ ($\eta = 2.7\%$), increasing sensitization time, ($\eta = 3\%$), and including chenodeoxycholic acid in the sensitization bath⁵⁵ ($\eta = 3.36\%$). PEG-DPPCN devices were then fabricated on a mesoporous TiO₂ scaffold with all of the optimizations included in the TiO₂ devices except for including chenodeoxycholic acid. This PEG-DPPCN device was the lowest-efficiency device of this set of devices with $\eta = 0.19\%$. When we compare the DSSCs with N719 to PEG-DPPCN, an un-optimized N719-TiO₂ DSSC ($\eta = 1\%$) outperforms an optimized PEG-DPPCN by half an order of magnitude. The PEG-DPPCN device on TiO₂ also achieved roughly half of the efficiency of a very similar device on a ZnO scaffold ($\eta = 0.39\%$). We attribute this difference in efficiency between the ZnO and TiO₂ devices to higher electron mobility in ZnO compared to TiO₂.⁵⁶

We performed EIS measurements on our PEG-DPPCN ($\eta = 0.19\%$) and N719 ($\eta = 3\%$) TiO₂ DSSCs to characterize and compare the kinetic processes in those devices. The EIS results are shown as Nyquist and Bode plots in figure 2.21. The 3 semicircles of the Nyquist plot (figure 2.21D) cor-

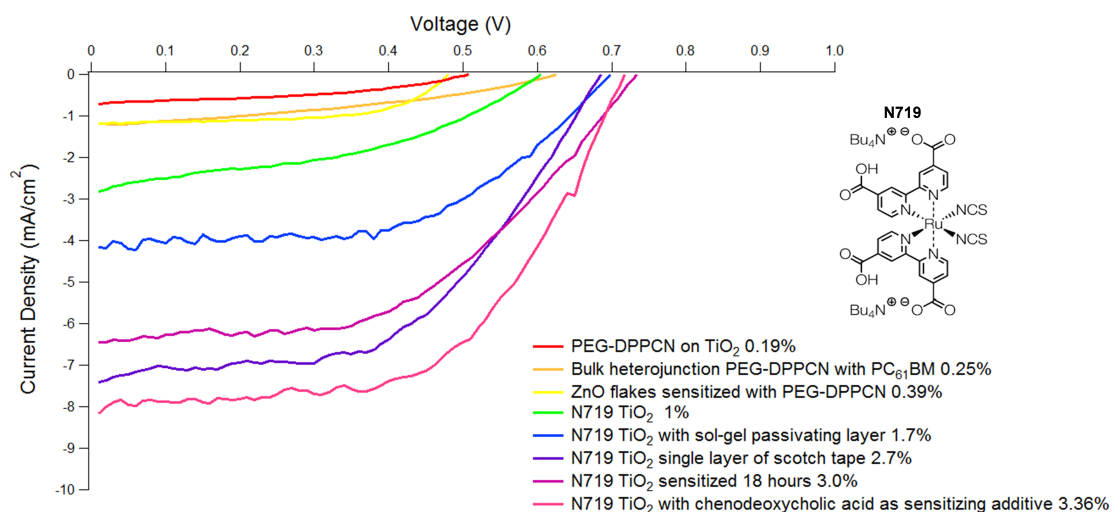


Figure 2.20: I-V curves of various PEG-DPPCN DSSC devices compared with N719-sensitized TiO_2

respond to 3 kinetic processes present in all DSSC devices. These processes are also represented by peaks in frequency in the Bode plot (figure 2.21e). The first (interpreted left-to-right on the x axis in the figure) peak on the Bode plot corresponds to low-frequency diffusion in the electrolyte, the second peak corresponds to intermediate-frequency electron transport and back reaction at the mesoscopic TiO_2 /electrolyte interface as well as the electron transfer at the FTO/ TiO_2 interface, and the third peak corresponds to charge transfer at the electrolyte/Pt-FTO interface.^{57,58} Accordingly, the (interpreted left-to-right on the x axis in the figure) third semicircle on the Nyquist plot corresponds to low-frequency diffusion in the electrolyte, the second semicircle corresponds to intermediate-frequency electron transport and back reaction at the mesoscopic TiO_2 /electrolyte interface as well as the electron transfer at the FTO/ TiO_2 interface, and the first semicircle corresponds to charge transfer at the electrolyte/Pt-FTO interface.

Figure 2.21C shows the line transmission equivalent circuit model used to represent these kinetic processes in our N719 device, and the fit for that circuit is superimposed over our data in figure 2.21D and E, indicating that this model is a good fit for our data. The shape of these curves

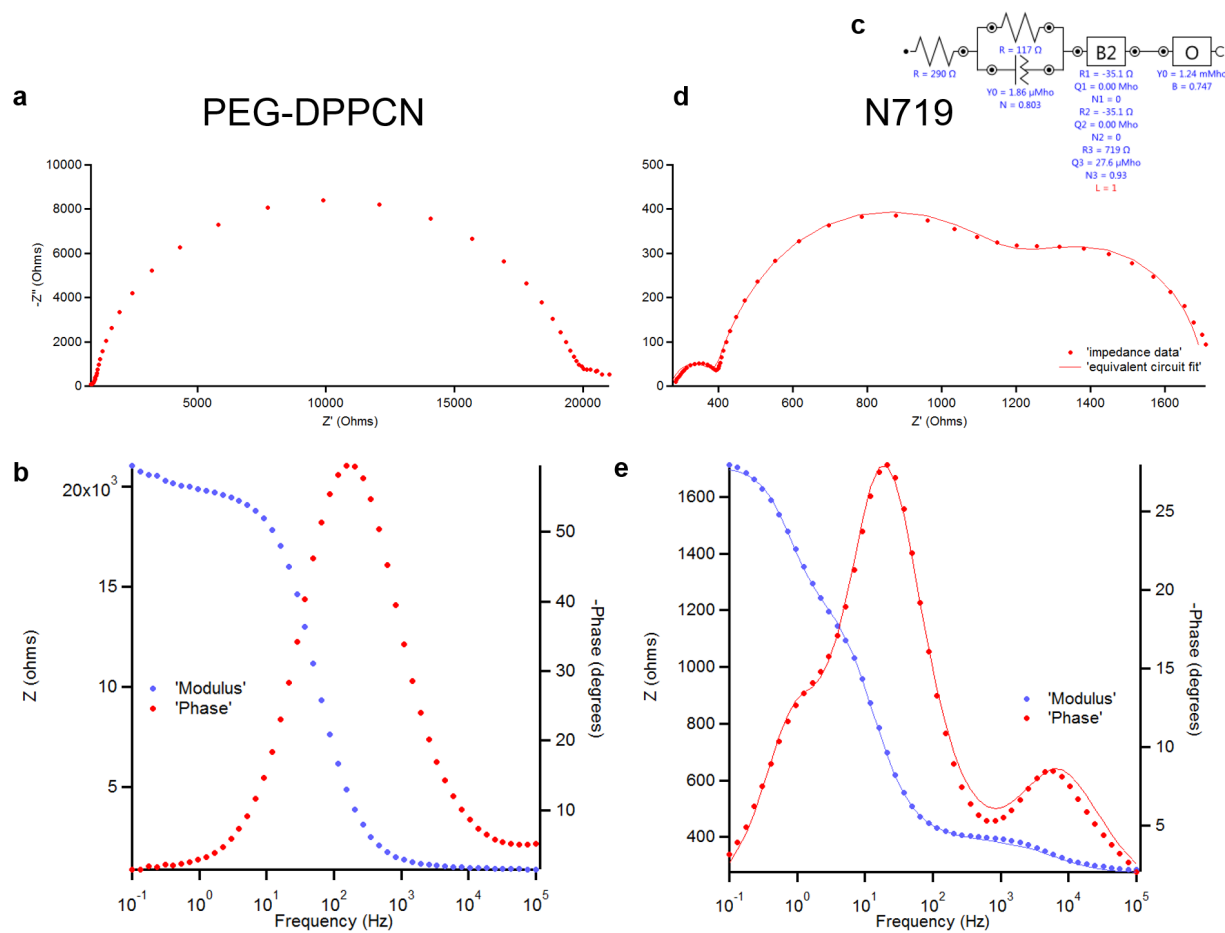


Figure 2.2.1: Electrochemical impedance spectroscopy data plotted as Nyquist (a, d) and bode (b, e) plots of PEGDPPCN (a, b) and N719 (c-e) sensitized onto a TiO_2 scaffold. The equivalent circuit for the N719 data is shown in (c) and the resulting fit from this circuit is overlaid over the data in (d) and (e).

as well as the frequency of the kinetic processes matches what we would expect given the precedent for these measurements in the literature.^{57,58} When we compare our PEG-DPPCN device, we see in the Bode plot (figure 2.21B) that only the intermediate-frequency process is well-represented by the data, and thus the lone semicircle shown in the Nyquist plot (figure 2.21A) also corresponds to that process. We observe that the frequency and impedance of the intermediate-frequency process is significantly higher for the PEG-DPPCN device compared to the N719 device. This result means that the electron transport and back reaction at the mesoscopic TiO₂/electrolyte interface in the PEG-DPPCN device is significantly faster which implies that there is significantly shorter electron lifetime and increased recombination at the dye-TiO₂ interface with the PEG-DPPCN dye. This shorter electron lifetime is most likely the result of unfavorable aggregation of the PEG-DPPCN dye on the TiO₂ surface. This EIS evidence supports our previous observation where the EQE of similar PEG-DPPCN DSSCs (figure 2.17) showed a spectral broadening compared to monomeric PEG-DPPCN absorption indicative of dye aggregation, which is typically not ideal for DSSC devices.²⁰

2.4 CONCLUSIONS, LIMITATIONS, AND FUTURE OUTLOOK

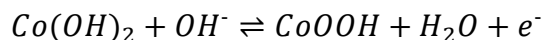
The work presented in this chapter on ZnO-based lamellar hybrid solar cells represents significant progress towards a new fabrication method for dye-sensitized solar cells. Our morphological study showed that the hybrid lamellar structure will electrodeposit with a variety of organic dyes with non-crystalline packing, but the inorganic domains are invariably sub-nanometer thick sheets based on the layered double hydroxide structure. We also showed how deposition conditions could be rationally tuned in these systems using control of temperature, concentration, and solvent composition to keep the dye molecule below its critical aggregation concentration in solution for deposition. Our subsequent device study showed that the electrodeposited lamellar hybrid films perform significantly better as DSSC devices than as thin film devices, but that dye aggregation leads to poor overall efficiency with these dye molecules in any device architecture. Across many different device

comparisons, the electrolyte does not appear to access the interior surfaces of the lamellar structure in our DSSCs, and as a result, the traditional sensitization process of mesoporous scaffolds for DSSCs leads to better-performing devices. Our electrodeposition process would have an advantage over this traditional process in that it can create active layers with an arbitrary shape and size with a much higher throughput. However, without the development of higher-performance dyes to fit into this structure, high-efficiency devices cannot be fabricated with this technique. Future work along this path would involve significantly more organic synthesis to screen the structure and photovoltaic performance of many dye molecules in the electrodeposited hybrid lamellar system, with attention given to the aggregation and crystallization behavior of the organic dye.

Aside from the significant expertise and investment necessary for further organic chemical synthesis in this project, our system suffers from a few other roadblocks to further progress. First, one of the key findings of our group's studies on organic scaffolds for hydrogen evolution is that crystallinity of the organic assemblies is important to electronic properties.^{59,60,61} Exciton diffusion distance and turnover numbers for hydrogen production in these systems are significantly improved when the organic assemblies in these gels are crystalline instead of amorphous. Similarly, organic photovoltaics benefit from some crystallinity in their donor molecule phase. High-efficiency OPV donor molecules have paracrystalline order as a compromise between the benefits of crystallinity on electronic properties and phase separation between donor and acceptor.¹⁹ Our hybrid ZnO lamellar system does not exhibit crystalline packing of the donor molecules within the organic galleries. Perhaps with higher crystallinity in the galleries we would observe higher participation of the chromophores within the galleries since they should be electronically accessible to the electrolyte if they had higher hole mobility.

Second, the lamellar ZnO hybrid active layer is unstable in typical electrolyte/solvent systems used in DSSCs. The active layers that we made in this study were stable enough for measurement and electronic characterization, but these layers would dissolve overnight soaking in the A6141 electrolyte. There are some electrolyte systems that are more compatible with ZnO, since A6141

is typically used in TiO₂-based DSSCs, however even with these systems, it is unclear whether the dye molecules will remain attached to the ZnO. Related to the problem of stability in electrolyte, one follow-up study inspired by the work in this chapter has been the development of cobalt hydroxide lamellar hybrid supercapacitors.³⁸ By changing the inorganic precursor from Zn(NO₃)₂ to Co(NO₃)₂ our group has formed templated Co(OH)₂ nanostructures. Co(OH)₂ is an interesting material because it has a very high theoretical specific capacitance (3500 F/g)⁶² as an electrochemical supercapacitor. Specifically, at the Co(OH)₂-electrolyte interface there is a redox reaction that occurs to store charge in the device pseudocapactively:



Our group's study on this process showed that nanotubular hybrid pyrenebutyric acid-cobalt hydroxide structures can be electrodeposited on stainless steel substrates. These nanotubes have significantly higher surface area than a flat film, and thus exhibit enhanced electrochemical performance. The study demonstrated that the conjugated pyrenebutyric acid molecules helped stabilize the Co(OH)₂ under basic pH conditions, analogous to how conjugated dyes have been demonstrated by our group to stabilize the lamellar structure under the annealing conditions necessary to transform Zn(OH)₂ to ZnO.³² One caveat to this added stability is that it requires the dye, pyrenebutyric acid, to be saturated in the electrolyte solution to prevent dissolution of pyrenebutyric acid from the nanotubes. This solvent additive takes advantage of Le Chatelier's principle to prevent dissolution of dye molecules from the solid phase.

There are two key points from the cobalt hydroxide supercapacitor work that are worth discussion with respect to the lamellar ZnO DSSC work. First, an approach to stabilization in which dye was added to the electrolyte would not work in a DSSC because dye dissolved in the electrolyte would interfere with light absorption and charge transfer in the electrolyte. In the supercapacitor cathode, the pyrenebutyric acid is used as a structural component and stabilizer, but it is not an active component. Second, the comparison in the cobalt hydroxide work is favorable because they

are comparing their nanostructures to a bulk, flat film control which is a fair comparison in the supercapacitor field. The comparisons for our ZnO-dye lamellar structures in the solar cell field are less favorable because there is a robust literature describing nanostructured BHJ and DSSC devices. Almost all examples of PV materials incorporating organics are nanostructured because organic dyes have poor hole mobility compared to inorganic semiconductors. Therefore, when we compare our ZnO-dye lamellar structures to other nanostructures, we find that they fall short of both BHJ and traditional DSSC architectures, as described in this chapter.

Finally, the purported advantages of DSSCs have largely been supplanted by the development of perovskite solar cells. Methylammonium lead iodide (MAPbI₃) perovskite solar cells (PSCs) were originally developed as solid-state DSSC devices. Prior to the development of PSCs, solid state DSSCs achieved significantly lower efficiency than liquid-electrolyte devices, but they had the advantage of simpler manufacturing processes. 3rd generation PV technologies, as outlined in Chapter 1, are promising because they can be made with earth-abundant materials on flexible substrates. If they can be made with high enough efficiency, OPVs, solid-state DSSCs, and even PSCs could one day be printed cheaply on flexible substrates in roll-to-roll processes. One of the most important developments in the field of solid-state DSSCs was the use of N²,N²,N^{2'},N^{2'},N⁷,N⁷,N^{7'},N^{7'}-octakis(4-methoxyphenyl)-9,9'-spirobi[9H-fluorene]-2,2',7,7'-tetramine (Spiro-OMeTAD) as a hole-transport material which was first reported in 1998.⁶³ Spiro-OMeTAD was later used as the hole transport layer used on the first PSC to have an efficiency of 9.7%⁶⁴ which represented a large step forward in both efficiency and stability of PSCs. Spiro-OMeTAD was subsequently used in many record-efficiency devices.^{65, 66} Whereas liquid-electrolyte DSSCs achieved relatively modest improvements in peak efficiency $\eta_{max} = 11.9\%$ ⁴ after decades of development, after only a few years of development, PSCs have achieved efficiency values of $\eta_{max} > 22\%$. This difference in efficiency takes advantage of the ambipolar conduction of MAPbI₃ compared to dye-based excitonic solar cells as well as the wealth of knowledge in solution-based PV devices due to the past decade of research in the field of OPVs.

The following two chapters of this dissertation, therefore, shift away from electrodeposited hybrids to attempt to address the biggest shortcoming of hybrid PSCs, specifically the instability of the MAPbI₃ active layer in operating conditions. The first study, creating a hybrid organic-inorganic through the addition of polymers to the active layer, attempts to address the instability through tailoring intermolecular interactions at the surface of the grains. The second study, creating new hybrid layered perovskite crystals by synthesizing new bulky organic cations, addresses the instability of the structure by eliminating the unstable methylammonium cation from the structure entirely.

2.5 MATERIALS AND METHODS

Chemical synthesis: All solvents and reagents were purchased from Sigma-Aldrich and used without further purification, unless otherwise noted.

2TDPP-C3CA: Under an atmosphere of N₂, tert-butyl 4-bromobutyrate (400 mg, 1.8 mmol) was added in one portion to a mixture of 2TDPP⁶⁷ (360 mg, 1.2 mmol) and K₂CO₃ (980 mg, 7.1 mmol) in DMF (50 ml) at a temperature of 110 °C. After stirring for 3 days, the reaction mixture was cooled to room temperature and the solvent was evaporated under reduced pressure. The residue was taken up in CH₂Cl₂ and filtered through a pad of silica gel. The filtrand was concentrated to a volume of 5 ml and mixed with trifluoroacetic acid (1 ml). After stirring for 3 h, the solvent was evaporated and the residue was triturated three times with hexanes, affording 2TDPP-C3CA as a red-brown solid. A schematic of these synthetic steps is shown in figure 2.22.

PEG-DPPCN: DPP was alkylated with tosylated triethylene glycol monomethyl ether, then brominated with N-Bromosuccinimide. The monobrominated product was then coupled to stannylated bithiophene carboxaldehyde via Stille coupling. The resulting product was then condensed with cyanoacetic acid to obtain the target molecule. A schematic of this synthesis is shown in figure 2.23.

3TE2: Synthesis of 3TE2 involved first the lithiation and subsequent carboxylation of terthiophene to give the terminal carboxylic acid. Next, NH₃-Glu(OBn)-OBn was coupled to

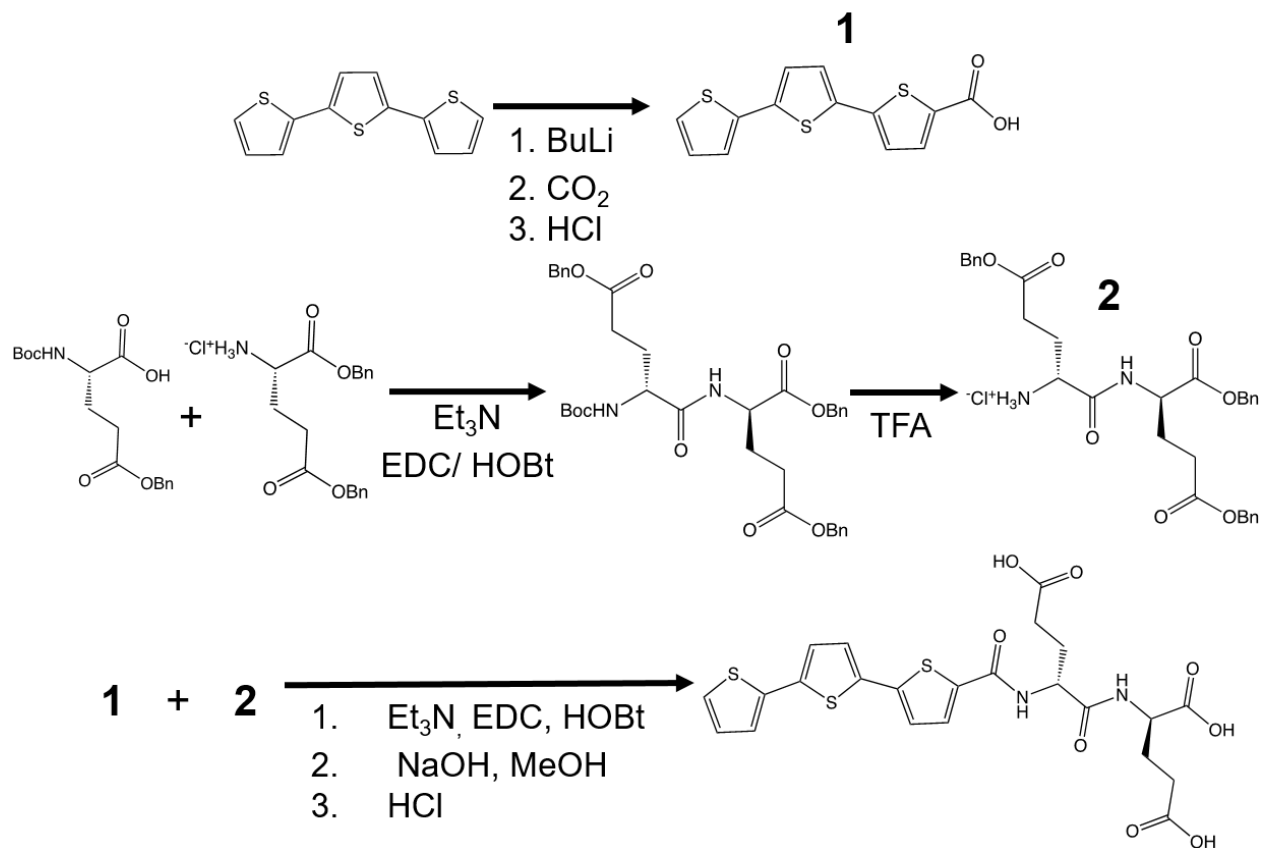


Figure 2.24: Synthetic scheme for 3T-E2

Boc-Glu(OBn)-OH via standard carbodiimide peptide coupling conditions. The dipetide was then purified and the Boc group removed using trifluoroacetic acid (TFA). The protonated peptide residue was then coupled to the carboxylated terthiophene, again, using standard peptide coupling conditions. The benzyl protecting groups were then removed using dilute basic conditions. A schematic of this synthesis is shown in figure 2.24.

3TE₃: Synthesis of 3TE₃ followed a similar path to 3TE₂. This time, two equivalents of NH₃⁺-Glu(OBn)-OBn were coupled to Boc-Glu(OH)-OH via standard carbodiimide peptide coupling conditions. The tripeptide was then purified and the Boc group removed using trifluoroacetic acid (TFA) as before. The protonated peptide residue was then coupled to the carboxylated terthiophene, us-

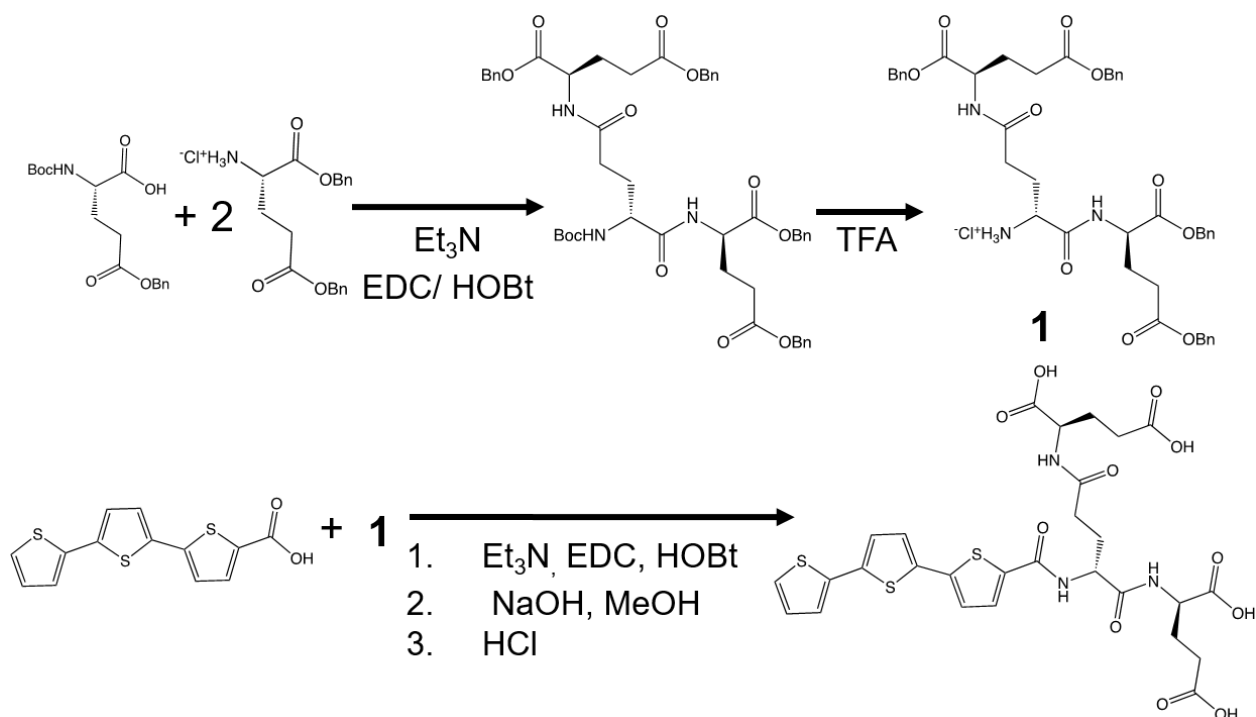


Figure 2.25: Synthetic scheme for 3T-E3

ing standard peptide coupling conditions. Similar to 3TE2, the benzyl protecting groups were then removed using dilute basic conditions. A schematic of this synthesis is shown in figure 2.25.

Substrate preparation: Glass and patterned ITO substrates (Thin Film Devices, 20 ohms/square) were cleaned by sequential sonication in hexane, soapy water, milli-q water, and a 1:1:1 mixture of isopropanol, acetone, and methanol. After drying, clean substrates were treated for 20 minutes in a UV-ozone cleaner (Bioforce Nanosciences). Poly(3,4-ethylenedioxythiophene) polystyrene sulfonate (PEDOT:PSS) (Heraeus) was filtered through a 0.45 μm PVDF filter before spin-coating at 5000 RPM with a 1000 RPM/second ramp rate for 60 seconds. PEDOT:PSS films were then annealed at 150°C for 20 minutes in a nitrogen-filled glovebox.

Sol-Gel ZnO Nanoparticle film preparation: 220mg zinc acetate dihydrate and 64mg ethanolamine were dissolved in 2mL anhydrous 2-methoxyethanol (0.5M solution). This solution was aged overnight without mixing. The aged solution was sonicated for 30 min, filtered with a PVDF filter, and spin coated onto the ITO surface at 5000 rpm for 60 seconds (for 30-40 nm thick

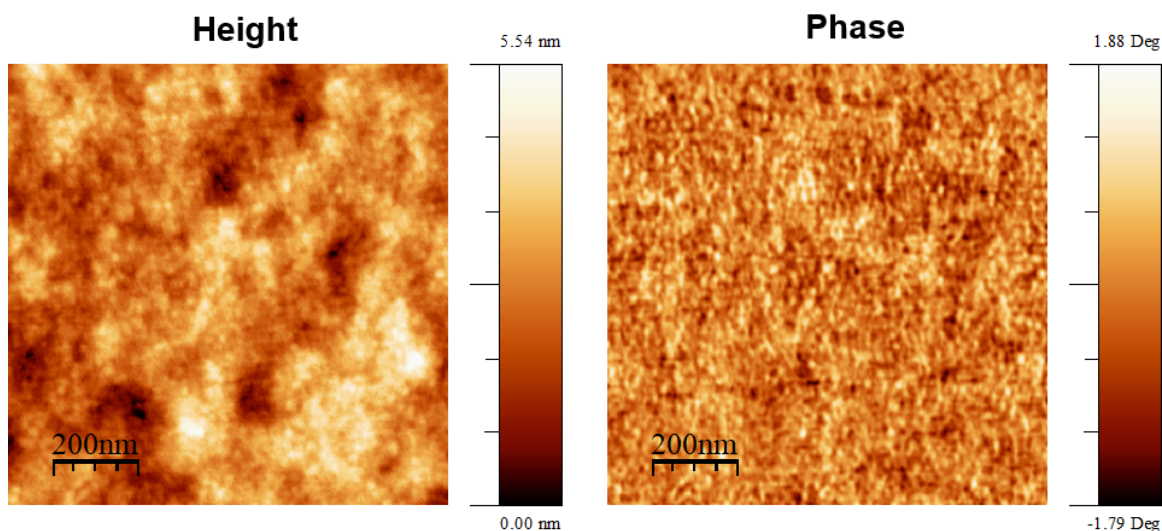


Figure 2.26: AFM height and phase images of a sol-gel ZnO nanoparticle thin film on ITO

film). Contacts were cleaned with isopropanol, and film was annealed immediately on a hotplate for 10 min in air at 180 °C. AFM of the resulting ZnO film surface is included as figure 2.26.

Electrodeposition: Electrodepositions were performed using a Princeton Applied Research Versastat 3 potentiostat with a three- electrode setup. Zn wire (Alfa Aesar, 99.9997%) was the counter electrode and the reference electrode was Ag/AgCl (BASi Inc., Model RE-5B). The deposition bath was prepared by adding 40 mM $\text{Zn}(\text{NO}_3)_2$ in water and a solution of the dye molecule in DMSO (see optimization section below for a more detailed explanation of concentration and solvent ratio) and heated with stirring in an oil bath at 70°C. This solution was then purged with Argon gas for 20 minutes to remove any dissolved oxygen. Patterned ITO substrates were then immersed in the bath and held at a constant cathodic (negative) potential relative to the reference electrode. After deposition, films were rinsed with water and dried with nitrogen gas. For solar cells, films were annealed at 150°C in a nitrogen-filled glovebox for 2 hours to convert $\text{Zn}(\text{OH})_2$ to ZnO.

Electrodeposition optimization: The optimization for electrodeposition with a new dye molecule can be a complicated process. Some of the variables for deposition include pH, temperature, solution concentration, surface chemistry, electrical potential, and water/DMSO solvent

ratio. A common problem in our initial setup was that either nothing would deposit onto the substrate, or a significant amount of material would precipitate out of solution upon addition of base, leading to poorly reproducible results. One set of experiments that we performed to simplify the optimization process as well as deposit material under reproducible conditions was a critical aggregation concentration assay. This assay uses the absorption maximum of the dye Nile red in solution as a metric for whether aggregates of the small molecule have formed. When an amphiphilic molecule assembles in solution, the hydrophobic part of the assembly will orient away from the solvent phase, creating a small hydrophobic region within the assembly. Under these hydrophobic conditions, the Nile red dye will intercalate and the fluorescence emission of the Nile red will blue shift. By creating a concentration series of our chromophore amphiphiles, we can track the fluorescence emission maximum of Nile red and assume that aggregation occurred at the concentration where the emission shifts. We have plotted a schematic of the general phase diagram in figure 2.27a, and included experimental data for 2TDPP-C3CA showing this trend in a real system (figure 2.27b). The optimum concentration for electrodeposition, from our empirical observations, is just below the solubility limit for that dye at a given temperature and solvent ratio. Generally, as the temperature and DMSO content is increased, the dye becomes more soluble, and a higher concentration is needed in solution to deposit ZnO hybrid lamellar films.

Characterization: SEM was performed on either a Hitachi S-4800-II SEM or Hitachi SU 8030 SEM operating at 3 kV accelerating voltage for both plane-view and cross-sectional SEM. For SEM samples, carbon tape was applied to the backside of the ITO/glass substrate, but no preparation was performed otherwise. 2D-GISAXS measurements were performed on a Rigaku Model MicroMax-002+ High-Intensity Microfocus Sealed Tube X-ray Generator (Cu K α radiation) with a Fujifilm phosphor image plate. 2D-GIWAXS measurements were performed at beamline 8-ID-E at the Advanced Photon Source, Argonne National Laboratory. Electrochemical impedance spectroscopy was performed using a Metrohm Autolab PGSTAT128N potentiometer. Full DSSCs were tested in the dark and under ambient light and a constant voltage equal to the V_{oc} was applied to the electrode

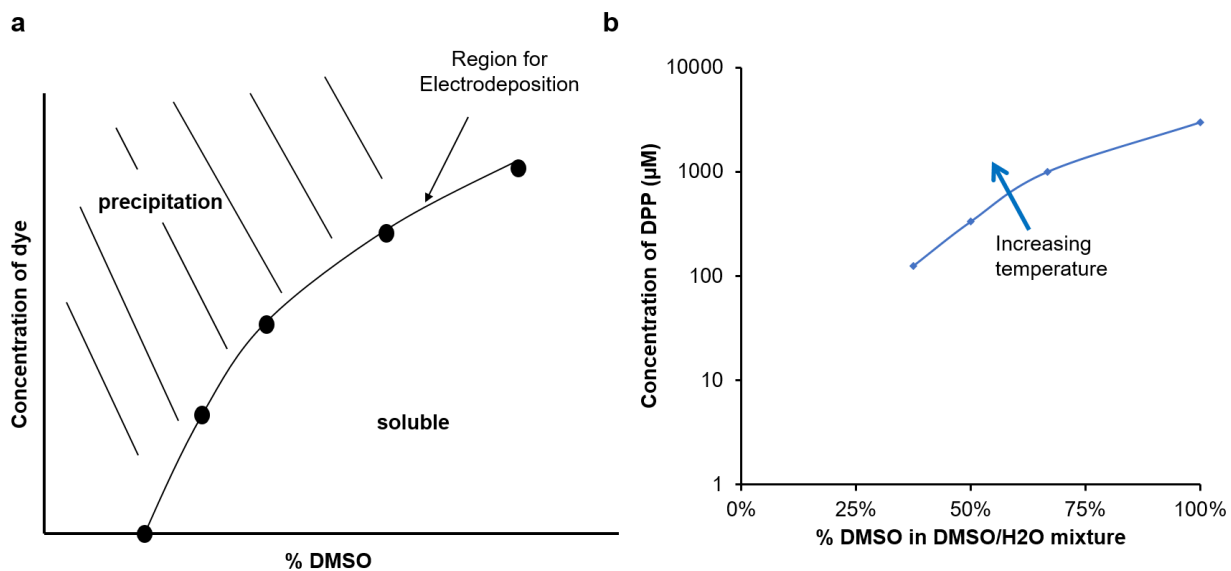


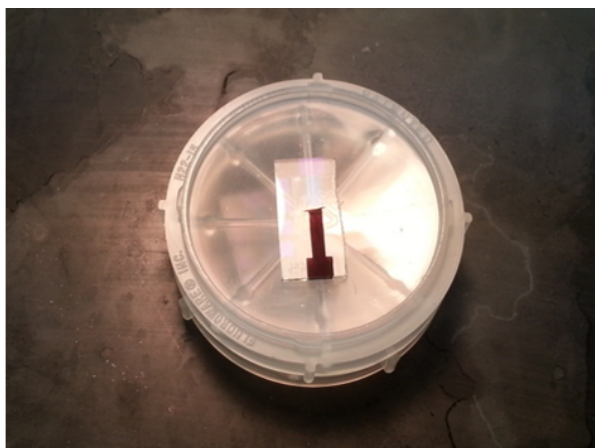
Figure 2.27: (a) a schematic of the phase diagram for dye molecules in water-DMSO mixtures for electrodeposition with zinc nitrate to form lamellar ZnO hybrids, and (b) the results of a Nile red assay showing the critical aggregation concentration of the DPP dye as a function of DMSO content in the solvent mixture.

during the EIS experiment. The oscillating voltage applied was 10mV and its frequency was swept from 0.1-105 Hz. Tapping mode atomic force microscopy (AFM) measurements were conducted on a Bruker ICON system.

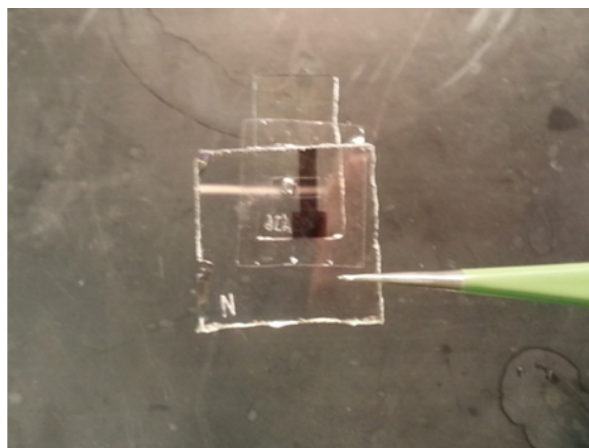
Bulk Heterojunction Device Fabrication: Devices in this study were fabricated in a nitrogen-filled glovebox. Starting from a clean ITO/glass substrate, a 10nm molybdenum oxide hole transport layer was thermally evaporated at 0.1 Å/s. The active layer solution was spin cast from 10mg/ml PEG-DPPCN and PC61BM in a 1:1 ratio by weight in chloroform. A lithium fluoride/aluminum top contact was then thermally evaporated onto the device at a pressure of $<10^{-6}$ mbar using a shadow mask to define 4 mm² devices. Finally, devices were tested in air on a Newport solar simulator with a Keithley 2400 sourcemeter at a rate of 0.2 V/s.

DSSC fabrication: Dye sensitized devices were fabricated following the scheme shown in figure 2.28. For TiO₂ devices, mesoporous TiO₂ (Solaronix) was deposited onto an FTO substrate with a doctor blade method using scotch tape as a guide for thickness and annealed at 450°C to sinter. For

ZnO devices, sol gel and electrodeposited active layers were deposited according to the conditions listed above. For sensitization, active layers were soaked overnight in a 0.1 mM ethanolic solution of the dye molecule. A 25 μm Surlyn spacer layer was patterned with a hole punch to define the gap between electrodes. The FTO top contact was platinized by wetting the substrate with a 5 mM chloroplatinic acid in ethanol, air drying for 5 minutes, and then annealing for 20 minutes at 380°C. Binder clips were used to press the two sides of the device together, and a soldering iron was used to melt the Surlyn spacer layer. Finally, a hole in the FTO top contact was pre-fabricated to align with the spacer so that electrolyte can infiltrate into the device. Electrolyte solution (A6141) was dripped over the hole in the FTO, and then the device was put under vacuum to pull solution into the mesoporous scaffold. The excess electrolyte was then wicked away and Surlyn was again melted on top of the device to seal the completed device from air. Devices were tested in air on a Newport solar simulator with a Keithley 2400 sourcemeter at a rate of 0.2 V/s, and a 4 mm² shadow mask was placed on top of the device during testing to define the active area.



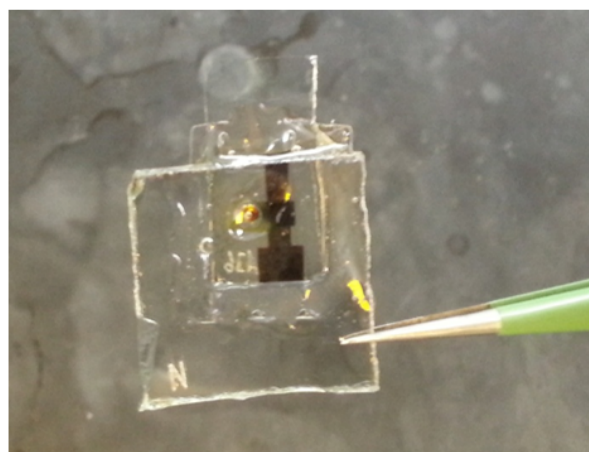
1. Lamellar growth on ITO



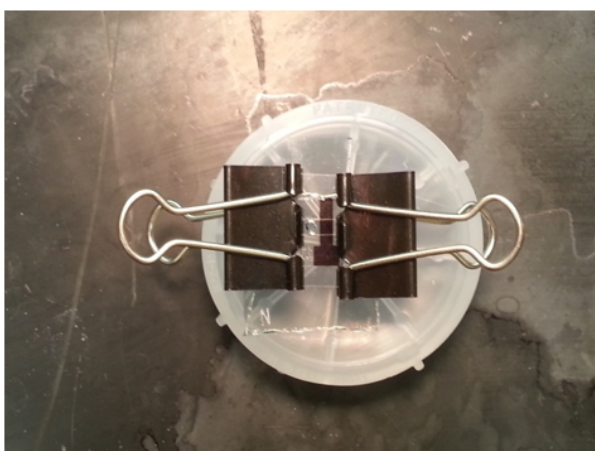
4. Melt spacer layer



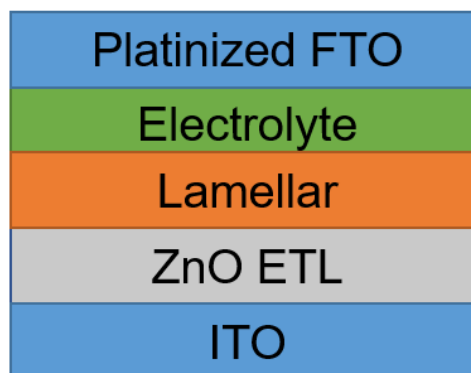
2. 25µm spacer layer



5. Seal with epoxy and infiltrate with electrolyte



3. FTO top contact applied



Cross section

Figure 2.28: Pictorial outline of the steps of DSSC device fabrication

3 STRUCTURE-PROPERTY RELATIONSHIPS IN PEROVSKITE-POLYMER HYBRID SOLAR CELLS

3.1 OBJECTIVES AND SIGNIFICANCE

Adding polymers to methylammonium lead iodide perovskite solar cell active layers has previously been shown to increase the stability of the perovskite devices in dark, ambient conditions, but the nanostructures and stabilization mechanisms of these hybrid materials are poorly understood. In this chapter, we present a structural and spectroscopic investigation into a number of polymer-perovskite hybrid materials, and compare their temporal stability as well as solar cell performance under operating conditions. We observe that the perovskite crystallite sizes decrease with the addition of polymers, and that the perovskite and the polymers form sub-micrometer-scale domains upon film casting. Acid-base interactions, as well as facet-dependent interfacial interactions between perovskite and polymer, contribute to differences in stabilities of these hybrid materials. The polymers that we studied tend to suppress the formation of the hydrate crystal phase that accelerates the degradation reaction. Among the polymers studied, adding poly(acrylic acid) significantly increases the stability of perovskite films under humid air and ambient illumination. Poly(acrylic acid)-perovskite hybrid solar cells maintain stable efficiency for the first 3 days and then slowly degrade over the next 6 days under humid air and illumination, whereas control perovskite solar cells degrade entirely within the first 2 days. These results highlight the importance of choosing suitable functional groups in the polymer phase of perovskite solar cells to prolong their device lifetime.

3.2 BACKGROUND

Methylammonium lead iodide (MAPbI_3) forms perovskite crystals via solution processing with promising opto-electronic properties including high carrier mobility,⁶⁸ high absorption coefficient in the visible and near-infrared spectrum,²² and high intrinsic carrier density.²¹ The MAPbI_3 per-

ovskite crystal structure is composed of a tetragonal unit cell with methylammonium at the corner sites, Pb^{2+} at the body center, and iodide at the face centers. Perovskite solar cells (PSCs) have shown impressive gains in photon conversion efficiency over the past 6 years, from their first demonstration as sensitizers in 3.8% efficient dye sensitized solar cells¹⁵ to >21%⁶⁹ through the use of cation mixtures in the active layer in addition to many incremental device engineering improvements. Developments such as mesoporous scaffolds,⁶⁵ two-step active layer processing,⁷⁰ planar heterojunctions,⁷¹ organic charge transport layers,⁷² and compositional tuning⁷³ have all played a role in the design improvements of these devices.

However, the chemical instability of the perovskite active layer has been a major roadblock to the commercialization of this technology. MAPbI_3 solar cells can degrade in the presence of humidity, light, or oxygen.^{74,75} One mechanism proposed for the decomposition suggests that, upon the addition of water to the MAPbI_3 lattice, methylammonium iodide (MAI) undergoes an acid-base reaction to form hydroiodic acid and gaseous methylamine.²³ The first step on this degradation pathway can be the formation of a solvate phase. N,N-dimethylformamide (DMF), dimethyl sulfoxide (DMSO), and water can all form solvates with the perovskite, which have been used to beneficially control crystal growth and formation in thin films.^{24,76} The intermediate that MAPbI_3 forms with water, $(\text{MA}^+)_2(\text{PbI}_3^-) \cdot (\text{H}_2\text{O})_2$, is an important species in the degradation process of the active layer since it forms reversibly and spontaneously at room temperature in high-humidity conditions.⁷⁶ Another recent study has shown that even under dry conditions, the combination of oxygen and light also degrades the perovskite rapidly.⁷⁴ The proposed mechanism for this degradation pathway is the formation of superoxide O_2^- when O_2 reacts with photogenerated electrons in the perovskite layer. O_2^- then degrades the perovskite structure to methylamine, PbI_2 , water, and I_2 . Because of these proposed degradation mechanisms, and likely many others that have yet to be identified, unencapsulated PSC devices are only stable for hours, and even encapsulated devices are only stable on the timescale of days in conditions relevant to stable outdoor operation.^{69,77}

Recent studies have shown that either small molecules⁷⁸ or polymers^{79,80,81} can be added to the active layer to improve the stability of PSCs. In the case of small molecules,⁷⁸ only 3 mol% of the MAI was replaced with alkylammonium phosphonate in the precursor solution. They propose that this zwitterionic molecule bonds to grain boundaries of the MAPbI₃ crystals, and that hydrogen bonding interactions between the phosphonic acid and MAI are important in stabilizing the MAPbI₃. Indeed, other ammonium iodide species, such as phenylethylammonium iodide, have been shown to contribute to stability of the MAPbI₃ perovskite even at very low concentrations by forming quasi-two-dimensional (2D) layers within MAPbI₃ crystals.⁸² These bulky cations replace methylammonium in the lattice and enhance stability by forming more robust capping layers at grain boundaries.⁸² With higher amounts of cation substitution, perovskite crystals can form Ruddlesden-Popper phases with better stability at the cost of some optoelectronic performance.^{83,84,85} Thus, these reports support the idea that molecular species with ammonium functionality can substitute into the crystal lattice to stabilize the overall structure while maintaining a single phase.

Polymers can be added to the MAPbI₃ active layer to increase their stability without substitution into the crystal lattice.^{79,80,81} Adding polymer to the spin-coating solution increases the viscosity of the solution, which affects the thickness, drying conditions, and crystallization kinetics of the perovskite active layer. This could be considered analogous to small molecule additives to organic photovoltaics, where additives such as 1,8-diiodooctane are added to the spin-coating solution to change the crystallization properties of the active layer.¹⁷ However, in contrast to organic photovoltaic additives, polymers remain in the active layer after annealing to form a two-phase hybrid film. When 3 – 6 wt% of polymer is added to the perovskite precursor solution, it can comprise up to around 25 vol% of the active layer when accounting for density differences between the perovskite (4.1 g/cm³)⁸⁶ and the polymer phases (~1.2 g/cm³). Because of the significant volume fraction of polymer present in these films, phase separation between the perovskite and polymer must occur, and examining the morphology of these perovskite-polymer hybrid films as two-phase systems is

critical to understanding their properties. Understanding how polymers interact with the perovskite will add to our understanding of the mechanism for improved stability, which has thus far not been fully understood. Previous studies^{79,80} have demonstrated the use of charge-neutral polymers such as polyethylene glycol (PEG) and polyvinylpyrrolidone (PVP) to improve the stability of PSCs.

Understanding how perovskite-polymer hybrid films form is critical to understanding how polymers improve the stability of PSCs while minimizing the negative impact on their optoelectronic properties. To that end, we report here on the microstructural changes induced by the introduction of four polymers, PAA, PEG, polyethyleneimine (PEI) and PVP in the active layer and the mechanism by which the stability is improved by these polymers. The choice of polymers reflects the currently tested polymers in the community and spans the different functional groups that can interact with perovskites. We then investigate the effect of polymer inclusion on the stability and performance of PSCs under humid air and ambient light.

3.3 RESULTS AND DISCUSSION

3.3.1 *Active layer morphology*

Similar to previous studies on incorporating polymers into PSC active layers,^{79,80,81} we observed that introduction of a polymer with an acidic functional group, PAA, changes the active layer morphology using AFM, XRD, and SEM (figure 3.1). Across all three characterization techniques, the mixing of PAA into the active layer decreases the domain size present in the thin films. The AFM data (figure 3.1a,b) indicate a reduction in grain size along with a reduced roughness in the films. Comparing the XRD patterns (figure 3.1c,d) reveals a broadening of the crystalline peaks, consistent with a smaller domain size. More importantly, the XRD data indicates that the crystal structure of the perovskite is preserved upon the addition of polymer. This result suggests that PAA phase separates from the perovskite because the crystal structure of the perovskite remains intact when

a significant volume fraction (~20%) of polymer is incorporated into the film. SEM images of the films (figure 3.1e,f) show a smaller domain size as well, consistent with our AFM data.

TEM can reveal nanoscale structural information about perovskite-polymer hybrid films. The MAPbI₃ crystals rapidly degrade to PbI₂ under electron beam illumination, but these PbI₂ domains still show dark regions of contrast in the TEM. Figure 3.2 shows the differences in morphology that different polymer additives cause in the perovskite grains. We observe a mostly faceted crystal structure in the MAPbI₃ crystals in the absence of polymer; however, when we add PAA to the precursor solution, the individual crystals have a more rounded morphology. We hypothesize that the degree of faceting on perovskite grains in perovskite-polymer hybrid films is a consequence of the polymer adhering to the perovskite grains as they grow. When we increase the concentration of polymer in these samples, the crystal size of the perovskites is decreased significantly for both MAPbI₃-PAA and MAPbI₃-polyethyleneimine (PEI). As an extreme example, at a 7:1 perovskite/polymer ratio by mass, PEI entirely prevents crystallization of perovskite in the film. When polyethylene glycol (PEG) is added, the faceted grain shape is mostly unaffected, however, as we have observed through XRD and AFM measurements, the domain size is smaller. This result with MAPbI₃-PEG suggests that the interaction between the PEG and the perovskite grains is different than what we observe in the PAA or PEI hybrid films. Our TEM characterization shows that differences in polymer composition can result in differences in perovskite grain faceting. These differences have the potential to affect the interconnectivity of perovskite grains within the active layer of PV devices. More rounded grains would tend to have less interfacial area to contact neighboring grains, and the grain size in these hybrid films is small enough that interconnectivity of the grains through the thickness of the film will affect device performance.

With respect to phase contrast, the polymer phase can be seen in some instances by TEM, but it is often hard to visualize compared to the higher-*z* MAPbI₃ phase. We have included micrographs showing polymer domains within very thin hybrid perovskite-polymer samples in the supplementary information (figure 3.3). These micrographs clearly show narrow polymer domains spanning

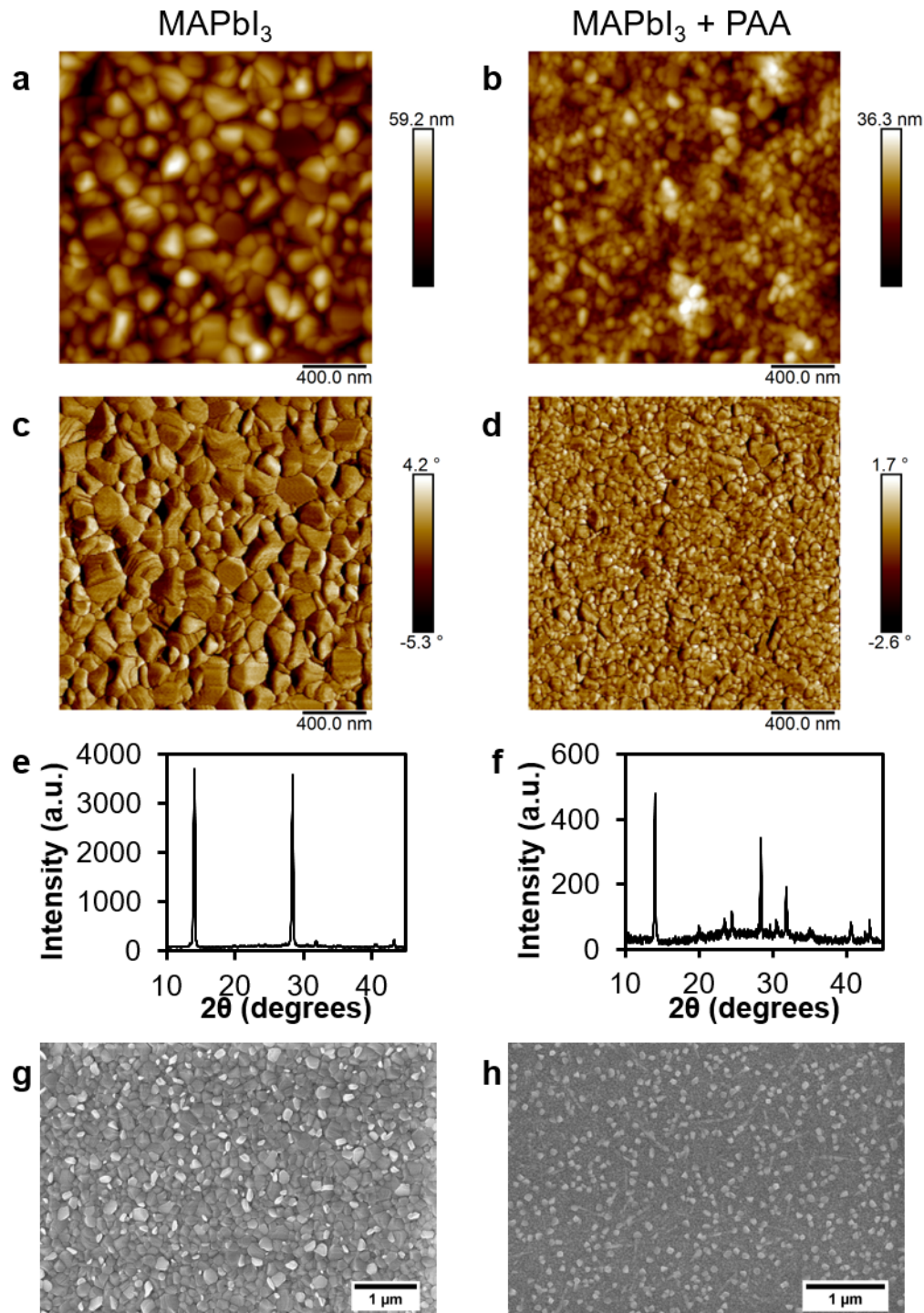


Figure 3.1: AFM height (a),(b), phase (c),(d), XRD (e), (f), and SEM (g), (h) of MAPbI₃ perovskite and MAPbI₃ perovskite mixed with 20mg/mL poly(acrylic acid). All 3 techniques show a reduction in grain size without showing contrast between polymer and perovskite domains.

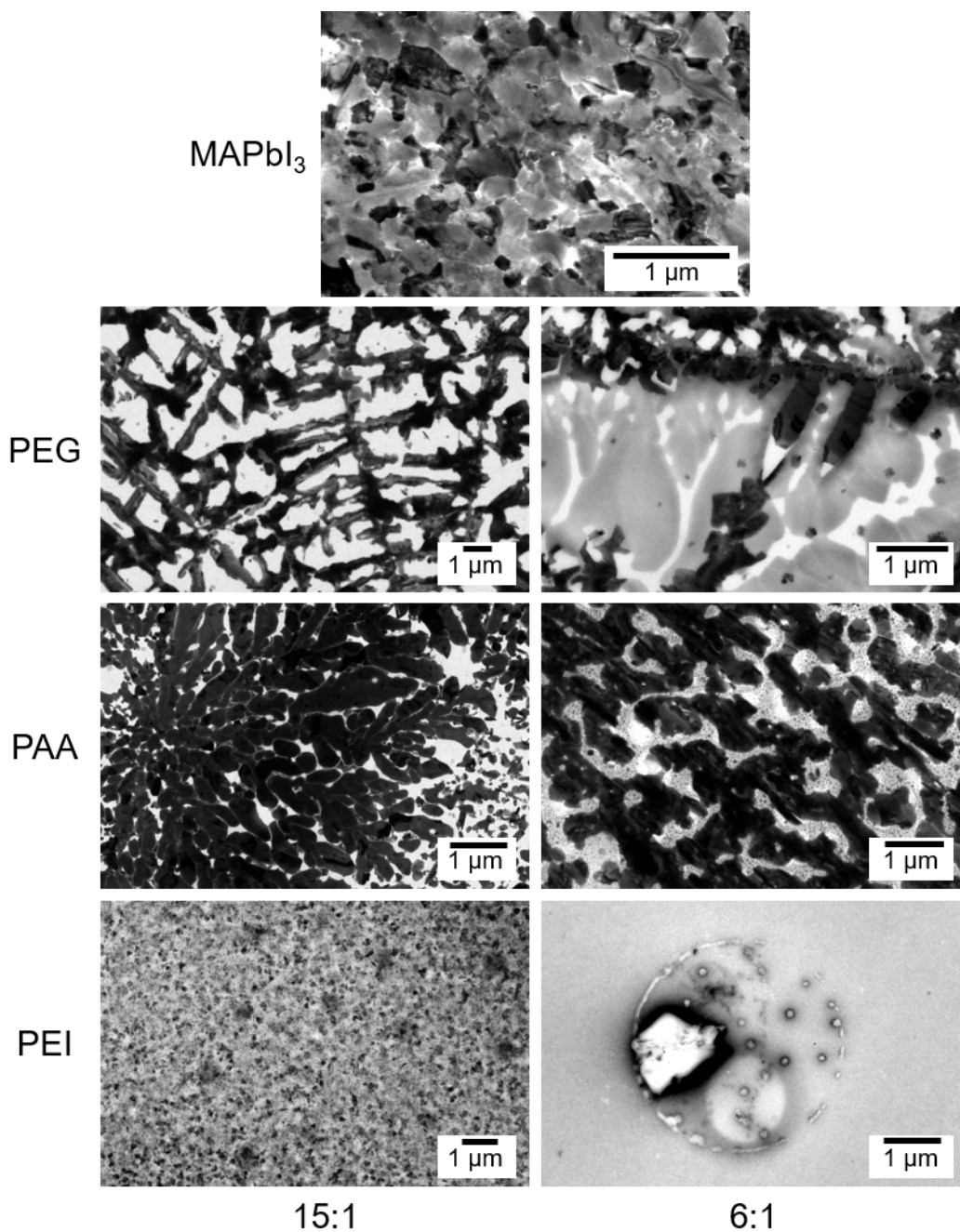


Figure 3.2: TEM images of drop-cast perovskite and perovskite/polymer hybrid films. Left column samples have mass ratios of perovskite to polymer of 15:1, while right column samples have 6:1. As we go down the columns, the crystal size gets smaller and the crystallization becomes more disrupted by the presence of polymer

the gap between much darker perovskite grains. However, TEM has not consistently or easily shown phase contrast in these materials because the preparation method for TEM samples (drop-casting) does not lead to samples with reproducible thickness.

Nanomechanical AFM can be used to map the local modulus and adhesion forces in perovskite-polymer hybrid films and thus show (figure 3.4) phase separation because the elastic modulus of perovskite (~ 14 GPa)⁸⁷ is significantly higher than that of the polymers that we studied. We see that MAPbI₃ perovskite films have a faceted grain structure, while the MAPbI₃-PAA hybrid films have smaller grains with softer structures present at the grain boundaries. The MAPbI₃ has a stepped structure on many of the grain surfaces, and the AFM tip adheres to some of these surfaces in an alternating fashion. This adhesion contrast is likely due to surface charges at the stepped surface of the crystal interacting with the silicon nitride AFM cantilever. To compare the mechanical properties at the grain boundaries, we have included line scans over these regions as a supplementary figure (figure 3.5). The grain boundaries in the MAPbI₃ control sample are softer than the crystal faces, but they do not show an increase in adhesion compared to the bulk of the crystal. In contrast, the micrographs of the MAPbI₃-PAA hybrid film indicate that the grain boundary regions appear softer and adhere to the tip significantly more than the surrounding grains (figure 3.4 d-f). This morphology indicates that perovskite grains nucleate and grow while the PAA polymer fills space in between the grains of the material. When we examine neat polymer films (no MAPbI₃ included) using this technique, they adhere to the AFM tip significantly more than the perovskite films (figure 3.6). Thus, a local increase in adhesion to the AFM tip combined with a local decrease in modulus relative to the surrounding area is an indication that polymer is at the grain boundary.

This result for MAPbI₃-PAA films can be compared with those for MAPbI₃-PEG and MAPbI₃-PVP films (figure 3.7). The MAPbI₃-PEG sample shows more faceted grains than the MAPbI₃-PAA sample, but the phase separation between the perovskite and polymer is similar to what we observe for the MAPbI₃-PAA sample. The grain boundary regions adhere to the AFM tip strongly which indicates that the perovskite and PEG are phase-separated. The MAPbI₃-PVP sample is interesting

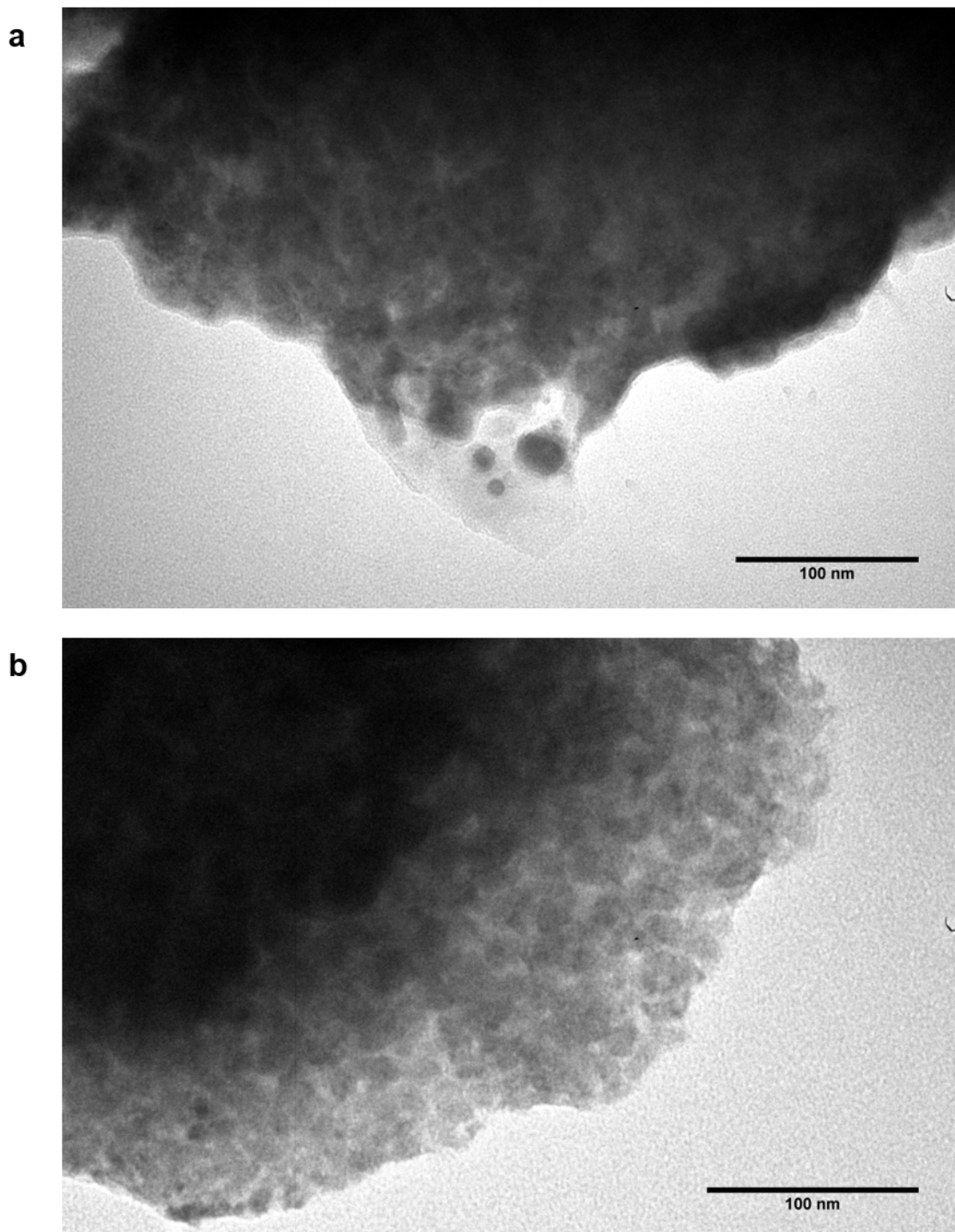


Figure 3.3: TEM micrographs of 15:1 MAPbI₃-PAA showing perovskite and polymer phase separation

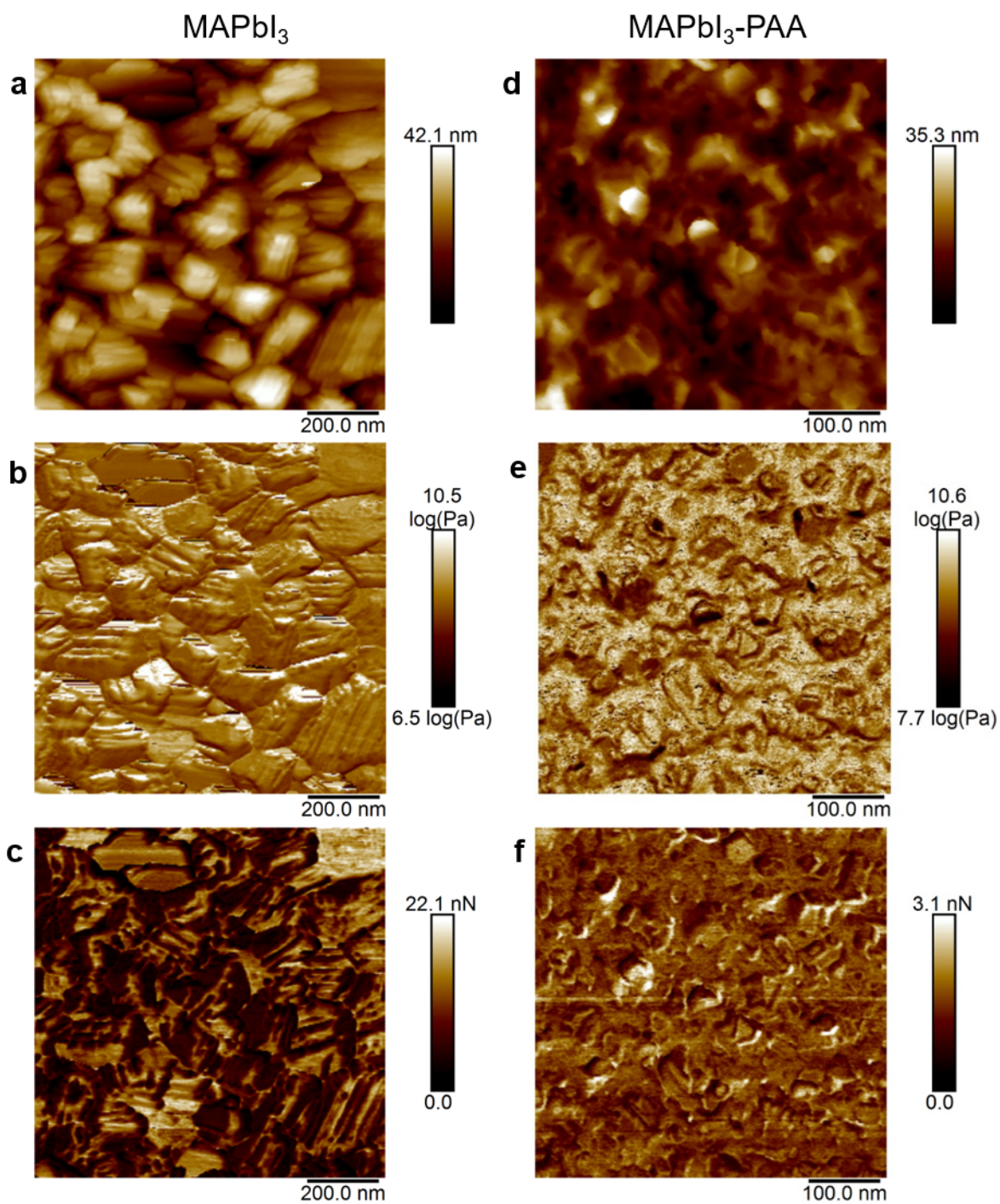


Figure 3.4: AFM height (a,d), log(DMT modulus) (b,e), and adhesion (c,f) micrographs of MAPbI₃ (a-c) and 15:1 MAPbI₃:PAA (d-f).

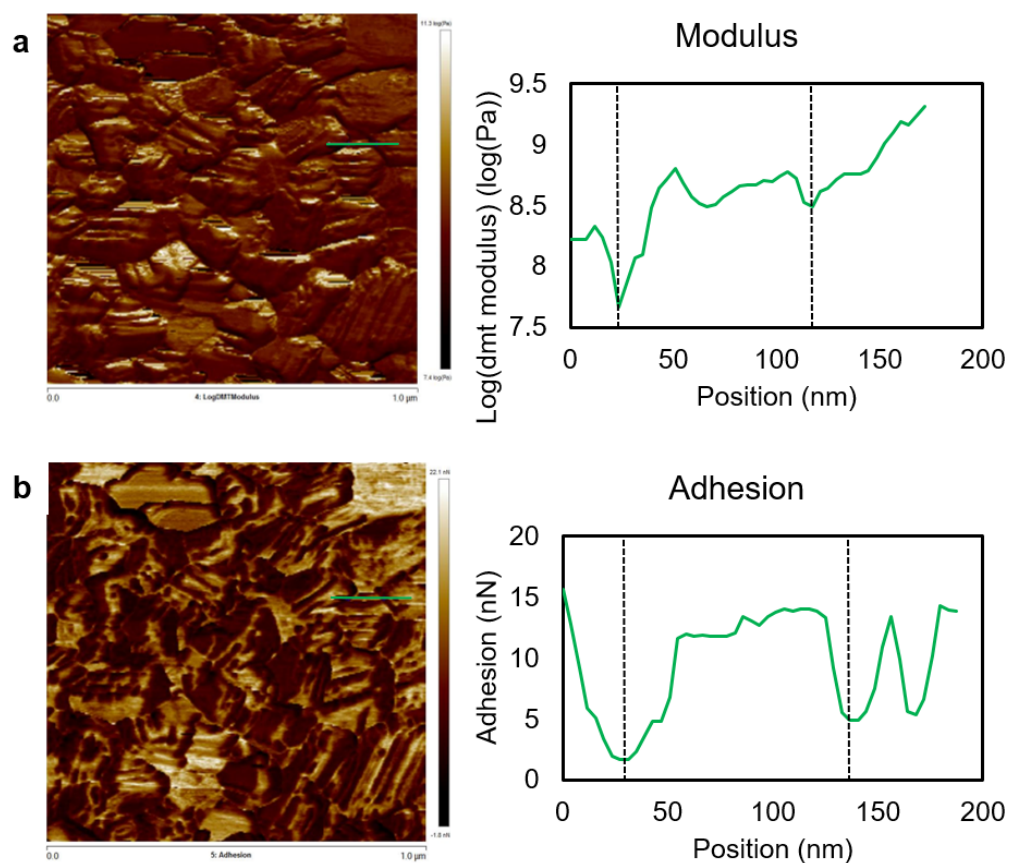


Figure 3.5: Log(modulus) (a) and adhesion (b) line cuts of nanomechanical AFM data MAPbI₃ film are shown. The green lines indicate where the line cuts were taken on the AFM data, and dashed lines on the graphs correspond to where the line cuts intersected with grain boundaries. This data indicates that for the control MAPbI₃ samples the modulus and adhesion tend to be at local minima at the grain boundaries.

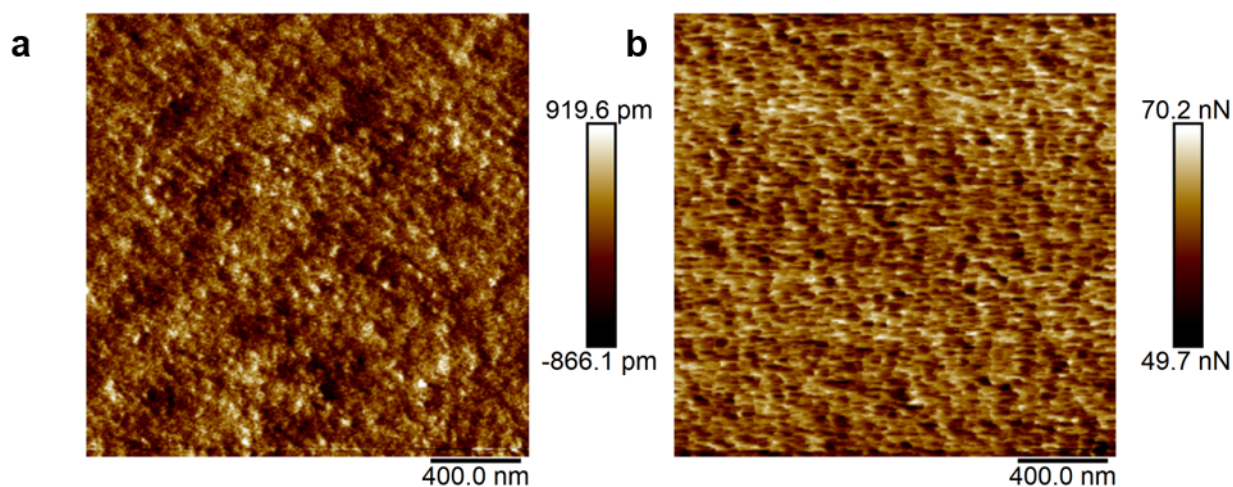


Figure 3.6: Nanomechanical AFM micrographs of poly(acrylic acid) showing local (a) height and (b) adhesion maps

in that we see what appears to be a three-phase mixture in the nanoscale morphology. We see larger, rectangular-shaped grains that have preferential faceting, and we see smaller rounded grains mixed intimately with the polymer phase. This morphology indicates that there is some miscibility limit to the PVP mixed with MAPbI₃ which can be observed on the nanoscale. These results show that the microstructure of the perovskite-polymer hybrid film depends on the polymer present.

3.3.2 *Film stability and intermolecular interactions*

In order to closely reflect the operating conditions of the device, we tested the stability of perovskite-polymer hybrid films in humid, illuminated conditions. At 100% relative humidity (RH) in air, both perovskite and perovskite-polymer hybrid films continuously absorb water from the atmosphere and degrade fully within 24 hours. However, at lower relative humidity levels, there are significant differences in the degradation rates of the pure perovskite and perovskite polymer hybrid films. We tested (figure 3.8 and figure 3.9) perovskite polymer hybrid film stability at 85% RH and 43% RH under ambient illumination. We examined MAPbI₃, MAPbI₃-PAA, MAPbI₃-PEG, and MAPbI₃-PVP at a 15:1 mass ratio of perovskite/polymer in the precursor solution and characterized their stability using XRD and XPS. At 43% relative humidity, the films

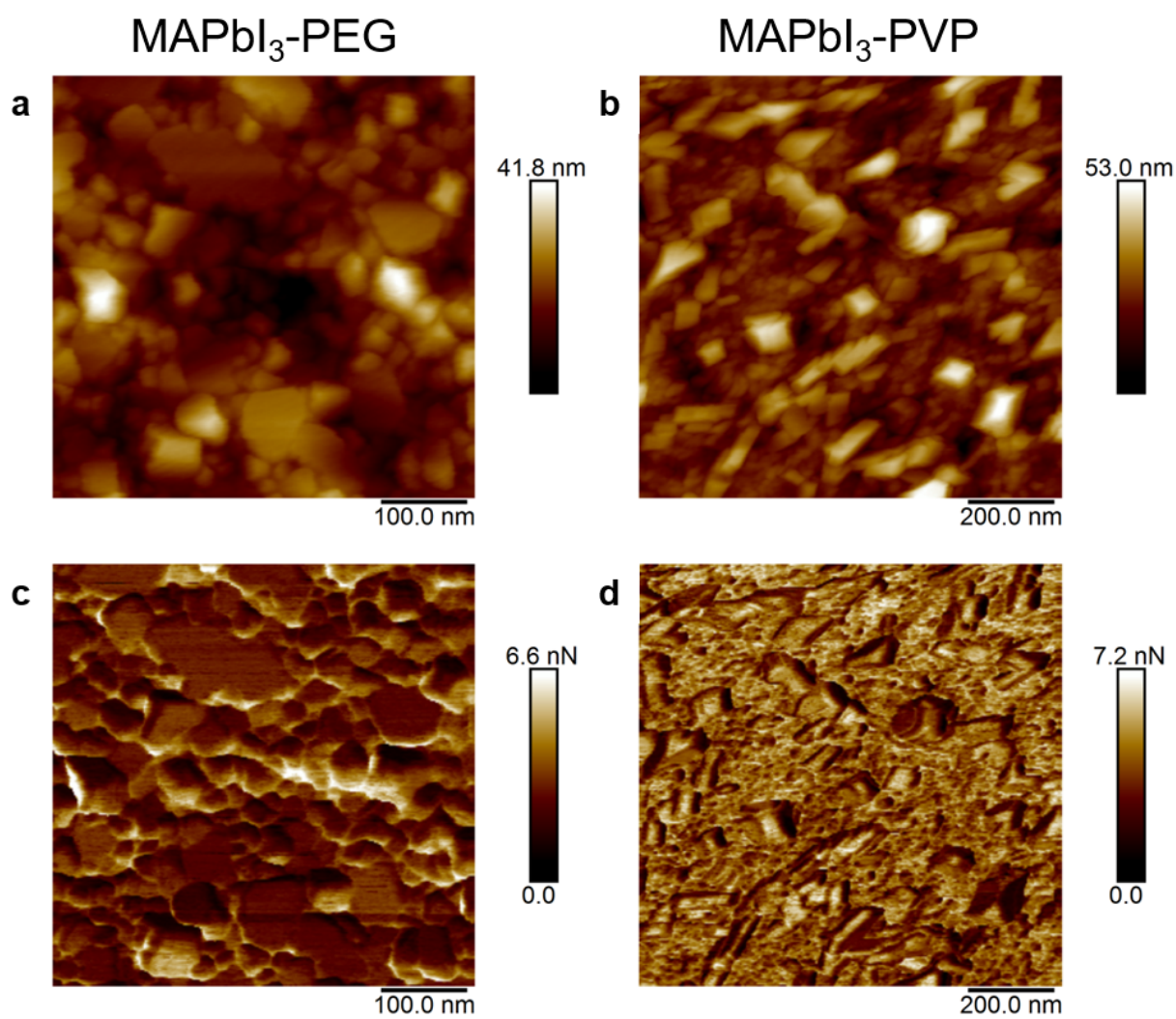


Figure 3.7: Nanomechanical AFM height (a), (b) and adhesion (c), (d) maps of MAPbI₃-PEG (a), (c) and MAPbI₃-PVP (b), (d).

degraded to PbI_2 slowly over the course of 3 weeks (figure 3.9). The control MAPbI_3 degraded within 10 days, while MAPbI_3 -PEG and MAPbI_3 -PVP degraded within 16 days, and finally the MAPbI_3 -PAA maintained some of its perovskite phase for 3 weeks. The accompanying XPS measurements showed no shift in the oxidation state of the Pb^{2+} over the course of the experiment, only a gradual reduction in the strength of the nitrogen signal as methylamine evaporated from the films. This contrasts with the results we found under 85% relative humidity (figure 3.8). The general trend in stability is the same between the two humidity conditions: MAPbI_3 -PAA is more stable than MAPbI_3 -PEG and MAPbI_3 -PVP which are both more stable than control MAPbI_3 . However, the XRD for the 85% RH case shows that the control MAPbI_3 film undergoes a phase transformation to a hydrate phase, and the presence of polymers appears to suppress this hydrate phase formation. This hydrate phase shows peaks in the XRD data at $2\theta = 8.5$ and 10.5 degrees which match those recently reported for the hydrate phase $(\text{MA}^+)_2(\text{PbI}_3)\cdot(\text{H}_2\text{O})_2$.⁷⁶ Their study⁷⁶ explains that the hydrogen-bonding ability of the solvent species, in this case water, affects the speed at which the hydrate phase is formed. Here, we observe that when polymer is present on the surface of the grains, the water-based hydrate phase $(\text{MA}^+)_2(\text{PbI}_3)\cdot(\text{H}_2\text{O})_2$ is not formed. The evidence of degradation to a different phase implies that the degradation proceeds through a different mechanism when polymer is present at the crystal surface. The XPS spectra show that the Pb^{2+} is reduced to Pb^0 at the 85% RH condition in the MAPbI_3 -PVP sample, which is a phase transition that is not observed for the other samples. The reduction of Pb^{2+} to Pb^0 also implies that the MAPbI_3 -PVP system follows a different degradation pathway than the other MAPbI_3 -polymer systems.

To explain the observed differences in stability between the perovskite control and the various perovskite-polymer hybrid thin films, we focused on the differences between these systems. Following from the hypothesis proposed in the previously-reported MAPbI_3 -PEG hybrid,⁷⁹ water absorption experiments on the polymers were performed to see if there was any correlation between absorption and stability. We found (figure 3.10) that while different polymers absorbed significantly

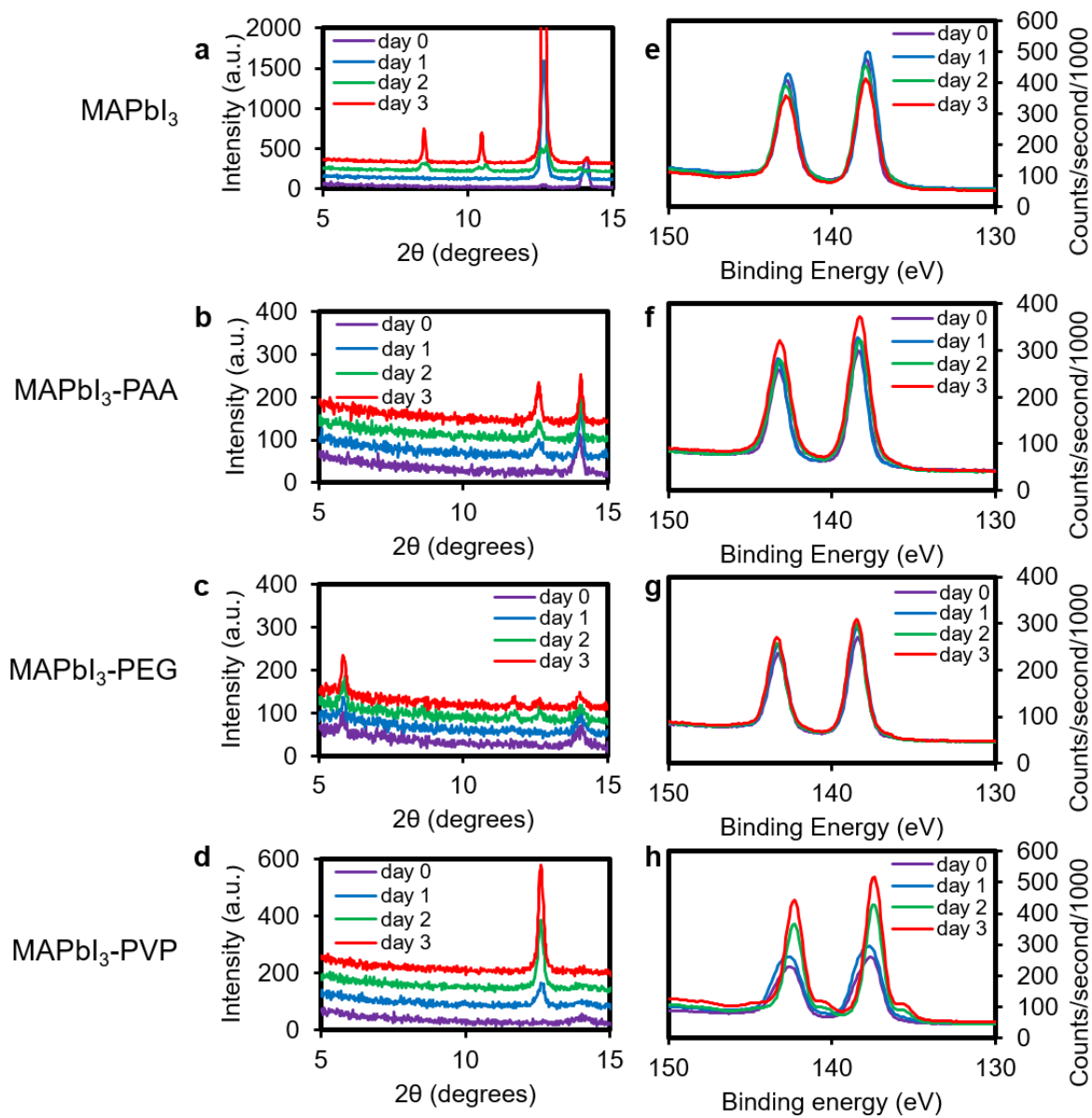


Figure 3.8: XRD (a-d) and XPS (e-h) of MAPbI₃ and MAPbI₃-polymer hybrid films aged at 85%RH under illumination. The new peaks appearing in the XPS data for the MAPbI₃-PVP sample correspond to Pb⁰.

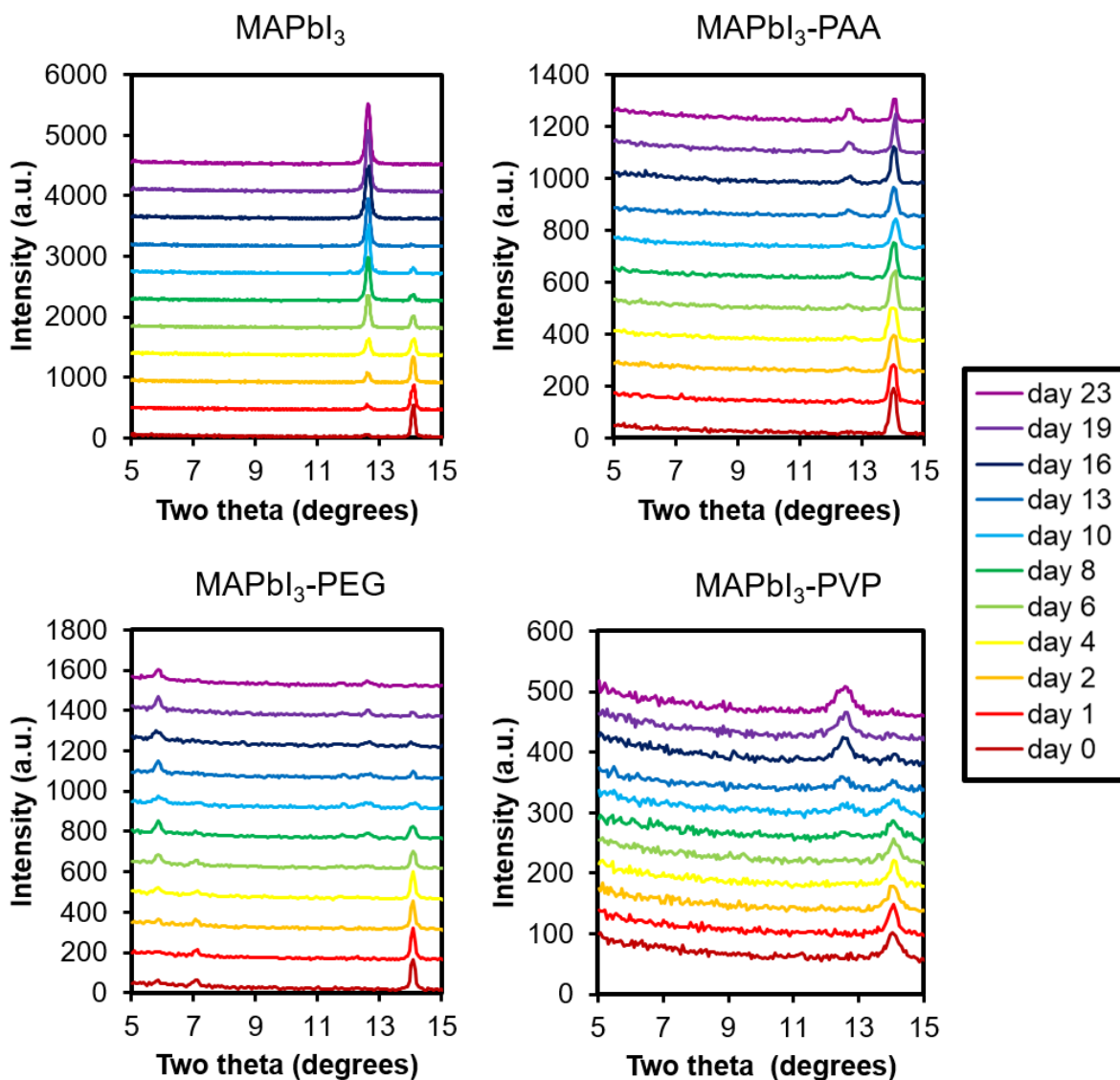


Figure 3.9: XRD of MAPbI_3 and MAPbI_3 -polymer hybrid films aged at 43%RH under illumination. MAPbI_3 degraded to PbI_2 (12°) entirely within the first 10 days. MAPbI_3 -PAA degraded much more slowly and retained some perovskite signal (14°) throughout the duration of the experiment. MAPbI_3 -PEG degraded about as quickly as MAPbI_3 , but it did not form strongly crystalline PbI_2 . Finally, MAPbI_3 degraded a bit more slowly than the control to form PbI_2 , but overall, the crystallinity of the PVP sample was lower.

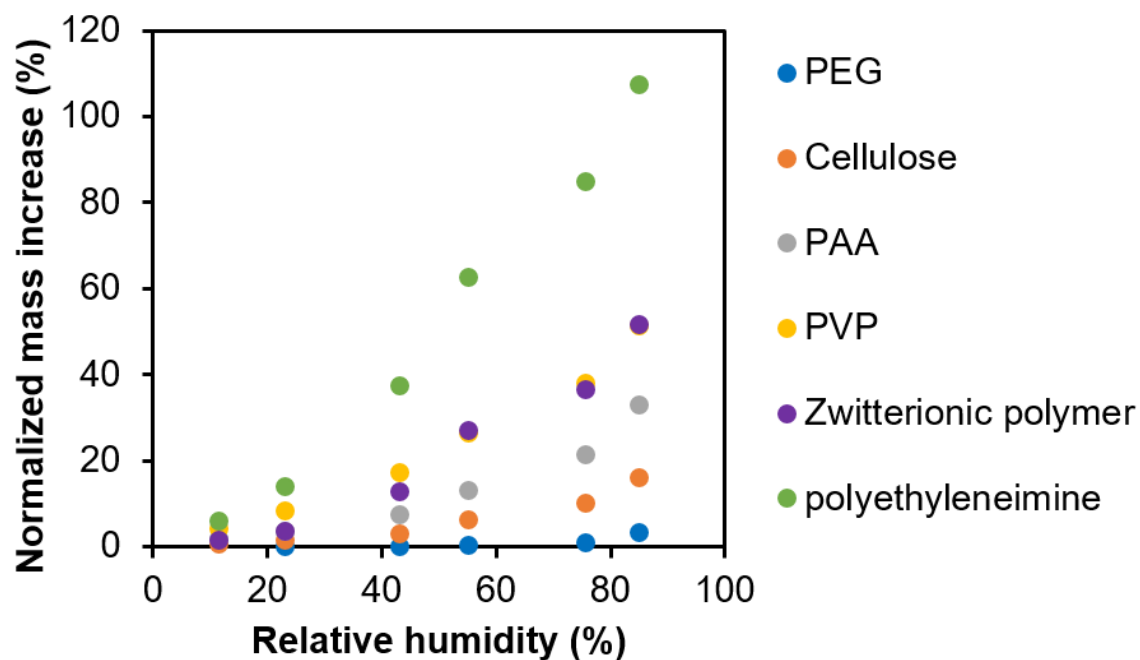


Figure 3.10: Normalized mass increase of various polymers with respect to dried mass at different relative humidity conditions.

different amounts of water in humid conditions, these differences did not correlate to our film stability observations. Next, we performed FT-IR experiments to characterize chemical interactions at the surface of MAPbI_3 -polymer powders (figure 3.11). Although our FT-IR data for MAPbI_3 -PVP matched a previous observation of the polar interaction between the amide $\text{C}=\text{O}$ and methylammonium,⁸⁰ the signal for this peak overlapped strongly with an MAPbI_3 peak. The FT-IR data we found for the MAPbI_3 -PEG and MAPbI_3 -PAA was similarly inconclusive. Thus, to explain the differences in stability between the various MAPbI_3 -polymer systems, we conducted a more thorough investigation of chemical stability using NMR spectroscopy, single crystal growth, and iodine-based film degradation experiments to better understand the mechanism for increased film stability.

To probe the interaction between the polymers and the perovskite precursors in solution, we performed NMR spectroscopy in an environment simulating that of the casting solution. figure 3.12 shows a series of NMR spectra of the MAPbI_3 precursor solution and MAPbI_3 -polymer precursor

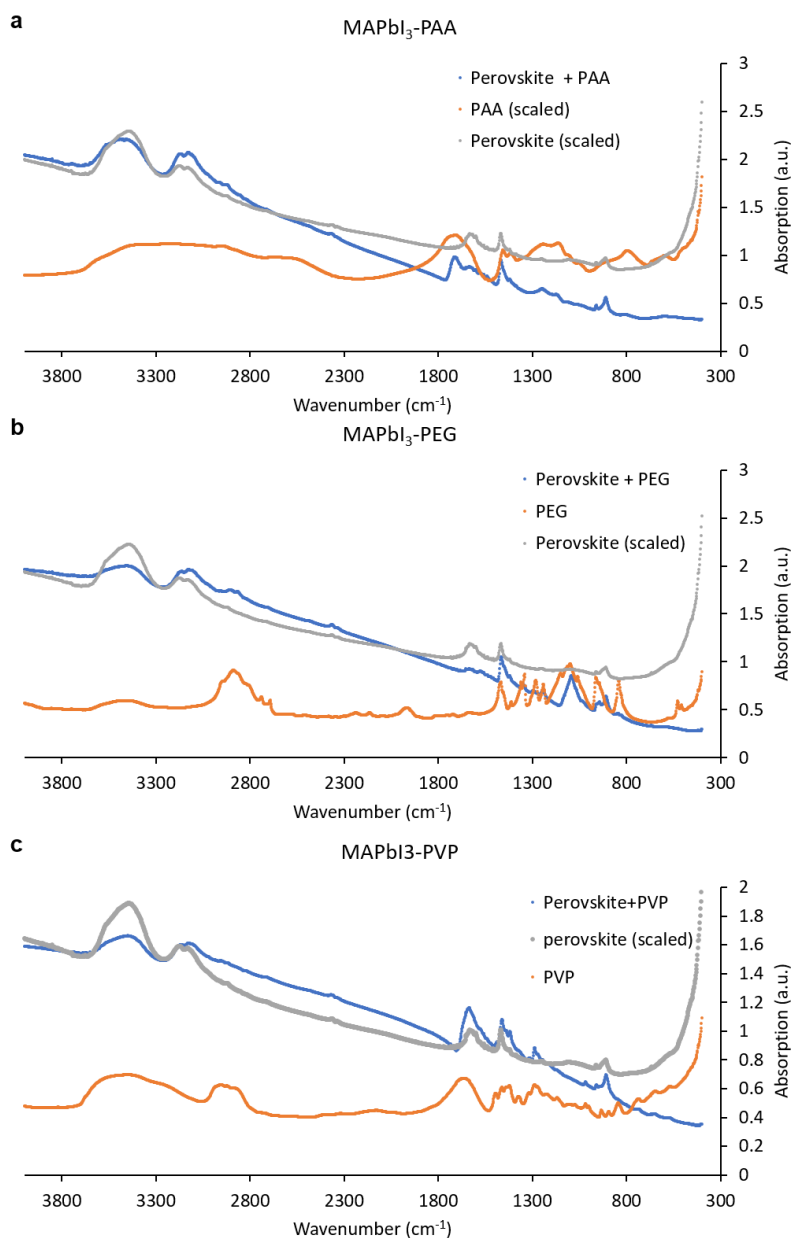


Figure 3.11: Fourier-transform Infrared spectroscopy (FT-IR) was performed on powders of perovskite-polymer hybrids to compare to perovskite and polymers separately. While there were some shifts present in the data, many of the differences in the combined samples could be attributed either to convolution of perovskite and polymer peaks, or to dilution effects. We do observe the shift noted in Guo et al⁸⁰ at 1660 cm⁻¹ corresponding to the amide C=O bond loosening, however in our case that peak overlaps strongly with the perovskite signal. Thus, we may have at least some evidence that there is an h-bonding interaction between the PVP and the ammonium proton on the methylammonium.

solutions in DMSO- d_6 . The peak at 7.23 ppm, corresponding to the ammonium protons, shifts downfield and sharpens upon addition of acidic polymers such as polyglutamic acid (PGA) or PAA, remains at the same position upon addition of neutral polymers such as PEG or PVP, and shifts upfield upon addition of basic polymers such as polyethyleneimine. Additionally, figure 3.13 shows a corresponding broadening and upfield shift of the carboxylic acid protons on PAA when mixed with MAPbI₃ precursor solution. This trend points to acid-base type interaction between MAI and the ionizable group of each polymer. Interestingly, we did not observe a strong interaction between methylammonium iodide and PEG, as claimed in a previous study.⁷⁹ We attribute this difference to the varying water content in the NMR samples, which may change the degree of hydrogen bonding.

Acid-base interactions have previously been shown to have a significant impact on the crystallization and stability of perovskite thin films. It has been shown that the formation of perovskite hydrate phases is dependent on the hydrogen-bond acceptor strength of the solvent,⁷⁶ which in the case of atmospheric degradation is water. Our NMR data suggest that the hydrogen-bonding ability of the methylammonium cations in solution are affected by the presence of polymers, and therefore we propose that these surface-based chemical interactions are important to the stability of the perovskite phase. As an analogous example, MAPbI₃ films are particularly unstable on ZnO surfaces because the basic ZnO surface deprotonates the methylammonium leading to rapid degradation.⁸⁸ Acidic oxides such as TiO₂ are more compatible with the crystallization of MAPbI₃, and so the increased stability we observe with acid-functionalized polymers is consistent with these previous studies. Therefore, based on our film stability experiments and NMR observations, we propose that the hydrogen-bonding ability of the polymer to the MAI affects the ability of atmospheric water vapor to bond to the MAI and form the perovskite hydrate phase (MA⁺)₂(PbI₃-)·(H₂O)₂, which ultimately influences the perovskite degradation pathway and film stability.

While NMR captures some of the interactions between these species in solution, there are also chemical interactions between the surface of the crystal and the polymer species that affect crystal formation and thin film morphology. To characterize these differences, we grew crystals via solvent

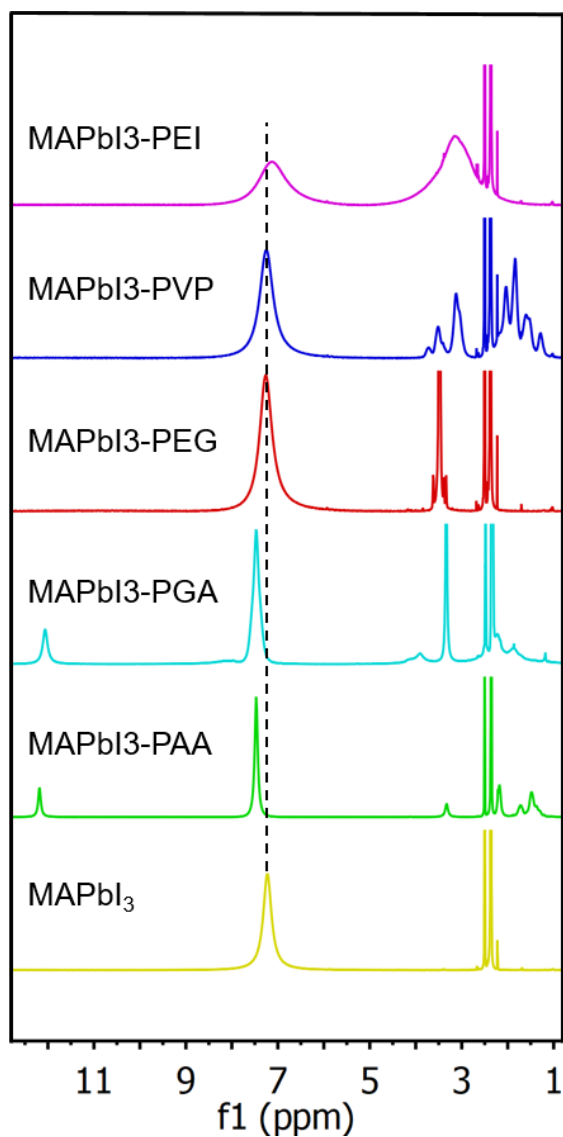


Figure 3.12: NMR spectra of the perovskite precursor solution and perovskite/polymer precursor solutions in DMSO-*d*₆. The peak at 7.23 ppm, corresponding to the ammonium protons, shifts downfield and sharpens upon addition of acidic polymers such as poly(glutamic acid) or polyacrylic acid, remains at the same position upon addition of neutral polymers such as poly(ethylene oxide) or polyvinylpyrrolidone, and shifts upfield upon addition of basic polymers such as polyethyleneimine.

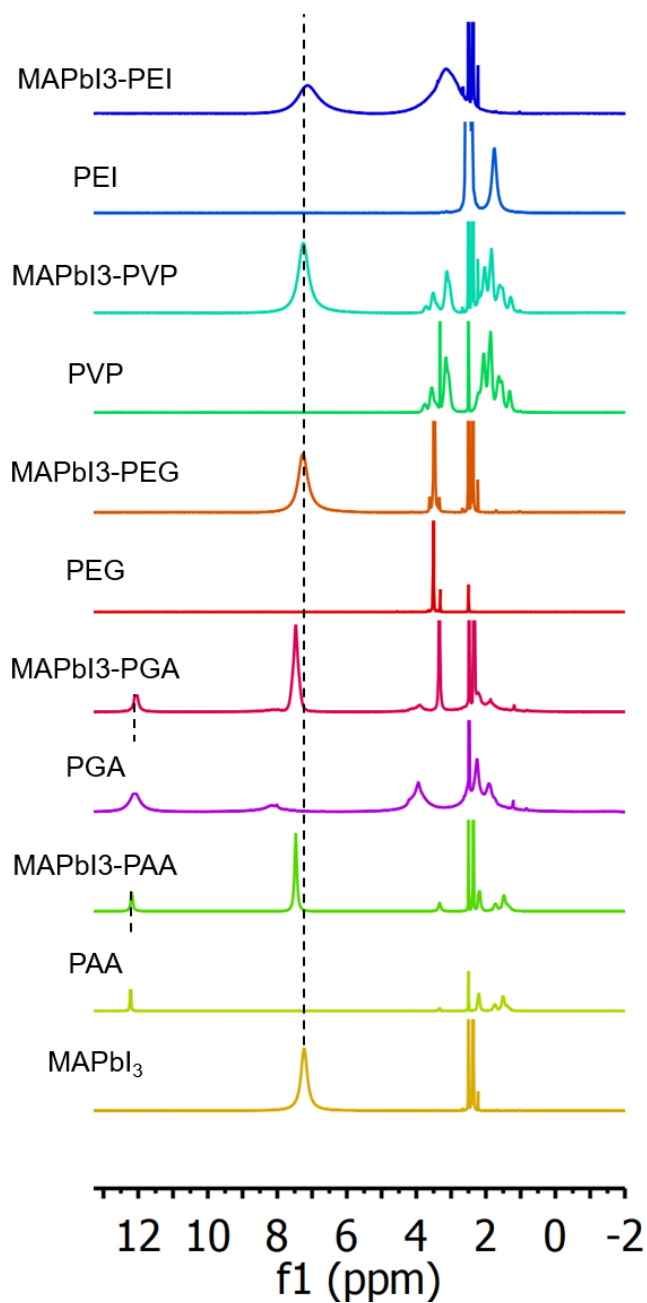


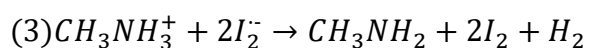
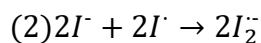
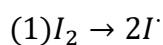
Figure 3.13: NMR spectra of the perovskite precursor solution and perovskite-polymer precursor solutions compared to polymers alone in $\text{DMSO-}d_6$. The dashed lines at 7.2 ppm and 12.1 ppm are included to show the relative shifts in the ammonium protons and carboxylic acid protons, respectively. It is clear that the carboxylic acid peaks on the polymers shift upfield when mixed with the perovskite precursors and the ammonium proton peaks shift downfield, indicating h-bonding between the two functional groups.

vapor diffusion of MAPbI₃ with PAA, PEG, and PVP dissolved in the crystallization solution (figure 3.14). When the crystals are grown with polymer present, the crystal growth rate was slowed compared to the MAPbI₃ control leading to smaller crystal sizes. MAPbI₃ alone exhibits a mixture of (100)-type and (110)-type faceting. MAPbI₃-PEG shows preference for (110)-type faceting leading to an elongated dodecahedron morphology. MAPbI₃-PAA and MAPbI₃-PVP grow with mainly (100)-type faceting and appear cuboid-shaped, although the MAPbI₃-PVP crystals are less faceted overall. The differences in faceting between the various polymers are likely due to differences in polymer adhesion to and interaction with the growing crystal faces. We hypothesize that neutral polymers such as PEG would tend to adhere to more neutral crystal faces, while polymers with polar interactions with the MAPbI₃ such as PAA and PVP would tend to adhere to more charged crystal faces. We have included atomic models of the MAPbI₃ cut along the (100) and (110) planes as figure 3.15. When the crystal is truncated along (110)-type planes, the resulting crystal face is either entirely positively charged (Pb²⁺ mixed with MA⁺) or entirely negatively charged (I⁻). When the crystal is truncated along (100)-type planes, however, the growth is significantly closer to charge-neutral. (100)-type crystal truncations have a mixture of positively and negatively charged species. Thus, as the crystals grow, polymers with polar interactions to the perovskite, PAA and PVP, would tend to adhere to charged crystal faces such as (110)-type planes and slow those growth directions. Similarly, polymers lacking polar interactions with the perovskite such as PEG would tend to adhere to more neutral crystal faces such as (100)-type planes while allowing the (110)-type planes to grow. If we re-examine the morphology of our perovskite-polymer thin films considering our observations on the single crystal growth we can explain more of the structural features present. First, we see that in the MAPbI₃-PVP sample, one of the phases present in that film is cuboid-like structures. Second, we observed a higher amount of faceting on the MAPbI₃-PEG samples in TEM which is consistent with what we observe in the single crystal growth. These two observations indicate that at least some of the chemical interactions we have observed in the single crystal growth and NMR studies translate to the thin film morphology. The kinetic processes associated with sol-

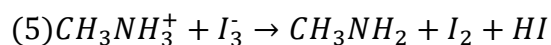
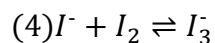
vent evaporation, perovskite crystallization, and phase separation are perhaps more important to the morphology of the thin film active layer than the thermodynamic processes of single crystal growth. Nevertheless, we have shown that chemical interactions between the perovskite precursors and polymers do have some effect on hybrid film morphology.

Iodine-based degradation mechanisms have recently been explored as an intrinsic source of MAPbI₃ perovskite instability.⁸⁹ Iodine has been shown to be a degradation product from moisture, light, and oxygen in MAPbI₃ perovskites.⁷⁵ To test perovskite stability to iodine-based degradation, we placed films of MAPbI₃, MAPbI₃-PAA, MAPbI₃-PEG, and MAPbI₃-PVP in contact with I₂-saturated silica gel to study their accelerated degradation (figure 3.16). Using the color of the thin films in UV-Vis spectroscopy as a metric for film degradation, we found that the control MAPbI₃ film fully degraded to PbI₂ within 4 minutes of exposure to iodine vapor, whereas the MAPbI₃-polymer films degraded in 6 minutes. The absorption onset of our MAPbI₃ is near 780 nm, and as the MAPbI₃ degrades to PbI₂, this absorption onset disappears. Iodine within the lattice contributes to MAPbI₃ degradation under light and dark conditions per the following equations:⁸⁹

Under light:



And under dark



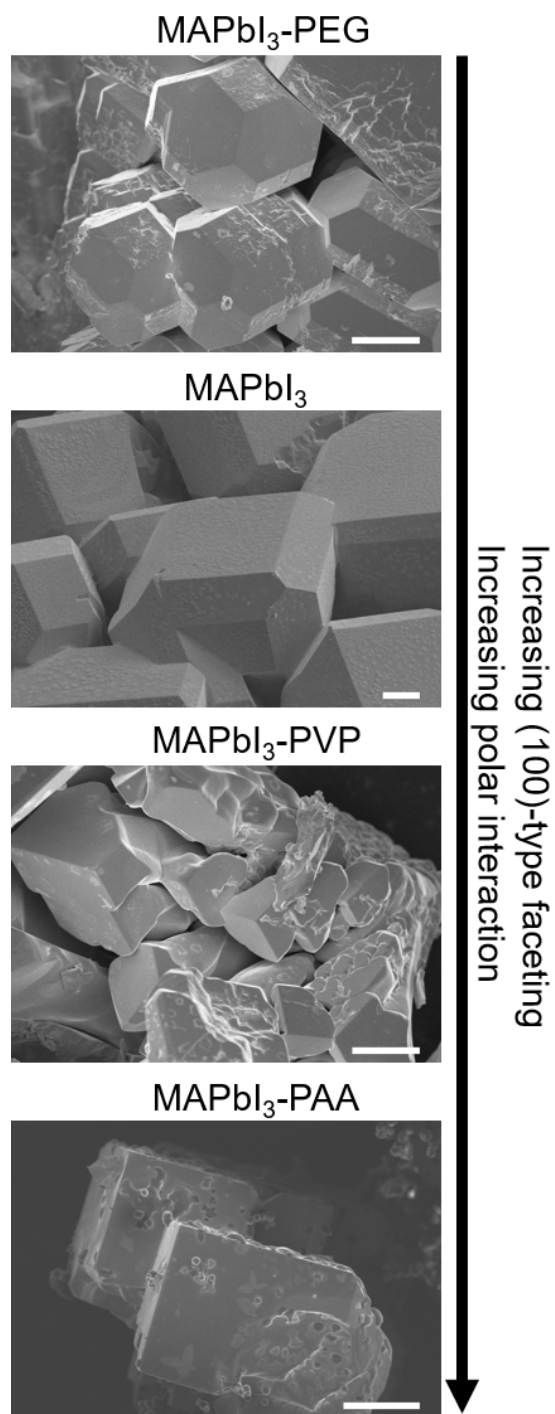


Figure 3.14: Single crystal growth of MAPbI₃ with various polymers added to the crystallization solution. MAPbI₃-PEG shows preference for (110)-type faceting leading to an elongated dodecahedron morphology. MAPbI₃ alone exhibits a mixture of (100)-type and (110)-type faceting. MAPbI₃-PVP and MAPbI₃-PAA grow mainly (100)-type faceting, although the MAPbI₃-PVP crystals are less faceted overall. (Scale bar: 50 μ m)

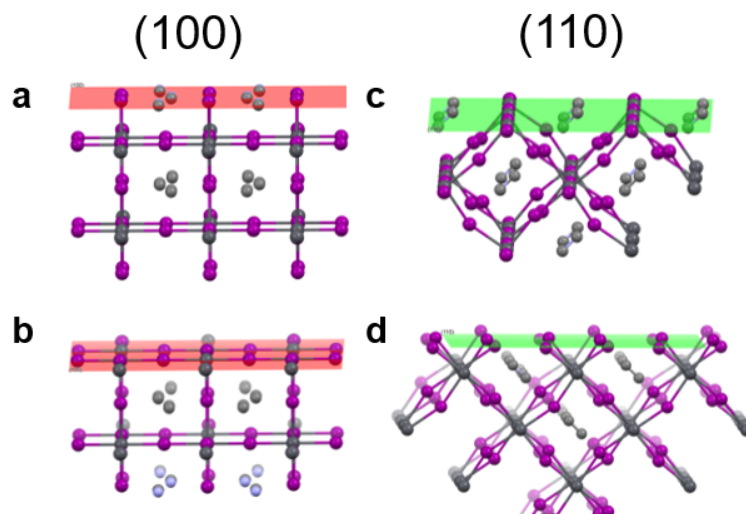


Figure 3.15: Cuts of the MAPbI₃ crystal along the (a,b) (100) and (c,d) (110) planes showing the surface termination atoms along those planes at different depths in the unit cell.

Since our goal is to slow or prevent these reactions from happening, we must first consider ways to prevent methylammonium from reacting with radical iodide species. Our NMR study suggests that acid-base type interactions between the methylammonium and the acidic polymers may play a role in stabilizing the methylammonium ion. Second, we must consider ways to prevent the I₂ degradation product from being released back into the crystal lattice. We tested (figure 3.17) the ability of PAA, PEG, and PVP to absorb iodine by mixing solid iodine with these polymers in a sealed vessel. Within minutes, PVP and PEG absorb significant amounts of iodine, indicated by color change. PAA, however, does not appear to absorb any iodine over the course of days. This difference in iodine absorption would be very significant in an unencapsulated PSC as it degrades. If I₂ is trapped in the grain boundaries by polymers like PEG and PVP, the polymer-bound iodine can participate in reaction (1) when irradiated and degrade the perovskite further. If, instead, the polymer does not absorb iodine, as in the case of PAA, then any I₂ that is released as a degradation product should evaporate from the thin film as it is formed.

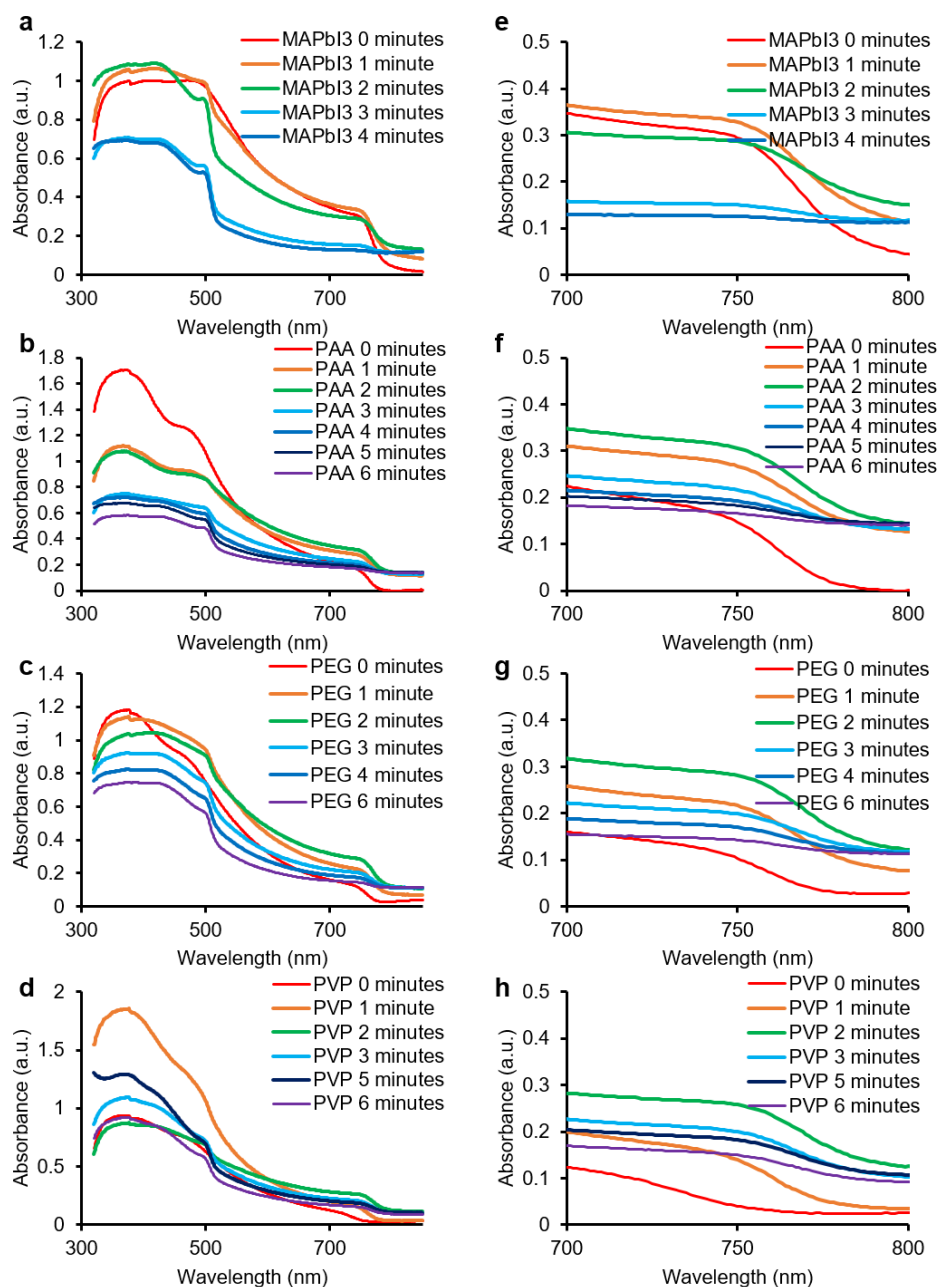


Figure 3.16: UV-Vis of MAPbI_3 and MAPbI_3 -polymer hybrid films degraded under saturated iodine atmosphere. (a)-(d) show the full spectrum, and (e)-(h) show a zoom in on the perovskite absorption onset near 780 nm. The perovskite control sample degrades entirely over 4 minutes, and the perovskite-polymer samples degrade over the course of 6 minutes. All perovskite-polymer hybrid samples in this experiment exhibited enhanced stability, but the differences between the different polymers is undetectable under such rapid degradation conditions.

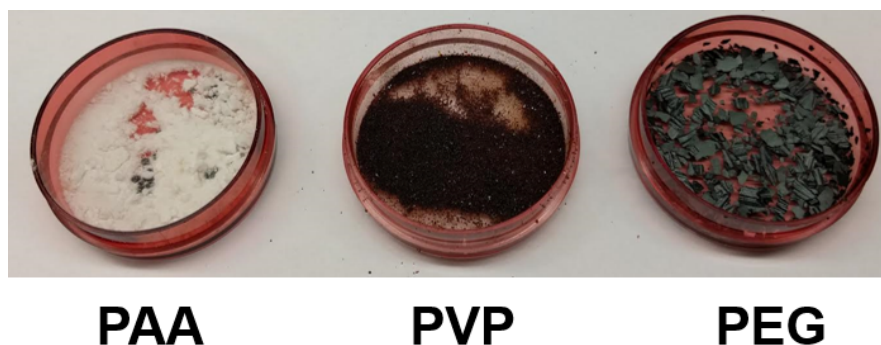


Figure 3.17: Solid iodine was added to sealed petri dishes filled with PAA, PVP, and PEG. PVP and PEG absorbed iodine vapor readily while over the course of days PAA did not appear to absorb any iodine.

3.3.3 Photovoltaic performance and stability

The goal of adding polymers to the active layer of the perovskite solar cell is to increase the longevity of devices. We carefully designed these devices so that the interlayers and contacts last longer than the active layer under degradative conditions. Typical hole transport materials (HTMs), such as Spiro-OMeTAD and polytriarylamine, are not compatible with long-term device stability, since the additives used on these HTMs to increase hole mobility and improve wetting properties (4-tert-butyl pyridine and lithium bis(trifluoromethane)sulfonamide) tend to dissolve and oxidize the perovskite active layer.⁹⁰ Additionally, the iodine released from the perovskite active layer can react with any non-noble metal counter electrode materials. Therefore, we designed (figure 3.18) our devices with an ITO transparent contact, PEDOT:PSS hole transport layer, perovskite active layer, [6,6]-phenyl-C61-butyric acid methyl ester (PC61BM) electron transport layer, bathocuproine (BCP) exciton blocking layer, and gold counter electrode. We chose gold as the counter electrode material because as the active layer decomposes, the released iodine can react with a silver or aluminum counter electrode in the presence of humidity, corroding the device contact. We then proceeded to optimize device performance for the control devices and for the perovskite polymer hybrid devices.

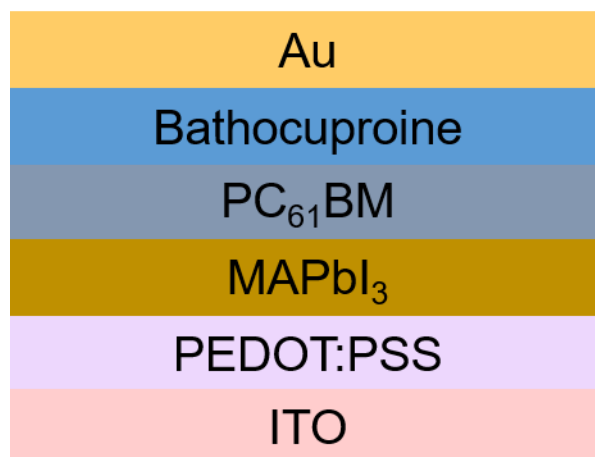


Figure 3.18: A schematic cross-section of our devices used for stability testing

To mitigate the negative effects of reduced grain size on device performance in experimental devices, we took steps to increase the domain size of our perovskite grains. We have increased domain size in these films by increasing annealing temperature to 120°C as well as changing the spin-coating solvent mixture to a DMF/DMSO mixture for our experimental devices (figure 3.19). One of the challenges associated with creating hybrid perovskite-polymer devices is the reduction in short circuit current density (J_{sc}) and fill factor (FF) for these devices. Whereas the control MAPbI₃ devices had J_{sc} 18 mA/cm₂ and FF = 0.75, even under our best-optimized conditions, devices with PAA had J_{sc} 15 mA/cm₂ and FF = 0.65. To investigate the effect of a polymer phase in the active layer on carrier lifetime we performed steady-state and time-resolved photoluminescence (TR-PL) experiments on our perovskite-polymer hybrid films (figure 3.20 and 3.21). In this experiment, we observed that PEG and PAA tend to increase the PL lifetime of the perovskite film, while PVP decreases the lifetime compared to the control MAPbI₃. This result suggests that while polymers in general do not necessarily decrease carrier lifetime in hybrid thin films, certain functional groups can be detrimental to carrier lifetime. With respect to MAPbI₃-PVP, there is a fast decay process (<1 ns) and a slow decay process (7 ns) that can be observed. The two distinct PL lifetimes in this sample may be a result of the two distinct phases we found in the morphological study leading to

different carrier decay processes. Carrier lifetime in these films can be affected by crystallinity of the perovskite phase, and we observe that the MAPbI₃-PVP film has both the lowest crystallinity and lowest PL lifetime of the films we tested.

From our TR-PL result, we attribute the lower fill-factor in hybrid perovskite-polymer devices to increased series resistance in the device rather than reduced carrier lifetime in the cases where PL lifetime is not decreased (MAPbI₃-PEG and MAPbI₃-PAA). The added series resistance can be attributed to smaller grain sizes necessitating charge transport across many more grain boundaries through the thickness of the device. This effect can be somewhat mitigated by making a thinner active layer. Adding less polymer to the system can also improve the initial electronic performance, but less polymer reduces the longevity added to the device. This trade-off between performance and stability needs to be considered in the design of any future perovskite-polymer hybrid solar cell.

Optimized PSC and polymer hybrid PSC device performance and stability over time are plotted in figure 3.22. We expose the cells to a controlled air environment with 43% relative humidity under ambient indoor illumination. The inclusion of PAA into the active layer reduces the peak power conversion efficiency (PCE) of the solar cells from 13% in pure PSCs to 9% in PAA hybrid PSCs, but increases their longevity significantly. The pure PSCs lose 50% of their original PCE within 24 hours, and they degrade to significantly less than 1% efficiency within 2 days. The PAA hybrid PSCs, however, retain their initial PCE for 3 days and slowly degrade to 50% of their original efficiency over 8 days. The device stability results under illumination are consistent with the film stability results that we obtained, showing that devices incorporating PAA into the active layer increase their long-term stability under humidity and illumination. We then compare MAPbI₃ devices to 20:1 MAPbI₃-PAA devices aged in the dark at 43% relative humidity figure 3.23. We find that the MAPbI₃ devices have an initial 6-day period of stable PCE followed by a moderate decline in efficiency over the next 8 days. The 20:1 MAPbI₃-PAA devices degrade at a slower but steady rate starting from day 1, and so they degrade in about the same amount of time as the MAPbI₃ devices.

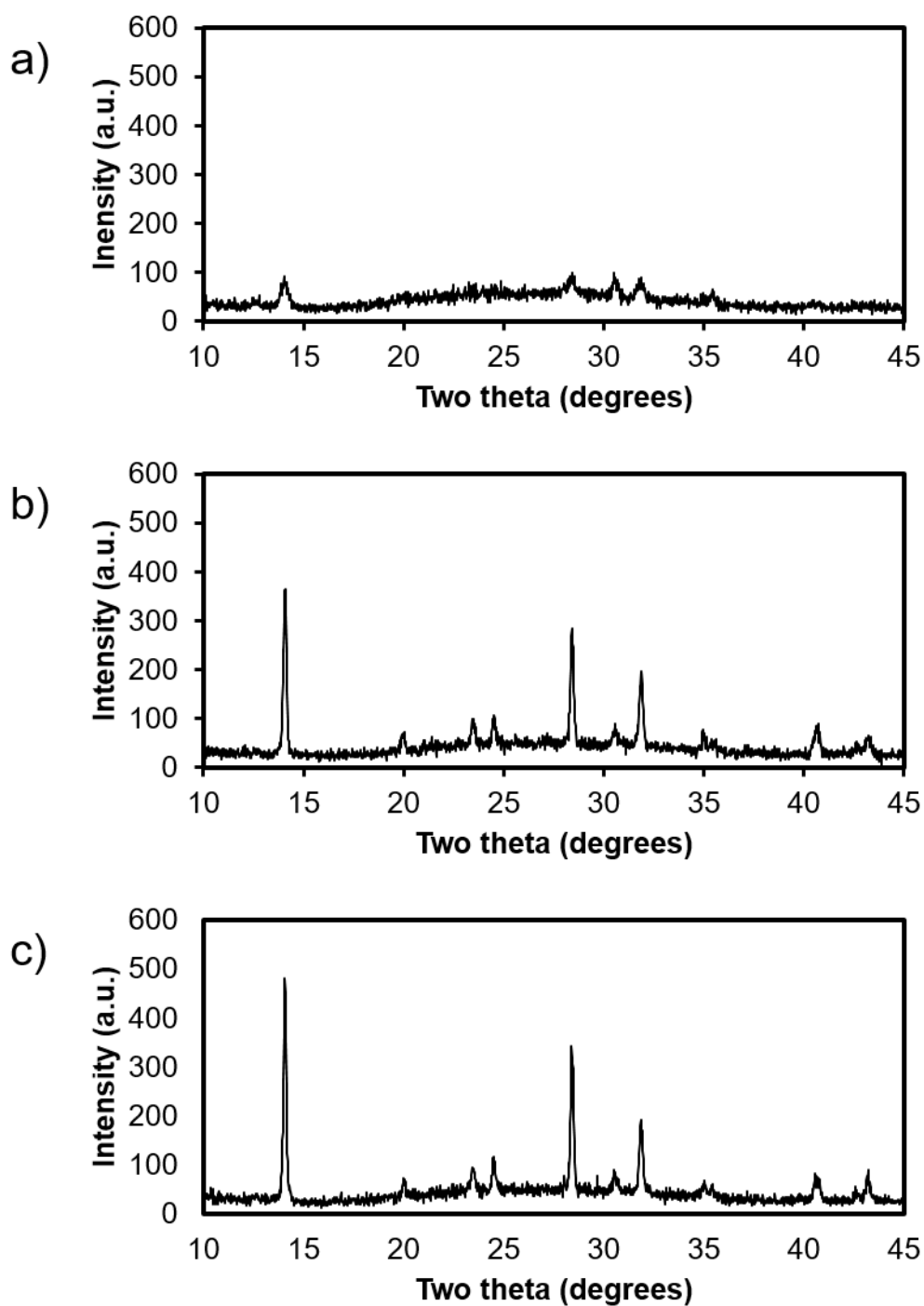


Figure 3.19: XRD on 15:1 perovskite: PAA mass ratio thin films prepared a) with GBL/DMSO annealed 10 minutes at 120°C and 10 minutes at 100°C, b) with DMF/DMSO annealed 20 minutes at 100°C, and c) with DMF/DMSO annealed 10 minutes at 120°C and 10 minutes at 100°C.

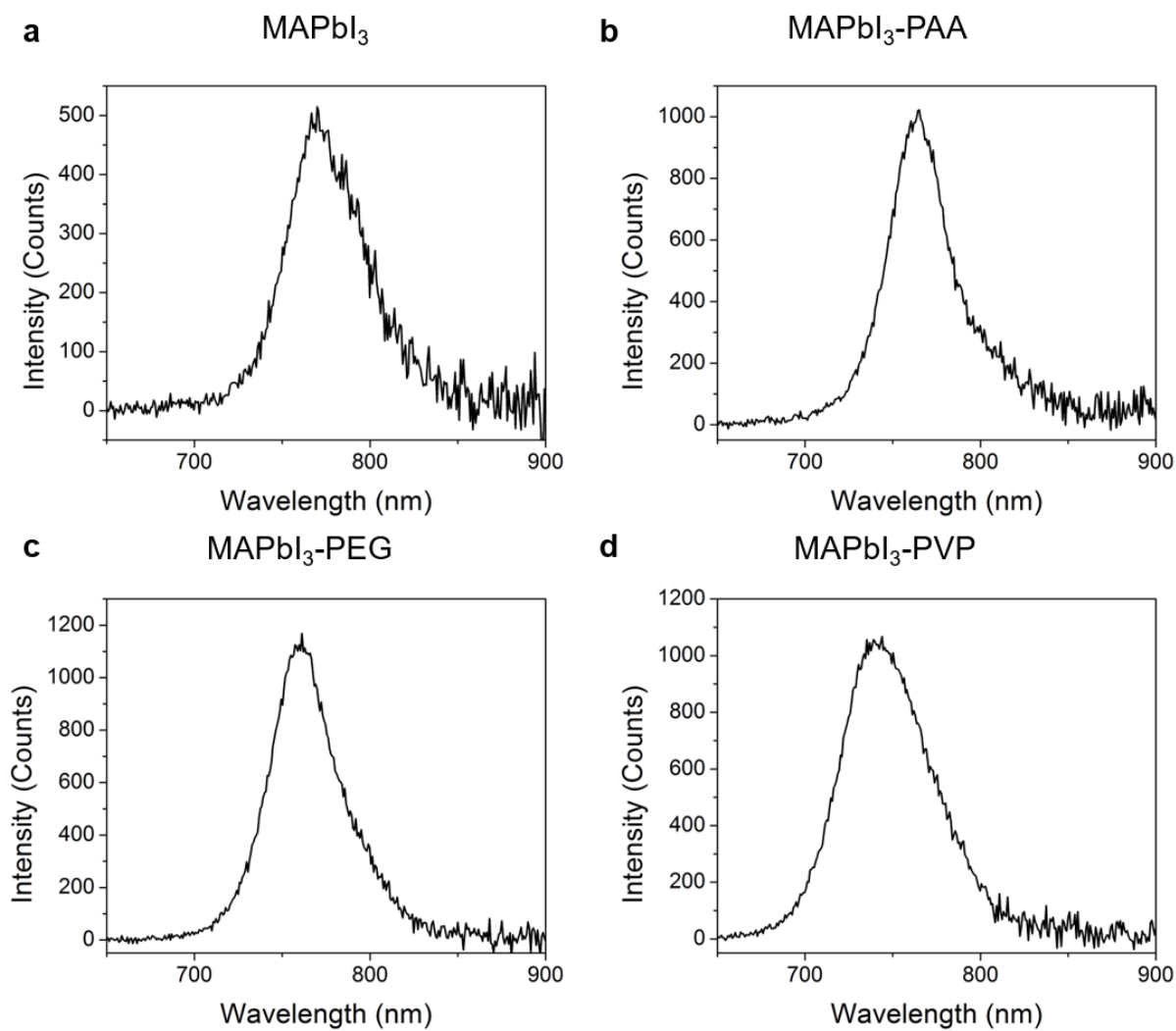


Figure 3.20: Steady-state-photoluminescence of the perovskite. The films were excited at 530nm. We observe that MAPbI_3 has a peak at 770 nm, MAPbI_3 -PAA and MAPbI_3 -PEG have peaks at 760 nm, while MAPbI_3 -PVP has a peak at 730 nm.

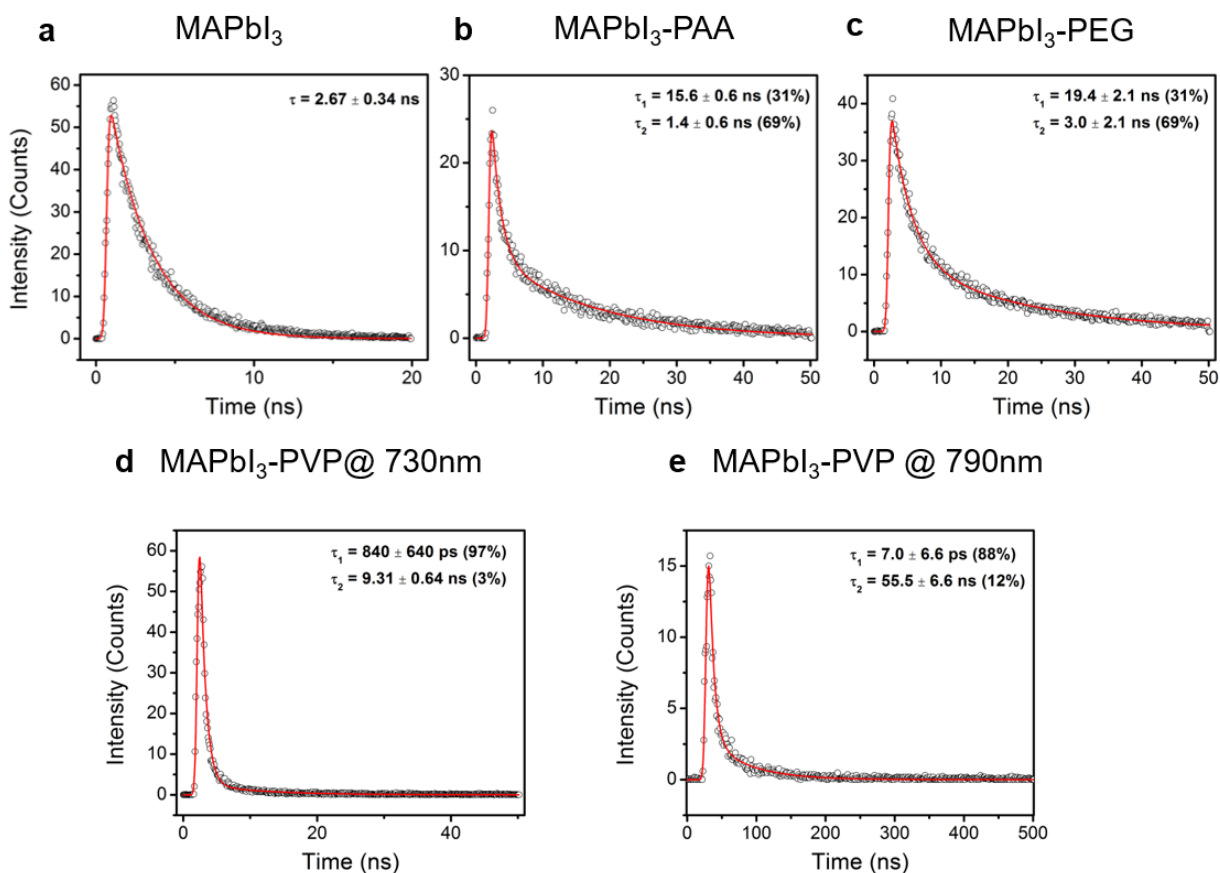


Figure 3.21: Time-resolved photoluminescence (TR-PL) of (a) MAPbI₃, (b) MAPbI₃-PAA, (c) MAPbI₃-PEG, and (d) MAPbI₃-PVP excited at 730 nm and (e) MAPbI₃-PVP excited at 790 nm. Data has been fit to a bi-exponential decay model in all cases except for the MAPbI₃ control, and TR-PL single wave kinetics were measured at the steady state PL peak for each sample unless otherwise noted. We see that PEG and PAA tend to increase the PL lifetime of the perovskite film, while PVP decreases the lifetime significantly. With respect to MAPbI₃-PVP, there is a fast decay (<1 ns) and a long decay that can be seen better at 790 nm (7 ns). The two separate decay lifetimes in this sample may be a result of the two distinct phases we found in the morphological study leading to different carrier decay processes.

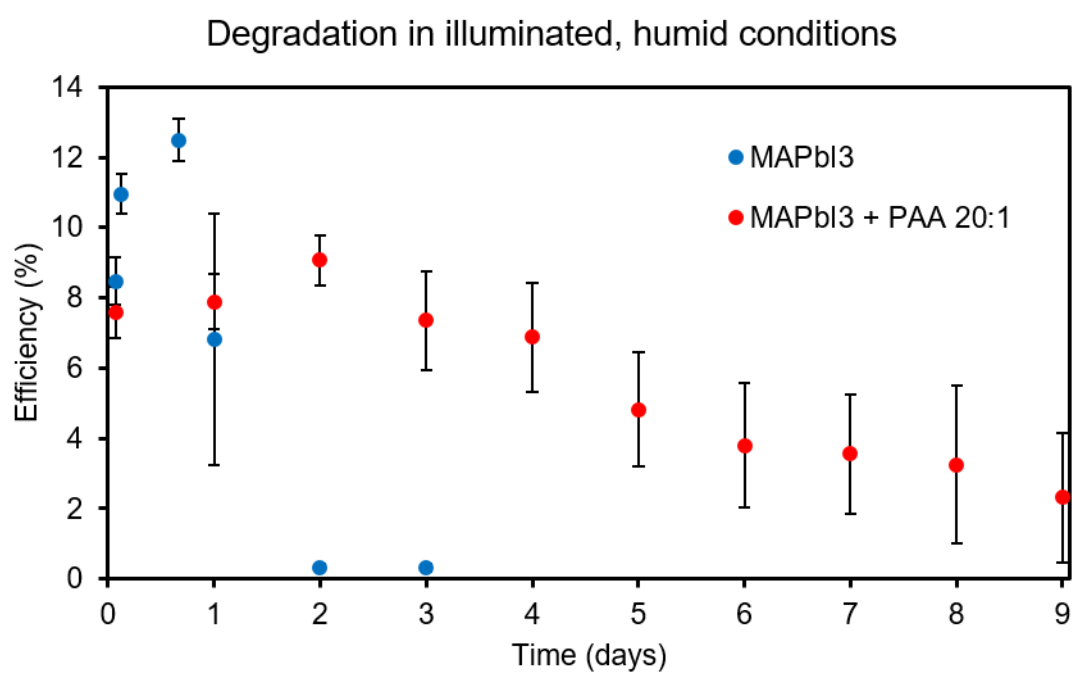


Figure 3.22: Perovskite solar cell stability over time under 43% relative humidity in air with illumination. Error bars indicate standard deviation across $n=7$ devices.

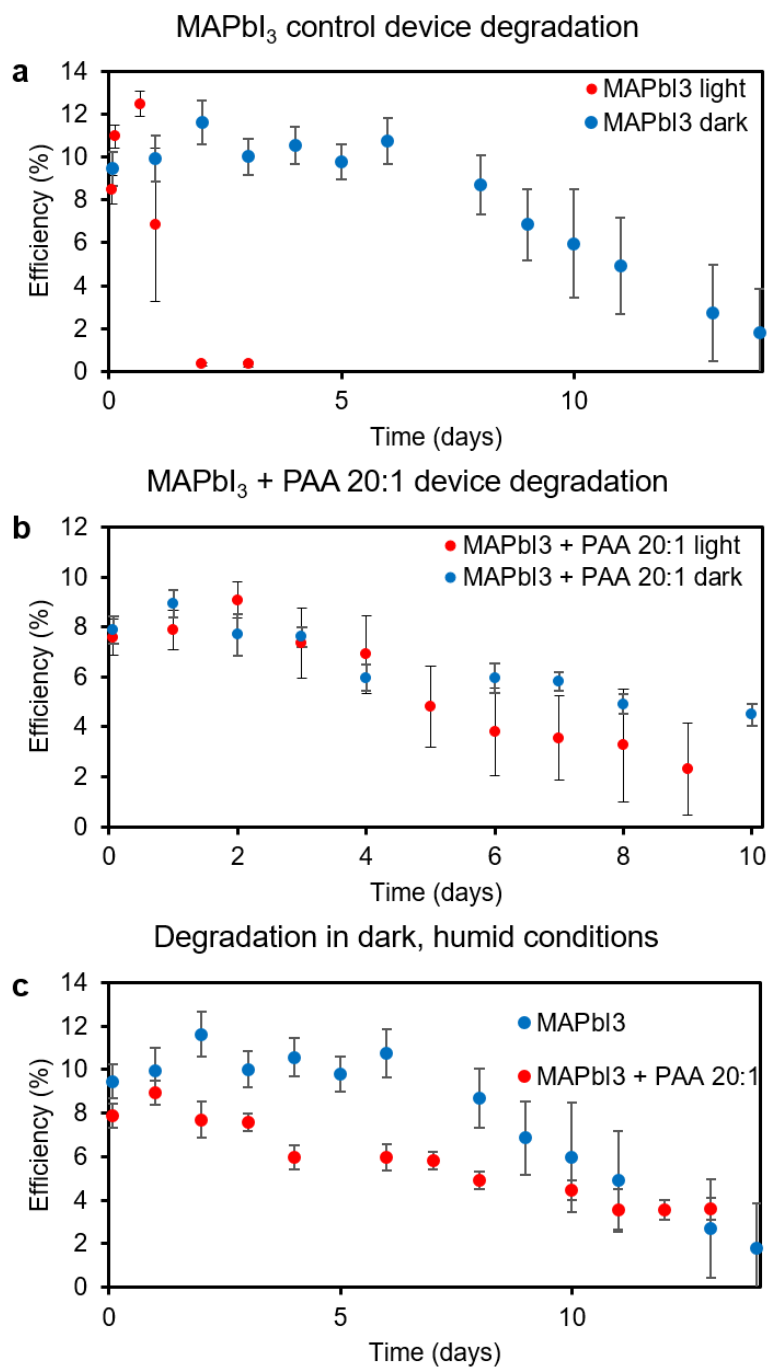


Figure 3.23: Perovskite solar cell stability over time under 43% relative humidity in air a) for MAPbI₃ control devices, b) for MAPbI₃ + PAA 20:1 devices, and c) a comparison between both sets of devices in the dark. Error bars indicate standard deviation across n=7 devices.

The initial stability of the control devices can be explained by changes in the stoichiometry of the perovskite grain boundaries. It has been reported that slight excesses of PbI_2 in the grain boundaries can be beneficial to the open circuit voltage and J_{sc} .⁹¹ Thus, as the devices start to degrade, the initially-stoichiometric mixture becomes slightly PbI_2 -rich, which is beneficial to the overall performance. As degradation progresses, however, excess PbI_2 accumulates further and rapidly reduces the efficiency of the devices. When we consider that the grain boundaries of the MAPbI_3 -PAA films are coated with polymer instead of PbI_2 , it is likely that local changes in stoichiometry at the grain boundaries are not possible. Instead, the MAPbI_3 -PAA devices degrade at a slower, but steady rate. It remains surprising that the 20:1 MAPbI_3 -PAA devices degraded as quickly as the MAPbI_3 devices in dark, humid conditions because our film stability experiments showed that the MAPbI_3 film degrades more quickly than the MAPbI_3 -PAA film. However, those experiments characterize only the bulk degradation rate and do not measure degradation at the interface between the perovskite and surrounding layers. In PSCs, degradation of the interface of the active layer with the transport layers is sufficient to degrade device performance. We observed that at the 14-day time point of the dark, humid stability test, both the control and PAA-hybrid PSCs still appear to have a brown color. Thus, the interfaces of these films with their contact layers must have degraded over time. Overall, the inclusion of PAA into PSCs tends to greatly increase the stability of the device under illuminated conditions at the expense of a modest amount of its starting efficiency.

3.4 CONCLUSIONS

In conclusion, we have demonstrated that incorporation of various polymers into the active layer of PSCs significantly impacts the film morphology and stability. We have observed the phase separation behavior of polymer perovskite hybrid thin films using nanomechanical AFM. These observations are important to device design because reduced grain size is detrimental to device performance, and different polymers can affect the grain size, grain shape, and photoluminescence lifetime. Solution NMR suggests that the acid-base interaction between acidic polymers and methy-

lammonium tends to stabilize the methylammonium within the perovskite unlike the previously-reported PEG or PVP hybrids. Furthermore, we have observed that the degradation pathways and preferential crystal faceting are different for various perovskite-polymer hybrids. We have demonstrated significant improvements on device stability under humid, illuminated conditions in PAA-perovskite hybrid PSCs. Understanding why certain polymers help the stability and how they change the morphology of the active layer is a critical step towards a more reliable design for perovskite solar cells.

3.5 MATERIALS AND METHODS

3.5.1 *Chemical synthesis*

Lead iodide (PbI_2 -99% perovskite grade) was purchased from Tokyo Chemical Inc. Poly(3,4-ethylenedioxythiophene) polystyrene sulfonate (PEDOT:PSS) was purchased from Heraeus. All other chemicals were used as received from Sigma-Aldrich.

Methylammonium iodide synthesis: As described in the literature,⁹² methylamine solution (40% in methanol) was reacted with hydroiodic acid (57% in water) in a round bottom flask stirring in an ice bath. The solvent was removed with rotary evaporation at 60°C, and then the MAI was dissolved in ethanol. MAI was precipitated from solution with diethyl ether. The MAI powder was then dried in a vacuum oven at 60°C overnight.

3.5.2 *Characterization*

Tapping mode atomic force microscopy (AFM) measurements were conducted on a Bruker ICON system. Nanomechanical AFM measurements were conducted on a Veeco Bioscope Catalyst AFM with a ScanAsyst-Air silicon nitride AFM probe with a stiffness of 0.4 N/m, and a nominal tip radius of 5 nm. 0.3 – 1.2 nN of force was applied to the sample to measure mechanical behavior, and our data was analyzed with Bruker Nanoscope Analysis software. Force-loading curves were mod-

eled using the Derjaguin, Muller and Toporov (DMT) model⁹³ to calculate the local elastic modulus. Profilometry measurements to determine film thickness were performed on a Veeco Dektak 150 surface profiler. X-ray diffraction (XRD) experiments were conducted on a Scintag XDS2000 using Cu K α radiation at 40kV and 20mA current. Secondary electron microscopy (SEM) was performed on a Hitachi SU8030. Transmission electron microscopy (TEM) experiments were performed on a Hitachi HT-7700 at 120 kV accelerating voltage. The thickness of the samples cast on TEM grids needs to be thinner than the typical PSC film thickness (150 nm) to see contrast. We prepared TEM samples by drop casting 10 μ L of solution onto a lacey carbon grid and wicking away the excess solution. Samples were then annealed for 10 minutes at 120°C and 10 minutes at 100°C. ¹H nuclear magnetic resonance (NMR) spectroscopy was performed on an Agilent DD2 500 MHz instrument. For sample preparation, dimethylsulfoxide-d₆ was dried with 4 Å molecular sieves overnight, and the polymer, MAI and PbI₂ were dissolved in a total solid concentration of 200 mg/mL. The mass ratio of the perovskite precursors to polymer was kept at 15:1. Fourier transform infrared (FT-IR) spectroscopy was performed using a Thermo Nicolet Nexus 870 spectrometer in transmission mode with perovskite films ground into a KBr pellet.

3.5.3 Substrate preparation

Patterned ITO substrates (Thin Film Devices, 20 ohms/square) were cleaned by sequential sonication in hexane, soapy water, milli-q water, and a 1:1:1 mixture of isopropanol, acetone, and methanol. After drying, clean substrates were treated for 20 minutes in a UV-ozone cleaner (Bio-force Nanosciences). Poly(3,4-ethylenedioxythiophene) polystyrene sulfonate (PEDOT:PSS) was filtered through a 0.45 μ m nylon filter before spin-coating at 5000 RPM with a 1000 RPM/second ramp rate for 60 seconds. PEDOT:PSS films were then annealed at 150°C for 20 minutes in the glovebox.

3.5.4 *Single crystal growth*

Single crystals were grown via vapor diffusion from 20 wt% solutions of MAPbI₃ in γ -butyrolactone (GBL) using dichloromethane as the antisolvent. Polymers were added to the crystallization solution before crystallization at a concentration of 20 mg/mL in GBL.

3.5.5 *Device fabrication*

Devices were fabricated in a nitrogen-filled glovebox. The spin coating procedure for the active layer follows a slightly modified procedure from that outlined by Jeon et al.²⁴ For control devices, MAPbI₃ solutions were dissolved in a solvent mixture of 70% γ -butyrolactone (GBL) 30% dimethyl sulfoxide (DMSO) overnight under stirring and heating at 65°C. The active layer was spin-cast onto PEDOT:PSS-coated ITO substrates for 10 seconds at 1000 RPM and 20 seconds at 5000 RPM. 700 μ L of toluene was cast with 5 seconds left on the 5000 RPM step. For experimental devices, MAPbI₃ solutions with polymer additives were dissolved in mixtures of 80% dimethylformamide (DMF) and 20% DMSO.⁹⁴ The active layer was spin-cast for 10 seconds at 1000 RPM and 60 seconds at 4000 RPM. 150 μ L of chlorobenzene was drop cast with 40 seconds left on the 4000RPM step. The spin-cast layers were annealed at 120°C for 10 minutes followed by 10 minutes at 100°C. The over-layer solution is a 16 mg/mL solution of PCBM spin-cast at 2000 RPM. This solution is dissolved with stirring and heating at 65°C overnight before spin-coating the solution (filtered through a 0.2 μ m PTFE filter). Bathocuproine (BCP) is dissolved at 0.5mg/mL in ethanol and spin cast onto a 5000 RPM substrate. 50 nm gold contacts were thermally evaporated onto the substrates at a pressure of $<10^{-6}$ mbar using a shadow mask to define 4 mm² devices. Finally, devices were tested in air on a Newport solar simulator with a Keithley 2400 sourcemeter.

3.5.6 *Long term stability testing*

Polymers and perovskite-polymer blends were tested for long term stability using saturated salt solutions inside sealed bell jars. Lithium chloride (11% relative humidity (RH)), potassium acetate

(23% RH), potassium carbonate (43% RH), calcium nitrate (55% RH), sodium chloride (75% RH), and potassium chloride (85% RH) were the salts we used to control the relative humidity of each chamber. For film degradation testing, perovskite films were analyzed with X-ray diffraction on a Scintag XDS2000 XRD with a copper K α source, UV-Vis absorption spectroscopy on a Perkin Elmer LAMBDA 1050 spectrophotometer, and X-ray Photoelectron Spectroscopy (XPS) on a Thermo Scientific ESCALAB 250Xi at regular intervals. For film degradation testing under the 43% RH condition, we made the perovskite polymer hybrid films thicker (310nm) than the control (170 nm) to visualize the perovskite peaks better for the polymer perovskite hybrid films in XRD. Under 85% RH, we matched the thickness of all 4 films to that of the control (170nm). Because different polymers changed the viscosity of the spin-coating solution, we had to optimize our perovskite and polymer concentrations to compare films with similar polymer content and thickness. Solar cells were degraded under 43% RH and fluorescent indoor lighting. They were placed 30 cm from a fluorescent lamp with 4100 K color temperature. We estimated the intensity of this illumination to be 0.5% as intense as incident solar illumination by using a photodiode to compare the intensity of our solar simulator illumination to the conditions under the fluorescent lamp.

4 ENHANCED OUT-OF-PLANE CONDUCTIVITY AND PHOTOVOLTAIC PERFORMANCE IN $n = 1$ LAYERED PEROVSKITES THROUGH ORGANIC CATION DESIGN

4.1 OBJECTIVES AND SIGNIFICANCE

Layered perovskites with the formula $(R-NH_3)_2PbI_4$ have excellent environmental stability but poor photovoltaic function due to the preferential orientation of the semiconducting layer parallel to the substrate and the typically insulating nature of the $R-NH_3^+$ cation. Here we report a series of these $n = 1$ layered perovskites with the form (aromatic-O-linker- NH_3) $_2PbI_4$ where the aromatic moiety is naphthalene, pyrene or perylene and the linker is ethyl, propyl or butyl. These materials achieve enhanced conductivity perpendicular to the inorganic layers due to better energy level matching between the inorganic layers and organic galleries. The enhanced conductivity and visible absorption of these materials led to a champion power conversion efficiency of 1.24%, which is the highest value reported for any $n = 1$ layered perovskite, and it is an order of magnitude higher efficiency than any other $n = 1$ layered perovskite oriented with layers parallel to the substrate. These findings demonstrate the importance of leveraging the electronic character of the organic cation to improve optoelectronic properties and thus the photovoltaic performance of these chemically-stable low n layered perovskites.

4.2 BACKGROUND

Two-dimensional organic-inorganic layered perovskites based on the lead halide framework have demonstrated many of the attractive optoelectronic properties and translational possibilities of their parent three-dimensional perovskites while achieving better stability.^{95,84,96} The structure of these layered perovskites can be generally viewed as the periodic splitting of the three-dimensional structure along a particular crystallographic axis, most commonly along the (100) plane, to form a

layered structure. Chemically, this is accomplished by substituting a bulky organic cation ($R-NH_3^+$) for the interstitial A-site cation according to the formula $(R-NH_3)_2Pb_nX_{3n+1}A_{n-1}$.^{85,47} In these structures, n corner-sharing PbX_4^{2-} octahedra span the thickness of the inorganic layer where n is modulated by tuning the ratio of the small interstitial A site cation to the bulky organic cation ($n = 1$ shown in figure 4.1A). These 2D semiconducting inorganic layers are separated by bulky organic cations, which are typically insulating and thus isolate the inorganic layers both physically and electronically.^{97,52,98}

In the modern photovoltaic literature, the role of the organic cation has been primarily structural, and the optoelectronic properties of these materials have been designed through the compositional tuning of inorganic layers (varying X and n)²⁵ and processing conditions.^{73,69} To date, these studies have achieved remarkable results with a reported power conversion efficiency (PCE) of 12.5% for a layered perovskite where $n = 4$, $R =$ butylammonium iodide, and $A =$ methylammonium iodide.⁹⁵ In this example, the inorganic layers were oriented perpendicular to the bottom contact through a hot-casting technique to mitigate the negative impact of the insulating butyl groups on conductivity between the inorganic layers.⁹⁵ Even though the introduction of hydrophobic cations into these $n > 1$ layered perovskites has been shown to improve stability compared to three-dimensional perovskites, most examples still utilize methylammonium iodide as the A-site cation, which is known to be intrinsically unstable under atmospheric conditions.²⁵ Furthermore, it is still unclear if the orientational control of the hot-casting technique is applicable to all cations in layered perovskites or for low n layered perovskites in general.

In this work, we study layered perovskites of the $n = 1$ variety where $X = I$. These $n = 1$ layered perovskites do not contain an A-site cation and are thus considerably more stable than the $n > 1$ variety. These materials, however, present new challenges due to their wide bandgap and, in all but one example,⁹⁹ their inorganic layers prefer orientation parallel to the substrate. This orientation therefore requires conduction of excited-state-carriers perpendicular to the inorganic layers and through typically insulating organic layers (out-of-plane conductivity) to reach the elec-

trodes. If enhanced out-of-plane conductivity can be achieved in these materials, it would obviate the need to reorient the inorganic layers with respect to the substrate surface in photovoltaic devices. Recent layered perovskite studies have, for the most part, only utilized well-known organic moieties such as butylammonium,⁸⁴ benzylammonium,⁹⁹ and phenylethyl ammonium⁹⁶ as structural components in perovskite solar cells. However, preceding research of layered perovskites as photovoltaic materials, a number of investigators studied optoelectronic properties and functions with cations containing conjugated moieties such oligothiophene,¹⁰⁰ pyrene,¹⁰¹ anthryl,¹⁰² naphthalene,¹⁰² and phenyl.¹⁰³ Much of this earlier work investigated the charge-transfer of photo-excited carriers between the inorganic and organic layers and explored electroluminescent properties.^{100,101} Their work showed the contribution that the organic chromophores can have on the optoelectronic properties and applications of these materials. They also demonstrated how the alignment of the highest occupied molecular orbital (HOMO) and the lowest unoccupied molecular orbital (LUMO) energy levels of the organic and inorganic layers can affect charge transfer between them in the hybrid.¹⁰¹ Since this work predated interest in these materials as photovoltaic active layers, it primarily considered charge transfer from inorganic-to-organic layers or vice versa as a single event. However, charge transfer in a photovoltaic active layer requires many charge transfer events across many organic-inorganic interfaces through the thickness of the device. Using inspiration from this pioneering work in organic-inorganic layered perovskites as well as our own work on hybrid systems where the organic components serve both structural and electronic functions,^{104,29,32} we seek enhance photovoltaic performance in $n = 1$ layered perovskite through organic cation design.

We report here on a new approach towards layered perovskite photovoltaics in which we utilize the electronic and structural properties of custom-synthesized organic cations to achieve enhanced optoelectronic properties and device performance. We have synthesized organic cations containing various aromatic moieties and have explored how the electronic properties and structural arrangement of the cation within the organic galleries contribute to overcoming the chief limitation of $n = 1$ layered perovskites, which is their poor out-of-plane conductivity. Specifically, we have synthesized

$n = 1$ layered perovskites with the formula (aromatic-O-linker-NH₃)₂PbI₄ for which bulky cations are synthesized to contain the aromatic groups naphthalene, pyrene, or perylene and the linkers ethyl, propyl or butyl conjugated through an ether bond (figure 4.1A and B). We have investigated the impact of the HOMO and LUMO alignment of the organic cation and the inorganic layer as well as the structural arrangement of the organic cations within the organic layer on out-of-plane conductivity and optical properties of these layered perovskite materials. Guided by our findings we fabricated photovoltaic devices and analyzed their performance.

4.3 RESULTS AND DISCUSSION

4.3.1 *Synthesis and characterization of organic ammonium iodide salts*

In this study, we pursued a modular synthetic approach which enabled the development of a homologous series of organic cations that varied in both electronic character of the aromatic moiety and length of aliphatic linker. This approach facilitates the study of how the energy levels of the aromatic moieties and packing of the organic cations affect the optoelectronic properties of the resulting layered perovskites. Specifically, we synthesized six aromatic ammonium iodide salts with the general form aromatic-O-linker-NH₃I where the aromatic moiety is naphthalene, pyrene, or perylene and the linker is ethyl, propyl or butyl. The aromatic moieties were chosen based on reported HOMO and LUMO levels for the non-functionalized aromatic core in relation to the HOMO and LUMO levels reported for typical $n = 1$ lead iodide layered perovskites with aliphatic cations. To synthesize these ammonium iodide salts, hydroxyl-naphthalene, pyrene or perylene were conjugated to either the protected bromo-ethyl, propyl or butyl amine under basic conditions. Following purification, the protecting groups were cleaved and the resulting amine protonated with hydroiodic acid to form the final ammonium iodide salt (see the materials and methods section for synthetic details). Once synthesized, the HOMO and LUMO levels of the ammonium iodide salts were determined by ultraviolet photoelectron spectroscopy (UPS) and optical absorption experiments. These

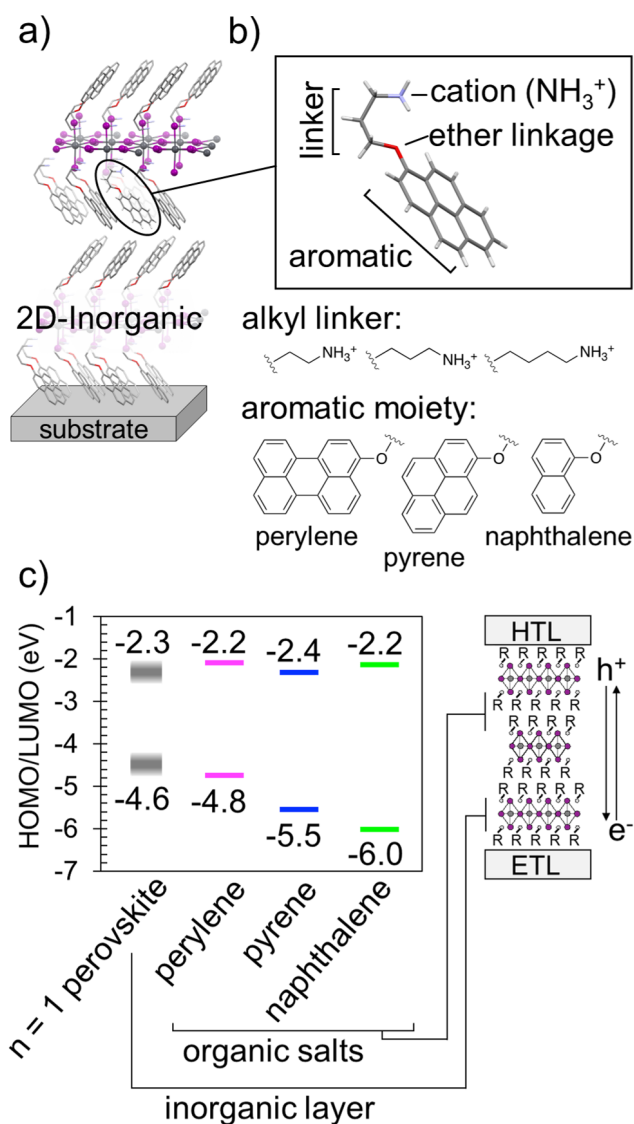


Figure 4.1: (a) $n = 1$ layered perovskites of the form $(R-NH_3)_2PbI_4$ showing alternating organic and inorganic layers that align parallel to the substrate. (b) Modular molecular design of the ammonium iodide cation consisting of an aromatic core joined by an ether bond to an alkyl linker of variable length. (c) Energy levels of typical $n = 1$ layered perovskites (grey) with values specific to $(butyl-NH_3)_2PbI_4$ compared to the energy levels of the conjugated organic ammonium iodide salts of interest: perylene-O-ethyl- NH_3I , pyrene-O-propyl- NH_3I , and naphthalene -O-propyl- NH_3I . HTL and ETL refer to hole and electron transport layers.

are plotted with respect to the HOMO and LUMO levels reported for the reported $n = 1$ layered perovskite $(\text{CH}_3(\text{CH}_2)_3\text{NH}_3)_2\text{PbI}_4$ ⁸⁴ in Figure 4.1C.

4.3.2 *Crystal growth and optical properties*

The six aromatic cations with structure aromatic-O-linker-NH₃I were successfully crystallized with lead (II) iodide into the desired (100) type $n = 1$ layered perovskite. Single crystals were prepared through vapor diffusion of dichloromethane (DCM) into γ -butyrolactone (GBL) solutions of 2:1 molar ratio of organic ammonium iodide salt: lead (II) iodide.¹⁰⁵ We will refer to the resulting perovskites using an abbreviated formula of the general type (aromatic-O-linker-NH₃)₂PbI₄. Here we report on seven $n = 1$ layered perovskites including (naphthalene-O-ethyl-NH₃)₂PbI₄, (naphthalene-O-propyl-NH₃)₂PbI₄, (naphthalene-O-propyl-NH₃)₂PbI₄·(C₄H₆O₂)_{0.5}, (pyrene-O-ethyl-NH₃)₂PbI₄, (pyrene-O-propyl-NH₃)₂PbI₄, (pyrene-O-butyl-NH₃)₂PbI₄, and (perylene-O-ethyl-NH₃)₂PbI₄. The structures of these layered perovskites were determined using single crystal X-ray diffraction. Crystallographic details are provided in table 4.1. Note that naphthalene-O-propyl-NH₃I can form two distinct layered perovskites. The first has the anticipated form and stoichiometry (naphthalene-O-propyl-NH₃)₂PbI₄ and the second contains GBL within the lattice (naphthalene-O-propyl-NH₃)₂PbI₄·(C₄H₆O₂)_{0.5}. This was the only structure in this work that contained solvent molecules within the unit cell, and this structure could not be produced in thin film. All other layered perovskites were crystallized in thin film by spin-casting and annealing the same stoichiometric ratios dissolved in a 1:1 volume ratio of dimethylformamide (DMF): dimethyl sulfoxide (DMSO). Grazing-incidence wide-angle X-ray scattering (GIWAXS) was used to verify that the same crystallographic phase was obtained in thin film as observed in single crystal (figure 4.2). All six of the crystal structures that crystallize in thin film are Monoclinic. In all cases the GIWAXS patterns appear to be orthorhombic (figure 4.3). We are confident of our crystal solutions and that the films are of the same structure as the single crystal. Although we are not completely sure where this difference in unit cell observed by GIWAXS as compared to

single crystal measurement arises from, we propose that the GIWAXS data appears as a higher symmetry due to extensive twinning. When the films are made isotropic (scraped into a powder), these twinning artifacts should be eliminated. The resulting powder pattern agrees well with the pattern predicted from the monoclinic single crystal data (figure 4.2A-D).

Optical absorption spectroscopy was used to determine the energy of the S₁ exciton peak (E_{S1}) in thin film samples of each layered perovskite (Table 4.1 and figure 4.4). These $n = 1$ layered perovskites have characteristically large exciton binding energy in the range of 250-500 meV that results from the dielectric confinement of the 2D-inorganic layer.¹⁰⁶ The large binding energy is apparent in the absorption spectra with a pronounced lowest energy electronic transition which is assigned to the S₁ exciton followed by a broader absorption onset typically assigned to the bandgap absorption (figure 4.5). The precise determination of the bandgap of these materials can be difficult to ascertain from the absorption spectra at room temperature. Thus, we used the E_{S1} transition as an indication of bandgap energy for these materials since this absorption has been shown to produce photocurrent and is thus important to photovoltaic performance.¹⁰⁷ A wide range of E_{S1} values (2.27 eV – 2.57 eV) have been observed for the layered perovskites investigated here. Increasing E_{S1} values are correlated with increasing distortion of the PbI_4^{2-} octahedra compared with the ideal, lowest energy arrangement in which Pb-I-Pb bond angles along the central plane of the inorganic layer are 180° (figure 4.6).^{108,109} The role that the organic cation plays in dictating octahedral distortion and thus the optical properties of layered perovskites has been previously linked to the position of the positively charged ammonium cation with respect to the negatively charged inorganic lattice.¹⁰⁸ Our materials generally follow this previously-defined model, except for (naphthalene-O-propyl-NH₃)₂PbI₄, which has the highest E_{S1} despite having moderate penetration of the ammonium cation into the inorganic lattice (figure 4.7). Recently, low octahedral distortion has been observed in an $n = 1$ layered perovskite containing tertiary ammonium groups.¹¹⁰ In this structure, substitution on the ammonium group may increase the distance between the cationic nitrogen and the negatively charged inorganic lattice. In our materials, we have observed that E_{S1} values increase linearly with de-

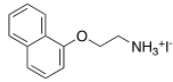
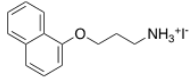
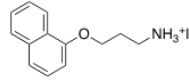
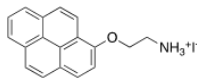
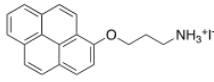
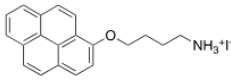
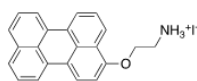
cation:	(Naphthalene-O-ethyl) ₂ PbI ₄	(Naphthalene-O-propyl) ₂ PbI ₄	(naphthalene-O-propyl-NH ₃) ₂ PbI ₄ · (C ₄ H ₆ O ₂) _{0.5}
			
empirical formula	(C ₁₂ H ₁₄ ON) ₂ PbI ₄	(C ₁₃ H ₁₆ ON) ₂ PbI ₄	C ₂ H ₃ O(C ₁₃ H ₁₆ ON) ₂ PbI ₄
formula weight (g/mol)	1091.27	1119.39	1162.37
cryst system	Monoclinic C	Monoclinic P	Triclinic
space group	C _c	P _{2₁/c}	P $\bar{1}$
unit cell dimension:			
a, Å	12.5228(17)	23.0465(10)	12.4181(3)
b, Å	12.4668(17)	8.8619(4)	12.5652(4)
c, Å	39.555(6)	8.2792(4)	23.8888(7)
α, β, γ, deg	90, 97.668(3), 90	90, 95.2834(19), 90	101.10, 104.07, 90.71
E _{S1} exciton (eV)	2.39 ¹	2.57 ¹	2.35 ²
cation:	(Pyrene-O-ethyl) ₂ PbI ₄	(Pyrene-O-propyl) ₂ PbI ₄	(Pyrene-O-butyl) ₂ PbI ₄
			
empirical formula	(C ₁₈ H ₁₆ ON) ₂ PbI ₄	(C ₁₉ H ₁₈ ON) ₂ PbI ₄	(C ₂₀ H ₂₀ ON) ₂ PbI ₄
formula weight (g/mol)	1239.42	1267.48	1293.63
cryst system	Monoclinic C	Monoclinic C	Monoclinic C
space group	C _c	C _c	C _{2/c}
unit cell dimension:			
a, Å	12.4263(3)	49.3795(13)	53.3048(16)
b, Å	12.4019(3)	8.4895(2)	6.1727(2)
c, Å	48.3623(3)	9.4484(2)	12.565(4)
α, β, γ, deg	90, 95.859(2), 90	90, 94.9469(13), 90	90, 90.318(2), 90
E _{S1} exciton (eV)	2.38 ¹	2.27 ¹	2.40 ¹
cation:	(Perylene-O-ethyl) ₂ PbI ₄		
			
empirical formula	(C ₄₄ H ₁₈ ON) ₂ PbI ₄		
formula weight (g/mol)	1339.54		
cryst system	Monoclinic P		
space group	P _{2₁/c}		
unit cell dimension:			
a, Å	26.2873(9)		
b, Å	8.8638(3)		
c, Å	8.7113(3)		
α, β, γ, deg	90, 94.282(2), 90		
E _{S1} exciton (eV)	2.41 ¹		
		(1) Energy of S ₁ exciton determined by optical absorption of thin films in transmission mode.	
		(2) Energy of S ₁ exciton determined by optical reflectance spectroscopy on finely powdered crystals.	
		Structures solved with direct methods using SHELXL and refined with least squares minimization using the SHELXS refinement package. Additional crystallographic detail provided in supporting information S.	

Table 4.1: Crystal data for n = 1 layered perovskites of the form (aromatic-O-linker-NH₃)₂PbI₄

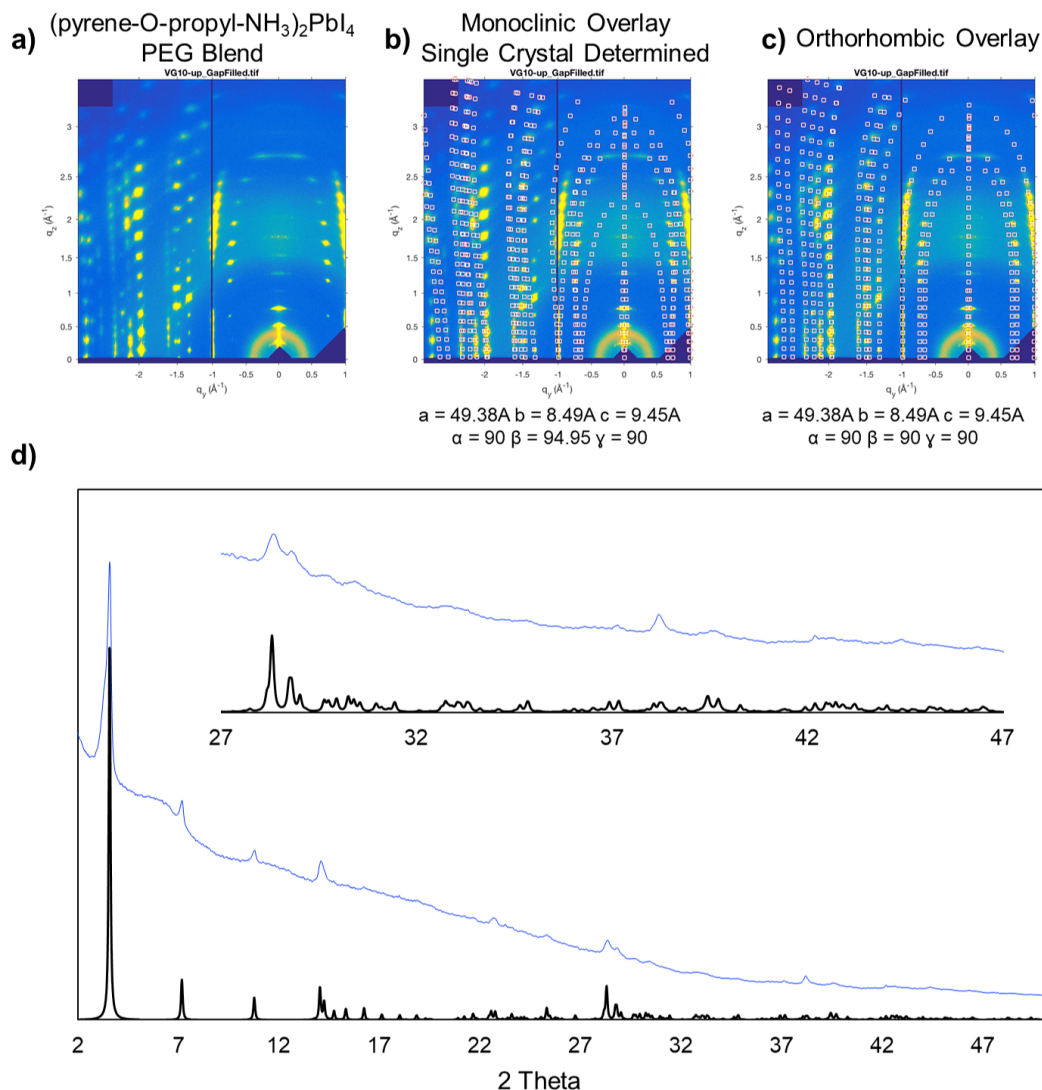


Figure 4.2: a) GIWAXS of (pyrene-O-propyl-NH₃)₂PbI₄ after formulation with 5 wt% polyethylene glycol. This formulation achieved better orientation and higher crystallinity likely due to slower evaporation of solvent but the resulting devices were not functional likely due to insulating properties of the polymer. (b) These GIWAXS images, however, illustrate well that when the unit cell is overlaid directly there is good matching of the layered peaks but there is poor matching of off axis reflections. (c) When an orthorhombic overlay is used with the same cell a,b and c axis, excellent agreement is seen. This likely indicated a high degree of twinning in the sample which produces a diffraction image that appears higher symmetry than is actually realized in single crystal measurements. (d) Predicted powder pattern for (pyrene-O-propyl-NH₃)₂PbI₄ (black) and experimental pattern (blue) which was obtained by scraping films of (pyrene-O-propyl-NH₃)₂PbI₄.

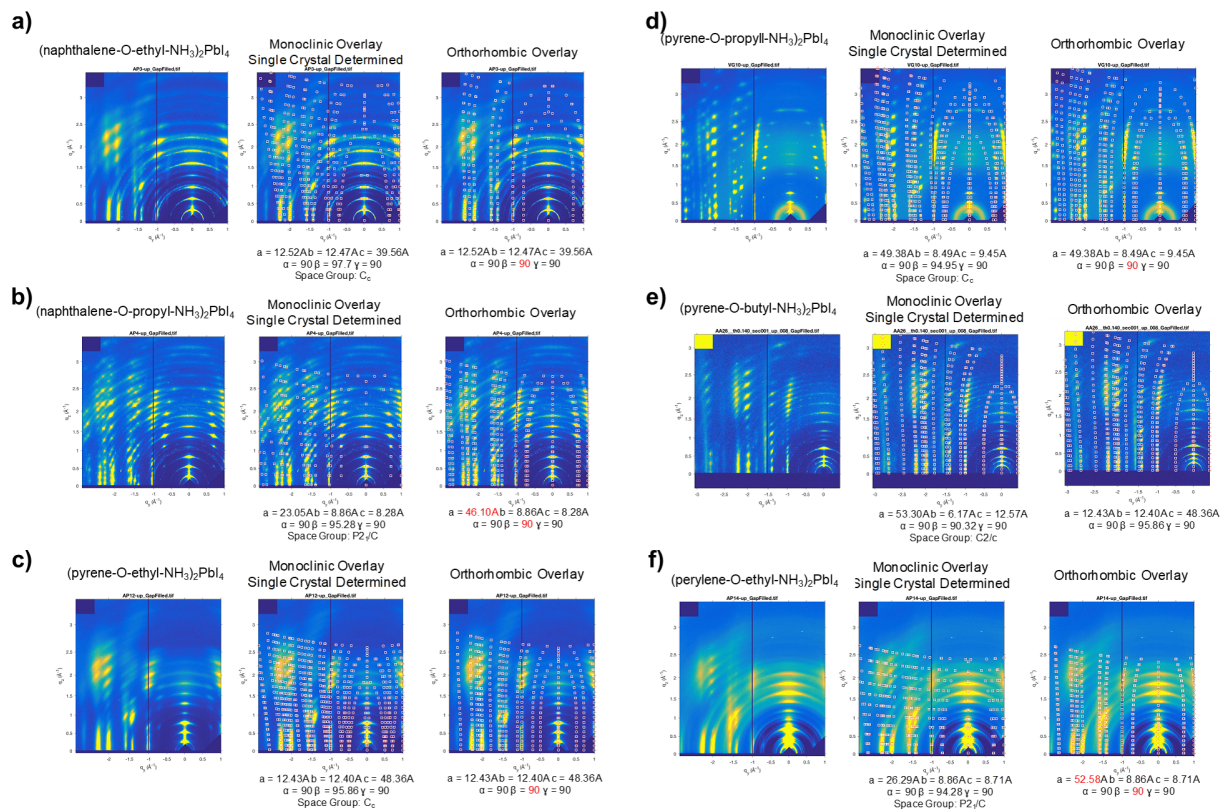


Figure 4.3: GIWAXS for (a) (naphthalene-O-ethyl-NH₃)₂PbI₄, (b) (naphthalene-O-propyl-NH₃)₂PbI₄, (c) (pyrene-O-ethyl-NH₃)₂PbI₄, (d) (pyrene-O-propyl-NH₃)₂PbI₄, (e) (pyrene-O-butyl-NH₃)₂PbI₄, (f) (perylene-O-ethyl-NH₃)₂PbI₄. The pattern is shown alongside the unit cell overlay of the single crystal structure and the orthorhombic derivative (beta = 90).

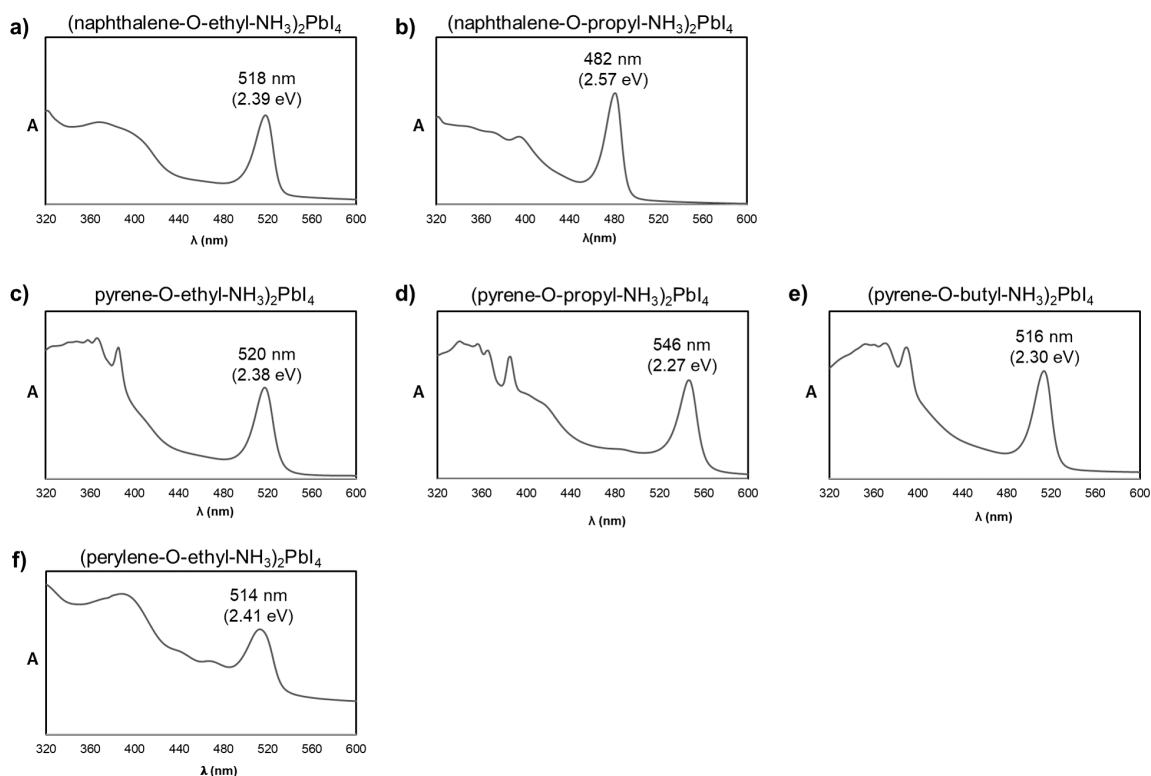


Figure 4.4: UV-Vis absorption spectra for layered perovskite films with the S_1 exciton peak labeled for perovskite phases (a) (naphthalene-O-ethyl- NH_3) $_2\text{PbI}_4$, (b) (naphthalene-O-propyl- NH_3) $_2\text{PbI}_4$, (c) (pyrene-O-ethyl- NH_3) $_2\text{PbI}_4$, (d) (pyrene-O-propyl- NH_3) $_2\text{PbI}_4$, (e) (pyrene-O-butyl- NH_3) $_2\text{PbI}_4$, (f) (perylene-O-ethyl- NH_3) $_2\text{PbI}_4$.

ing average cationic nitrogen to peripheral-iodide distance (d_{N-I}) (figure 4.8A). As d_{N-I} decreases, the electrostatic interaction between the cationic nitrogen and negatively-charged inorganic lattice increases, resulting in octahedral distortion and a higher E_{S_1} . The structural features of the organic cation must dictate d_{N-I} and thus influence the resulting electrostatic interaction. Understanding and harnessing the structural properties of the organic cation to influence E_{S_1} and the bandgap of the layered perovskite will be crucial to the further development of these materials.

As mentioned previously, the E_{S_1} values observed for the seven layered perovskites investigated here span 0.3 eV, a significant range for $n = 1$ layered perovskites. In most of these layered perovskites, the alkyl linker to the ammonium cation adopts an extended conformation within the organic galleries. However, this does not occur in (pyrene-O-propyl- NH_3) $_2\text{PbI}_4$ where we observe

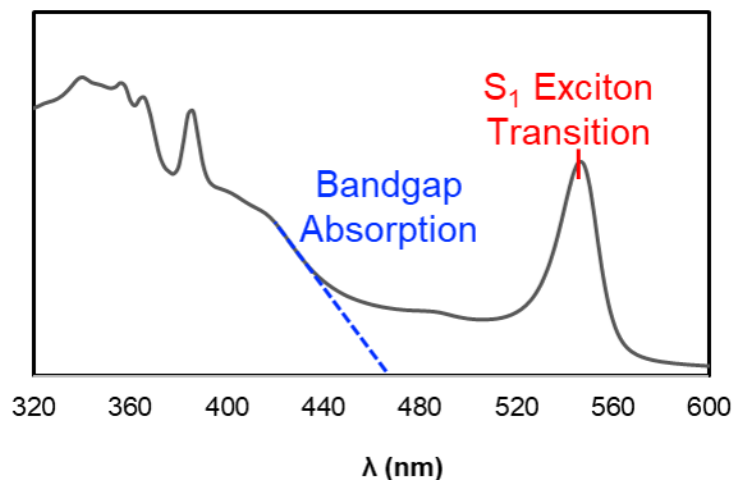


Figure 4.5: Annotated UV-Vis absorption spectra showing the two distinct characteristics of $n = 1$ lead iodide layered perovskite absorption spectra (Red) sharp excitonic absorption followed by a low cross section region of the spectrum followed by the bandgap absorption onset (Blue). Precise determination of bandgap is challenging from room temperature optical absorption so we will use track the S_1 exciton instead.

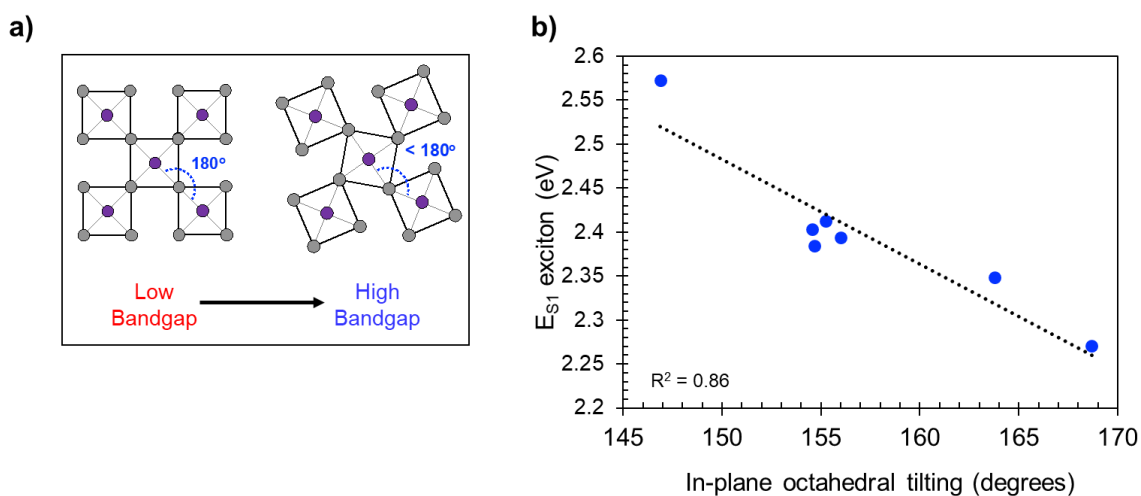


Figure 4.6: Octahedral distortion effects the bandgap (and S_1 exciton transition) in these materials. (a) as the Pb-I-Pb bond angles along the central plane decrease from the maximum 180° as a result of octahedral tilting, the bandgap in these materials is raised. (b) We observe the expected correlation between octahedral tilting and bandgap (measured by S_1 exciton energy) in the seven layered perovskites in this work.

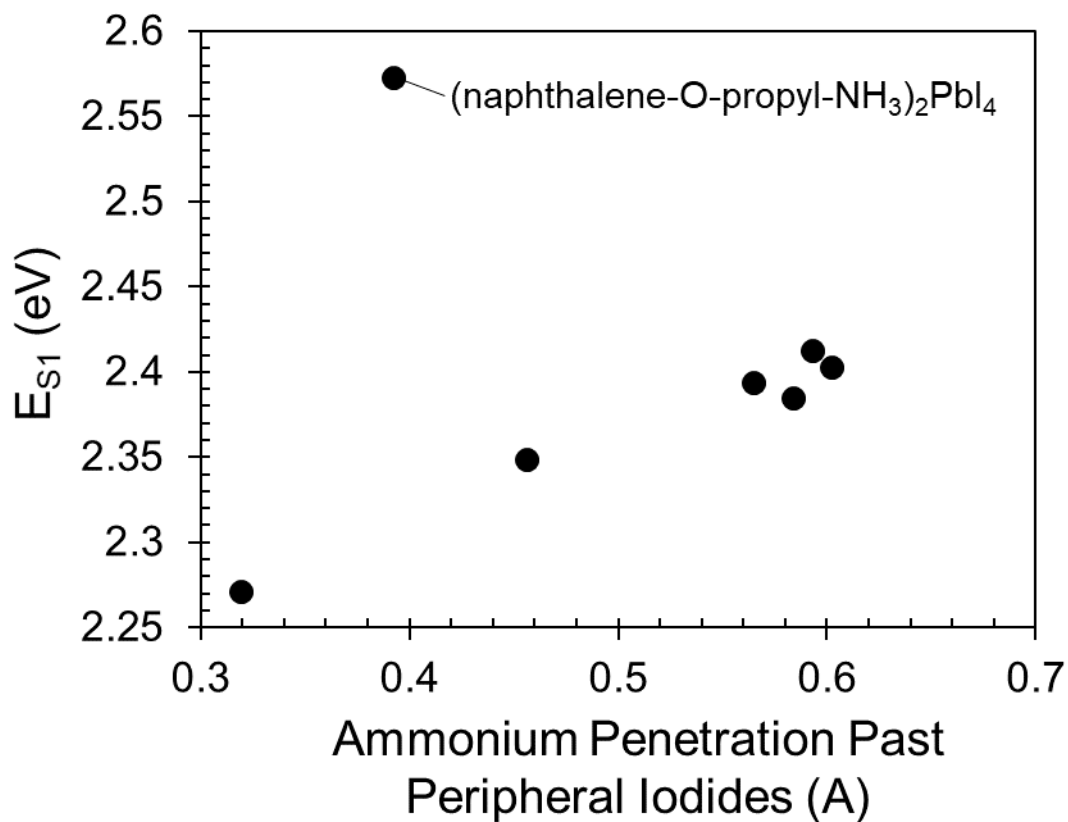


Figure 4.7: The energy of the S₁ exciton is plotted against the penetration distance of the nitrogen of the ammonium cation into the mean plane formed by the peripheral iodine of the octahedra. This trends well but the highest bandgap structure $(\text{naphthalene-O-propyl-NH}_3)_2\text{PbI}_4$ does not fit in this trend.

an intramolecular hydrogen bond between the ammonium cation and the ether linkage (figure 4.8B). This intramolecular hydrogen bond hinders the extended conformation of the alkyl linker resulting in just a 0.22 Å increase in the inorganic-to-inorganic layer spacing from (pyrene-O-ethyl-NH₃)₂PbI₄ to (pyrene-O-propyl-NH₃)₂PbI₄. This is compared to a 1.77 Å spacing increase from (pyrene-O-propyl-NH₃)₂PbI₄ to (pyrene-O-butyl-NH₃)₂PbI₄. The intramolecular hydrogen bond observed in (pyrene-O-propyl-NH₃)₂PbI₄ also appears to affect the d_{N-I} , resulting in the longest observed d_{N-I} and correspondingly the lowest E_{S1} of 2.27 eV. Interestingly, when crystallized as a thin film, the same pyrene-O-propyl-NH₃I molecule that creates (pyrene-O-propyl-NH₃)₂PbI₄ can form a different perovskite phase with a higher E_{S1} of 2.53 eV (figure 4.9). This high E_{S1} phase has a larger inorganic-to-inorganic layer spacing than (pyrene-O-propyl-NH₃)₂PbI₄, suggesting that the alkyl linker in this phase adopts a more extended conformation. This conformation may decrease the d_{N-I} and thus raise E_{S1} compared to (pyrene-O-propyl-NH₃)₂PbI₄ which contains an intramolecular hydrogen bond.

As noted previously, the naphthalene-O-propyl-NH₃I molecule can form both (naphthalene-O-propyl-NH₃)₂PbI₄ and (naphthalene-O-propyl-NH₃)₂PbI₄·(C₄H₆O₂)_{0.5}. These perovskites demonstrate a similar structural trend to the two layered perovskites formed by the pyrene-O-propyl-NH₃I molecule. The propyl linker in (naphthalene-O-propyl-NH₃)₂PbI₄ adopts an extended conformation and the material exhibits a high E_{S1} of 2.57 eV (figure 4.8C). The second layered perovskite, (naphthalene-O-propyl-NH₃)₂PbI₄·(C₄H₆O₂)_{0.5}, has a lower E_{S1} of 2.35 eV, and in two of the four molecules within the asymmetric unit of the crystal structure the propyl linker is disordered between two conformations. In one, it adopts an extended conformation, but in the other it exhibits the same type of intramolecular hydrogen bond observed in (pyrene-O-propyl-NH₃)₂PbI₄ (figure 4.8D). In both (naphthalene-O-propyl-NH₃)₂PbI₄·(C₄H₆O₂)_{0.5} and (pyrene-O-propyl-NH₃)₂PbI₄, the propyl linker can form a six-membered intramolecular ring when the ammonium cation hydrogen bonds to the aromatic ether. When this intramolecular hydrogen bonding occurs it reduces the optical bandgap by increasing d_{N-I} within the structure.

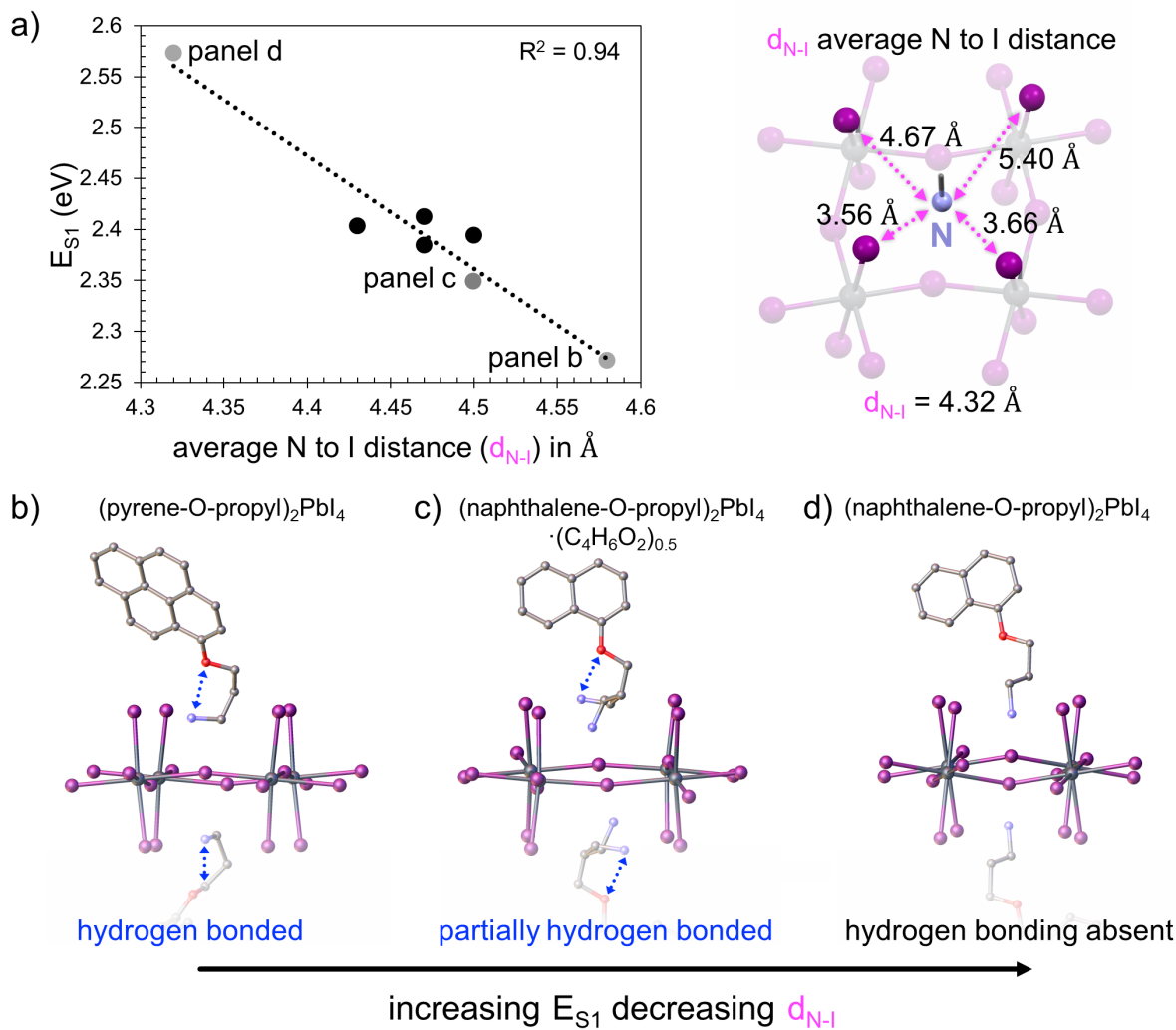


Figure 4.8: (a) Energy of the S₁ exciton vs. average distance between the nitrogen cation and the peripheral iodides of the inorganic layers (d_{N-I}) (left); (naphthalene-O-propyl-NH₃)₂PbI₄ structure showing with dashed lines the four different N-I distances used to calculate d_{N-I} (right). Crystal structures showing intramolecular hydrogen bonding (if present) for (b) (pyrene-O-propyl-NH₃)₂PbI₄, (c) (naphthalene-O-propyl-NH₃)₂PbI₄·(C₄H₆O₂)_{0.5}, and (d) (naphthalene-O-propyl-NH₃)₂PbI₄. Note that the presence of an intramolecular hydrogen bond in the crystal structure acts to increase d_{N-I} and reduce E_{S1} .

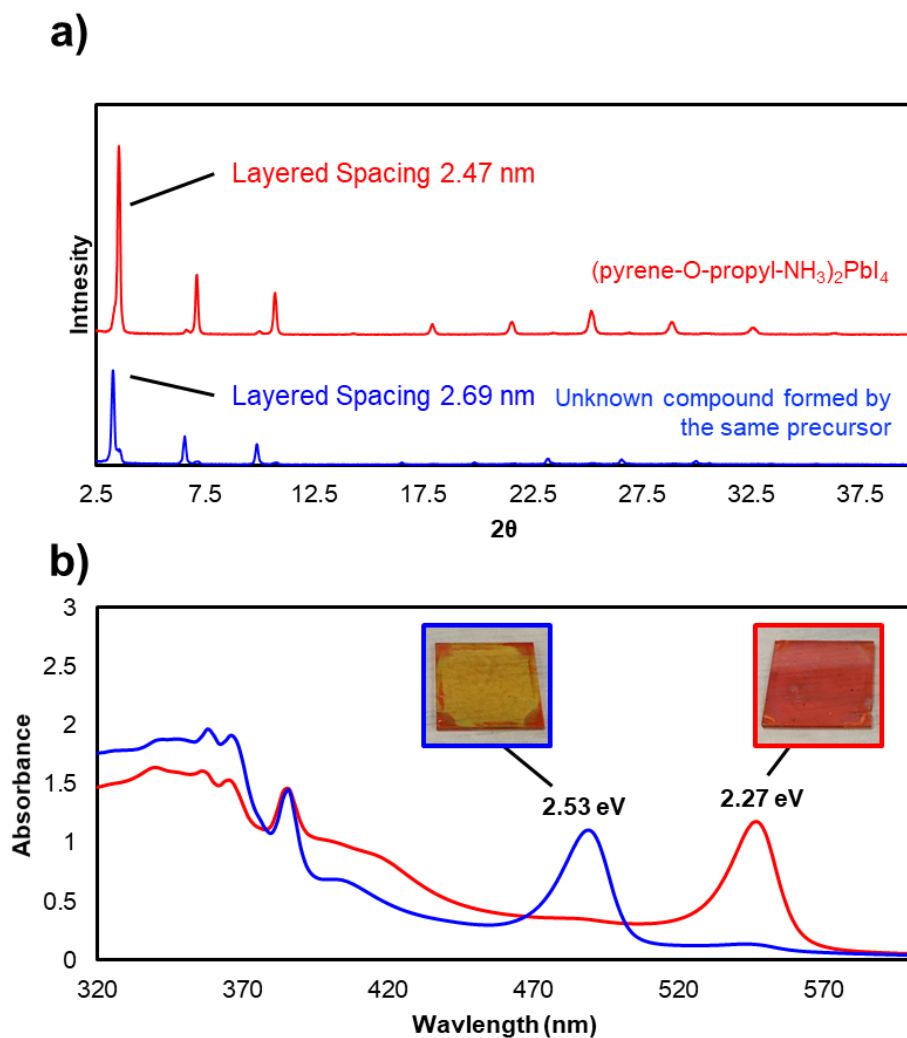


Figure 4.9: Two phases of that the pyrene-O-propyl-NH₃I molecule can make in thin film the first (pyrene-O-propyl-NH₃)₂PbI₄ (red line) has been crystallized and the structure is reported in this work but there is another high bandgap phase (blue line) which appears in thin film. (a) XRD of two thin film phases showing a larger d-spacing in the unknown yellow phase and (b) UV-Vis absorption of the two thin film materials.

These results demonstrate the structural role that the organic cation can play in dictating the optical properties of the resultant perovskite and suggests new strategies to tune the optoelectronic properties by influencing d_{N-I} through intramolecular bonding and steric control.

4.3.3 *Out-of-plane conductivity*

To investigate how the electronic character of the organic cation affects out-of-plane conductivity, we measured the relative out-of-plane conductivity along the layered axis of single crystals for all of the layered perovskites reported in this work (except (naphthalene-O-propyl-NH₃)₂PbI₄·(C₄H₆O₂)_{0.5} due to the small sizes of crystals) as well as three aliphatic control crystals ((butyl-NH₃)₂PbI₄, (hexyl-NH₃)₂PbI₄, and (octyl-NH₃)₂PbI₄). These measurements were carried out using the devices described in figure 4.10A, which used single crystals in order to eliminate the effects of grain boundaries on conductivity. These measurements were performed on multiple devices per crystal as well as multiple crystals of the same layered perovskite. The conductivity results show that the median conductivity spans close to four orders of magnitude, and the results are summarized in figure 4.10B (under illumination) and figure 4.11 in the dark. Generally, layered perovskites containing aliphatic cations were found to have the lowest conductivity, followed closely by the naphthalene-containing layered perovskites. Layered perovskites with pyrene and perylene cations were found to have substantially higher conductivity than those containing aliphatic moieties. This trend in conductivity mirrors the better alignment of energy levels between perylene and pyrene and the inorganic lattice (figure 4.1C). This result indicates that the electronic character of the aromatic moieties within the organic galleries can be utilized to enhance out-of-plane conductivity in these materials.

In the design of these molecules we included a variable linker length to study the effect of spacing between aromatic moieties and inorganic layers on out-of-plane conductivity. When comparing the three aliphatic controls and (naphthalene-O-propyl-NH₃)₂PbI₄ we found that their conductivities are on the same order of magnitude with a slight trend towards lower out-of-plane conduc-

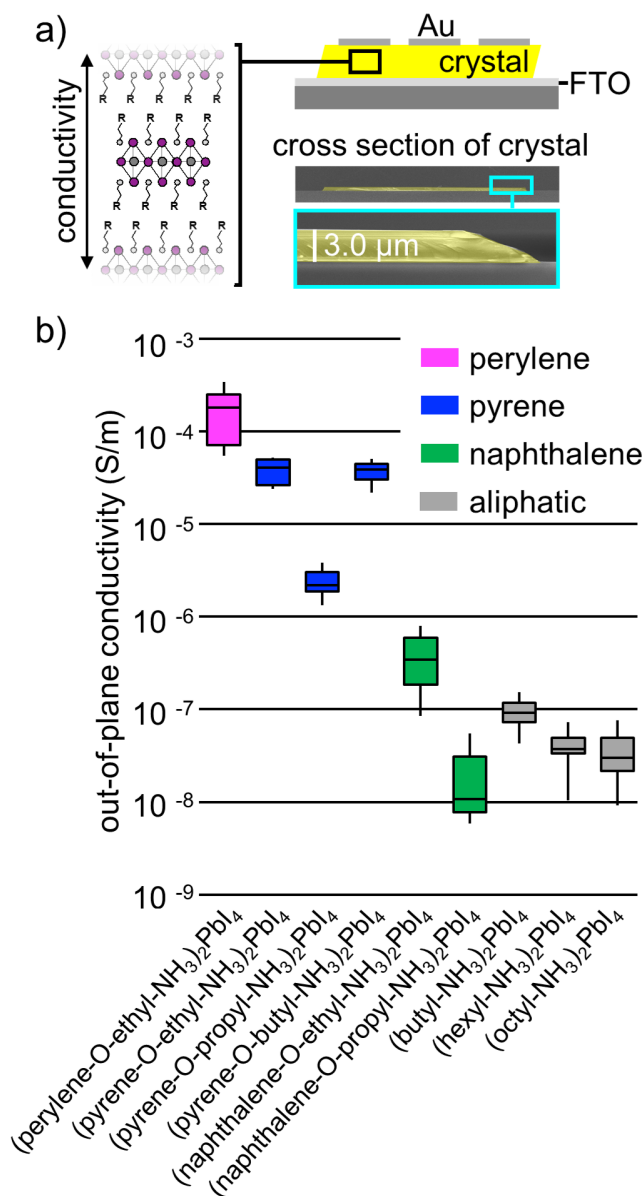


Figure 4.10: (a) Schematic representation of the layered perovskite indicating the direction of conductivity measurements (left), and schematic of the device used to measure the out-of-plane conductivity and a colorized SEM of a single crystal drop-cast on a silicon wafer cleaved to reveal the cross section (right) (note the crystal is flat over its width (0.5 mm) and makes good contact with the substrate). (b) Conductivity of nine different $n = 1$ layered perovskite with either an aliphatic cation or cation containing naphthalene, pyrene, or perylene (higher conductivity is observed for the pyrene and perylene samples which possess better energy level alignment with the inorganic lattice). FTO refers to fluorine-doped tin oxide.

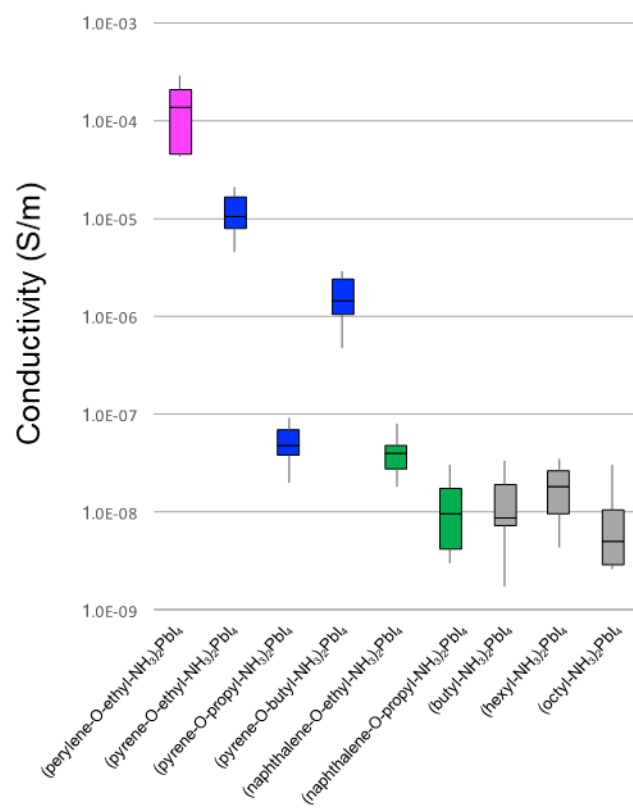


Figure 4.11: Conductivity measured in the absence of light. Enhanced conductivity is observed in samples with better energy level matching of the aromatic moiety to the inorganic layer.

tivity with increasing inorganic-to-inorganic layer spacings (figure 4.12). Interestingly, a different trend was observed for layered perovskites containing pyrene. In this subset of layered perovskites, (pyrene-O-ethyl-NH₃)₂PbI₄ and (pyrene-O-butyl-NH₃)₂PbI₄ have effectively the same high conductivity of 4×10^{-5} S/m, while the conductivity of (pyrene-O-propyl-NH₃)₂PbI₄ is 2×10^{-6} S/m which is considerably lower. This indicates that there is an additional structural aspect that is more significant than just the spacing between the inorganic layer and the aromatic core. Examination of crystal structures for the three pyrene-containing layered perovskites indicates that in the higher conductivity (pyrene-O-ethyl-NH₃)₂PbI₄ and (pyrene-O-butyl-NH₃)₂PbI₄ the organic cations exhibit edge-to-face type π -stacking interactions when viewed down the layered axis across the Van der Waals gap (figure 4.13A and B). However, for the lower conductivity (pyrene-O-propyl-NH₃)₂PbI₄, an edge-to-edge arrangement was observed in the crystal structure (figure 4.13C).

Similar to the pyrene-containing layered perovskites, there is a significant difference in out-of-plane conductivity between the two naphthalene-containing layered perovskites. The lowest conductivity sample of all the layered perovskites measured was (naphthalene-O-propyl-NH₃)₂PbI₄ which has a conductivity of 1×10^{-8} S/m, while (naphthalene-O-ethyl-NH₃)₂PbI₄ has a significantly higher conductivity of 3×10^{-7} S/m. In the higher conductivity (naphthalene-O-ethyl-NH₃)₂PbI₄ we observe edge-to-face type interactions (figure 4.13d), whereas in the lower conductivity (naphthalene-O-propyl-NH₃)₂PbI₄ the structure reveals a staggered edge-to-edge stacking. This trend between the type of packing across the Van der Waals gap and out-of-plane conductivity is the same as in the pyrene-containing layered perovskites. Lastly, (perylene-O-ethyl-NH₃)₂PbI₄ shows edge-to-edge type interactions (figure 4.14) although it has the highest recorded out-of-plane conductivity of all the layered perovskites studied here. We attribute this to a better energy level alignment with the inorganic lattice compared to materials containing the pyrene, naphthalene, or aliphatic cations.

The results described above suggest that in addition to the electronic character of the aromatic moiety, their structural arrangement within the organic galleries plays a role in the observed out-

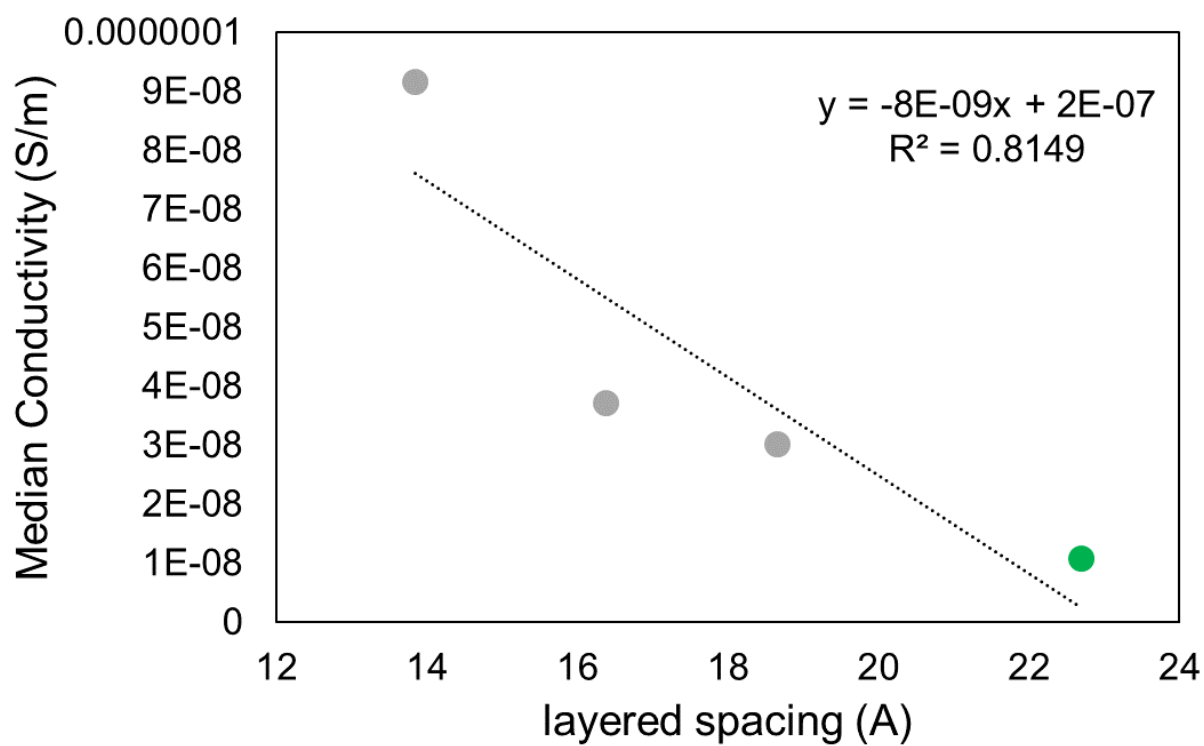


Figure 4.12: Trend between median out-of-plane conductivity and layered spacing for four layered perovskites measured in this study. From smallest to largest layered spacing these are $(\text{butyl-NH}_3)_2\text{PbI}_4$, $(\text{hexyl-NH}_3)_2\text{PbI}_4$, $(\text{octyl-NH}_3)_2\text{PbI}_4$, and $(\text{naphthalene-O-propyl-NH}_3)_2\text{PbI}_4$.

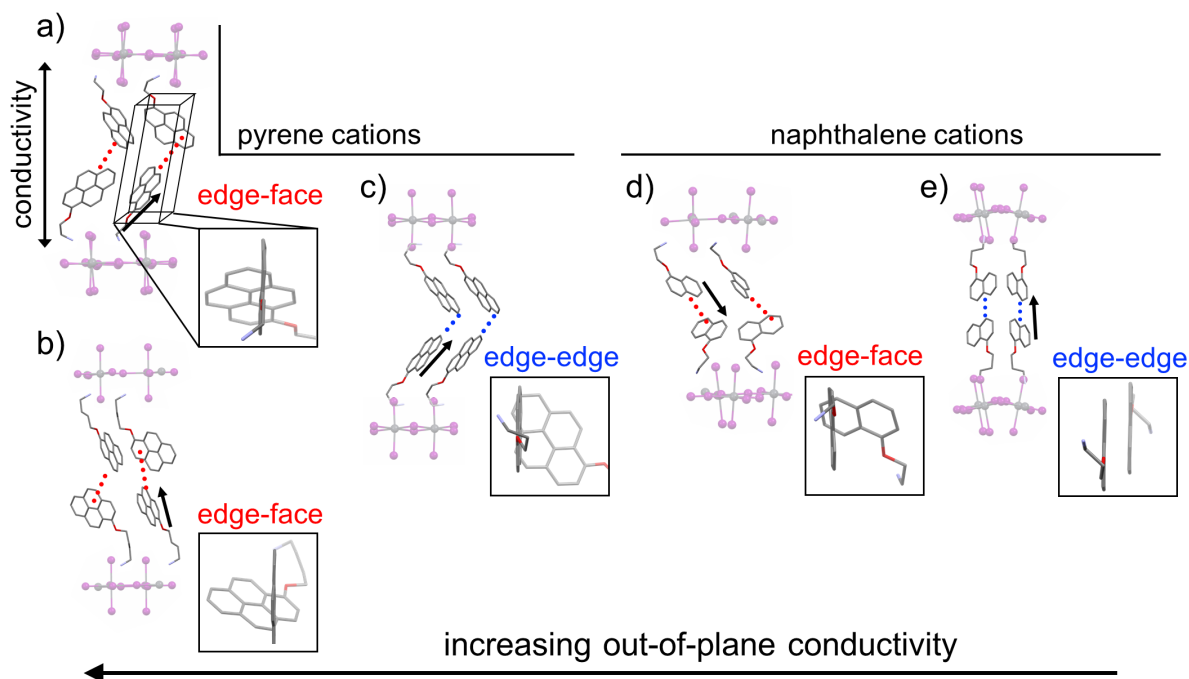


Figure 4.13: Crystal structures of $n = 1$ layered perovskites ranked from left to right by highest out-of-plane conductivity to lowest where the structures in panels a and b have similar conductivity values: (a) (pyrene-O-ethyl- NH_3) $_2\text{PbI}_4$, (b) (pyrene-O-butyl- NH_3) $_2\text{PbI}_4$, (c) (pyrene-O-propyl- NH_3) $_2\text{PbI}_4$, (d) (naphthalene-O-ethyl- NH_3) $_2\text{PbI}_4$, and (e) (naphthalene-O-propyl- NH_3) $_2\text{PbI}_4$. The stacking of aromatic cores is highlighted with dashed lines within the organic galleries and the square inserts show a view down the layered axis from the perspective of an eclipsed aromatic core (viewing direction is denoted by the black arrow in the crystal structures).

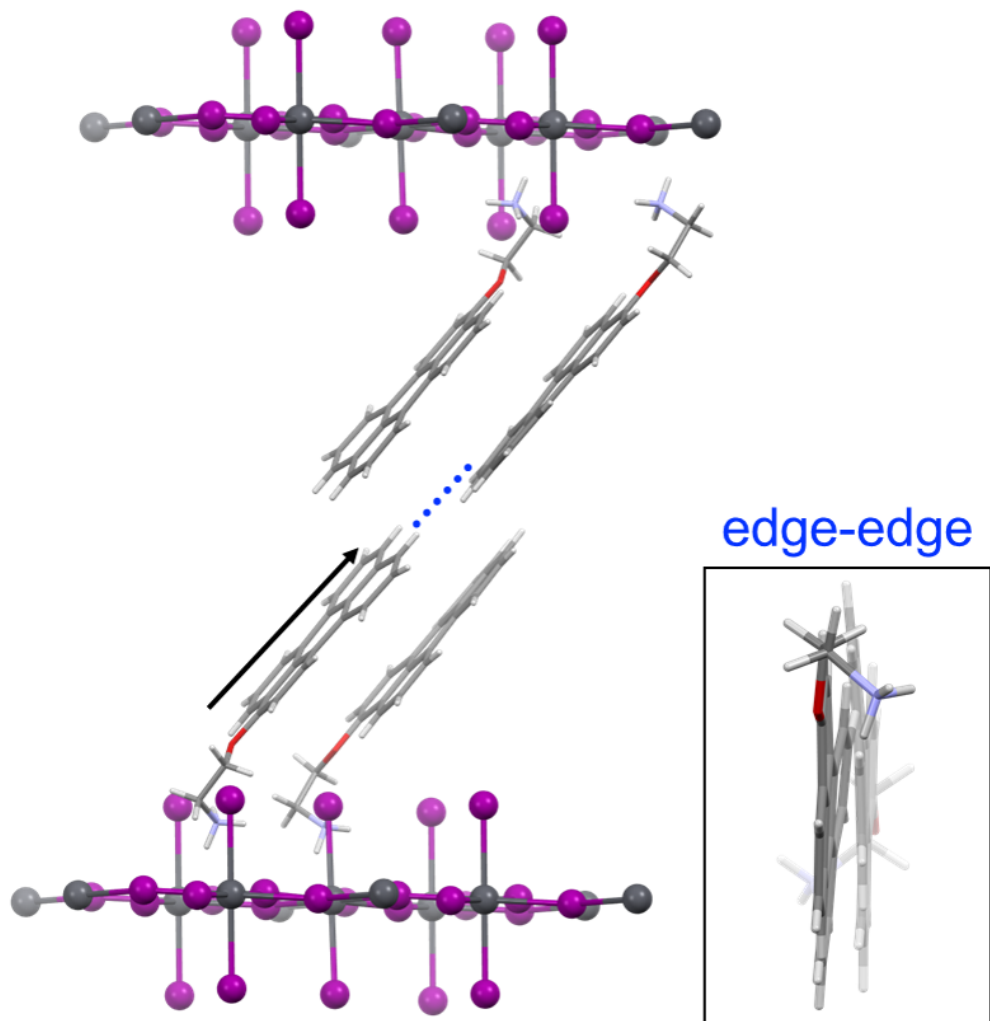


Figure 4.14: Crystal structure of (perylene-O-ethyl-NH₃)₂PbI₄ showing edge-to-edge type stacking across the van der Waals gap. This compound maintains the highest reported conductivity likely due to its amiable HOMO/LUMO levels.

of-plane conductivity. Specifically, edge-to-face interactions across the Van der Waals gap yield enhanced conductivity compared to edge-to-edge interactions. This is likely due to better orbital overlap of the aromatic moieties and thus more efficient out-of-plane charge transport. This observation implies that future efforts to improve conductivity need to focus on how one controls the spatial arrangements of electronically active cations within the perovskite crystal. Finding strategies to further enhance orbital overlap possibly through face-to-face interactions may further improve out-of-plane conductivity.

4.3.4 *Device fabrication and photovoltaic performance*

Given that poor out-of-plane conductivity is the chief limitation to the application of $n = 1$ layered perovskites in photovoltaic devices, the higher-conductivity layered perovskites in this work should exhibit enhanced photovoltaic device performance. Photovoltaic performance is of course also affected by optical absorption, crystallinity, and morphology of the active layer. Thus, we chose to focus on (pyrene-O-propyl-NH₃)₂PbI₄ for photovoltaic devices since it has the lowest energy S₁ exciton and therefore its absorption better matches the solar spectrum. Although this layered perovskite did not have the highest conductivity, it offered the best balance of properties for photovoltaic performance. As noted previously, thin films of (pyrene-O-propyl-NH₃)₂PbI₄ can crystallize into two different phases, and thus we selected annealing conditions (140 °C for 1 minute) that resulted in exclusive formation of (pyrene-O-propyl-NH₃)₂PbI₄ rather than the higher E_{S1} phase.

Our best reproducible device architecture (figure 4.15A) using (pyrene-O-propyl-NH₃)₂PbI₄ achieved a power conversion efficiency (PCE) of $1.16 \pm 0.08\%$ with a champion device performance of 1.24% (figure 4.15B). These devices had a Voc of 1.07 V, Jsc of 2.48 mA/cm², and fill factor of 0.44 across 4 devices. To our knowledge, this is the highest reported PCE for an $n = 1$ layered perovskite solar cell. This result is noteworthy given that grazing-incidence wide-angle X-ray scattering (GIWAXS) of our thin films shows a clear preferential orientation of the inorganic layers parallel to the substrate (figure 4.15C), while the previously-reported highest-efficiency $n = 1$ de-

vice had inorganic layers oriented perpendicular to the substrate.⁹⁹ Furthermore, our device is an order of magnitude higher efficiency than any other reported $n=1$ layered perovskite with the inorganic layers oriented parallel to the substrate. With respect to charge transport layers, a low work function PEDOT:PSS formulation was used for better energy level alignment with the active layer, and no electron transport layer was added because the pyrene-O-propyl-NH₃I molecule forms a native electron-transporting capping layer on the top surface of the active layer. A more detailed discussion of this capping layer, each device layer, device optimization, and UPS measurements are included as supporting information (figure 4.16).

The energy level alignment of the charge transport layers in $n = 1$ layered perovskite solar cells is crucial to optimize the power conversion efficiency (PCE). We therefore selected poly(3,4-ethylenedioxythiophene):polystyrene sulfonate (PEDOT:PSS) as the hole transport layer for the devices. Multiple formulations of PEDOT:PSS are commercially available which allows for some tunability of the work function of this material. Ideally, a hole transport layer for $n = 1$ layered perovskites would have a shallower work function than that of the most common formulation of PEDOT:PSS (Clevios AL 4083) because the HOMO level of (pyrene-O-propyl-NH₃)₂PbI₄ is shallower than the work function of PEDOT:PSS (5.2 eV) (figure 4.15A). We found that a different PEDOT:PSS formulation (HTL solar 3, referred to as PEDOT:complex) has a work function (4.4-4.8eV) much closer to the HOMO level of typical $n=1$ layered perovskites. We fabricated devices with (pyrene-O-propyl-NH₃)₂PbI₄ as the active layer using both PEDOT:PSS and PEDOT:complex because our initial investigation revealed that PEDOT:PSS devices were functional despite poor energy level alignment. For comparison of various active layers and electron transport layers, we used PEDOT:PSS, and then for our best devices we used PEDOT:complex. Typical charge transport layers in photovoltaic devices were not designed for active layers with such large bandgaps ($>2.2\text{eV}$) and shallow HOMO levels, but both PEDOT:PSS formulations functioned to block electrons at the ITO contact in our devices. Additional efforts to develop charge transport layers will be required if $n = 1$ layered perovskites are going to be developed for single junction or tandem photovoltaic

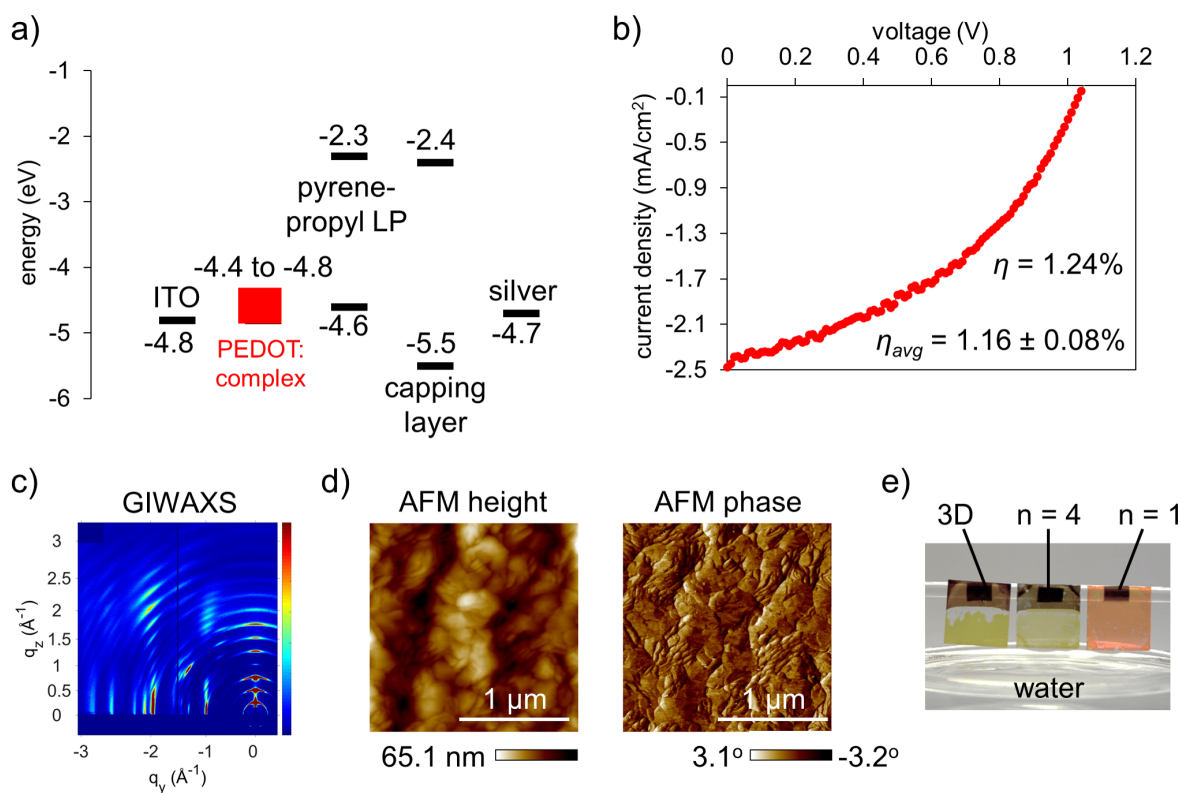


Figure 4.15: (a) Energy levels of the layers in the $(\text{pyrene-O-propyl-NH}_3)_2\text{PbI}_4$ layered perovskite solar cell. (b) I-V curve for the champion device with 1.24% efficiency (only forward sweep is shown for clarity but the average includes forward and reverse curves where little hysteresis was observed). (c) Grazing-incidence wide-angle X-ray scattering of $(\text{pyrene-O-propyl-NH}_3)_2\text{PbI}_4$ crystallized on a PEDOT:PSS-coated substrate. (d) AFM height and phase images for $(\text{pyrene-O-propyl-NH}_3)_2\text{PbI}_4$ crystallized on PEDOT:PSS. (e) Comparison of dipping three substrates in water: the 3D perovskite with the formula $(\text{CH}_3\text{NH}_3)\text{PbI}_3$, $n = 4$ layered perovskite with the formula $(\text{butyl-NH}_3)_2(\text{CH}_3\text{NH}_3)_3\text{Pb}_4\text{I}_{13}$, and $n = 1$ layered perovskite $(\text{pyrene-O-propyl-NH}_3)_2\text{PbI}_4$. Perovskites containing the methylammonium cation degrade as soon as immersed.

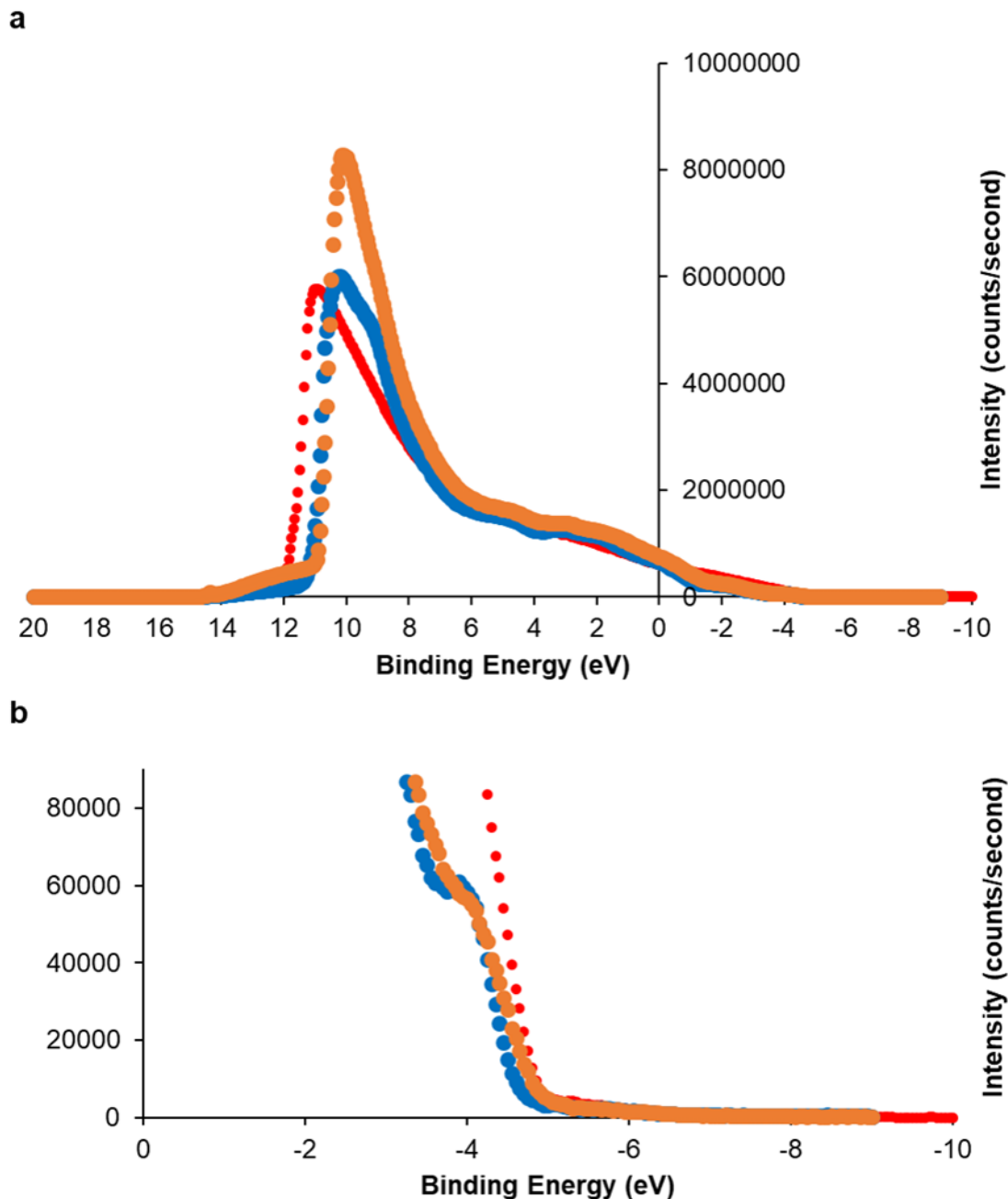


Figure 4.16: UPS spectra of the $(\text{pyrene-O-propyl-NH}_3)_2\text{PbI}_4$ freshly cast (Orange) compared to $(\text{pyrene-O-propyl-NH}_3)_2\text{PbI}_4$ etched for 10 minutes using an argon plasma etch (red) and compared to the pyrene-O-propyl-NH₃I molecule (blue). (a) shows the entire spectrum, and (b) shows a zoom-in on the low binding energy onset. There is a significant difference in the width of the binding energy curve which is clearly shown by the shift of the etched sample (red) curve near 12 eV with respect to the other two (fresh $(\text{pyrene-O-propyl-NH}_3)_2\text{PbI}_4$ and molecule alone).

devices in the future. When we use PEDOT:PSS instead of PEDOT:complex for the hole transport layer, we achieved somewhat lower performance devices. For PEDOT:PSS devices, we achieved a PCE of $0.7 \pm 0.08\%$ with a champion device of 0.8%, an average V_{oc} of 1.12 V, J_{sc} of 1.58 mA/cm², and fill factor of 0.4 across 7 devices. The J_{sc} is significantly decreased when the energy levels are misaligned between the HOMO level of the perovskite and work function of the hole transport layer. The HOMO level of (pyrene-O-propyl-NH₃)₂PbI₄ was determined using ultraviolet photoelectron spectroscopy (UPS). In this process, we discovered that there is likely a thin layer of the pyrene-O-propyl-NH₃I molecule that resides on the surface of the layered perovskite. The as-synthesized thin-film perovskite has a HOMO level at -5.5 eV, which matches that of the pyrene-O-propyl-NH₃I molecule when measured independently (Fig. S10). After removing this layer using a plasma etch, the HOMO level of the underlying material was found to be -4.6 eV, which is in the range of typical $n = 1$ layered perovskites. This thin layer of the pyrene-O-propyl-NH₃I molecule that resides at the top surface of the active layer acts as an intrinsic electron transport layer. This intrinsic electron transport layer may explain why the short circuit current (J_{sc}) and open circuit voltage (V_{oc}) are reduced when an additional electron transport layer, such as phenyl-C₆₁-butyric acid methyl ester (PCBM), is added on top of the active layer (Table 4.24).

In our devices, the metal cathode material is important to achieving high V_{oc} . We initially tried gold as the contact material because of its stability, but the V_{oc} in our devices with gold was limited to about 0.75 V. Because (pyrene-O-propyl-NH₃)₂PbI₄ has such a high LUMO level, shallow work function metals would be ideal to make contact with the active layer. However, reactivity with iodine in air is a significant problem for shallow work function metals such as calcium, aluminum, and titanium in halide perovskites.¹¹¹ The reaction between iodine and these metals was observed to be nearly instantaneous, leading to poor photovoltaic devices. Ultimately, we chose silver as the cathode material as a compromise between stability and work function alignment. Silver still reacts with the layered perovskite active layer, but on a time scale of hours rather than seconds. This provides enough time to make and test $n=1$ photovoltaic devices and observe V_{oc} values as high as

	Overlayer	J_{sc} (mA/cm²)	Voc (V)	Fill Factor	Efficiency (%)
(pyrene-O-propyl-NH ₃) ₂ PbI ₄	None (native capping layer)	1.58	1.12	0.40	0.7 ± 0.08
(pyrene-O-propyl-NH ₃) ₂ PbI ₄	4000RPM 1-propoxypyrene, 5mg/mL in chlorobenzene	1.32	1.035	0.34	0.46
(pyrene-O-propyl-NH ₃) ₂ PbI ₄	2000 RPM PCBM, 16mg/mL in chlorobenzene	1.31	0.875	0.35	0.40
(butyl-NH ₃) ₂ PbI ₄ perovskite	4000RPM 1-propoxypyrene, 5mg/mL in chlorobenzene	0.15*	0.39*	0.50*	0.030*
(butyl-NH ₃) ₂ PbI ₄ perovskite	2000 RPM PCBM, 16mg/mL in chlorobenzene	0.047	0.26	0.30	0.0037

Table 4.2: Photovoltaic parameters for control devices comparing the (pyrene-O-propyl-NH₃)₂PbI₄ to (butyl-NH₃)₂PbI₄ perovskite with 1-propoxypyrene and PCBM overlayers * indicates reverse sweep only

1.3 V. With respect to active layer optimization, we identified that the stoichiometry of precursors, annealing conditions, and film thickness were critical to obtain reproducible and high-performance devices. A stoichiometric imbalance of the ammonium iodide salt and lead (II) iodide that deviated from the ideal ratio of 2:1 by as little as 3 mol% was enough to significantly decrease device performance. We also found that a short annealing time (1 minute) was important to device performance. Longer annealing times do not significantly change the crystallinity of the thin films because of the poor diffusion of both the lead (II) iodide and pyrene-O-propyl-NH₃I molecule and intermediates, but the initial device performance as well as electrode stability is significantly reduced with longer annealing times. Devices that are annealed for longer times maintain a high Voc, while Jsc is decreased significantly as compared to shorter annealing times. This difference in device performance is likely due to decomposition of the pyrene-O-propyl-NH₃I molecule either within the crystals or in the capping layer. With respect to device thickness, thinner films generally performed better, but reducing the concentration of the precursor solution resulted in poorly crystalline thin films, thus

the optimized devices required a compromise between lowering the concentration and increasing spin speed in order to minimize film thickness while maintaining crystallinity.

The PCE of our devices using (pyrene-O-propyl-NH₃)₂PbI₄ is at least an order of magnitude higher than control devices with (butyl-NH₃)₂PbI₄ as the active layer using the same device architecture (Table S4). The (butyl-NH₃)₂PbI₄ device required a charge transport layer to achieve photovoltaic function because butylammonium iodide does not form an electron-transporting capping layer on the surface of the active layer, unlike (pyrene-O-propyl-NH₃)₂PbI₄. Thus, to compare the two layered perovskites, we added a thin layer of 1-propoxypyrene on both (pyrene-O-propyl-NH₃)₂PbI₄ and (butyl-NH₃)₂PbI₄ active layers to mimic the native electron transport layer on the (pyrene-O-propyl-NH₃)₂PbI₄ active layer. These control devices demonstrate that 1-propoxypyrene functions as an electron transport for layered perovskite active layers, and that in this device architecture (pyrene-O-propyl-NH₃)₂PbI₄ performs significantly better than (butyl-NH₃)₂PbI₄ as a photovoltaic active layer.

As previously discussed, GIWAXS was utilized to compare the orientation of the crystalline domains in these thin films. In both (pyrene-O-propyl-NH₃)₂PbI₄ and the (butyl-NH₃)₂PbI₄ (figure 4.17), the films were found to be crystalline and oriented with the 2D layers parallel to the substrate. We analyzed the orientation of the thin films using Herman's orientation factor S to define orientational ordering.¹¹² An S value of 1 indicates perfect parallel orientation of domains, S = 0 indicates isotropic domains, and S = -0.5 indicates perfect perpendicular orientation of domains. By analyzing data along the azimuthal angle χ from 0 to 90 degrees within the q range of the (600) peak of (pyrene-O-propyl-NH₃)₂PbI₄ we found that S = 0.95, and within the q range of the (002) peak of (butyl-NH₃)₂PbI₄ we found that S = 0.97. This indicates strong alignment of the layered axis parallel to the substrate for both thin films. From the line cuts we performed Herman's orientation factor analysis on the (600) peak of (pyrene-O-propyl-NH₃)₂PbI₄ and the (002) peak of the

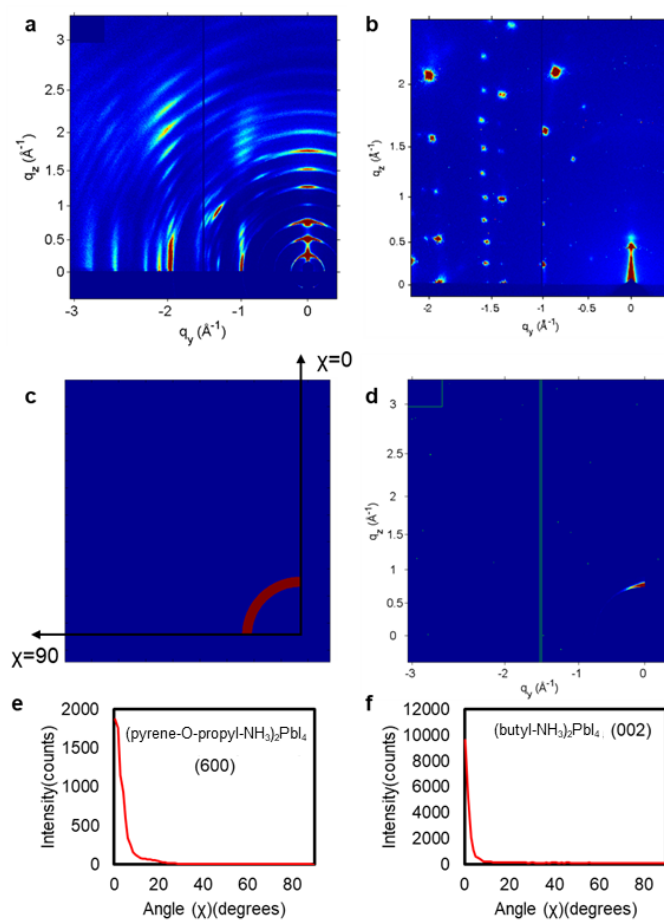


Figure 4.17: 2D-GIWAXS images of (a) (pyrene-O-propyl-NH₃)₂PbI₄ and (b) (butyl-NH₃)₂PbI₄ layered perovskites. (c) and (d) show the line cut mask and line cut area for the (pyrene-O-propyl-NH₃)₂PbI₄ data from $0 < \chi < 90$ and $0.75 < q < 0.9$, and (e) shows the integrated line cut from this area of the image. (f) shows a similar line cut from the (002) peak of the (butyl-NH₃)₂PbI₄ perovskite.

(butyl-NH₃)₂PbI₄ perovskite. In this analysis, we define:

$$S = \frac{1}{2}(3f_{\perp} - 1)$$

$$f(\chi) = \int_0^{\frac{\pi}{2}} \cos^2(\chi) \cdot f(\chi) d\chi$$

where $f(\chi)$ = our normalized linecut intensity. We normalize our linecut intensity, $\int_0^{\frac{\pi}{2}} f(\chi) d\chi = 1$ and in the case of the (butyl-NH₃)₂PbI₄ perovskite we perform a flat background subtraction due to higher background intensity in that data. From this analysis we find that for (pyrene-O-propyl-NH₃)₂PbI₄ $S = 0.95$ and for (butyl-NH₃)₂PbI₄ perovskite $S = 0.97$ indicating that both have layered domains aligned parallel to the substrate surface. When analyzed by atomic force microscopy, thin films of (pyrene-O-propyl-NH₃)₂PbI₄ exhibit significant roughness and small grain sizes (Figure 4.15D). This is potentially caused by the low diffusivity of the bulky organic cation during the annealing process. The small grain size observed with this technique may explain some of the azimuthal peak broadening observed in GIWAXS. Importantly, the active layer in these devices is chemically-stable. Although the complete devices suffer from limited stability in atmospheric conditions due to reactions between the active layer and the cathode material, the active layer itself is exceptionally stable; it can withstand immersion in water for several minutes without any decomposition to lead (II) iodide (figure 4.18). This property is unique when compared to the prototypical 3D perovskite (CH₃NH₃)PbI₃ and the $n = 4$ layered perovskite (butyl-NH₃)₂(CH₃NH₃)₃Pb₄I₁₃ (Figure 4.15E and 4.19).

4.4 CONCLUSIONS AND FUTURE OUTLOOK

We have introduced an approach to enhance the out-of-plane conductivity in chemically-stable $n = 1$ layered perovskites using energy level matching of the conjugated organic layers with the inorganic layers. This increased out-of-plane conductivity by several orders of magnitude relative to

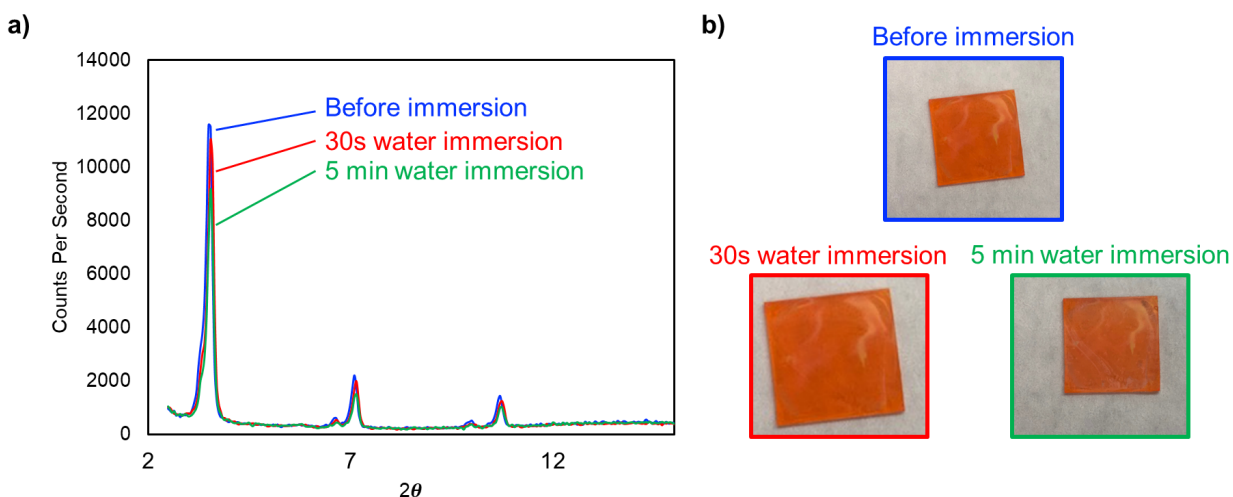


Figure 4.18: X-ray characterization of thin films of $(\text{pyrene-O-propyl-NH}_3)_2\text{PbI}_4$ before DI water immersion and after 30 seconds and 5 minutes of water immersion. (b) corresponding photographs. Notice that there is no appearance of the lead (II) iodide in the X-ray signature. Slight reduction in intensity is due to slow dissolution of film into water.

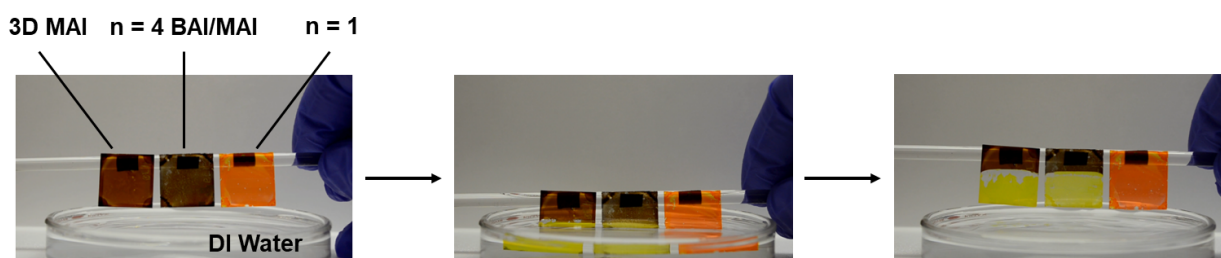


Figure 4.19: Comparison of dipping the $n = 4$ layered perovskite $(\text{butyl-NH}_3)_2(\text{CH}_3\text{NH}_3)_3\text{Pb}_4\text{I}_{13}$ (left), the 3D methylammonium lead triiodide perovskite $(\text{CH}_3\text{NH}_3)\text{PbI}_3$ (center) and $n = 1$ $(\text{pyrene-O-propyl-NH}_3)_2\text{PbI}_4$ (right). Perovskites containing the methylammonium cation are degraded as soon as immersed (center frame taken immediately after immersion). The $n = 1$ compound remains intact even after several minutes.

traditional aliphatic layered perovskite structures. When applied to a photovoltaic device, we observed the highest reported power conversion efficiency (1.24%) for any $n = 1$ layered perovskite. Additionally, this study revealed two key structure-property relationships between cation conformation and optoelectronic properties. First, hydrogen bonding within the organic galleries can be used to avoid distortions of the inorganic lattice, resulting in narrower bandgaps. Second, out-of-plane conductivity in layered perovskites is enhanced by favorable π -stacking interactions within the organic galleries.

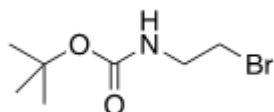
While a vast amount of effort has gone into optimizing nearly every other aspect of perovskite photovoltaics, this work demonstrates the potential of utilizing organic synthesis to improve the function of the chemically-stable 2D layered form of these materials. There are two follow-up studies that could be readily done on this set of layered perovskites within the scope of what has already been demonstrated in the literature. First, it should be relatively straightforward to make higher- n ($n = 2,3,4$) layered perovskites to make higher-efficiency devices. In fact, we have begun work on $n = 2$ layered perovskites, and they maintain better stability in water than $n = 2$ devices that use aliphatic bulky cations. Furthermore, the crystal structure of the $n = 2$ (pyrene-O-propyl-NH₃)₂MAPbI₇ appears to maintain the intramolecular hydrogen bonding and red-shifted E_{S1} exciton absorption feature that we observed in the (pyrene-O-propyl-NH₃)₂PbI₄. The PCE of these devices is preliminarily higher than what we have observed in the (pyrene-O-propyl-NH₃)₂PbI₄ devices, but the expectation in higher- n devices is that they will have a significantly higher PCE. Another related study using the layered perovskites that we developed would be to explore the effect of orientation on conductivity in these materials. The use of a hot-casting technique to alter the orientation of the grains in thin film has been a breakthrough in ruddlesden-popper high- n layered perovskite solar cells. Our study has shown that reorienting these structures may not be strictly necessary to improve efficiency, but it does not exclude the possibility that reorienting the crystalline domains with respect to the substrate surface could still improve the charge transport properties in the PV device. It would be a great step forward in understanding charge transport in these materials if, in

addition to PV devices, we were able to both model the band structure in these crystals as well as measure their anisotropic charge transport properties in more detail.

Future efforts using the approach outlined in this work could leverage these structure-property relationships to design new organic cations that further improve charge transport and photovoltaic performance in these systems. One of the hypotheses that we had at the outset of this project was that only cations of a certain size and linker length would form a layered perovskite structure. However, almost every molecule that we synthesized for this project formed a layered perovskite structure. Therefore, there is a great deal of flexibility in the molecules that could be used in future studies examining layered perovskite crystals. The perylene-containing ammonium salts used in this study have approached the upper size limit in terms of both solubility and lateral dimensions, but there are still many molecules that could be synthesized to fit into this space. A modeling approach may yield more potential candidates for synthesis of novel layered perovskites.

4.5 MATERIALS AND METHODS

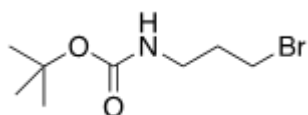
4.5.1 *Synthesis*



2-(Boc-amino)ethyl bromide (1): To a 1L round bottom flask was added 20g (97.6 mmol) of 1-Bromoethylamine hydrobromide (Sigma-Aldrich) a stir bar and 400 mL of dichloromethane (DCM). To this was added 10.8g (107.4 mmol) of triethylamine (TEA) and the solution was stirred at room temp (RT) until all of the solid dissolved. To this was added di-tert-butyl dicarbonate (Oakwood Chemical) 18.05 g (82.9 mmol) in one portion. The flask was then loosely capped with a rubber septum that contained two 18G needles to release CO₂ produced in the reaction. The reaction was allowed to stir at RT overnight under ambient atmosphere. To this 1L flask was added 300 mL of water. The entire contents of the flask were then transferred to a 1L separatory funnel and

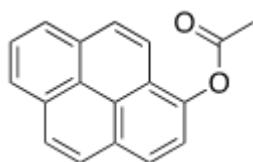
the funnel shaken and the layers allowed to separate and the water layer was discarded. The DCM layer was washed two more times with 300 mL of water each time followed by a final washing with 150 mL of saturated NaCl. The organic phase was then dried over MgSO₄ and rotovapped to a clear oil (14.96 g, 80% yield). This crude product was used without further purification.

¹H NMR (400 MHz, Chloroform-d) δ 5.05 (s, 1H), 3.46 (q, J = 6.0 Hz, 2H), 3.38 (t, J = 6.0 Hz, 2H), 1.38 (s, 9H).



2-(Boc-amino)propyl bromide (2): This was synthesized in the same manner as 2-(Boc-amino)ethyl bromide except 1-Bromopropylamine hydrobromide (Sigma-Aldrich) (21.27g, 97.6 mmol) was substituted for 1-Bromoethylamine hydrobromide. Result a clear oil (20.2 g, 87% yield).

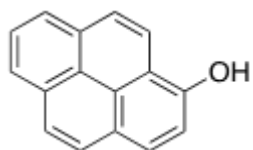
¹H NMR (400 MHz, Chloroform-d) δ 4.77 (s, 1H), 3.40 (t, J = 6.5 Hz, 2H), 3.23 (q, J = 6.4 Hz, 2H), 2.01 (p, J = 6.5 Hz, 2H), 1.40 (s, 9H).



Acetoxy-Pyrene (3): Synthesis followed an adapted literature prep.¹¹³ Pyrene (Aldrich, 40.45 g, 200 mmol) was dissolved in 160 mL acetic acid (Across Organic) and 600 mL benzene (sigma Aldrich) in a 1L RBF. The mixture was stirred at RT until all of the pyrene dissolved. The vessel was then fitted with a reflux condenser and purged with Ar (g). To the flask was added 98.3 g (222 mmol) of lead (IV) acetate (Across Organic stabilized with 5% acetic acid). The reaction vessel was then purged again with Ar (g) and left on an Ar (g) bubbler. The reaction was then refluxed for three hours. The reaction was then allowed to cool to RT. Here we find that the best workup that minimized lead waste and contaminated glassware is to first rotovap the reaction mixture under

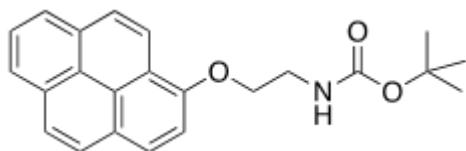
reduced pressure to a brown tar like sludge being careful to avoid bumping. The sludge was then dissolved in chloroform (ca 200 mL three times. Some of the inorganic salts did not dissolve and were reserved in the original RBF) and passed through a plug of silica gel. The resulting brown solution was then rotovapped to ca. 100mL. To this was added ca. 50 mL of silica gel. The resulting slurry was rotovapped and then held under reduced pressure for several hours to remove residual solvents (mostly the acetic acid). Once the silica gel was free flowing, it was added to a silica gel column packed using a mobile phase of 15:85 hexanes: toluene. The column was eluded with 15:85 hexanes: toluene. The product was rotovapped from the eluent. White solid (21.86 g, 42% yield)

^1H NMR (400 MHz, Chloroform-d) δ 8.20 – 8.14 (m, 3H), 8.13 – 8.05 (m, 2H), 8.03 (s, 2H), 8.00 (t, $J = 7.6$ Hz, ^1H), 7.79 (d, $J = 8.3$ Hz, ^1H), 2.56 (s, 3H).



Hydroxyl-pyrene (4): Acetoxy-pyrene (15g, 69 mmol) was dissolved in 450 mL of ethanol and 280 mL of DI water in a 1L RBF fitted with a reflux condenser. To this was added 15 g (375 mmol) of sodium hydroxide (Sigma Aldrich). The resulting reaction mixture was first purged with Ar (g) then heated under Ar (g) at 75 oC for 3 hr's. The resulting solution was allowed to cool to RT. The ethanol was then evaporated under reduced pressure on a Rotovap (this must be done slowly to avoid bumping). The RBF was then transferred to an ice bath. Concentrated HCl (37% Sigma-Aldrich) was then added dropwise. Eventually the product will precipitate as a white powder. The pH was adjusted to 1 though further addition of HCl. The resulting suspension was filtered and the powder washed with a copious amount of water. The powder was dried overnight on the frit to remove excess water. White solid (14.3g, 95% yield). This material was used without furfur purification or characterization.

pyrene-O-ethyl-BOC (5): To a 100 mL RBF was added 1g (4.58 mmol) of 4, 3.14 g (22.8 mmol) of potassium carbonate (Fisher Chemical) and 30 mL acetonitrile. The hydroxyl pyrene was allowed

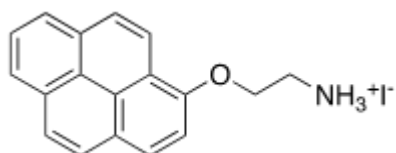


to dissolve under stirring and 2.56 g (11.4 mmol) of **1** was added. The reaction mixture was purged with Ar (g) and the reaction stirred overnight under Ar (g) at 65 °C. The reaction was then allowed to cool. To the reaction was added 50 mL water and the resulting suspension was then added to 500 mL of water. The solid was separated by filtration and allowed to dry on the frit for 2 hours. The resulting solid was chromatographed in 85:15 Hexanes: Ethyl acetate. White solid (450 mg, 27% yield)

^1H NMR (400 MHz, Chloroform- d) δ 8.44 (d, $J = 9.2$ Hz, ^1H), 8.15 – 8.03 (m, 4H), 8.00 – 7.94 (m, 2H), 7.90 (d, $J = 9.0$ Hz, ^1H), 7.53 (d, $J = 8.4$ Hz, ^1H), 5.13 (s, ^1H), 4.39 (t, $J = 5.1$ Hz, 2H), 3.78 (q, $J = 5.5$ Hz, 2H), 1.49 (s, 9H).

^{13}C NMR (101 MHz, Chloroform- d) δ 131.86, 131.77, 127.36, 126.69, 126.32, 125.62, 125.36, 124.57, 124.43, 121.13, 109.30, 68.48.

HRMS (ESI-TOF) Expected 361.1678 Observed 361.1687

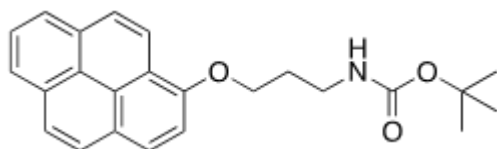


pyrene-O-ethyl- NH_3I (**6**): To a 50 mL RBF was added 370 mg (1.03 mmol) of **5**. To this was added 35 mL of dioxane and **5** was allowed to dissolve. To this was added 0.69g (3.08 mmol) of 57 wt% hydroiodic acid containing no stabilizer (Sigma-Aldrich). The resulting solution was purged with Ar (g) and the reaction mixture stirred under Ar (g) at 50 °C for 1 hr. The reaction was then allowed to cool to RT and the product filtered. The product was washed with a copious amount of diethyl ether and dried under vacuum for several days. White powder (408 mg, 100% yield)

^1H NMR (400 MHz, DMSO- d_6) δ 8.67 (d, $J = 9.2$ Hz, ^1H), 8.42 – 7.94 (m, 10H), 7.80 (d, $J = 8.5$ Hz, ^1H), 4.66 – 4.41 (m, 2H), 3.54 – 3.44 (m, 2H).

^{13}C NMR (101 MHz, DMSO- d_6) δ 152.28, 131.63, 131.53, 127.69, 126.97, 126.65, 126.38, 125.52, 125.50, 125.34, 124.96, 124.76, 122.01, 119.91, 110.21, 65.77.

HRMS (ESI-TOF) Expected 262.1232 Observed 262.1226

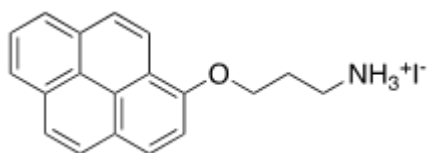


pyrene-O-propyl-BOC (7): To a 250 mL RBF was added 5g (218 mmol) of 4, 12.7 g (92 mmol) of potassium carbonate and 125 mL of acetonitrile. The hydroxyl pyrene was allowed to dissolve under stirring and 8.21 g (34.5 mmol) of 2 was added. The reaction mixture was purged with Ar (g) and the reaction stirred overnight under Ar (g) at 65 oC. The reaction was then allowed to cool. To the reaction was added 100 mL water and the resulting suspension was then added to 500 mL of water. The solid was separated by filtration and allowed to dry on the frit for 2 hours. The resulting solid was chromatographed in 80:20 Hexanes: Ethyl acetate slowly switching to 60:40 Hexanes Ethyl acetate. White solid (5.4 g, 63% yield)

^1H NMR (400 MHz, Chloroform- d) δ 8.44 (d, J = 9.1 Hz, ^1H), 8.14 – 8.07 (m, 3H), 8.04 (d, J = 9.2 Hz, ^1H), 8.01 – 7.93 (m, 2H), 7.89 (d, J = 9.0 Hz, ^1H), 7.53 (d, J = 8.4 Hz, ^1H), 4.92 (s, ^1H), 4.39 (t, J = 5.9 Hz, 2H), 3.51 (q, J = 6.4 Hz, 2H), 2.21 (p, J = 6.3 Hz, 2H), 1.47 (s, 9H).

^{13}C NMR (101 MHz, Chloroform- d) δ 156.19, 152.88, 131.86, 131.78, 127.36, 126.62, 126.26, 125.97, 125.59, 125.51, 125.22, 125.06, 124.46, 124.34, 109.14, 67.06, 38.50, 29.98.

HRMS (ESI-TOF) Expected 375.1834 Observed 375.1841



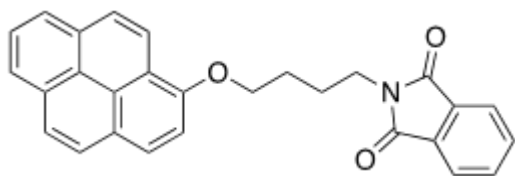
pyrene-O-propyl-NH $_3$ I (8): To a 250 mL RBF was added 5g (13.3 mmol) of 7. To this was added 150 mL of dioxane and 7 was allowed to dissolve. To this was added 8.98 g (40 mmol) of 57 wt% hydroiodic acid containing no stabilizer (Sigma-Aldrich). The resulting solution was purged

with Ar (g) and the reaction mixture stirred under Ar (g) at 50 oC for 1 hr. The reaction was then allowed to cool to RT and the product filtered. The product was washed with a copious amount of diethyl ether and dried under vacuum for several days. White powder (5.10 g, 95% yield)

^1H NMR (400 MHz, DMSO- d_6) δ 8.41 (d, J = 9.2 Hz, ^1H), 8.27 (d, J = 8.5 Hz, ^1H), 8.24 – 8.12 (m, 3H), 8.11 – 7.94 (m, 3H), 7.80 (s, 3H), 7.76 (d, J = 8.5 Hz, ^1H), 4.46 (t, J = 5.9 Hz, 2H), 3.18 (q, J = 6.4 Hz, 2H), 2.35 – 2.09 (m, 2H).

^{13}C NMR (101 MHz, DMSO- d_6) δ 152.25, 131.22, 131.06, 127.28, 126.48, 126.37, 125.97, 124.93, 124.83, 124.72, 124.47, 124.22, 124.10, 120.82, 119.35, 109.82, 65.51, 36.63, 27.15.

HRMS (ESI-TOF) Expected 276.1362 Observed 276.1387

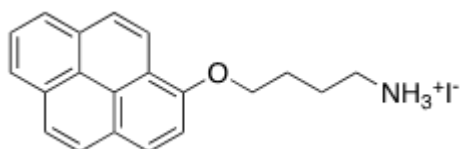


pyrene-O-butyl-phthalimide (9): To a 100 mL RBF was added 2g (9.16 mmol) of 4, 3.80 g (27.5 mmol) of potassium carbonate (Fisher Chemical) and 70 mL acetonitrile. The hydroxyl pyrene was allowed to dissolve under stirring and 3.10 g (11 mmol) of N-(4-bromobutyl)phthalimide (Across Organic) was added. The reaction mixture was purged with Ar (g) and the reaction stirred overnight under Ar (g) at 65 oC. The reaction was then allowed to cool. The reaction mixture was then poured into 250 mL of water. The water layer was then extracted with DCM once with 100mL and twice with 50 mL. The organic layers were combined and dried over MgSO_4 . The DCM was then Roto-vapped to yield the crude product. The resulting solid was chromatographed in 55:45 DCM: Hexanes switching to 70:30 DCM: Hexanes once residual N-(4-bromobutyl)phthalimide was eluted. Product is a yellow solid (3.10 g, 80% yield). Note that product does not fluoresce under 365 nm irradiation on the column.

^1H NMR (400 MHz, Chloroform- d) δ 8.43 (d, J = 9.1 Hz, ^1H), 8.14 – 7.84 (m, 7H), 7.77 (dd, J = 5.4, 3.1 Hz, 2H), 7.61 (dd, J = 5.4, 3.0 Hz, 2H), 7.50 (d, J = 8.4 Hz, ^1H), 4.50 – 4.20 (m, 2H), 3.88 – 3.83 (m, 2H), 2.10 – 1.94 (m, 4H).

^{13}C NMR (101 MHz, Chloroform- d) δ 168.43, 152.82, 133.73, 131.95, 131.68, 131.65, 127.18, 126.34, 126.01, 125.74, 125.40, 125.19, 124.90, 124.14, 124.09, 123.05, 121.18, 120.35, 109.10, 68.02, 37.69, 26.85, 25.44.

HRMS (ESI-TOF) Expected 419.1521 Observed 429.1529

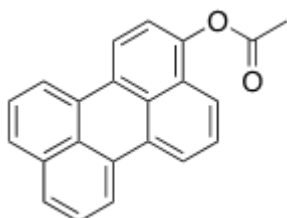


pyrene-O-butyl-NH₃I (10): To a 500 mL RBF was added 150 mL of ethanol and 3g (7.15 mmol) of 9. To this was added 8.95 g of hydrazine monohydrate. The reaction was flushed with Ar (g) and stirred under Ar (g) for 5 hr's at 65 °C. The reaction was cooled to RT and ca. ½ of the ethanol was rotovapped off. To the resulting suspension, 100 mL of DCM was added and this mixture was filtered and the resulting solid washed with 50 mL of DCM twice. The filtrate was collected and rotovapped to a solid. This solid was suspended in 100 mL DCM and filtered. The solid was washed 2X with DCM and the filtrate collected. This process was repeated one more time. The resulting oil recovered after rotovapping was precipitated with 100 mL water. The solid was filtered off and washed with a copious amount of water to remove residual hydrazine. This solid was then dissolved in 100 mL of dioxane and to this was added 1.76g (7.86 mmol) hydroiodic acid containing no stabilizer (Sigma-Aldrich). The resulting solution was rotovapped to a solid and this solid first sonicated with diethyl ether and then transferred to a frit where it was washed with a copious amount of diethyl ether. The resulting white solid was then dried under vacuum for several days (2.80g, 94% yield).

^1H NMR (400 MHz, DMSO- d_6) δ 8.39 (d, J = 9.1 Hz, ^1H), 8.26 (d, J = 8.5 Hz, ^1H), 8.20 (td, J = 8.0, 1.1 Hz, 2H), 8.14 (d, J = 9.2 Hz, ^1H), 8.10 – 8.00 (m, 2H), 7.97 (d, J = 9.0 Hz, ^1H), 7.77 (d, J = 8.5 Hz, ^1H), 7.71 (s, 3H), 4.40 (t, J = 6.0 Hz, 2H), 3.06 – 2.90 (m, 2H), 2.10 – 1.95 (m, 2H), 1.95 – 1.82 (m, 2H).

^{13}C NMR (101 MHz, DMSO- d_6) δ 152.47, 131.22, 131.05, 127.28, 126.43, 126.28, 126.00, 124.94, 124.71, 124.57, 124.41, 124.14, 124.13, 120.75, 119.30, 109.82, 38.81, 25.91, 24.18.

HRMS (ESI-TOF) Expected 290.1545 Observed 290.1545

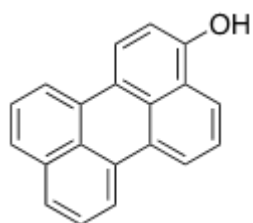


acetoxy-perylene (11): To a 1L RBF was added 5g (19.8 mmol) of perylene (Acros Organic), 200 mL of benzene and 200 mL of chloroform and 10 mL of acetic acid. The RBF was then purged with nitrogen and heated in an oil bath at 80 oC until most (but not all) of the perylene dissolved. To this was added 9.25g (19.84 mmol) lead (IV) acetate stabilized with 5% acetic acid in one portion. The flask was then stoppered and flushed again with nitrogen. The resulting solution was heated at 80 oC for 3 hr's. The RBF was then allowed to cool to RT. The solvent was then removed by rotary evaporation until brown-black solid was recovered. To this was added 200 mL of DCM and the slurry was agitated mechanically and sonicated to dissolve most of the product. This slurry was then passed over a pad of silica gel. The flask was washed twice with 100 mL of DCM each time and these washings also passed through the silica gel plug. The filtrate was combined and rotovapped extensively to remove the acetic acid. The resulting yellow-brown powder was then redissolved in 150 mL of DCM and silica gel added to the RBF. The DCM was then removed by rotary evaporation and the resulting powder added to the top of a silica gel column packed with 50:50 DCM: Hexanes. The product was then isolated through elution with DCM to yield a yellow powder (2.83g, 46% yield).

^1H NMR (400 MHz, Chloroform- d) δ 8.25 – 8.10 (m, 4H), 7.74 – 7.65 (m, 3H), 7.55 – 7.43 (m, 3H), 7.28 (d, J = 8.2 Hz, ^1H), 2.48 (s, 3H).

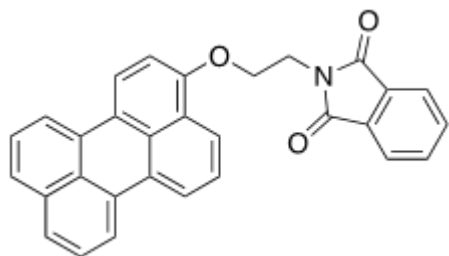
^{13}C NMR (101 MHz, Chloroform- d) δ 169.86, 146.61, 135.11, 132.12, 132.09, 131.28, 131.21, 130.27, 129.98, 128.90, 128.63, 128.34, 128.32, 121.20, 121.14, 121.01, 120.79, 120.26, 119.41, 21.55.

HRMS (ESI-TOF) Expected 310.0994 Observed 310.0991



hydroxyl-perylene (12): To a 1L RBF was added 2.4 g of 11 (7.7 mmol) and 2.4g sodium hydroxide (60 mmol). To this was added 300 mL of ethanol and 150 mL of DI water. The flask was then purged with nitrogen and heated with an oil bath at 70 oC for 3 hrs. In this reaction, the original yellow powder will not dissolve to a significant extent. As the ester is hydrolyzed, the resulting phenoxide is soluble in this ethanol/water cosolvent and dissolves to form a dark red solution. The reaction should be run until all of the powder dissolves and the solution presents as a dark red color. Sometimes this takes longer than 3 hrs depending on how powdered 11 is. Once all of the starting material is reacted, the resulting solution is cooled to RT. The majority of the ethanol is then removed by rotary evaporation. The phenoxide product will start to precipitate as the solvent becomes mostly water. The rotary evaporation was ceased at this point. The RBF was transferred to an ice bath and allowed to cool for several minutes. To the resulting slurry was concentrated HCl was slowly added until the pH reached ca. 1. The RBF was then allowed to return to RT and allowed to stir vigorously for ¹Hr. The solid was then recovered by filtration. The resulting solid was first washed with a copious amount of DI water and allowed to dry on the frit for several minutes and then transferred to a RBF and dried on a vacuum line overnight. The resulting crude product was used in the next step without further purification, yellow-green solid (1.21 g, 58% yield, significant yield lost in filtration process).

Perylene-O-ethyl-phthalimide (13): Please note that typically the boc protecting group is used for the deprotection step because it is more convenient than using the Gabriel synthesis. In this case, the boc protected ammine product was nearly insoluble and in our hands impossible to chromatograph effectively. The use of the phthalimide strategy in this case greatly improved solubility and



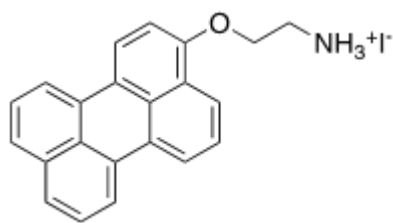
ease of purification. To a RBF was added 0.75g (2.8 mmol) of 12, 1.77g (7 mmol) of 2-bromoethyl phthalimide (Sigma Aldrich) and 2.32g (138 mmol) of potassium carbonate. To this was added 150 mL of acetonitrile. The RBF was then purged with nitrogen and the mixture heated under nitrogen overnight at 75 oC. The RBF was then allowed to cool. The resulting solution was then poured into 500 mL of DI water. The resulting precipitate was collected by filtration and dried on the frit for ca. 2hrs. This solid was then dissolved in 200 mL of DCM and the DCM dried with a small amount of MgSO₄ and passed through a cotton pad to remove insoluble materials. Silica gel was then added to the resulting solution and the DCM removed by rotary evaporation. The resulting powder was then loaded onto the top of a silica gel column and the material chromatographed with 100% DCM. Note that the product band does not fluoresce significantly on the column. The isolated product was then recovered by rotary evaporation to yield an orange powder (576 mg, 46% yield).

¹H NMR (400 MHz, Chloroform-d) δ 8.19 (dd, J = 7.7, 1.1 Hz, ¹H), 8.13 (dd, J = 7.6, 1.0 Hz, ¹H), 8.10 – 8.01 (m, 3H), 7.89 (dd, J = 5.5, 3.0 Hz, 2H), 7.72 (dd, J = 5.5, 3.1 Hz, 2H), 7.66 – 7.57 (m, 2H), 7.50 – 7.40 (m, 3H), 6.84 (d, J = 8.4 Hz, ¹H), 4.43 (t, J = 5.3 Hz, 2H), 4.30 (t, J = 5.3 Hz, 2H).

¹³C NMR (101 MHz, Chloroform-d) δ 134.05, 132.04, 127.61, 126.53, 126.40, 126.18, 123.38, 122.02, 120.95, 120.43, 119.82, 118.87, 105.54, 37.43. (Compound poorly soluble – Low I/Sig)

HRMS (ESI-TOF) Expected 441.1365 Observed 441.1365

perylene-O-ethyl-NH₃I (14): To a RBF was added 450 mg (1.02 mmol) of 13, 200 mL of EtOH and 1.53g of Hydrazine monohydrate. The RBF was then flushed with nitrogen and heated overnight under nitrogen at 70 oC. By then end of the reaction, the starting material should mostly dissolve to



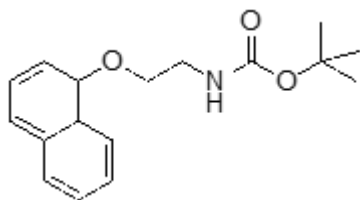
form a yellow solution. Some precipitate is normal but this should be yellow after the complete reaction of starting material. Once this did not occur overnight and an additional portion of hydrazine was added and the reaction allowed to proceed at 70 °C for several more hours. The RBF was then allowed to cool to RT and the solution poured into 1L of DI water. The resulting yellow precipitate was recovered by filtration. The solid was then washed with 50 mL of water three times. This wet solid was then checked by ^1H NMR to ensure that all phthalhydrazide was removed from the recovered product. The wet solid was then transferred to a RBF containing 250 mL of dioxane. The RBF was sonicated to disperse the free-base product. To this was added 577 mg of 57 wt% hydroiodic acid containing no stabilizer. The RBF was then sonicated for 20 min and stirred for an additional 40 min. The resulting solid was then allowed to settle and was recovered by filtration. This solid was then washed with a copious amount of diethyl ether and dried on the frit for ca. 5 min. The solid was then dried under vacuum for several days, yellow solid (324 mg, 72% yield).

^1H NMR (400 MHz, DMSO- d_6) δ 8.42 (dd, $J = 7.7, 1.1$ Hz, ^1H), 8.38 – 8.28 (m, 3H), 8.25 (dd, $J = 7.6, 1.0$ Hz, ^1H), 8.05 (s, 3H), 7.77 (d, $J = 8.1$ Hz, ^1H), 7.74 – 7.69 (m, ^1H), 7.62 – 7.45 (m, 3H), 7.10 (d, $J = 8.4$ Hz, ^1H), 4.40 (t, $J = 4.9$ Hz, 2H), 3.41 (t, $J = 5.0$ Hz, 2H).

^{13}C NMR (101 MHz, DMSO- d_6) δ 153.39, 134.41, 130.70, 130.50, 130.34, 128.76, 127.88, 127.61, 126.93, 126.81, 126.75, 126.17, 125.60, 123.63, 122.43, 121.51, 121.36, 120.46, 119.47, 106.68, 64.80, 38.52.

HRMS (ESI-TOF) Expected 312.1388 Observed 312.1388

naphthalene-O-ethyl-BOC (15): To a 100 mL RBF was added 1g (6.9 mmol) of 1-naphthol (Sigma Aldrich), 6.67g (48.3 mmol) of potassium carbonate and 50 mL of acetonitrile. To this was added 3.88g (17.3 mmol) of 1. The resulting reaction mixture was flushed with nitrogen and

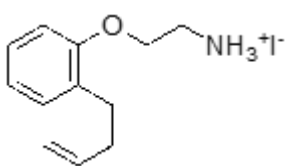


heated overnight at 65 oC under nitrogen. The reaction was then allowed to cool and 50 mL of water was then added to the reaction mixture. The entire contents of the RBM were then poured into 500 mL of water. At this point an oil segregated to the surface. This was left for 20 min in which time, this oil crystallized. The resulting solid was recovered by filtration. Once this solid was dry it was chromatographed on silica gel with 50:50 DCM: Hexanes. The product was recovered by rotary evaporation (0.92g, 46% yield).

^1H NMR (400 MHz, Chloroform-d) δ 8.33 – 8.20 (m, ^1H), 7.85 – 7.76 (m, ^1H), 7.54 – 7.43 (m, 3H), 7.39 – 7.34 (m, ^1H), 6.80 (dd, $J = 7.6, 1.0$ Hz, ^1H), 5.07 (s, ^1H), 4.20 (t, $J = 5.1$ Hz, 2H), 3.70 (q, $J = 5.4$ Hz, 2H), 1.47 (s, 9H).

^{13}C NMR (101 MHz, Chloroform-d) δ 156.07, 154.38, 134.63, 127.66, 126.59, 125.96, 125.59, 125.37, 104.87, 79.73, 67.65, 40.37, 28.54.

HRMS (ESI-TOF) Expected 287.1521 Observed 287.1524

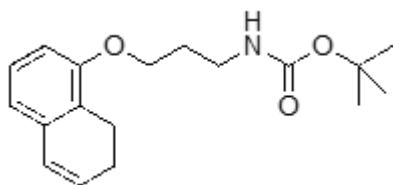


naphthalene-O-ethyl-NH₃I (16): To a 50 mL RBF was added 800mg (2.78 mmol) of 15 and 25 mL of dioxane. To this was added 1.56g (6.97 mmol) of hydroiodic acid 57% containing no stabilizer. The reaction was stirred under nitrogen at 50 oC for one hour. The resulting solution was then rotovapped to a solid. This solid was then suspended in diethyl ether and sonicated. The solid was then recovered by filtration and washed with a copious amount of diethyl ether. The resulting white solid was dried under vacuum for several days (791mg, 90% yield).

^1H NMR (400 MHz, DMSO- d_6) δ 8.50 – 8.38 (m, ^1H), 8.03 (s, 3H), 7.92 – 7.84 (m, ^1H), 7.59 – 7.48 (m, 3H), 7.44 (dd, J = 8.3, 7.6 Hz, ^1H), 7.00 (dd, J = 7.7, 1.0 Hz, ^1H), 4.52 – 4.12 (m, 2H), 3.39 (t, J = 4.9 Hz, 2H).

^{13}C NMR (101 MHz, DMSO- d_6) δ 153.86, 134.43, 127.78, 127.03, 126.54, 125.58, 125.19, 122.73, 121.04, 105.71, 65.01, 38.99.

HRMS (ESI-TOF) Expected 188.1075 Observed 188.1071



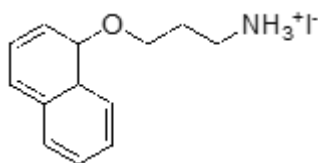
naphthalene-O-propyl-BOC (17): To a 100 mL RBF was added 1g (6.9 mmol) of 1-naphthol (Sigma Aldrich), 4.76g (34.5 mmol) of potassium carbonate and 50 mL of acetonitrile. To this was added 3.2g (13.9 mmol) of 2. The resulting reaction mixture was flushed with nitrogen and heated overnight at 65 oC under nitrogen. The reaction was then allowed to cool and 50 mL of water was then added to the reaction mixture. The entire contents of the RBM were then poured into 500 mL of water. The resulting precipitate was recovered by filtration. Once this solid was dry it was chromatographed on silica gel with 70:30 DCM: Hexanes eventually switching to 100% DCM. The product was recovered by rotary evaporation (1.56g, 75% yield).

^1H NMR (400 MHz, Chloroform- d) δ 8.37 – 8.20 (m, ^1H), 7.83 – 7.74 (m, ^1H), 7.54 – 7.41 (m, 3H), 7.37 (dd, J = 8.3, 7.5 Hz, ^1H), 6.81 (dd, J = 7.5, 1.1 Hz, ^1H), 4.90 (s, ^1H), 4.21 (t, J = 5.9 Hz, 2H), 3.44 (td, J = 6.5, 4.9 Hz, 2H), 2.13 (p, J = 6.2 Hz, 2H), 1.45 (s, 9H).

^{13}C NMR (101 MHz, Chloroform- d) δ 156.15, 154.59, 134.62, 127.63, 126.53, 125.96, 125.69, 125.36, 122.00, 120.50, 104.70, 66.30, 38.53, 29.71, 28.55.

HRMS (ESI-TOF) Expected 301.1678 Observed 301.1680

naphthalene-O-propyl-NH $_3$ I (18): To a 50 mL RBF was added 1.30g (4.3 mmol) of 18 and 25 mL of dioxane. To this was added 2.42g (10.8 mmol) of hydroiodic acid 57% containing no

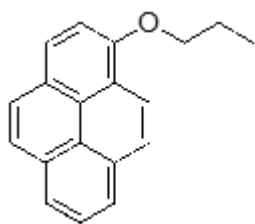


stabilizer. The reaction was stirred under nitrogen at 50 oC for one hour. The resulting solution was then rotovapped to a solid. This solid was then suspended in diethyl ether and sonicated. The solid was then recovered by filtration and washed with a copious amount of diethyl ether. The resulting white solid was dried under vacuum for several days (1.03g, 72% yield).

^1H NMR (400 MHz, DMSO- d_6) δ 8.22 – 8.14 (m, ^1H), 7.91 – 7.84 (m, ^1H), 7.75 (s, 3H), 7.57 – 7.47 (m, 3H), 7.43 (dd, J = 8.3, 7.4 Hz, ^1H), 6.97 (dd, J = 7.6, 1.1 Hz, ^1H), 4.25 (t, J = 5.9 Hz, 2H), 3.18 – 2.95 (m, 2H), 2.27 – 1.99 (m, 2H).

^{13}C NMR (101 MHz, DMSO- d_6) δ 153.71, 134.01, 127.51, 126.48, 126.19, 125.28, 124.85, 121.47, 120.10, 105.22, 64.76, 36.62, 26.96.

HRMS (ESI-TOF) Expected 202.1232 Observed 202.1228



1-Propoxyphenanthrene (19): To a 100 mL RBF was added 1g (4.58 mmol) of 4, 2.53g (18.33 mmol) of potassium carbonate, and 40 mL of acetonitrile. To this was added 1.13g (9.16 mmol) 1-bromopropane (Sigma Aldrich). The resulting mixture was flushed with nitrogen and stirred overnight under nitrogen at 60 oC. The reaction was allowed to cool and then poured into 250 mL of water. The aqueous layer was then extracted three times with 100 mL of DCM three times. The organic extracts were combined and dried over MgSO_4 . The DCM was removed with rotary evaporation and the resulting solid was chromatographed in 75:25 Hexanes: DCM. A white powder was recovered from the eluent (825 mg, 69% yield).

^1H NMR (400 MHz, Chloroform- d) δ 8.50 (d, J = 9.2 Hz, ^1H), 8.14 – 8.02 (m, 4H), 7.99 – 7.93 (m, 2H), 7.89 (d, J = 8.9 Hz, ^1H), 7.54 (d, J = 8.4 Hz, ^1H), 4.29 (t, J = 6.4 Hz, 2H), 2.38 – 1.92 (m, 2H), 1.21 (t, J = 7.4 Hz, 3H).

^{13}C NMR (101 MHz, Chloroform- d) δ 153.39, 131.91, 131.87, 127.40, 126.39, 126.18, 126.01, 125.63, 125.27, 125.15, 125.02, 124.30, 124.22, 121.45, 120.60, 109.33, 70.64, 23.05, 10.96.

4.5.2 *Single crystal preparation for structure evaluation and conductivity measurements*

All single crystal samples were prepared using vapor diffusion of dichloromethane into γ -butyrolactone (GBL) solutions containing 2:1 molar ratio of organic ammonium iodide salt: lead (II) iodide. The concentration of GBL solution was critical to obtain high quality samples for both single crystal X-ray diffraction and for electrical measurements (table 4.3).

The control molecules butyl, hexyl, and octyl ammonium iodide were synthesized through the equimolar reaction of hydroiodic acid using the corresponding amine in dioxane. The dioxane was then removed by rotary evaporation and the resulting solid washed extensively with diethyl ether and then dried under vacuum for several days.

Detailed crystal preparation procedures: The following procedures were followed to prepare devices for conductivity measurements. These procedures were utilized to ensure minimal disturbance to the crystals and particularly the crystal faces and to ensure good electrical contact with the FTO substrate. First, six 4 mL glass vials were prepared with the following solvents. To vials 1 and 2, 800 μL of Chlorobenzene (CB) and 200 μL of GBL were added and mixed. To vial 3, 1800 μL of CB and 200 μL of GBL were added. To Vial 4, 1950 μL CB and 50 μL GBL added and to Vials 5 and 6 2000 μL of CB was added. This gradient to less and less GBL prevented the precipitation of precursor solution without causing noticeable degradation of the crystals. To wash the crystals, a 1000 μL micropipette tip was used. First, the tip of the pipet tip was cut off to create a larger opening of ca 5mm. The pipet was set at 500 μL volume. The piped tip was first placed into the crystallization solution and 500 μL of solvent and crystals extracted. The pipet was then held vertically

	Solvent	Anti Solvent	Starting Solution Concentration (wt%)	Crystals appeared around (hrs)
(naphthalene-O-ethyl-NH ₃) ₂ PbI ₄	GBL	DCM	35	24
(naphthalene-O-propyl-NH ₃) ₂ PbI ₄	GBL	DCM	5-10	24
(naphthalene-O-propyl-NH ₃) ₂ PbI ₄ (C ₄ H ₆ O ₂) _{0.5}	GBL	DCM	40	1
(pyrene-O-ethyl-NH ₃) ₂ PbI ₄	GBL	DCM	1	36
(pyrene-O-propyl-NH ₃) ₂ PbI ₄	GBL	DCM	0.5-1	48
(pyrene-O-butyl-NH ₃) ₂ PbI ₄	GBL	DCM	10	12
(perylene-O-ethyl-NH ₃) ₂ PbI ₄	GBL	DCM	0.25-1	24
(butyl-NH ₃) ₂ PbI ₄	GBL	DCM	60	4
(hexyl-NH ₃) ₂ PbI ₄	GBL	DCM	60	4
(octyl-NH ₃) ₂ PbI ₄	GBL	DCM	35	48

Table 4.3: Crystallization conditions: Crystals were prepared by adding 200 ul of the following GBL solutions to individual 4 mL glass vials. These glass vials were then placed in a larger outer container containing dichloromethane. The initial concentration of the precursor solution was important to achieve large, high-quality crystals.

for ca 20s until the dense crystals had settled to the bottom. The tip of the pipet was then placed just under the surface of the first wash vial and the crystals allowed to fall from the pipet solution into the wash vial with minimal transfer of the crystallization solution. This transfer process was repeated from vial to vial to progressively clean the crystals. In rare cases, precipitate was visible after a transfer step. This usually resulted from too much of the previous solution being transferred with the crystals. If this was observed, then that sample was discarded over fear that this would lead to defects on the crystal surface that would affect the conductivity measurement. Once the crystals were transferred to the final wash solution, they were put onto a substrate within 2 hrs. Right before device preparation, 5 μL of GBL was added to this solution. This small amount of GBL helps the crystals adhere and recrystallize at the interface of the substrate affording good adhesion and more reproducible conductivity measurements. After this GBL was added, a pipet was prepared in the same way as previously described and the crystals were transferred to un-pattered FTO by briefly touching the tip of the pipette to the FTO and dragging the meniscus around the surface. The crystals were then allowed to dry for 10 min. After drying, good quality and large crystals were selected by polarized optical microscopy. TEM grid with $113\mu\text{m} \times 113\mu\text{m}$ open squares were then placed on these crystals and gold was evaporated in a thermal evaporator to a final thickness of 50 nm. After evaporation, these crystals were kept in a glove box until measurement.

In all cases, plate-like crystals which ranged in color from yellow to red appeared in ca. 24 hrs. These plate-like crystals form due to preferential crystal growth along the 2D inorganic galleries. To measure conductivity along the layered axis of these plate-like crystals, they were separated from their mother liquor and washed before being drop-cast on a freshly cleaned unpatterned FTO substrates (Solaronix, $15\Omega/\text{square}$). Small square gold pads of $113\mu\text{m} \times 113\mu\text{m} \times 50\text{nm}$ were then thermally evaporated on top of the crystals through a TEM shadow mask (Electron Microscopy Sciences T200-Cu) and conductivity was measured on the single crystal samples in a 2-electrode geometry (Signatone probe station, Agilent 4155C semiconductor parameter analyzer). The conductivity was then measured through the thickness of the crystals and normalized by pad area and

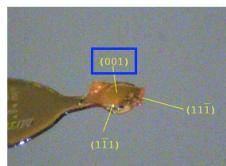
crystal thickness. Out-of-plane conductivity was measured both with the microscope lamp turned to full power (MLC-150C illuminator - 150W EKE halogen lamp) and in the absence of any light. The conductivity was calculated using the linear region of the I-V curve (voltage sweep from -5 to 5 V) and parameterized based on individual device thicknesses. The thickness of each device was determined by optical profilometry (Zygo 3D Optical Profiler and Bruker Contour GT-K). The averages of multiple devices per crystal and across several crystals was taken to determine the out-of-plane conductivity of a given structure.

4.5.3 *Crystal structure determination*

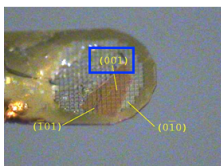
Single crystal X-ray data were collected at room temperature on a Kappa Apex 3 diffractometer. For control crystals with previously-reported structures, partial data sets were collected for unit cell determination (between 60 and 90 frames) to validate against the previously reported structures. For all other crystals, a complete data set was collected for structure solution and refinement. In all cases the face-indexing tool in Apex 3 was utilized to verify the direction of the layered axis for electrical measurements (Figure 4.20). Using Olex 2, crystal structures were solved using ShelXS structure solution program using direct methods and refined using ShelXL refinement package using least squares minimizations. The inorganic lattice was refined anisotropically without restraints. The organic cations were refined anisotropically with the exception of hydrogen atoms which were placed in idealized positions. Additional restraints to the bond lengths and thermal ellipsoids for the organic cations were applied where necessary. Structural information for seven layered perovskites in this work is provided in table 4.1.

4.5.4 *Substrate preparation*

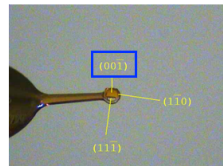
Glass and patterned ITO substrates (Thin Film Devices, 20 ohms/square) were cleaned by sequential sonication in hexane, soapy water, milli-q water, and a 1:1:1 mixture of isopropanol, acetone, and methanol. After drying, clean substrates were treated for 20 minutes in a UV-ozone

a) (butyl-NH₃)₂PbI₄

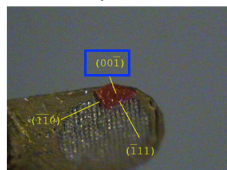
a = 8.71 b = 8.90 c = 27.70
 $\alpha = 90^\circ \beta = 90^\circ \gamma = 90^\circ$ Ortho P

b) (hexyl-NH₃)₂PbI₄

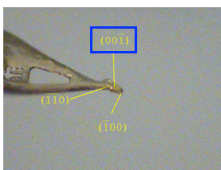
a = 8.70 b = 8.96 c = 32.77
 $\alpha = 90^\circ \beta = 90^\circ \gamma = 90^\circ$ Ortho C

c) (octyl-NH₃)₂PbI₄

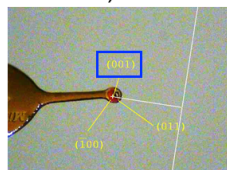
a = 8.65 b = 8.95 c = 37.32
 $\alpha = 90^\circ \beta = 90^\circ \gamma = 90^\circ$ Ortho P

d) (naphthalene-O-ethyl-NH₃)₂PbI₄

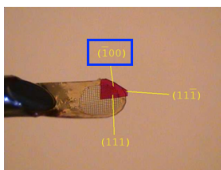
a = 12.52 b = 12.47 c = 39.55
 $\alpha = 90^\circ \beta = 97.66^\circ \gamma = 90^\circ$ Mono C

e) (naphthalene-O-propyl-NH₃)₂PbI₄

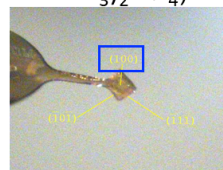
a = 23.05 b = 8.86 c = 8.28
 $\alpha = 90^\circ \beta = 95.28^\circ \gamma = 90^\circ$ Mono P

f) (pyrene-O-ethyl-NH₃)₂PbI₄

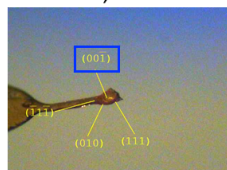
a = 12.43 b = 12.40 c = 48.36
 $\alpha = 90^\circ \beta = 95.86^\circ \gamma = 90^\circ$ Mono C

g) (pyrene-O-propyl-NH₃)₂PbI₄

a = 49.38 b = 8.48 c = 9.45
 $\alpha = 90^\circ \beta = 94.95^\circ \gamma = 90^\circ$ Mono C

h) (pyrene-O-butyl-NH₃)₂PbI₄

a = 53.30 b = 6.17 c = 12.56
 $\alpha = 90^\circ \beta = 90.32^\circ \gamma = 90^\circ$ Mono C

i) (perylene-O-ethyl-NH₃)₂PbI₄

a = 26.29 b = 8.86 c = 8.71
 $\alpha = 90^\circ \beta = 94.28^\circ \gamma = 90^\circ$ Mono P

Figure 4.20: Unit cell parameters as determined by APEX 3 using either Difference Vectors or Fast Fourier Transform and Face Indexing Tool in APEX 3 showing that the layered axis is perpendicular to the plate.

cleaner (Bioforce Nanosciences). Poly(3,4-ethylenedioxythiophene) polystyrene sulfonate in toluene (PEDOT:complex) (Ossila) was filtered through a 0.25 μm PTFE filter before spin-coating at 5000 RPM with a 5000 RPM/second ramp rate for 30 seconds. PEDOT:complex (Ossila) films were then annealed at 120 $^{\circ}\text{C}$ for 10 minutes in a nitrogen-filled glovebox. Poly(3,4-ethylenedioxythiophene) polystyrene sulfonate in water (PEDOT:PSS) (Heraeus) was filtered through a 0.45 μm nylon filter before spin-coating at 5000 RPM with a 1000 RPM/second ramp rate for 60 seconds. PEDOT:PSS (Heraeus) films were then annealed at 150 $^{\circ}\text{C}$ for 20 minutes in a nitrogen-filled glovebox.

4.5.5 *Thin film preparation*

Thin film samples other than those intended for device active layers were prepared by spin-casting 2:1 molar ratios of organic ammonium iodide salt: lead (II) iodide (TCI Chemical) dissolved in 20-30 wt% in 50 vol% DMF 50 vol% DMSO onto freshly cleaned glass slides at 2000 RPM. With respect to solubility, we found that a combination of DMF and DMSO as a solvent mixture was very helpful in dissolving the poorly soluble bulky organic cations in our layered perovskite materials. From this solvent mixture, we spin-coated and annealed crystalline thin films of each of the layered perovskite materials. Each of the layered perovskites crystallized easily in thin films except for that containing the perylene derivative. These substrates were then annealed on a hotplate at 110 $^{\circ}\text{C}$ for 30 min. The resulting thin films were characterized by powder X-ray diffraction (PXRD) (Scintag XDS2000 using Cu $K\alpha$ radiation at 40kV and 1-20 mA current), ultraviolet-visible absorption spectroscopy (Perkin Elmer LAMBDA 1050) and by grazing incidence wide angle X-ray scattering (GIWAXS) (Beamline 8-ID-E Advanced Photon Source, Argonne National Laboratory). GIWAXS was performed with beam energy 10.92 KeV and with 0.140 incidence angle. The unit cell determined from single crystal X-ray diffraction was compared by overlaying a predicted pattern¹¹⁴ onto the GIWAXS patterns to verify the formation of the same phase in thin films and single crystals (figure 4.2 and 4.3).

4.5.6 Device fabrication

We designed the layers of our photovoltaic devices as shown in Figure 5A. The devices in this study were fabricated in a nitrogen-filled glovebox. Pyrene-O-propyl-NH₃I and lead iodide were dissolved at a 2:1 molar ratio in a 25 wt% solvent mixture of 50 vol% DMF 50 vol% DMSO and heated for 30 minutes at 65 °C. For optimized (pyrene-O-propyl-NH₃)₂PbI₄ devices, the active layer was spin cast onto PEDOT:PSS-coated, patterned ITO substrates for 25 seconds at 4000 RPM with a ramp time of 7 seconds. The active layer was then annealed for 1 minute at 140 °C. 50 nm silver contacts were thermally evaporated onto the substrates at a pressure of 10^{-6} mbar using a shadow mask to define 4 mm² devices. Finally, devices were tested in air on a Newport solar simulator with a Keithley 2400 sourcemeter with a voltage ramp rate of 0.2 V/s.

4.5.7 NMR characterization

NMR spectra (¹H and ¹³C) were collected on a 400 MHz Agilent DD MR-400 system. Deuterated solvents (Dimethyl sulfoxide and Chloroform) were purchased from sigma Aldrich and all chemical shifts are reported from spectra internally referenced to the solvent residual. Peaks reported in ¹³C spectra are those achieving 3I/s or greater and are clearly resolved from residual solvent or in peak-peak overlap.

4.5.8 Mass determination

Mass Determination: High-resolution mass spectrometry was acquired using an Agilent 6210 LC-TOF high-resolution time of flight mass spectrometer with an Agilent 1200 series LC pump stack and Autosampler. Electrospray ionization was used in all cases.

4.5.9 UPS Measurements

Ultraviolet Photoelectron Spectroscopy (UPS) data was used to determine the HOMO level of the perovskite crystals and the organic molecules alone. UPS data was collected using a Thermo

Scientific ESCALAB 250Xi with a -8.0 V sample bias and a He I ($h\nu = 21.2$ eV) source. The spectrum width of UPS data is related to the work function, ϕ , according to the equation $\phi = h\nu - BE$. The edges of the spectrum were fit in order to determine the binding energy.¹¹⁵ In the inelastic cutoff region, the intercept between the tangent to the main peak and a linear fit to the background level was used as the edge of the spectrum. At the Fermi edge, the onset of the peak was determined as energy at which the intersection between the local tangent to the spectrum and a linear fit to the background level occurs. The difference in energy between the Fermi edge and the inelastic cutoff region was then subtracted from the incident energy (21.2 eV) in order to determine the HOMO level of the material.

5 SUMMARY

The work in this dissertation demonstrates the development of a deeper understanding of structure-property relationships in hybrid organic inorganic photovoltaics. We explored three different hybrid photovoltaic active layer architectures. In chapter 2, we investigated an electrodeposited hybrid zinc oxide-organic lamellar structure. While the constituent chromophore amphiphiles in this system influenced the morphology and orientation of the lamellar domains, the organics themselves did not pack in a crystalline fashion. Within a dye-sensitized solar cell constructed from this film, it was clear that the internal surfaces of the lamellar structure were not electronically accessible to liquid electrolyte. This led to devices that performed with lower efficiency than conventional device architectures such as DSSCs and BHJs. We were able to characterize the differences between our lamellar active layer and conventional architectures by fabricating various types of control devices and performing quantum efficiency and impedance spectroscopy measurements.

In chapter 3 and 4, we transitioned towards investigating perovskite solar cells. Perovskite solar cell active layers are crystalline hybrid semiconducting materials, and as such, they have significantly better optoelectronic properties than the lamellar structures we synthesized in chapter 2. While the MAPbI_3 active layer in a PSC is technically a hybrid crystal due to the presence of the methylammonium cation, the instability of the methylammonium cation is also the reason PSC devices are so unstable. Our work has taken two different approaches towards improving the stability of these devices. We began with examining the stability on an intergranular length scale. Perovskite-polymer hybrid films have been explored to some extent by other groups, but their morphological characterization did not identify a way to see phase contrast between perovskite and polymer domains. We have achieved that with our study by using the differences in stiffness between the perovskite and polymer domains to mechanically probe the hybrid structure on the nanoscale using AFM. The chemical interactions between the polymer functional groups and the perovskite grains play an

important role in improving chemical stability on the perovskite active layer. Through our study, we were able to identify a polymer, poly(acrylic acid), which imparts significantly better stability under humid, illuminated conditions than other polymers. In addition to stabilizing the perovskite phase from degrading to its hydrate phase under humidity, this polymer also acts to stabilize the methylammonium cation in the MAPbI_3 lattice through acid-base interactions. Our device stability experiments showed that polymer species in the perovskite active layer tend to decrease efficiency to some extent while improving their lifetime. Achieving a balance between efficiency and device lifetime ultimately does not reach the goal of constructing a device that has both high-efficiency and high stability, which may be impossible in devices that contain the methylammonium cation.

Our second study towards improving the stability of perovskite solar cells was to synthesize a number of organic cations to fit into 2D layered perovskite structures. Our approach to fitting conjugated organic chromophores into the layered perovskite structure was inspired by the work we performed on lamellar hybrid structures in chapter 2. The PCE of layered perovskite solar cells is significantly lower than MAPbI_3 , but by removing the methylammonium cation entirely, the stability is greatly improved in these structures. We synthesized a series of layered perovskites containing organic chromophores of the form $(\text{aromatic-O-linker-NH}_3)_2\text{PbI}_4$ where the aromatic moiety is naphthalene, pyrene or perylene and the linker is ethyl, propyl or butyl. Through our investigation we found that organic packing and intramolecular hydrogen bonding influence the inorganic lattice structure and optoelectronic properties of the resultant 2D perovskite material. Improved conduction and optical absorption in these materials leads to improved photovoltaic device efficiency. Specifically, the out-of-plane conductivity was improved over three orders of magnitude compared to an aliphatic control, and our best photovoltaic device achieved a record efficiency of 1.24%. This study may prove to be fertile ground for future research as there are several different directions that this investigation could go. Higher-n devices, anisotropic charge transfer studies, band structure calculations, and new synthetic targets for layered perovskites are all reasonable directions to pursue in the future.

REFERENCES

1. Lewis, N. S. & Nocera, D. G. Powering the planet: Chemical challenges in solar energy utilization. *Proceedings of the National Academy of Sciences* **103**, 15729–15735 (2006).
2. Hosenuzzaman, M. *et al.* Global prospects, progress, policies, and environmental impact of solar photovoltaic power generation. *Renewable and Sustainable Energy Reviews* **41**, 284–297 (2015).
3. British Petroleum. BP Statistical Review of World Energy 2017. *British Petroleum*, 1–52 (2017).
4. International Energy Agency. *Key World Energy Statistics 2017* tech. rep. (2017), 1–97.
5. Pachauri, R. & Reisinger, A. *Climate Change 2007 : An Assessment of the Intergovernmental Panel on Climate Change* tech. rep. (IPCC, Geneva, Switzerland, 2007), 36–40.
6. Dlugokencky, E. & Tans, P. *ESRL Global Monitoring Division - Global Greenhouse Gas Reference Network*
7. Fu, R. *et al.* *U.S. Solar Photovoltaic System Cost Benchmark : Q1 2017* U.S. Solar Photovoltaic System Cost Benchmark : Q1 2017 tech. rep. September (2017).
8. Kalowekamo, J. & Baker, E. Estimating the manufacturing cost of purely organic solar cells. *Solar Energy* **83**, 1224–1231 (2009).
9. Hashmi, G. *et al.* Review of materials and manufacturing options for large area flexible dye solar cells. *Renewable and Sustainable Energy Reviews* **15**, 3717–3732 (2011).
10. Scharber, M. C. & Sariciftci, N. S. Efficiency of bulk-heterojunction organic solar cells. *Progress in Polymer Science* **38**, 1929–1940 (2013).
11. Pierret, R. F. *Semiconductor Device Fundamentals* (Addison-Wesley, 1996).
12. Rühle, S. Tabulated values of the Shockley-Queisser limit for single junction solar cells. *Solar Energy* **130**, 139–147 (2016).
13. Tao, Y. & Rohatgi, A. in *Nanostructured Solar Cells* (InTech, Feb. 2017).
14. Shockley, W. & Queisser, H. Detailed Balance Limit of Efficiency of p-n Junction Solar Cells *. *Journal of Applied Physics* **1640**, 510–519 (1960).
15. Kojima, A., Teshima, K., Shirai, Y. & Miyasaka, T. Organometal halide perovskites as visible-light sensitizers for photovoltaic cells. *Journal of the American Chemical Society* **131**, 6050–6051 (2009).
16. Yang, Z. *et al.* Unraveling the Exciton Binding Energy and the Dielectric Constant in Single-Crystal Methylammonium Lead Triiodide Perovskite. *Journal of Physical Chemistry Letters* **8**, 1851–1855 (2017).
17. Lee, J. K. *et al.* Processing additives for improved efficiency from bulk heterojunction solar cells. *Journal of the American Chemical Society* **130**, 3619–3623 (2008).

18. Ruiz-Carretero, A. *et al.* Stepwise self-assembly to improve solar cell morphology. *Journal of Materials Chemistry A* **1**, 11674 (2013).
19. Aytun, T., Barreda, L., Ruiz-Carretero, A., Lehrman, J. A. & Stupp, S. I. Improving solar cell efficiency through hydrogen bonding: A method for tuning active layer morphology. *Chemistry of Materials* **27**, 1201–1209 (2015).
20. Grätzel, M. Dye-sensitized solar cells. *Journal of Photochemistry and Photobiology C: Photochemistry Reviews* **4**, 145–153 (2003).
21. Manser, J. S. & Kamat, P. V. Band filling with free charge carriers in organometal halide perovskites. *Nat. Photonics* **8**, Ahead of Print (2014).
22. Green, M. A., Ho-Baillie, A. & Snaith, H. J. The emergence of perovskite solar cells. *Nat Photon* **8**, 506–514 (2014).
23. Frost, J. M. *et al.* Atomistic origins of high-performance¹. Frost, J. M. *et al.* Atomistic origins of high-performance in hybrid halide perovskite solar cells. *Nano Lett.* **14**, 2584–90 (2014).e in hybrid halide perovskite solar cells. *Nano letters* **14**, 2584–90 (2014).
24. Jeon, N. J. *et al.* Solvent engineering for high-performance inorganic-organic hybrid perovskite solar cells. *Nature materials* **13**, 1–7 (2014).
25. Wang, Z., Shi, Z., Li, T., Chen, Y. & Huang, W. Stability of Perovskite Solar Cells: A Prospective on the Substitution of the A Cation and X Anion. *Angewandte Chemie International Edition*, 2–25 (2016).
26. Sanchez, C., Galo, G. J., Ribot, F. & Grosso, D. Design of functional nano-structured materials through the use of controlled hybrid organic-inorganic interfaces. *Comptes Rendus Chimie* **6**, 1131–1151 (2003).
27. Israelachvili, J. N. *Soft and Biological Structures* 535–576 (2011).
28. Braun, P. V., Osenar, P. & Stupp, S. I. Semiconducting superlattices templated by molecular assemblies. *Nature* **380**, 325–328 (Mar. 1996).
29. Sofos, M. *et al.* Nanoscale structure of self-assembling hybrid materials of inorganic and electronically active organic phases. *Journal of Physical Chemistry C* **112**, 2881–2887 (2008).
30. Oosterhout, S. D. *et al.* The effect of three-dimensional morphology on the efficiency of hybrid polymer solar cells. *Nature Materials* **8**, 818–824 (2009).
31. Blom, P. W. M., Mihailetschi, V. D., Koster, L. J. A. & Markov, D. E. Device physics of polymer:Fullerene bulk heterojunction solar cells. *Advanced Materials* **19**, 1551–1566 (2007).
32. Sofos, M. *et al.* A synergistic assembly of nanoscale lamellar photoconductor hybrids. *Nature Materials* **8**, 68–75 (Jan. 2009).
33. Herman, D. J., Goldberger, J. E., Chao, S., Martin, D. T. & Stupp, S. I. Orienting periodic organic-inorganic nanoscale domains through one-step electrodeposition. *ACS Nano* **5**, 565–573 (2011).
34. Bruns, C. J., Herman, D. J., Minuzzo, J. B., Lehrman, J. A. & Stupp, S. I. Rationalizing molecular design in the electrodeposition of anisotropic lamellar nanostructures. *Chemistry of Materials* **25**, 4330–4339 (2013).

35. Kodali, H. K. & Ganapathysubramanian, B. Computer simulation of heterogeneous polymer photovoltaic devices. *Modelling and Simulation in Materials Science and Engineering* **20** (2012).
36. Schmidt-Mende, L. & MacManus-Driscoll, J. L. ZnO - nanostructures, defects, and devices. *Materials Today* **10**, 40–48 (2007).
37. Yu, J., Wang, Q., O'Hare, D. & Sun, L. Preparation of two dimensional layered double hydroxide nanosheets and their applications. *Chem. Soc. Rev.* **46**, 5950–5974 (2017).
38. Lau, G. C. *et al.* Oriented Multiwalled Organic-Co(OH)₂ Nanotubes for Energy Storage. *Advanced Functional Materials* **1702320**, 1702320 (2017).
39. Lehrman, J. A., Cui, H., Tsai, W.-W., Moyer, T. J. & Stupp, S. I. Supramolecular control of self-assembling terthiophene – peptide conjugates through the amino acid side chain. *Chemical Communications* **48**, 9711 (2012).
40. Briseno, A. L. *et al.* Oligo- and polythiophene/ZnO hybrid nanowire solar cells. *Nano Letters* **10**, 334–340 (2010).
41. Izaki, M. & Omi, T. Transparent zinc oxide films prepared by electrochemical reaction. *Applied Physics Letters* **68**, 2439–2440 (1996).
42. Izaki, M., Watase, S. & Takahashi, H. Low-temperature electrodeposition of room-temperature ultraviolet-light-emitting zinc oxide. *Advanced Materials* **15**, 2000–2002 (2003).
43. Yoshida, T., Komatsu, D., Shimokawa, N. & Minoura, H. Mechanism of cathodic electrodeposition of zinc oxide thin films from aqueous zinc nitrate baths. *Thin Solid Films* **451-452**, 166–169 (2004).
44. Choi, K. S. & Steinmiller, E. M. Electrochemical synthesis of lamellar structured ZnO films via electrochemical interfacial surfactant templating. *Electrochimica Acta* **53**, 6953–6960 (2008).
45. Li, W. *et al.* Efficient small bandgap polymer solar cells with high fill factors for 300 nm thick films. *Advanced Materials* **25**, 3182–3186 (2013).
46. Mitzi, D. B. Templating and structural engineering in organic-inorganic perovskites. *Journal of the Chemical Society, Dalton Transactions*, 1–12 (2001).
47. Saparov, B. & Mitzi, D. B. Organic-Inorganic Perovskites: Structural Versatility for Functional Materials Design. *Chemical Reviews* **116**, 4558–4596 (2016).
48. Yoshida, T. *et al.* Electrodeposition of Inorganic/Organic Hybrid Thin Films. *Advanced Functional Materials* **19**, 17–43 (2009).
49. Schaefer, D. W., Martin, J. E., Wiltzius, P. & Cannell, D. S. Fractal geometry of colloidal aggregates. *Physical Review Letters* **52**, 2371–2374 (1984).
50. Wang, Z. S., Sayama, K. & Sugihara, H. Efficient eosin Y dye-sensitized solar cell containing Br⁻/Br₃⁻ electrolyte. *Journal of Physical Chemistry B* **109**, 22449–22455 (2005).
51. Shi, Y. *et al.* Solid-state synthesis of ZnO nanostructures for quasi-solid dye-sensitized solar cells with high efficiencies up to 6.46%. *Advanced Materials* **25**, 4413–4419 (2013).

52. Zhang, S. *et al.* Synthesis and optical properties of novel organic-inorganic hybrid nanolayer structure semiconductors. *Acta Materialia* **57**, 3301–3309 (2009).
53. Loser, S. *et al.* A naphthodithiophene-diketopyrrolopyrrole donor molecule for efficient solution-processed solar cells. *Journal of the American Chemical Society* **133**, 8142–8145 (2011).
54. Hu, X. *et al.* Rigid triarylamine-based D – A – π – A structural organic sensitizers for solar cells: the significant enhancement of open-circuit photovoltage with a long alkyl group. *RSC Advances* **3**, 22544 (2013).
55. Tian, H. *Molecular Devices for Solar Energy Conversion and Storage* (eds Tian, H., Boschloo, G. & Hagfeldt, A.) (Springer Singapore, Singapore, 2018).
56. Magne, C., Moehl, T., Urien, M., Grätzel, M. & Pauporté, T. Effects of ZnO film growth route and nanostructure on electron transport and recombination in dye-sensitized solar cells. *J. Mater. Chem. A* **1**, 2079–2088 (2013).
57. Wang, Q., Moser, J.-E. & Grätzel, M. Electrochemical Impedance Spectroscopic Analysis of Dye-Sensitized Solar Cells. *The Journal of Physical Chemistry B* **109**, 14945–14953 (2005).
58. Wang, Q. *et al.* Characteristics of high efficiency dye-sensitized solar cells. *J. Phys. Chem. B* **110**, 25210 (2006).
59. Weingarten, A. *et al.* Supramolecular Packing Controls H₂ Photocatalysis in Chromophore Amphiphile Hydrogels. *Journal of the American Chemical Society* **137**, 15241–15246 (2015).
60. Weingarten, A. S. *et al.* Self-assembling hydrogel scaffolds for photocatalytic hydrogen production. *Nature chemistry* **6**, 964–970 (2014).
61. Kazantsev, R. V. *et al.* Crystal-Phase Transitions and Photocatalysis in Supramolecular Scaffolds. *Journal of the American Chemical Society* **139**, 6120–6127 (2017).
62. Cao, L., Xu, F., Liang, Y. Y. & Li, H. L. Preparation of the novel nanocomposite Co(OH)₂/ultra-stable Y zeolite and its application as a supercapacitor with high energy density. *Advanced Materials* **16**, 1853–1857 (2004).
63. Bach, U. *et al.* Solid-state dye-sensitized mesoporous TiO₂ solar cells with high photon-to-electron conversion efficiencies. *Nature* **395**, 583–585 (1998).
64. Kim, S. B. *et al.* Simple, large-scale patterning of hydrophobic ZnO nanorod arrays. *ACS Applied Materials and Interfaces* **4**, 3910–3915 (2012).
65. Lee, M. M., Teuscher, J., Miyasaka, T., Murakami, T. N. & Snaith, H. J. Efficient Hybrid Solar Cells Based on Meso-Superstructured Organometal Halide Perovskites. *Science* **338**, 643–647 (2012).
66. Bi, D. *et al.* Efficient luminescent solar cells based on tailored mixed-cation perovskites. *Science Advances* **2**, e1501170–e1501170 (2016).
67. Tamayo, A. B., Tantiwivat, M., Walker, B. & Nguyen, T. Q. Design, synthesis, and self-assembly of oligothiophene derivatives with a diketopyrrolopyrrole core. *Journal of Physical Chemistry C* **112**, 15543–15552 (2008).

68. Dong, Q. *et al.* Electron-hole diffusion lengths > 175 nm in solution-grown CH₃NH₃PbI₃ single crystals. *Science* **347**, 967–970 (Feb. 2015).
69. Saliba, M. *et al.* Cesium-containing triple cation perovskite solar cells: improved stability, reproducibility and high efficiency. *Energy Environ. Sci.* **9**, 1989–1997 (2016).
70. Burschka, J. *et al.* Sequential deposition as a route to high-performance perovskite-sensitized solar cells. *Nature* **499**, 316–320 (2013).
71. Ball, J. M., Lee, M. M., Hey, A. & Snaith, H. J. Low-temperature processed meso-structured thin-film perovskite solar cells. *Energy & Environmental Science* **6**, 1739 (2013).
72. Malinkiewicz, O. *et al.* Perovskite solar cells employing organic charge-transport layers. *Nature Photonics* **8**, 128–132 (2014).
73. Li, Z. *et al.* Stabilizing Perovskite Structures by Tuning Tolerance Factor: Formation of Formamidinium and Cesium Lead Iodide Solid-State Alloys. *Chemistry of Materials* **28**, 284–292 (2016).
74. Bryant, D. *et al.* Light and oxygen induced degradation limits the operational stability of methylammonium lead triiodide perovskite solar cells. *Energy Environ. Sci.* (2016).
75. Wang, Z., Shi, Z., Li, T., Chen, Y. & Huang, W. Stability of Perovskite Solar Cells: A Prospective on the Substitution of the A Cation and X Anion. *Angewandte Chemie - International Edition* **56**, 1190–1212 (2017).
76. Nakamura, E., Shoyama, K., Sato, W. & Guo, Y. Effects of Water on the Forward and Backward Conversions of Lead(II) Iodide to Methylammonium Lead Perovskite. *J. Mater. Chem. A* (2017).
77. Leijtens, T. *et al.* Overcoming ultraviolet light instability of sensitized TiO₂ with meso-structured organometal tri-halide perovskite solar cells. *Nature communications* **4**, 2885 (2013).
78. Li, Z. *et al.* Stabilizing Perovskite Structures by Tuning Tolerance Factor: Formation of Formamidinium and Cesium Lead Iodide Solid-State Alloys. *Chemistry of Materials* **28**, 284–292 (2016).
79. Zhao, Y. *et al.* A polymer scaffold for self-healing perovskite solar cells. *Nature Communications* **7**, 10228 (2016).
80. Guo, Y., Shoyama, K., Sato, W. & Nakamura, E. Polymer Stabilization of Lead(II) Perovskite Cubic Nanocrystals for Semitransparent Solar Cells. *Advanced Energy Materials* **6**, 1–9 (2016).
81. Xiang, W. *et al.* Improved air stability of perovskite hybrid solar cells via blending poly(dimethylsiloxane)-Urea copolymer. *J. Mater. Chem. A* **00**, 1–9 (2017).
82. Quan, L. N. *et al.* Ligand-Stabilized Reduced-Dimensionality Perovskites. *Journal of the American Chemical Society* **138**, 2649–2655 (2016).
83. Mitzi, D. B. Synthesis, Crystal Structure, and Optical and Thermal Properties of (C₄H₉NH₃)₂MI₄ (M = Ge, Sn, Pb). *Chemistry of Materials* **8**, 791–800 (1996).

84. Cao, D. H., Stoumpos, C. C., Farha, O. K., Hupp, J. T. & Kanatzidis, M. G. 2D Homologous Perovskites as Light-Absorbing Materials for Solar Cell Applications. *Journal of the American Chemical Society* **137**, 7843–7850 (2015).
85. Stoumpos, C. C. *et al.* Ruddlesden – Popper Hybrid Lead Iodide Perovskite 2D Homologous Semiconductors. *Chemistry of Materials* **28**, 2852–2867 (2016).
86. Stoumpos, C. C., Malliakas, C. D. & Kanatzidis, M. G. Semiconducting Tin and Lead Iodide Perovskites with Organic Cations: Phase Transitions, High Mobilities, and Near-Infrared Photoluminescent Properties. *Inorganic Chemistry* **52**, 9019–9038 (2013).
87. Rakita, Y., Cohen, S. R., Kedem, N. K., Hodes, G. & Cahen, D. Mechanical Properties of APbX₃ (A=Cs or CH₃NH₃; X=I or Br) Perovskite Single Crystals. *Arxiv preprint* **3**, 1–20 (2015).
88. Yang, J., Siempelkamp, B. D., Mosconi, E., De Angelis, F. & Kelly, T. L. Origin of the Thermal Instability in CH₃NH₃PbI₃ Thin Films Deposited on ZnO. *Chemistry of Materials* **27**, 4229–4236 (2015).
89. Wang, S., Jiang, Y., Juarez-Perez, E. J., Ono, L. K. & Qi, Y. Accelerated degradation of methylammonium lead iodide perovskites induced by exposure to iodine vapour. *Nature Energy* **2**, 16195 (2016).
90. Nguyen, W. H., Bailie, C. D., Unger, E. L. & McGehee, M. D. Enhancing the Hole-Conductivity of Spiro-OMeTAD without Oxygen or Lithium Salts by Using Spiro(TFSI)₂ in Perovskite and Dye-Sensitized Solar Cells. *Journal of the American Chemical Society* **136**, 10996–11001 (2014).
91. Jacobsson, T. J. *et al.* Unreacted PbI₂ as a Double-Edged Sword for Enhancing the Performance of Perovskite Solar Cells. *Journal of the American Chemical Society* **138**, 10331–10343 (2016).
92. Im, J.-H., Lee, C.-R., Lee, J.-W., Park, S.-W. & Park, N.-G. 6.5% Efficient Perovskite Quantum-Dot-Sensitized Solar Cell. *Nanoscale* **3**, 4088 (2011).
93. Derjaguin, B. V., Muller, V. M. & Toporov, Y. U. P. Effect of contact deformation on the adhesion of particles. *Journal of colloid and interface science* **52**, 105–108 (1975).
94. Ahn, N. *et al.* Highly Reproducible Perovskite Solar Cells with Average Efficiency of 18.3% and Best Efficiency of 19.7% Fabricated via Lewis Base Adduct of Lead(II) Iodide. *Journal of the American Chemical Society* **137**, 8696–8699 (2015).
95. Tsai, H. *et al.* High-efficiency two-dimensional ruddlesden-popper perovskite solar cells. *Nature* **536**, 312–317 (2016).
96. Smith, I. C., Hoke, E. T., Solis-Ibarra, D., McGehee, M. D. & Karunadasa, H. I. A Layered Hybrid Perovskite Solar-Cell Absorber with Enhanced Moisture Stability. *Angewandte Chemie - International Edition* **53**, 11232–11235 (2014).
97. Tanaka, K. *et al.* Two-dimensional Wannier excitons in a layered-perovskite-type crystal (C₆H₁₃NH₃)₂PbI₄. *Solid State Communications* **122**, 249–252 (2002).

98. Ishihara, T., Takahashi, J. & Goto, T. Exciton state in two-dimensional perovskite semiconductor $(\text{C}_{10}\text{H}_{21}\text{NH}_3)_2\text{PbI}_4$. *Solid State Communications* **69**, 933–936 (1989).
99. Mao, L. *et al.* Role of Organic Counterion in Lead- and Tin-Based Two-Dimensional Semiconducting Iodide Perovskites and Application in Planar Solar Cells. *Chemistry of Materials* **28**, 7781–7792 (2016).
100. Mitzi, D. B., Chondroudis, K. & Kagan, C. R. Design, Structure, and Optical Properties of Organic–Inorganic Perovskites Containing an Oligothiophene Chromophore. *Inorganic Chemistry* **38**, 6246–6256 (1999).
101. Braun, M., Tuffentsammer, W., Wachtel, H. & Wolf, H. Tailoring of energy levels in lead chloride based layered perovskites and energy transfer between the organic and inorganic planes. *Chemical Physics Letters* **303**, 157–164 (1999).
102. Braun, M., Tuffentsammer, W., Wachtel, H. & Wolf, H. Pyrene as emitting chromophore in organic – inorganic lead halide-based layered perovskites with different halides. *Chemical Physics Letters* **307**, 373–378 (1999).
103. Kitazawa, N. Excitons in two-dimensional layered perovskite compounds: $(\text{C}_6\text{H}_5\text{C}_2\text{H}_4\text{NH}_3)_2\text{Pb}(\text{Br},\text{I})_4$ and $(\text{C}_6\text{H}_5\text{C}_2\text{H}_4\text{NH}_3)_2\text{Pb}(\text{Cl},\text{Br})_4$. *Materials Science and Engineering: B* **49**, 233–238 (1997).
104. Stupp, S. I. Molecular Manipulation of Microstructures: Biomaterials, Ceramics, and Semiconductors. *Science* **277**, 1242–1248 (Aug. 1997).
105. Lédée, F. *et al.* Fast growth of monocrystalline thin films of 2D layered hybrid perovskite. *CrystEngComm* **19**, 2598–2602 (2017).
106. Muljarov, E. A., Tikhodeev, S. G., Gippius, N. A. & Ishihara, T. Excitons in self-organized semiconductor/insulator superlattices: PbI-based perovskite compounds. *Physical Review B* **51**, 14370–14378 (1995).
107. Ahmad, S. *et al.* Strong Photocurrent from Two-Dimensional Excitons in Solution-Processed Stacked Perovskite Semiconductor Sheets. *ACS Applied Materials and Interfaces* **7**, 25227–25236 (2015).
108. Du, K. Z. *et al.* Two-Dimensional Lead(II) Halide-Based Hybrid Perovskites Templated by Acene Alkylamines: Crystal Structures, Optical Properties, and Piezoelectricity. *Inorganic Chemistry* **56**, 9291–9302 (2017).
109. Knutson, J. L., Martin, J. D. & Mitzi, D. B. Tuning the band gap in hybrid tin iodide perovskite semiconductors using structural templating. *Inorganic Chemistry* **44**, 4699–4705 (2005).
110. Hautzinger, M. P. *et al.* Two-Dimensional Lead Halide Perovskites Templated by a Conjugated Asymmetric Diammonium. *Inorganic Chemistry*, acs.inorgchem.7b02285 (2017).
111. Behrouznejad, F., Shahbazi, S., Taghavinia, N., Wu, H.-P. & Wei-Guang Diao, E. A study on utilizing different metals as the back contact of $\text{CH}_3\text{NH}_3\text{PbI}_3$ perovskite solar cells. *J. Mater. Chem. A* **4**, 13488–13498 (2016).

112. Rogers, J. T., Schmidt, K., Toney, M. F., Bazan, G. C. & Kramer, E. J. Time-resolved structural evolution of additive-processed bulk heterojunction solar cells. *Journal of the American Chemical Society* **134**, 2884–2887 (2012).
113. Barabanov, I. I., Polukhin, A. V., Korolev, V. V., Kuibida, L. V. & Nefedov, A. A. Novel covalently linked pyrene-aryl azide systems: synthesis of 1-(4-azidobenzoyloxy)pyrene. *Mendeleev Communications* **25**, 260–261 (2015).
114. Jiang, Z. GIXSGUI: A MATLAB toolbox for grazing-incidence X-ray scattering data visualization and reduction, and indexing of buried three-dimensional periodic nanostructured films. *Journal of Applied Crystallography* **48**, 917–926 (2015).
115. Park, Y., Choong, V., Gao, Y., Hsieh, B. R. & Tang, C. W. Work function of indium tin oxide transparent conductor measured by photoelectron spectroscopy. *Applied Physics Letters* **68**, 2699–2701 (1996).

VITA

Daniel J. Fairfield

PhD in Materials Science and Engineering
d.j.fairfield@u.northwestern.edu

Education

Northwestern University	Evanston, IL
PhD Candidate, Materials Science and Engineering	2011-2018
Thesis Topic: Design and Synthesis of Hybrid Organic-Inorganic Photovoltaics	
GPA: 3.83	
University of Illinois	Urbana-Champaign, IL
Bachelor of Science, Materials Science and Engineering, Electronic Materials, May 2011	
GPA: 3.79	

Relevant Skills

- Scientific expertise—materials characterization (SEM, XRD, XPS), process development, thin film deposition, polymer science, electrodeposition, photovoltaic device fabrication, electrical characterization, mechanical testing, photocatalysis
- Soft skills—project management, laboratory management, scientific communication, collaborative research, mentorship

Research Experience

- | | |
|---|--------------|
| PhD Candidate, Stupp Laboratory Fall 2013-Present | Evanston, IL |
| <ul style="list-style-type: none"> • Discovered a mechanism by which polymer additives stabilize perovskite solar cells. Our team has shown that intermolecular interactions between polymers and halide perovskites increase film and device stability under humidity and illumination. • Designed a new layered perovskite crystal which is water stable and photoactive. Typical layered perovskites are insulating across their organic layers, however by incorporating conjugated organic molecules into these layers we have been able to increase conductivity and demonstrate the highest efficiency solar cells for this type of crystal. We have characterized the crystallinity and orientation of these crystals at the Advanced Photon Source at Argonne National Laboratory. • Collaborated on several projects involving photocatalytic production of hydrogen from water using self-assembled gels. XPS and GIXS studies that I performed on these assemblies were critical to understanding their structure. My expertise in this area has led to co-authorship on four manuscripts. | |
| Graduate research assistant, Stupp Laboratory Fall 2011-2013 | |
| <ul style="list-style-type: none"> • Developed a new method to create dye-sensitized solar cell active layers. Thin, porous films of organic-inorganic hybrid lamellar structures can be formed via electrodeposition rather than soaking a mesoporous scaffold with dye. This new technique is more scalable than blade-casting, however these devices showed poor long-term performance. • Optimized growth conditions for electrodeposited zinc oxide hybrid lamellar structures. The domain size and orientation of these structures can be tuned through rational design of the organic component. | |
| Research assistant, Sottos Research Group 2009-2011 | Urbana, IL |
| <ul style="list-style-type: none"> • Performed and analyzed Fluorescent Digital Image Correlation experiments—imaging the strain around a microchannel by digitally comparing optical microscopy images of the channel in a stressed and unstressed state. Our study found that nanoscale reinforcement | |

of microvascular networks for self-healing mitigates the weakening of bulk material caused by the vascular network.

- Designed and performed a proof-of concept experiment for microvascular self-healing foam
- Wrote a senior thesis and received an acknowledgement for this work in “Microvascular based self-healing polymeric foam” *Polymer* **2012**, 4231–4240
- Applied knowledge from coursework to develop a method for image-reversal photoresist processing for liftoff of electron beam deposited gold on a silicon substrate. I designed the photolithography mask used in this process using AutoCAD, and the substrates were used in experiments to pattern thin film polymers via laser spallation.

Research Assistant, Center for Plasma-Material Interactions, Summer 2008 Urbana, IL

- Assembled significant portions of the divertor edge and vapor shielding experiment—an experiment looking at the interaction of shielding materials with plasma for nuclear fusion
- Fabricated electronic circuits and maintained vacuum systems

Publications

“Structural reinforcement of microvascular networks using electrostatic layer-by-layer assembly with halloysite nanotubes” Solar C. Olugebefola, Andrew R. Hamilton, **Daniel J. Fairfield**, Nancy R. Sottos. Scott R. White. *Soft Matter*, **2014**, 10, 544

“Supramolecular Packing Controls H₂ Photocatalysis in Chromophore Amphiphile Hydrogels” Weingarten, Adam; Kazantsev, Roman; Palmer, Liam; **Fairfield, Daniel**; Koltonow, Andrew; Stupp, Samuel. *J. Am. Chem. Soc.*, **2015**, 137 (48), 15241–15246

“Molecular Packing of Amphiphilic Nanosheets Resolved by X-ray Scattering” Boris Harutyunyan, Adam Dannenhoffer, Sumit Kewalramani, Taner Aytun, **Daniel J. Fairfield**, Samuel I. Stupp, Michael J. Bedzyk. *J. Phys. Chem. C*, **2017**, 121 (2), 1047–1054

“Crystal Phase Transitions and Photocatalysis in Supramolecular Scaffolds” Roman V. Kazantsev, Adam J. Dannenhoffer, Adam S. Weingarten, Brian T. Phelan, Boris Harutyunyan, Taner Aytun, Ashwin Narayanan, **Daniel J. Fairfield**, Job Boekhoven, Hiroaki Sai, Andrew Senesi, Pascual I. O’Dogherty, Liam C. Palmer, Michael J. Bedzyk, Michael R. Wasielewski, Samuel I. Stupp. *J. Am. Chem. Soc.*, **2017**, 139 (17), 6120–6127

“Molecular Control of Internal Crystallization and Photocatalytic Function in Supramolecular Nanostructures” Roman V Kazantsev, Adam Dannenhoffer, Taner Aytun, Boris Harutyunyan, **Daniel J. Fairfield**, Michael J. Bedzyk, Samuel I. Stupp. Under review at Chem

“Enhanced Out-of-Plane Conductivity and Photovoltaic Performance in n = 1 Layered Perovskites through Organic Cation Design” **Daniel J. Fairfield***, James Passarelli*, Nicholas Sather, Mark Hendricks, Hiroaki Sai, Charlotte Stern, Liam Palmer, Samuel I. Stupp. Accepted for publication in *JACS* *co-first author

“Structure-Property Relationships and Chemical Stability in Polymer-Perovskite Hybrid Photovoltaic Active Layers” **Daniel J. Fairfield**, Hiroaki Sai, Ashwin Narayanan, James Passarelli, Michelle Chen, Joseph Palasz, Karen Qu, Liam C. Palmer, Michael Wasielewski, Samuel I. Stupp. In Preparation

Teaching and mentoring experience

Graduate research mentor

- Mentored a chemistry and two materials science PhD students in the Stupp group
- Taught electrodeposition and x-ray techniques to two PhD students in order for them to explore layered hybrid organic-inorganic cobalt hydroxide structures for energy storage

MRSEC Research Experience for Undergraduates Summer 2014

Mentored an REU student in a project on electrodeposited molybdenum sulfide for photocatalytic hydrogen production.

Teaching Assistant for Materials Science 301 Fall 2014, Fall 2015

- Designed a laboratory experiment for the class and assisted with lab instruction
- Held office hours and graded assignments

Undergraduate research mentor Winter 2015-Winter 2017

Mentored a chemistry undergraduate in the integrated science program. He learned about solar cell device engineering and organic chemical synthesis. His research was partially supported by an Institute for Sustainability and Energy at Northwestern grant and a Weinberg summer undergraduate research grant.